



รายงานวิจัยฉบับสมบูรณ์

โครงการ: ศึกษาการจับตัวของยากลุ่ม DAPY กับ double mutant K103N/Y181C HIV-1 RT โดยใช้ระเบียบวิธี ONIOM quantum chemical และ molecular dynamics simulation

เพ็ญศรี ศรีวับ

กันยายน 2554

รายงานวิจัยฉบับสมบูรณ์

โครงการ: ศึกษาการจับตัวของยากลุ่ม DAPY กับ double mutant K103N/Y181C HIV-1 RT โดยใช้ระเบียบวิธี ONIOM quantum chemical และ molecular dynamics simulation

เพ็ญศรี ศรีวับ สังกัดคณะวิทยาศาสตร์และเทคโนโลยี มหาวิทยาลัยเทคโนโลยีราชมงคลศรีวิชัย

สนับสนุนโดยสำนักงานคณะกรรมการการอุดมศึกษา และสำนักงานกองทุนสนับสนุนการวิจัย

(ความเห็นในรายงานนี้เป็นของผู้วิจัย สกอ. และ สกว. ไม่จำเป็นต้องเห็นด้วยเสมอไป)

Acknowledgments

The authors thank Associate Professor Dr. Supa Hannongbua for valuable critical comment and suggestion. This work was supported with grants from the Thailand Research Fund (MRG5280214). The Commission on Higher Education, Ministry of Education and Rajamangala University of technology Srivijaya is acknowledged for partial financial support. Thanks to Pongtep Nokkaew and Warabhorn Booyarat for their supporting, helpful assistance and sharing useful ideas.

เอกสารแนบหมายเลข 2

Abstract

Project Code: MRG5280214

Project Title: A study of the Binding of DAPY Inhibitors to Double Mutant K103N/Y181C

HIV-1 RT Based on the ONIOM quantum chemical และ molecular dynamics simulation

Investigator: Pensri Sivub, Faculty of Science and Technology, Rajamangala University

of Technology Srivijaya, Nakronsri Thammarat, 80110 Thailand.

E-mail Address: pensir srivub@hotmail.com

Project Period: 2009-2010

The multi-layered integration (ONIOM method) was used to study the interactions between DAPY inhibitors and the different binding sites of HIV-1 reverse transcriptase: the wild- type and a double mutation (K103N/Y181C or L100I/K103N). The calculated binding energy using the MP2/6-31G(d,p):B3LYP/6-31G(d,p):PM3 method for the TMC278-K103N/Y181C HIV-1 RT complex (-28.31 kcal/mol) is slightly decrease compared to wild-type (-30.01 kcal/mol). This lead to the specific interactions between TMC278 and key residues in binding pocket of the two complex structures being investigated. It was found that interaction energies calculated at MP2/6-31G(d,p) level between TMC278 and individual residues surrounding the binding pocket for both wild-type and K103N/Y181C HIV-1 RT are not significantly different excepted for mutated residue C181. These results are consistent with the observation that TMC278 shows high inhibitory affinities against for both wild type and K103N/Y181C enzymes. Consequently, the influence of X spacer connecting the left phenyl A ring and the pyrimidine was investigated to determine binding energy of compound 2 (O-linker) and compound 3(S-linker) to a double mutant K103N/Y181C enzyme compared with TMC278. Binding energies of compound 2 and 3(11.92 and 11.64 kcal/mol, respectively) were less than TMC278 (-28.31 kcal/mol). These results indicate that the NH- group of TMC278 as the most appropriate spacer to achieve high-level potency on double mutant K103N/Y181C. Therefore, NH- linker of TMC278 was used to study the effect of the substituent at position 2 and 6 on the left phenyl A ring. The binding energy of mono-substituted derivative 4 is less than TMC278 2 for both wild-type and K103N/Y181C enzymes, with the difference of -2.66 and -2.03, respectively. Moreover, it was found that binding energies of compound 5 (non-2,6-substituent on phenyl A-ring of TMC278) is less than that TMC278 for both wild-type and K103N/Y181C enzymes, with the greatest difference of -5.81 and

-5.11 kcal/mol, respectively. It is clearly that the substituent at position 2 and 6 on the left phenyl A ring of TMC278 is necessity maintained to achieve a high level of inhibition on wild type and K103N/Y181C enzymes. Furthermore, it point out that the other functionalities including electron-donating group (-OMe) and electron-withdrawing group (-CI) for compound 6 can replace the methyl group in TMC278 without loss of activity of this drug. This data can support further development of TMC278 derivatives.

With the L100l/K103N enzyme, the binding energy for TMC278-L100l/K103N HIV-1 RT complex is less than that of the wild-type complex by 9.71 kcal/mol. Also, the attractive interactions between TMC278 and K101, K103 and W229 were reduced compared to the wild-type by 5.92, -4.69 and 3.21 kcal/mol, respectively. It is important to note that hydrogen bonding occurring between TMC278 and K101 was also disturbed. Moreover, N103 in the binding pocket of the L100l/K103N enzyme creates a repulsive interaction with the inhibitor. This confirmed that TMC278 shows higher inhibitory affinities against wild-type and K103N/Y181C enzymes than L100l/K103N enzyme.

Keywords: Binding energy, HIV-1 RT, Interaction energy, DAPY inhibitors, TMC278, ONIOM method.

บทคัดย่อ

รหัสโครงการ: MRG5280214

ชื่อโครงการ: ศึกษาการจับตัวของยากลุ่ม DAPY กับ double mutant K103N/Y181C HIV-1 RT

โดยใช้ระเบียบวิธี ONIOM quantum chemical และ molecular dynamics

simulation

ชื่อนักวิจัย และสถาบัน: เพ็ญศรี ศรีวับ คณะวิทยาศาสตร์และเทคโนโลยี มหาวิทยาลัย

เทคโนโลยีราชมงคลศรีวิชัย วิทยาเขตนครศรีธรรมราช

E-mail Address: pensir_srivub@hotmail.com

ระยะเวลาโครงการ: ปี 2552-2553

งานวิจัยชิ้นนี้จึงมีเป้าหมายที่จะศึกษาการอันตริกริยาระหว่างยากลุ่ม DAPY ในเชื้อที่ไม่มีการ กลายพันธุ์และเชื้อที่มีการกลายพันธ์สองตำแหน่ง (K103N/Y181C หรือ L100l/K103N). โดยระเบียบวิธี ONIOM (B3LYP/6-31G(d,p):PM3 ค่าพลังงานการจับของสารเซิงซ้อน TMC278-K103N/Y181C HIV-1 RT (-28.31 kcal/mol) ที่ได้จากการคำนวณโดยระเบียบวิธี MP2/6-31G(d,p):B3LYP/6-31G(d,p):PM3 มี ค่าลดลงเล็กน้อยเมื่อเปรียบเทียบกับพลังงานการจับของเชื้อที่ไม่มีการกลายพันธุ์ (-30.01 kcal/mol) จากนั้นนำไปสู่การศึกษาอันตริกิริยาระหว่าง TMC278 และแอมิโนหลักในบริเวณการจับของเอนไซม์ทั้ง สองโครงสร้าง จากการศึกษาพบว่าค่าพลังงานการจับจากอันตรกิริยาระหว่างยาและแอมิโนแต่ละตัวใน โพรงการจับของเชื้อที่ไม่การกลายพันธ์และเชื้อที่มีการกลายพันธ์สองตำแหน่งมีค่าไม่แตกต่างกัน แสดง 278มีประสิทธิภาพการยับยั้งสูงทั้งในกรณีเชื้อที่ไม่มีการกลายพันธุ์และเชื้อที่มีการกลาย พันธ์สองตำแหน่ง K103N/Y181C จากนั้นศึกษาผลของ X spacer ที่เชื่อมต่อระหว่างวงแหวนฟีนิล ด้านซ้ายและไพริมีดีน (pyrimidine) ที่มีผลต่อค่าพลังงานการจับของสารประกอบ 2 (O-linker) และ สารประกอบ 3(S-linker) ในกรณีในเชื้อที่ไม่มีการกลายพันธุ์และเชื้อที่มีการกลายพันธ์สองตำแหน่ง K103N/Y181C พบว่าพลังงานการจับของสารประกอบ 2 และ 3(11.92 and 11.64 kcal/mol, ตามลำดับ) ี่มีค่าน้อยกว่าTMC278 ((-28.31 kcal/mol) ชี้ให้เห็นว่า NH- linker ในยาTMC278 เป็นกลุ่มที่เหมาะที่สุด ที่ทำให้ยา TMC มีประสิทธิภาพการออกฤทธิ์ได้สูงในเชื้อที่มีการกลายพันธ์สองตำแหน่ง 278 K103N/Y181C ดังนั้น ยา TMC 278 ที่มี NH- linker ถูกเลือกใช้เพื่อศึกษาผลหมู่แทนที่ที่ตำแหน่ง 2 and 6 บนวงแหวน phenyl A พบว่าค่าพลังงานการจับของสารประกอบที่ 4 มีค่าน้อยกว่า TMC278 2 ทั้งในกรณีเชื้อที่ไม่มีการกลายพันธุ์และเชื้อที่มีการกลายพันธ์สองตำแหน่ง K103N/Y181C มีค่าความ แตกต่างของพลังงานการจับสารประกอบที่ 4 และ TMC278ในกรณี เชื้อที่ไม่มีการกลายพันธุ์ และ ใน กรณี เชื้อที่มีการกลายพันธ์สองตำแหน่ง K103N/Y181C มีค่าเท่ากับ-2.66 และ -2.03 kcal/mol ตามลำดับ และพบว่าพลังงานการจับของสารประกอบที่ 5 (ไม่มีหมู่แทนที่ที่ตำแหน่งที่ 2,6- ของวง แหวน phenyl A) มีค่าน้อยกว่า TMC278 ทั้งกรณีเชื้อที่ไม่การกลายพันธ์และเชื้อที่มีการกลายพันธ์สอง ตำแหน่งมีค่าไม่แตกต่างกัน ซึ่ง มีค่าความแตกต่างของพลังงานการจับสารประกอบที่ 5 และ TMC278 ในกรณี เชื้อที่ไม่มีการกลายพันธุ์ และ ในกรณี เชื้อที่มีการกลายพันธ์สองตำแหน่ง K103N/Y181C มีค่า สูงถึง -5.81 and -5.11 kcal/mol ตามลำดับ จึงเห็นได้อย่างชัดเจนว่าจำเป็นต้องมีหมู่แทนที่ที่ตำแหน่ง 2 และ 6 ที่วงแหวน phenyl A ของ TMC278 เพื่อที่จะทำให้ยามีประสิทธิภาพการยับยั้งเชื้อที่ไม่มีการกลายพันธุ์ และ เชื้อที่มีการกลายพันธ์สองตำแหน่ง K103N/Y181C และนอกจากนี้หมู่ฟังก์ชันอื่นเช่น กลุ่มที่ให้อิเล็กตรอน(-OMe) และกลุ่มที่รับอิเล็กตรอน(-Cl) (สารประกอบที่6) สามารถใช้แทนกลุ่มเมทิล ใน TMC278 ทำให้ยาไม่สูญเสียประสิทธิภาพการออกฤทธิ์ ข้อมูลที่ได้สามารถนำไปสู่การพัฒนาการ ออกแบบของอนุพันธ์ในอนาคต

ค่าพลังงานการจับของ TMC278 ในเชื้อที่มีการกลายพันธ์สองตำแหน่ง L100l/K103N มีค่า น้อยกว่า เชื้อที่ไม่มีการกลายพันธุ์ ประมาณ 9.71 kcal/mol เนื่องมาจากอันตรกิริยาแบบดึงดูดระหว่าง TMC278 และ แอมิโนไลซีนตำแหน่ง101 แอมิโนไลซีนตำแหน่ง 103 และทริปโตแพนตำแหน่ง 229 ใน กรณีเชื้อที่มีการกลายพันธ์สองตำแหน่ง L100l/K103N ลดลงเมื่อเปรียบเทียบกับเชื้อที่ไม่มีการกลาย พันธุ์ ประมาณ 5.92, -4.69 และ 3.21 kcal/mol ตามลำดับ จุดสำคัญคือมีพันธะไฮโดรเจนระหว่าง TMC278 และแอมิโนตำแหน่งถูกรบกวน และนอกจากนี้พบว่ากรดแอมิโนแอสพาราจีนตำแหน่ง 103 ใน โพรงการจับของเชื้อที่มีการกลายพันธ์สองตำแหน่ง L100l/K103N มีอันตรกิริยาแบบผลักกับยา แสดง ให้เห็นว่า TMC278 มีประสิทธิภาพการยับยั้งสูงในกรณีเชื้อที่ไม่มีการกลายพันธ์ และเชื้อที่มีการกลาย พันธ์สองตำแหน่ง K103N/Y181C และสูงกว่าเชื้อที่มีการกลายพันธ์สองตำแหน่ง

คำหลัก: พลังงานการจับของยา เอนไซม์reverse transcriptase พลังงานการเกิดอันตรกิริยาระหว่างตัว ยากับกรดอะมิโนในโพรงการจับของเอนไซม์ ยากลุ่ม DAPY ยา TMC278 และระเบียบวิธี ONIOM

Introduction

Currently, more than 33 million people are infected with human immunodeficiency virus type 1 (HIV-1) which is the etiological agent of the Acquired Immune Deficiency Syndrome (AIDS). Essential enzymes for the replication cycle of this virus include reverse transcriptase (RT), protease (PR), and integrase (IN), all of which are attractive targets for the development of new anti-AIDS drugs. This research work concentrates on HIV-1 RT because it is highly essential for HIV replication. It is an essential enzyme involved in the life cycle of the HIV responsible for virus replication from single-stranded RNA viral genome into a double-stranded proviral DNA, which is subsequently integrated into the host chromosome (Jacobo-Molina et al., 1991; Whitcomb et al., 1992; De Clercq, 1995a, 1995b). Therefore, HIV-1 RT is one of the most important enzymes in the HIV-1 life cycle targeted for the development of new anti-AIDS drugs to treat HIV-1 infections. The inhibitor of HIV-1 RT can be divided into two main classes, nucleoside reverse transcriptase inhibitors (NRTIs) and non-nucleoside reverse transcriptase inhibitors (NNRTIs). Nucleoside reverse transcriptase inhibitors (NRTIs) are relatively toxic, which coupled with the emergence of drug-resistant viral variants, limited the therapeutic efficacy of the NRTIs (Schinazi, 1997; Tantillo et al., 1994; De Clercq, 1994 and 1995a). NNRTs are non-competitive inhibitors which are highly specific for HIV-1 RT at a common allosteric site approximately 10 Å from the polymerase active site. The NNRTIs show similar butterfly-like shapes that consist of two (or more) wings. The three-dimensional structure of HIV-1 RT was distorted by NNRTIs directly bound to it, resulting in decreasing catalytic function. (Ren et al., 1995). NNRTIs (Figure 3), e.g. nevirapine, delavirdine, loviride, 9-Cl TIBO [(+)-(S)-4,5,6,7-Tetrahydro-9chloro-5-methyl-6-(3-methyl-2-butenyl)-imiazo[4,5,1-jk] [1,4]benzodiazepin-2(1H)-thione], 8-Cl TIBO[(+)-(S)-4,5,6,7-Tetrahydro-8-chloro-5-methyl-6-(3-methyl-2-butenyl)-imiazo[4,5,1-jk][1,4]benzodiazepin-2(1H)thione], HEPT(1-[(2-hydroxyethoxy)-methyl]-6-(phenylthio)thymine), emivirine and Efavirenz, ((-)-6-chloro-4-cyclopropylethynyl-4-trifluoromethyl-1,4-dihydro-2h-3,1-benzoxazin-2-one) (Hannongbua et al., 2001; Saen-Oon et al., 2003), are non-competitive inhibitors which are highly specific for HIV-1 RT at a common allosteric site approximately 10 Å from the polymerase active site. The NNRTIs show similar butterfly-like shapes that consist of two (or more) wings. The three-dimensional structure of HIV-1 RT was distorted by NNRTIs directly bound to it, resulting in decreasing catalytic function. (Ren et al., 1995).

Figure 1 First generation NNRTIs

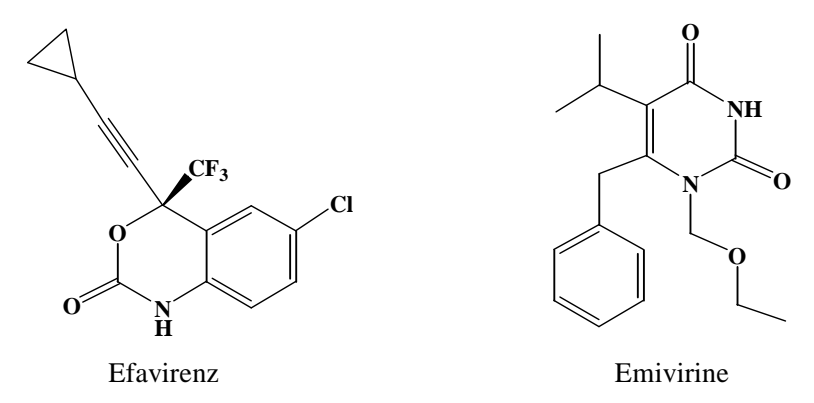


Figure 2 Second generation NNRTIs

Left wing A
$$R_1$$

$$R_1$$

$$R_2$$

$$R_2$$

$$R_1$$

$$R_2$$

$$R_1$$

$$R_2$$

$$R_2$$

$$R_1$$

$$R_2$$

$$R_1$$

$$R_2$$

$$R_2$$

$$R_1$$

$$R_2$$

$$R_2$$

$$R_1$$

$$R_2$$

$$R_1$$

$$R_2$$

$$R_2$$

$$R_1$$

$$R_2$$

$$R_1$$

$$R_2$$

$$R_2$$

$$R_1$$

$$R_2$$

$$R_1$$

$$R_2$$

$$R_1$$

$$R_2$$

$$R_1$$

$$R_2$$

$$R_2$$

$$R_1$$

$$R_1$$

$$R_1$$

$$R_2$$

$$R_1$$

$$R_1$$

$$R_1$$

$$R_1$$

$$R_1$$

$$R_2$$

$$R_1$$

$$R_1$$

$$R_1$$

$$R_1$$

$$R_1$$

$$R_1$$

$$R_1$$

$$R_2$$

$$R_1$$

Figure 3. Structures of diarylpyrimidine (DAPY) family

Although NNRTIs are highly specific and less toxic than nucleoside inhibitors, their therapeutic effectiveness is limited by drug-resistant HIV-1 because of the rapid emergence of mutation. The most common RT mutations that confer resistance to NNRTIs include Leu100Ile (L100I), Val106Ala (V106A), Lys103Asn (K103N), Tyr181Cys (Y181C) (Das *et al.*, 1996; Ren *et al.*, 2000; Hsiou *et al.*, 2001; Ren *et al.*, 2001; Wang *et al.*, 2001a; Lindberg *et al.*, 2002; Ren *et al.*, 2004). Mutations can affect inhibitor binding by: (i) loss of important contacts between protein and inhibitor; (ii) reduction in the size of the binding pocket or modification of pocket shape, and (iii) interference with inhibitor entry into the binding pocket. Nevirapine fails to treat the Y181C mutation (Richman *et al.*; Kuno *et a.l.*, 2003), while the K103N mutation confers resistance to efavirenz (Ren *et al.*, 2000; Mei et al., 2005). The L100I mutation and combined dual mutations such as K103N/Y181C and L100I/K103N are fully resistant to almost all NNRTIs drugs including nevirapine, efavirenz and delavirdine (Das *et al.*, 2007; Bethune *et al.*, 2010). This is a key problem to developing new anti-AIDS drugs. A new series of NNRTIs was discovered that belongs to the

diarylpyrimidine (DAPY) family (Figure 3). DAPY compounds, with TMC278 and its derivatives, demonstrated high potency against wild-type, single and the double mutant strains compared to marked drugs (Das *et al.*, 2008; Tian *et al.*, 2009; Gyseghem *et al.*, 2008; Mordant *et al.* 2007).

The enzyme structure is difficult to model using ab initio quantum chemical calculations due to large and complex system. As such, many other methods have been developed to study large molecular systems including quantum mechanics/molecular mechanics (QM/MM) (Ridder et al., 2003; Mulholland et al., 2005), molecular fractionation with conjugate caps (MFCC) (Mei et al., 2005), and our own n-layered integrated molecular orbital and molecular mechanics (ONIOM) (Morokuma, 2002). The ONIOM method which was developed by Morokuma and coworkers is a powerful hybrid method to study enzymes (Svensson et al., 1996; Dapprich et al., 1999; Karadakov et al., 2000; Morokuma et al., 2006; Guo, et al. 2010). In the ONIOM method, the system is divided into many layers like an onion. The active center is treated with the highest level ab initio QM method, while outer layers are treated with less computationally expensive QM methods such as low-level QM, semiempirical or MM methods. The main objectives in this work are to investigate particular interaction of DAPY inhibitors bound to HIV-1 RT involving the L100I/K103N and K103N/Y181C enzymes and to understand the resilience of DAPY inhibitors for bound to the HIV-1 RT binding pocket. It is expected that this understanding will be helpful in the design of new inhibitors especially active against mutant enzymes, and thus better anti-AIDs agents.

Objectives

- 1. To prepare the structural complex of double mutant (L100I/K103N or K103N/Y181C)/DAPY inhibitors-HIV-1 RT by docking method or obtain these the structural complex from X-ray crystallography.
- 2. To determine the interaction energy between individual pair of DAPY inhibitors including TMC278/amino acids surrounding the binding pocket using quantum mechanics.
- 3. To calculate the binding energy of DAPY inhibitors bound to binding pocket of wild type, K103N/Y181C and L100I/K103N HIV-1 RT using ONIOM2 and ONIOM3 methods.

4. To compare the binding energy of HIV-1 RT/DAPY inhibitors complex structures between wild type and mutant type Y181C and K103N/Y181C enzymes.

Computational Methods

System studied

The starting models for calculations were obtained from the X-ray structures of TMC278 bound to HIV-1 RT for the wild-type, K103N/Y181C and L100I/K103N enzymes, listed in the Protein Data Bank with PDB entry codes 2ZD1, 3GBR and 2ZE2 respectively (Das *et. al.*, 2008). The structural complex of the wild-type and K103N/Y181C HIV-1 RT/other DAPY (compound 2-6) was prepared by a docking method. Compound 2-6 were docked into the binding pocket of wild-type (PDB code: 2ZD1) and K103N/Y181C (PDB code:3GBR) HIV-1 RT using Autodock 3.05 (Moris *et al.* 2000) and MD simulations by GROMACS Program was used to optimize these complex. System set up in GROMACS Program were at NPT ensemble, Temperature= 300 K, Pressure = 1.0 atp, time step 0.0005 ps and time of simulations = 300 ps.

The studied binding pocket included residues surrounding the non-nucleoside inhibitor binding pocket (NNIBP) with at least one atom interacting with any of the atoms of the DAPY inhibitors within an interatomic distance of 7.0 Å These residues of the studied system are Pro95, Leu100(Ile100), Lys101, Lys102, Lys103(Asn103), Val106, Val179, Ile180, Tyr181(Cys181), Gln182, Tyr183, Tyr188, Val189, Gly190, Pro225, Pro226, Phe227, Leu228, Trp229, Leu234, Pro236, Asp237 and Tyr318 from the p66 domain of RT, and Glu138(b) from the 51 domain of RT (Figure4). All residues were assumed to be in their neutral form. The N-and C-terminal ends of cut residues were capped with an acetyl group (CH₃CO-) and a methyl amino group (-NHCH₃), respectively [(H₃C-C(=O)-{NH-CH(-R)-C(=O)}_n-NH-CH₃)]. Hydrogen atoms were added to generate the complete structures and their positions were optimized by the semi-empirical PM3 method available in the GAUSSIAN 03 program running in Linux on a Pentium IV 3.2 GHz PC (Frisch *et al.*, 2003). The optimizations were carried out with fixed heavy atoms and the final structures produced were used as the starting geometries for all subsequent calculations.

Figure 4 Model system used for DAPY inhibitors bound to the allosteric site, NNIBP, of HIV-1 RT consisting of 24 residues.

Interaction energy calculations

The interaction energies, $E_{(TMC278+Xi)}$, between TMC278 and individual residues, X_i , were calculated at the MP2/6-31G(d,p) levels of theory using the geometry described above. The total interaction energy, INT, can be expressed as: (Sea-oon *et al.* 2005)

$$INT_{(EFZ+Xi)} = E_{(EFZ+Xi)} - E_{(EFZ)} - E_{(Xi)},$$
 (1)

where $E_{(TMC278)}$ and $E_{(Xi)}$ are energies of TMC278 and each individual residue, respectively.

Binding energy calculations

Two and three layer ONIOM calculations were performed to determine the binding energy of DAPY inhibitors bound to the double mutant K103N/Y181C or L100I/ K103N as compared to the wild-type. The total ONIOM energy of the entire system was obtained from three and five independent energy calculations in ONIOM2 and ONIOM3 methods, respectively (Morokuma, 2003). All calculations were carried out using the GAUSSIAN 03 package (Frisch *et al.*, 2003).

More precisely, the binding energy of DAPY inhibitors bound to the allosteric pocket of HIV-1 RT was determined using equations (2) and (3) for the ONIOM2 and ONIOM3 methods, respectively (Kuno *et al.*, 2003).

$$\Delta E^{ONIOM2} = E[Cpx]_{opt} - E[P]_{opt} - E[L]_{opt}$$

$$= \Delta E \text{ (High, A+B)} + [\Delta E \text{ (Low, ABC)} - \Delta E \text{ (Low, AB)}]$$

$$= \Delta E \text{ (High, A+B)} + [\Delta \Delta E \text{ (Low, ABC-AB)}]$$

$$\Delta E^{ONIOM3} = E [Cpx]_{opt} - E[P]_{opt} - E[L]_{opt}$$

$$= \Delta E \text{ (High, A)} + [\Delta E \text{ (Mid, AB)} \Delta E \text{ (Mid, A)}] + [\Delta E \text{ (Low, ABC)} \Delta E \text{ (Low, AB)}]$$

$$= \Delta E \text{ (High, A)} + [\Delta \Delta E \text{ (Mid, AB-A)}] + [\Delta \Delta E \text{ (Low, ABC-AB)}]$$
(3)

Where E[Cpx]_{opt} is the total optimized energy of the TMC278-binding pocket complex, Cpx; E[P]_{opt} is the optimized energy of binding pocket; and E[L]_{opt} is the optimized energy of the DAPY inhibitor. Also, Δ E (High, A) is the interaction energy in the region A which is treated at the high level of theory, $\Delta\Delta$ E (Mid, AB-A) is the interaction energy from interactions between the regions A and B and is evaluated at the medium level of theory, and $\Delta\Delta$ E

13

(low, ABC-AB) is the interaction energy from interactions between the regions AB and C

which is evaluated at the low level of theory.

Binding energy of TMC278 inhibitor bound to the allosteric pocket of K103N /Y181

HIV-1 RT compared with wild type

The three layer ONIOM calculations were performed to determine the binding

energy of TMC278 inhibitor bound to the mutant K103N/Y181C HIV-1 RT as compared to the

wild-type. The inner layer (region A) including TMC278 and Y181 or C181 was treated at

the MP2/6-31G(d,p) and The medium layer (region B) including K101 and K103 was

treated at the B3LYP/6-31G(d,p) methods. The remainder of the residues was taken as the

outer layer (region C) which was treated at the PM3 level. For this study, the following

models were generated (Figure 5):

ONIOM3 calculation: MP2/6-31G(d,p)[TMC278+(Y181 or C181)]:B3LYP/6-31G(d,p)

[K101+K103 or N103]:PM3[real]

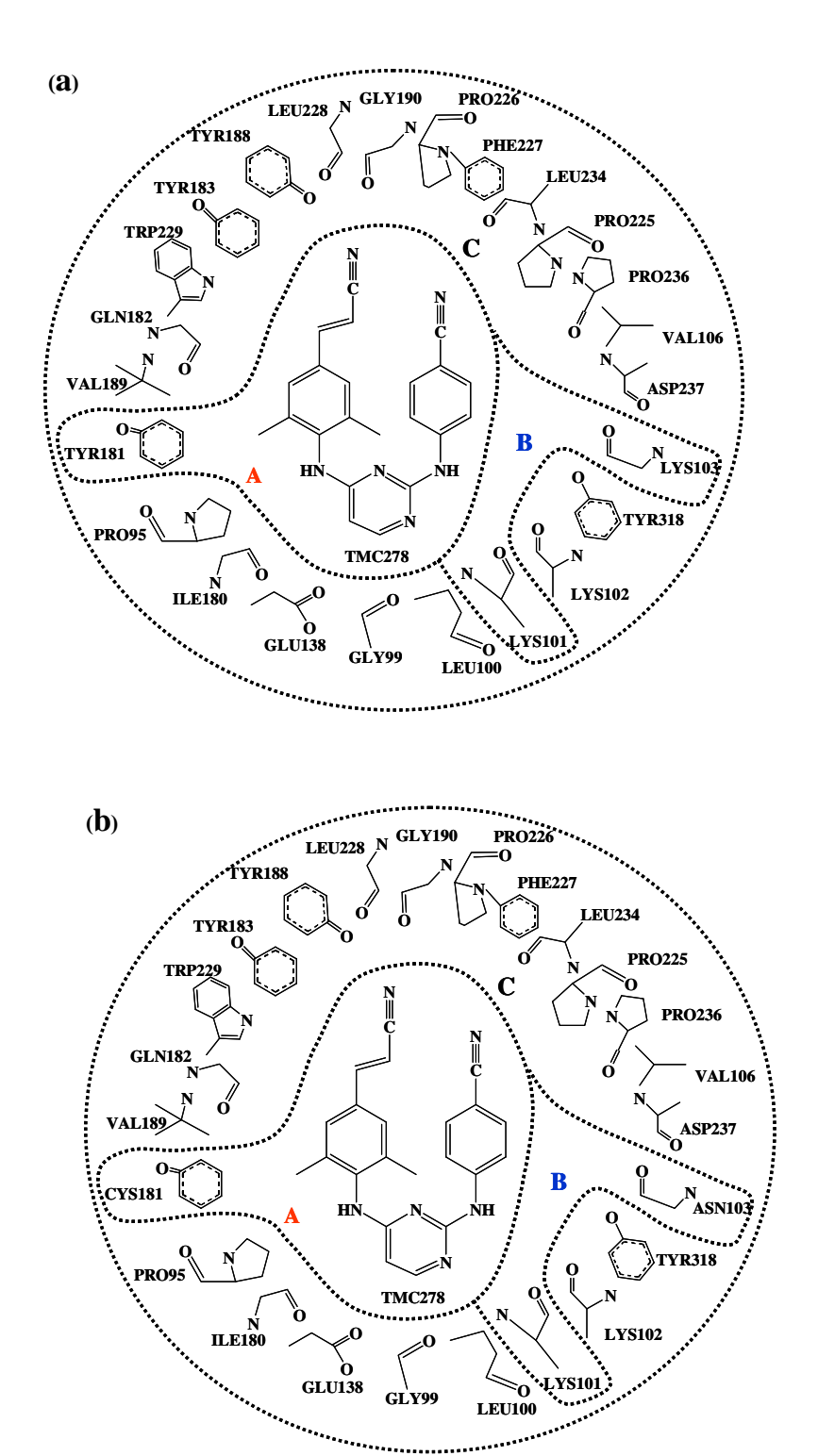


Figure 5 Model system used for TMC278 bound to allosteric site of HIV-1 RT consisting of 24 residues; (a) wild-type HIV-1 RT NNIBP, and (b) K103N/Y181C HIV-1 RT NNIBP.

Binding energy of DAPY inhibitors bound to the allosteric pocket of wild type and K103N /Y181 HIV-1 RT

The two layer ONIOM calculations were performed to determine the binding energy of DAPY inhibitors bound to the mutant K103N/Y181C HIV-1 RT as compared to the wild-type. The inner layer or interaction region including the DAPY inhibitors and K101 was treated by the B3LYP/6-31G(d,p) method. The remainder of the residues was taken as the outer layer which was treated by the PM3 method. For this study, the following models were generated (Figure 6):

ONIOM2 calculation: B3LYP/6-31G(d,p) [TMC278+ K101]:PM3[real]

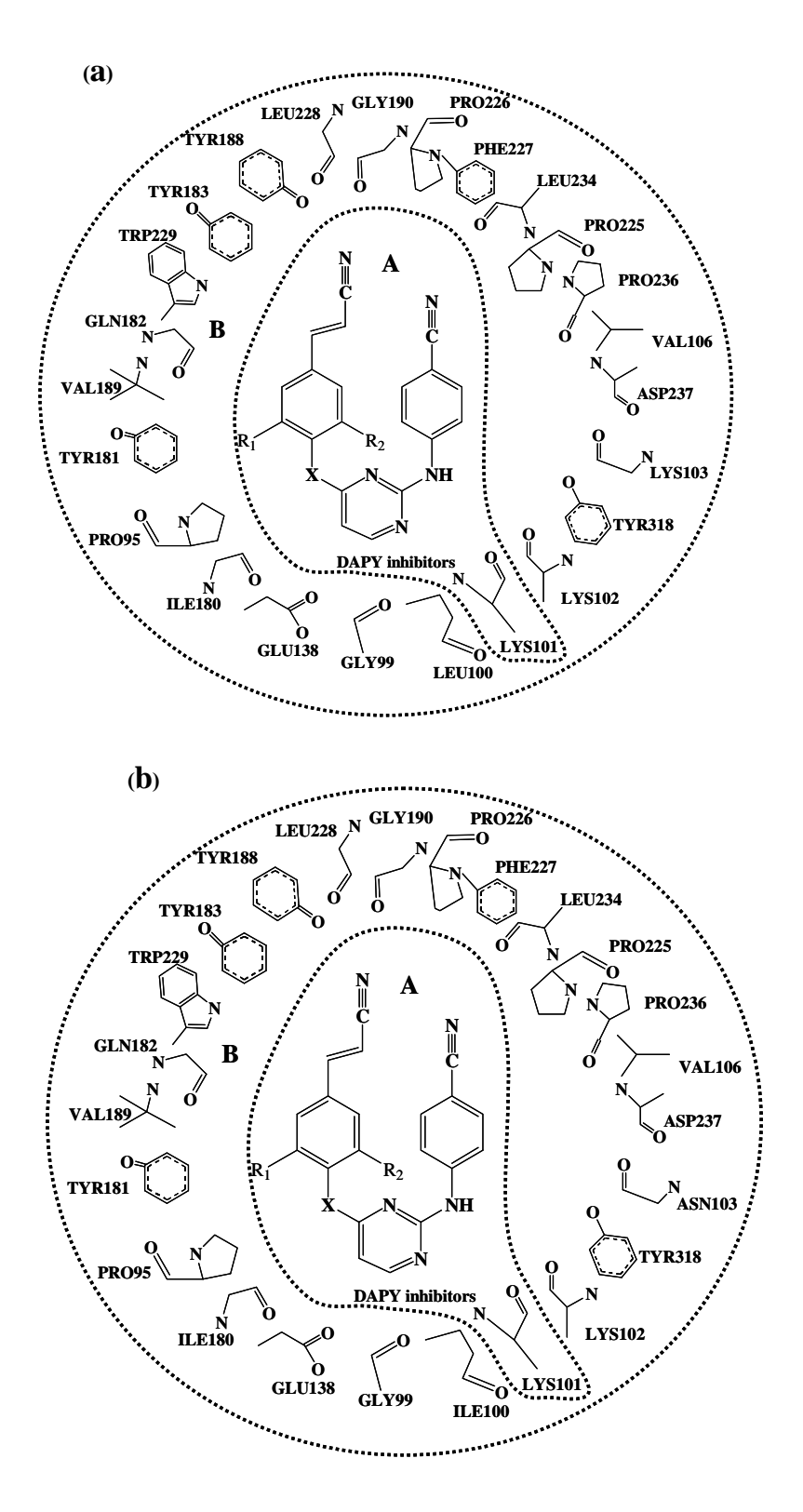


Figure 6 Model system used for DAPY inhibitors bound to allosteric site of HIV-1 RT consisting of 24 residues; (a) wild-type HIV-1 RT NNIBP, and (b) K103N/Y181C HIV-1 RT NNIBP.

Binding energy of TMC278 inhibitor bound to the allosteric pocket of L100l/K103N

HIV-1 RT compared with wild type

The three layer ONIOM calculations were performed to determine the binding energy of TMC278 inhibitor bound to the mutant L100I/K103N HIV-1 RT as compared to the wild-

type. The inner layer or interaction region including the TMC278 and L100 or I100 was

treated by the MP2/6-31G(d,p) methods. The medium layer including K101 and either K103

or N103 were treated by the B3LYP/6-31G(d,p) method. The remainder of the residues

were taken as the outer layer which was treated by the PM3 method. For this study, the

following models were generated (Figure 7):

ONIOM3 calculation: MP2/6-31G(d,p)[TMC278+(L100I or I100)]:B3LYP/6-31G(d,p)

[K101+(K103 or N103)]:PM3[real]

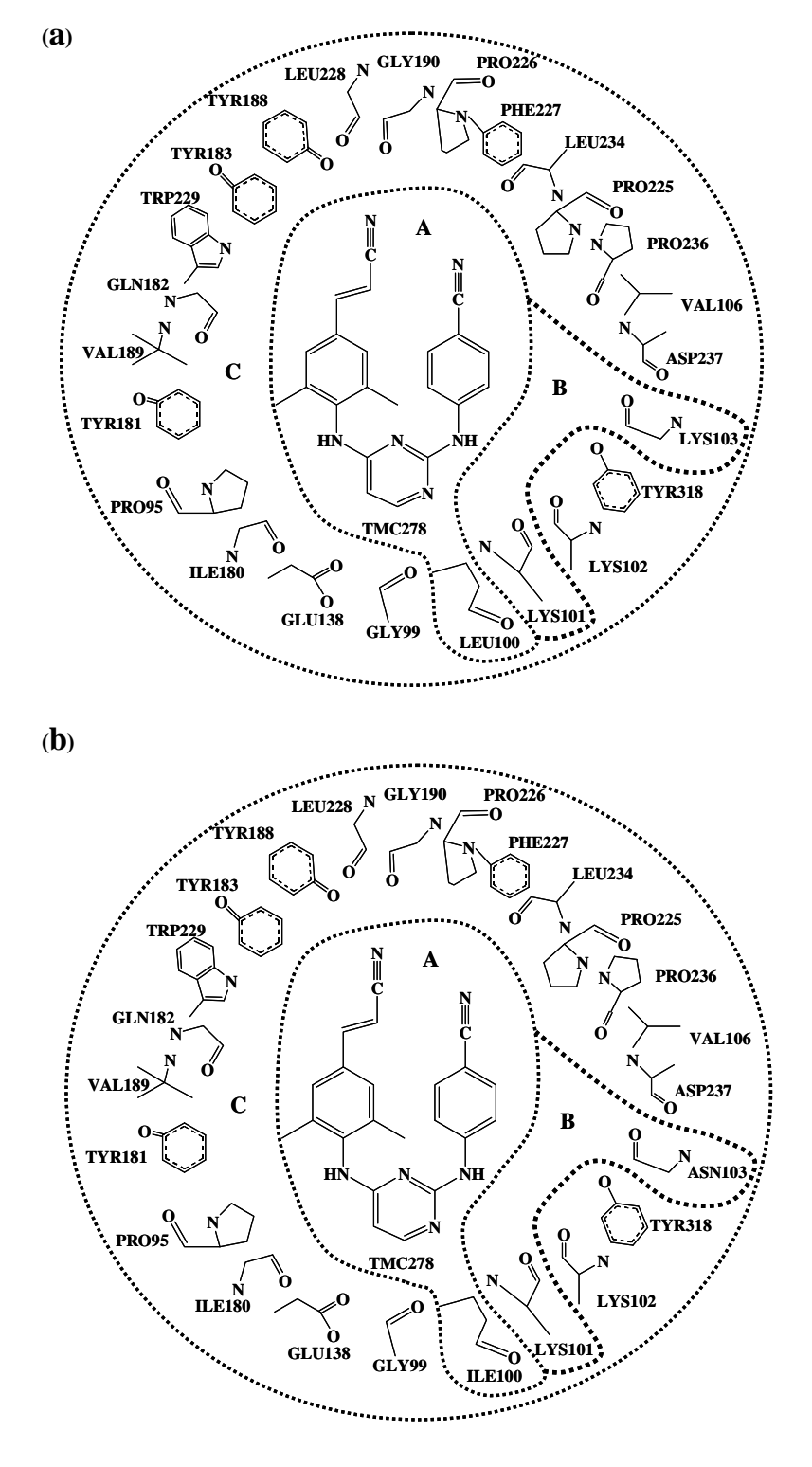


Figure 7. Model system used for TMC278 bound to allosteric site of HIV-1 RT consisting of 24 residues; (a) wild-type HIV-1 RT NNIBP, and (b) L100I/K103N HIV-1 RT NNIBP.

Results and discussion

Comparing interaction energy and binding energy calculations between wild-type and K103N/Y181C enzymes

Interaction energy of TMC278 with individual residues of the wild type and K103N/Y181C HIV-1 RT binding pocket

The interaction energies between TMC278 and the individual residues (Xi) of HIV-1 RT binding pocket for wild-type, L100I/K103N or K103N/Y181C enzymes were calculated at MP2/6-31G(d,p) levels of theory and are shown in Table 1. As the MP2 method includes the dispersion interactions, it is expected to give more accurate interaction energies than B3LYP [Tsuzuki et al., 2001]. In wild-type RT, the main contributions to the interactions with TMC278 come from K101, Y181, F227 and W229 which produce attractive interactions greater than 3 kcal/mol, calculated at MP2/6-31G(d,p) level. Considered in greater detail (Figure 2), hydrogen bonding between a linker nitrogen atom of TMC278 (Figure 3) and the main-chain carbonyl oxygen of K101 causes the strongest interaction, 8.15 kcal/mol at the MP2/6-31G(d,p) level, and is conserved in the binding of many NNRTIs. The cyanovinyl group is positioned to fit into a hydrophobic tunnel formed by the side chains of amino acid residues F227 and W229 that may explain why TMC278 is the most potent of DAPY analogues. TMC278 can be flexible to bind to HIV-1 RT and interacts with aromatic side chains of Y181 and W229 via H- π interactions. Comparing the wild-type RT and K103N/Y181C RT at the MP2/6-31G(d,p) method shows no significant difference between the interactions, except for the mutated residue C181. The attractive interactions between TMC278 and C181 in the K103N/Y181C enzyme were reduced by 2.93 kcal/mol.

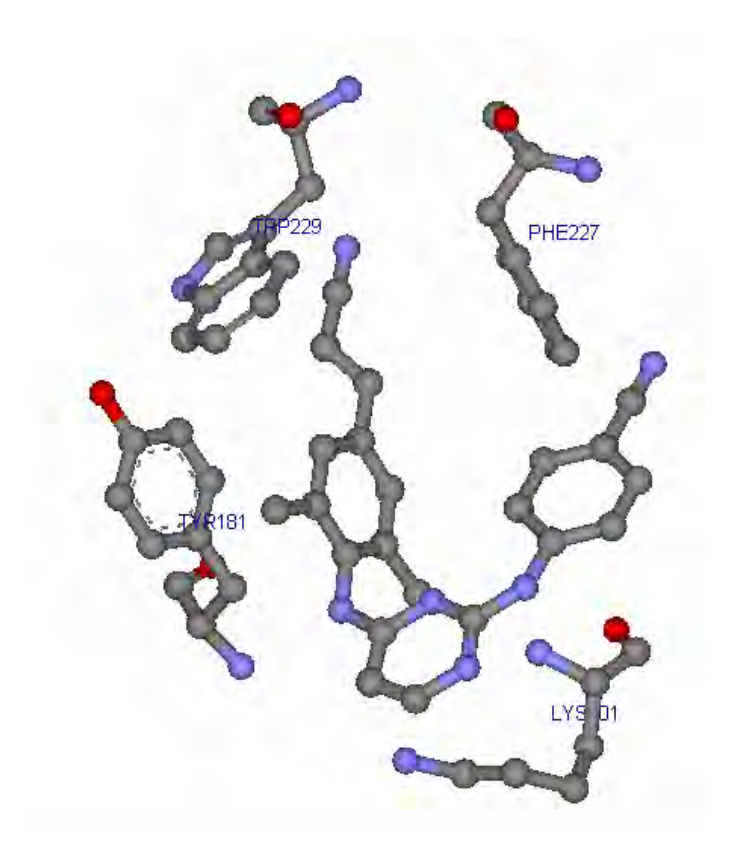


Figure 8 Orientation of TMC278 and the residues with the largest interactions in the binding pocket of wild-type HIV-1 RT.

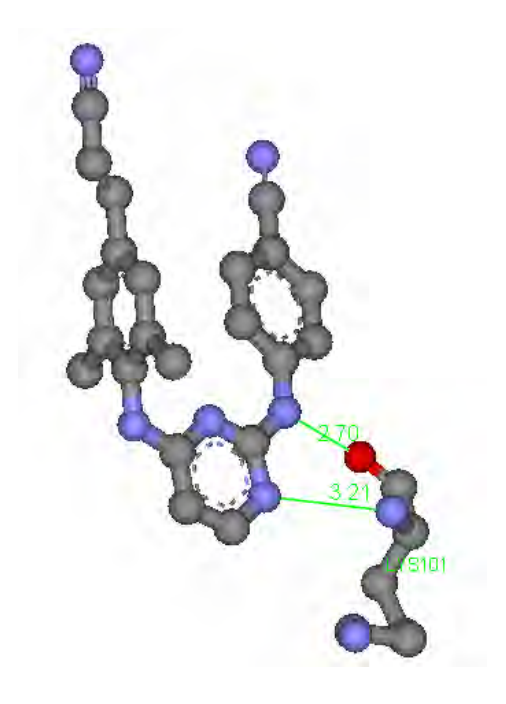


Figure 9 Hydrogen bonding between K101 and TMC278

Table 1 The calculated interactions between TMC278 and individual residues (X_i) from the MP2/6-31G(d,p) method.

Residue(X _i)	Interaction energy (kcal/mol)			
	Wild-type	K103N/Y181C	ΔE_{a}	
PRO95	-0.46	-0.39	-0.07	
GLY99	-0.13	-0.16	0.03	
LEU100	-1.86	-3.27	1.41	
LYS101	-8.15	-7.76	-0.39	
LYS102	-0.13	-0.22	0.09	
LYS103 (ASN)	-1.80	-2.28	0.48	
VAL106	-0.39	-0.21	-0.18	
ILE180	-0.92	-1.11	0.19	
TYR181(CYS)	-4.52	-1.60	-2.92	
GLN182	-0.37	0.03	-0.40	
TYR183	-0.55	-1.38	0.83	
TYR188	-2.24	-1.33	-0.91	
VAL189	-0.26	-0.36	0.10	
GLY190	-0.72	-0.87	0.15	
PRO225	-1.52	-1.19	-0.33	
PRO226	-0.60	-1.19	0.59	
PHE227	-3.09	-2.43	-0.66	
LEU228	0.46	0.61	-0.15	
TRP229	-5.46	-5.51	0.05	
LEU234	-0.94	-1.02	0.08	
PRO236	-2.18	-2.98	0.80	
ASP237	-1.50	-2.44	0.94	
TYR318	-1.50	-1.44	-0.06	
GLU138	-2.95	-2.44	-0.51	
Total Energy	-41.76	-40.94	-0.82	

 $\Delta E_a = IE_{wild-type} - IE_{K103N/Y181C mutant}$

 $\Delta E_b = IE_{wild-type} - IE_{L100I/K103N mutant}$

Binding energy of TMC278 bound to the allosteric pocket of K103N /Y181 HIV-1 RT compared with wild type

K103N and Y181C are the two drug-resistant mutations most frequently observed in patients treated with NNRTIs, and viruses carrying these mutations show high levels of resistance to existing NNRTIs. However, TMC278 inhibits K103N/Y181C RT and K103N/Y181C RT mutants at an EC₅₀ < 1 nM (Das et al. 2008). From Table 1, it can be seen that the K101 residue has the strongest interaction with TMC278. The interaction energies between TMC278 and each residue of both the wild-type RT and K103N/Y181C RT are similar excepted for the mutated position C181. The mutated Y181C has less contact between TMC278 and C181 because TMC278 interacts with Y181 via hydrogen atoms of its dimethylphenyl ring with the aromatic ring of the residue. For better accuracy, the MP2 method was used in ONIOM3 calculations to include these dispersion interactions. With all the ONIOM methods used, it was found that the binding energy differences (Table2) between wild-type RT and K103N/Y181C RT are small, with 1.48 kcal/mol from MP2/6-31G(d,p):B3LYP/6-31G(d,p):PM3 calculations. This is in good agreement with the experimentally observed EC₅₀ for 0.0004 μ M wild type and EC₅₀ = 0.0008 μ M for K103N/Y181C RT (Das *et al.*,2008). Only the interaction energy in region (A+B) [Δ E (High, A+B)] of Y181C enzyme is less than that in the wild- type, with a greatest difference of 1.65 kcal/mol (-10.21 kcal/mol for wild type and -8.56 kcal/mol for Y181C enzymes) using B3LYP/6-31G(d,p):PM3 method (Table2).

With the ONIOM3 method (Table2), binding energy of TMC278 is determined from three terms: (i) the interaction energy in region A [Δ E (High, A)], (ii) interaction between the regions A and B [$\Delta\Delta$ E (Mid, AB-A)], and (iii) the interaction energy between the regions A+B and C [$\Delta\Delta$ E (Iow, ABC-AB)]. The main contributions come from both the interaction energy between regions A and B (-14.25 kcal/mol for wild-type RT and -13.58 kcal/mol for K103N/Y181C RT). The calculated interaction energy in region A of the K103N/Y181C RT is less attractive than that in region A of the wild-type by 1.70 kcal/mol, indicating that change from an aromatic side chain of Y181 to a non-aromatic side chain of C181 leads to a reduction of contact between TMC278 and this residue. However, the main contribution to binding energy from K101 is not much changed, which corresponds well with the little change in hydrogen bonding distance between

TMC278 and the carbonyl (-C=O) and amino (-NH) groups of K101 (Table 3). This also agrees with the X-ray structure data (Table 3). Moreover, residues in outer layer of binding pocket, such as Y183, Leu100, Pro236 and Asp237, help to compensated for the loss of interactions caused by C181 mutation. This mode of compensatory interaction is different from that observed for other NNRTI such as HBY097. Thus it can be concluded that TMC278 shows similar high inhibitory affinities for both wild-type and Y181C enzymes.

Table 2 Binding energy for the wild-type RT and K103N/Y181C mutant HIV-1 RT complexed with TMC278 by ONIOM3 methods [MP2/6-31G(d,p):B3LYP/6-31G(d,p):PM3].

Calculated energies (kcal/mol)	Wild-Type	K103N/Y181C mutant
Δ E (high, A)	-5.89	-4.19
$[\Delta\Delta$ E (M, AB-A)]	-14.25	-13.58
[$\Delta\Delta$ E (Low, ABC-C]	-8.15	-9.04
Binding Energy (kcal/mol)	-28.29	-27.31
$^{ t a}\Delta$ E		-1.48

 $^{^{}a}\Delta$ E = BE_{wild-type} - BE _{K103N/Y181C} mutant

Table 3 Calculated distances of the hydrogen bonds (Å) between TMC278 and the backbone carbonyl oxygen (-C=O) and backbone amino hydrogen (-NH) of K101, based on X-ray structure, ONIOM3 methods for wild-type and K103N/Y181C mutant.*

	Wild-type		K103N/Y181C mutant	
	-C=O _K H-N _{TMC278}	-N-H _K N=C- TMC278	-C=O _K H-N _{TMC278}	-N-H _K N=C- _{TMC278}
Methods				
MP2/6-31G(d,p):B3LYP/631G(d,p):PM3	2.80	3.41	2.93	3.38
X-ray	2.70	3.21	2.52	3.07

^{*}Hydrogen bond distances of (-C=O $_{K}$ ----H-N $_{TMC278}$) and (-N-H $_{K}$ ---N=C $_{TMC278}$) are in \hat{A}

Comparing binding energy of TMC278 and its derivatives bound to the allosteric pocket of K103N /Y181 HIV-1 RT

Table 4 Binding energy for the K103N/Y181C mutant HIV-1 RT complexed with TMC278, compound 4 and compound 5 by ONIOM3 methods [MP2/6-31G(d,p):B3LYP/6-31G(d,p):PM3].

Energy	TMC278	Compound 2	Compound 3	ΔE^{a}	$\Delta E^{^b}$
Binding Energy	-27.31	-15.39	-15.67	-11.92	-11.64
(kcal/mol)					
Δ E (high, A)	-4.19	-0.81	-1.50	-3.38	-2.69
$[\Delta\Delta$ E (M, AB-A)]	-13.58	-11.07	-9.66	-2.51	-3.92
[$\Delta\Delta$ E (Low, ABC-C	-9.04	-3.51	-4.51	-5.53	-4.53

 $[\]Delta E^a = E_{K103N/Y181C \text{ mutant -TMC}} - E_{K103N/Y181C \text{ mutant-compound }}$

The influence on activity of the X spacer connecting the left phenyl ring and the pyrimidine in K103N/Y181C HIV-1 RT was investigated. Compound 2 and 3, in which the NH- linker of TMC278 was respectively replaced by and O- and S- linker, respectively. The three layer ONIOM calculations were performed to determine the binding energy of compound 2 and compound 3 as compared with TMC278. The inner layer (region A) including DAPY inhibitors (TMC278, compound 2 or compound 3) and Y181 or C181 was treated at the MP2/6-31G(d,p) and The medium layer (region B) including K101 and K103 was treated at the B3LYP/6-31G(d,p) methods. The remainder of the residues was taken as the outer layer (region C) which was treated at the PM3 level. The differences in binding energies between compound 2 or 3, and TMC278 is more significant (-11.92 and -11.64 kcal/mol, repectively) (Table4). This result indicated that the NH- group as the most appropriate spacer to achieve high-level potency on double mutant K103N/Y181C corresponding with experimental ($E_{50} = 3.2$, 4.3 and 18.6 nM for TMC278, compound 2 and compound 3, respectively)(Mordant *et al.* 2007).

 $[\]Delta \text{E}^{\text{b}}$ = E $_{\text{K103N/Y181C mutant -TMC}}$ - E $_{\text{K103N/Y181C mutant-compound 5}}$

Binding energy of TMC278 and its derivatives bound to the allosteric pocket of K103N /Y181 HIV-1 RT compared with wild type

The effect of the left phenyl A-ring 2, 6-disubstitution of TMC278 on wild type and K103N/Y181C enzymes was investigated. Binding energy of other DAPY inhibitors (compound 4, 5 and 6) as compared TMC278 to describe the activity of these drugs with wild-type and the K103N/Y181C enzymes. The strongest interaction between TMC278 and K101, exhibiting moderate hydrogen bond was considered as part of the interacting core for ONIOM2 calculation. The inner layer or interacting core (Figure 6, region A) including DAPY inhibitors and K101 was treated by the B3LYP/6-31G(d,p) methods. The outer layer (Figure 6, region B) was treated at the PM3 method. The calculated binding energy of TMC278 (-11.69 kcal/mol) on K103N/Y181C enzyme was slightly decreased as compared with wild-type (-9.21 kcal/mol) which agrees well with the experimentally observed E_{50} = 0.0004 nM for K103N/Y181C enzyme and $E_{50} = 0.0008$ nM for K103N/Y181C enzyme. Only the interaction energy between region A and B [$\Delta\Delta$ E (Low, AB-A)] of K103N/Y181C enzyme (-2.53 kcal/mol) is less than that in the wild type (-4.59 kcal/mol), with the difference of -2.06 kcal/mol. This indicates the mutation, K103N/Y181C induce a slight loss of contact of residues in region B (K101 and ASN103) with TMC 278 and eliminate favorable contacts of the aromatic ring of the Y181 with TMC278 leading to reduce contact between mutate residues Y181. However, the main contribution to binding energy from K101 is not much changed, which corresponds well with the little change in hydrogen bonding distance between TMC278 and the carbonyl (-C=O) and amino (-NH) groups of K101 (Table 5). This also agrees with the X-ray structure data (Table 5). Noticeably, the differences in binding energy between wild-type and K103N/Y181C enzymes for the other DAPY drugs (compound 4-6) is similar trend with TMC278. The left phenyl A-ring of TMC278 shows π - π main interactions with residues Y181 and Y188 of binding pocket. 2,6-dimethyl on phenyl A ring of TMC278 prevent great conformational shift and limit the rotational freedom resulting in the conformation favoring this specific interaction(Mordant et.al, 2007). Consequently, the binding energy of monosubstituted derivative 4 is less than TMC278 2 for both wild-type and K103N/Y181C enzymes, with the difference of -2.66 and -2.03, respectively (Table 6). Moreover, it was found that binding energy of compound 5 (non-2,6-substituent on phenyl A-ring of TMC278) is less than that TMC278 for both wild-type and K103N/Y181C enzymes, with the greatest difference of -5.81 and -5.11 kcal/mol, respectively. This indicates that removal of 6- or 2,6substituent on phenyl A-ring of TMC278 might increase the conformational degrees of freedom and weaken π - π main interactions between compound 4 or 5, with residues Y181 and Y188 in binding pocket of wild-type and K103N/Y181C enzymes. At position 2 and 6 on phenyl A-ring of TMC278 was substituted with –OMe as electron-donating and –Cl as electron-withdrawing group (compound 6). The calculated binding energy of compound 6 is similar to the TMC278 on wild-type and K103N/Y181C enzymes (Table 6). It is point out that the dimethyl groups on phenyl A ring of TMC278 could be replaced by electron-donating and electron-withdrawing group without loss of binding of compound 6 to wild-type and K103N/Y181C enzymes. This data could support further development of the DAPY inhibitors. This concluded that maintain a 2,6-disubstitution on phenyl A ring of DAPY to achieve a high level of inhibition on wild-type and K103N/Y181C enzymes

Table 5 Calculated distances of the hydrogen bonds (Å) between TMC278 and the backbone carbonyl oxygen (-C=O) and backbone amino hydrogen (-NH) of K101, based on X-ray structure, ONIOM2 methods for wild-type and K103N/Y181C mutant.*

	V	Wild-type		K103N/Y181C mutant	
	$-C=O_KH-N_{\overline{1}}$	-N-H _K N=C- TMC278	-C=O _K H-N _{TMC278}	-N-H _K N=C- _{TMC278}	
Methods					
B3LYP/631G(d,p):PM3	2.87	3.32	2.82	3.30	
X-ray	2.70	3.21	2.52	3.07	

^{*}Hydrogen bond distances of (-C=O $_{K}$ ----H-N $_{TMC278}$) and (-N-H $_{K}$ ---N=C $_{TMC278}$) are in \mathring{A}

Table 6 Binding energy for the wild-type RT and K103N/Y181C mutant HIV-1 RT complexed with DAPY inhibitors by ONIOM2 methods [B3LYP/6-31G(d,p):PM3].

Compounds	Calculated energies (kcal/mol)			
	ΔΕ	Δ E (High, A)	$\Delta\Delta$ E (Low, AB-A)	
Compound 1 (TMC278)				
Wild-type	-11.69	-7.10	-4.59	
K103N /Y181 mutant	-9.21	-6.68	-2.53	
$^{a}\DeltaE$	-2.48	-0.42	-2.06	
Compound 4				
Wild-type	-9.03	-6.72	-2.31	
K103N /Y181 mutant t	-7.18	-6.62	-0.56	
$^{ t a}\Delta$ E	-1.85	-0.10	-1.75	
$^{ t b}\!\Delta$ E	-2.66	-0.38	-2.28	
$^{\circ}\Delta$ E	-2.03	-0.06	-1.97	
Compound 5				
Wild-type	-5.88	-3.61	-2.26	
K103N /Y181 mutant	-4.10	-3.53	-0.57	
$^{ t a}\Delta$ E	-1.78	-0.08 -1.69	-1.69	
$^{ t b}\!\Delta$ E	-5.81	-3.49	-2.33	
$^{\mathrm{c}}\!\DeltaE$	-5.11	-3.15	-1.96	
Compound 6				
Wild-type	-11.96	-7.05	-4.91	
K103N /Y181 mutant	-9.46	-6.50	-2.96	
$^{a}\DeltaE$	-2.50	-0.55	-1.95	
$^{ t b}\!\Delta$ E	0.27	-0.05	0.32	
$^{ extsf{c}}\DeltaE$	0.25	-0.18	0.43	
$^{a}\DeltaE$	-2.50	-0.55	-1.95	
Experiment binding loss				

 $^{^{\}rm a}\Delta$ E = E_{wild-type} - E _{K103N /Y181 mutant}

 $^{^{\}mathrm{b}}\Delta\mathrm{E}$ = BE_{TMC278}, wild-type</sub> - BE derivative of TMC27, wild- type

 $^{^{\}rm c}\Delta{\rm E} = {\rm BE}_{\rm TMC278}, {\rm K103N}.{\rm Y181}\,{\rm mutant} - {\rm BE}\,\,{\rm derivative\,\,of\,\,TMC27}, {\rm K103N}.{\rm Y181}\,{\rm mutant}$

2. Comparing interaction energy and binding energy calculations between wild-type and L100l/K103 enzymes

Interaction energy of TMC278 with individual residues of the wild type and L100l/K103 HIV-1 RT binding pocket

The repulsive interactions between TMC278 and residues of the binding pocket for the L100I/K103N RT are greater than in wild-type RT. Also, the attractive interactions between TMC278 and K101, K103 and W229 in the L100I/K103N RT were reduced to 5.92, 4.69 and 3.21 kcal/mol, respectively ($^b\Delta$ E in Table 7, MP2/6-31G(d,p) method), compared to the wild-type RT. These results indicate that the mutated residues L100I and K103N not only reduce the binding stability of TMC278, but actually destabilize the cavity, leading the W229 residue to lose contact with the inhibitor.

Binding energy of TMC278 inhibitor bound to the allosteric pocket of L100l/K103N HIV-1 RT compared with wild type

Among the known NNRT-resistance mutations, the L100I/K103N double mutation has the greatest effect on the potency of TMC278. However, TMC278 still inhibits the double mutant at ~0.008 μM EC₅₀ [Das, et al., 2008]. In the wild-type RT/TMC278 structure, L100 is near the centre of the pocket and primarily interacts with the central pyrimidine ring of TMC278, while K103 is located on the other side of the pyrimidine ring of TMC278. Comparison of structures of the L100I/K103N mutant RT/TMC278 and wild-type RT/TMC278 complexes (Figure 10) shows that β -branching of I100 in the L100I mutant lead to steric conflict with the inhibitor TMC278. To avoid this steric conflict, TMC278 shifts away from the I100 and towards the N103. However, NNRTIs do not have the ability to flex and move, to "wiggle and jiggle", and adapt their shape to the various pockets found in the NNRTI-resistant. RTs fail against the known mutants because their binding is susceptible to steric hindrance, as they lose key hydrophobic interactions, or mutation K103N interferes with entry of the NNRTIs into the pocket [Das, et al., 2008]. From Table 7, the double mutations L100I and K103N lead to the loss of contact between TMC278 and K101, N103 and W229, with the interaction energies to these residues reduced by 5.92, 4.69 and 3.21 kcal/mol, respectively, as compared with the wildtype RT. Table 8 shows the binding energies for the wild-type and L100l/K103N complexes using three-layer ONIOM calculations. It can be seen that the difference in binding energy

between wild-type (-20.29 kcal/mol) and L100I/K103N enzymes (-9.71 kcal/mol) is far more significant (10.58 kcal/mol with the MP2/6-31G(d,p):B3LYP/6-31G(d,p):PM3 method which agrees well with the experimentally observed $E_{50} = 0.0004~\mu M$ for L100I/K103N enzyme and $E_{50} = 0.008~\mu M$ for L100I/K103N enzyme (Das *et al.*, 2008). The interaction energy in region A and the interaction energy between regions AB and C of the L100I/K103N enzyme are less than wild-type by 4.47 and 8.94 kcal/mol, respectively. This indicates that the double mutation L100I/K103N causes a large reduction in attractive interactions between TMC278 and residues in core regions (mutated residue, I100) and in region B (K101 and N103). The mutation L100I introduces a significant distortion in the NNRTI-binding pocket that causes a loss of contact between TMC278 and I100 leading to a weakly attractive interaction in region A (-0.38 kcal/mol at MP2/6-31G(d,p):B3LYP/6-31G(d,p):PM3 calculations). The mutation K103N interferes with entry of the NNRTIs into the pocket. N103 creates repulsive interactions with TMC278 (Figure 11b) when compared with the interaction between K103 and TMC278(Figure 11a).

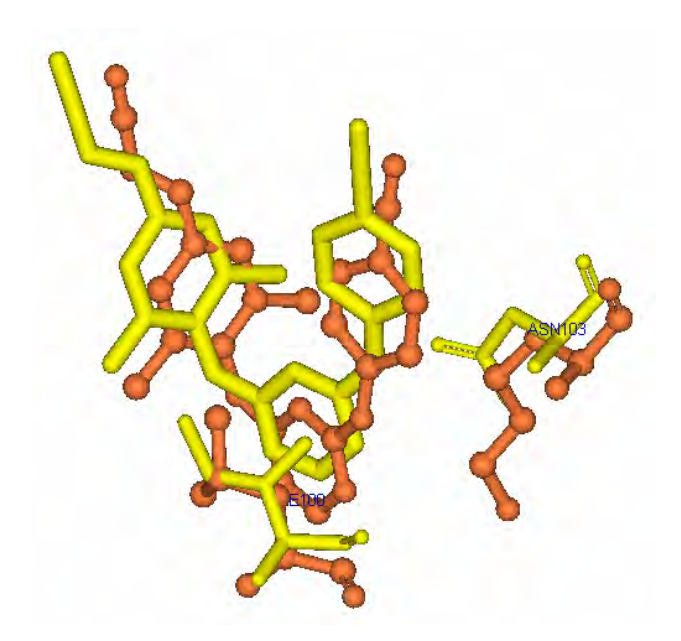


Figure 10 Comparison of structures of TMC278 and mutated residues in the L100l/K103N mutant RT (orange colour) as compared with wild-type.

Table 7 The calculated interactions between TMC278 and individual residues (X_i) from the MP2/6-31G(d,p) method.

Residue(X _i)	Interaction energy (kcal/mol)			
	Wild-type	L100/I/K103N	ΔE_{b}	
PRO95	-0.46	-0.19	-0.27	
GLY99	-0.13	-0.67	0.54	
LEU100	-1.86	-0.08	-1.78	
LYS101	-8.15	-2.23	-5.92	
LYS102	-0.13	-0.20	0.07	
LYS103 (ASN)	-1.80	2.89	-4.69	
VAL106	-0.39	-1.55	1.16	
ILE180	-0.92	-0.55	-0.37	
TYR181(CYS)	-4.52	-4.03	-0.49	
GLN182	-0.37	-0.16	-0.21	
TYR183	-0.55	-1.35	0.80	
TYR188	-2.24	-4.34	2.10	
VAL189	-0.26	-0.40	0.14	
GLY190	-0.72	-0.41	-0.31	
PRO225	-1.52	-1.19	-0.33	
PRO226	-0.60	-0.80	0.20	
PHE227	-3.09	-3.78	0.69	
LEU228	0.46	0.76	-0.30	
TRP229	-5.46	-2.25	-3.21	
LEU234	-0.94	1.22	-2.16	
PRO236	-2.18	-1.07	-1.11	
ASP237	-1.50	-0.11	-1.39	
TYR318	-1.50	-1.21	-0.29	
GLU138	-2.95	-0.68	-2.27	
Total Energy	-41.76	-22.36	-19.40	

 $\Delta E_a = E_{wild-type} - E_{K103N/Y181C\ mutant}$, $\Delta E_b = E_{wild-type} - E_{L100I/K103N\ mutant}$

Table 8 Binding energy for the wild-type and L100I/K103N mutant HIV-1 RT complexed
with TMC278 using ONIOM3[MP2/6-31G(d,p):B3LYP/6-31G(d,p):PM3].

Calculated energies (kcal/mol)	Wild-Type	I100L/K103N mutant
Δ E (high, A)	-4.85	-0.38
$[\Delta\Delta$ E (M, AB-A)]	-9.27	-0.33
[$\Delta\Delta$ E (Low, ABC-C]	-6.17	-6.04
Binding Energy,BE(kcal/mol)	-20.29	-9.71
å∆E		-10.58

 $^{^{}a}\Delta$ E = BE_{wild-type} - BE_{I100L/K103N mutant}

Table 9 Calculated distances of the hydrogen bonds (Å) between TMC278 and the backbone carbonyl oxygen (-C=O) and backbone amino hydrogen (-NH) of K101, based on X-ray structure, ONIOM3 methods for wild-type and L100l/K103N mutant.*

	Wild-type		L100I/K103N mutant	
	-C=O _K H-N _{TMC278} -N-H _K N=C- _{TMC278}		-C=O _K H-N _{TMC278}	-N-H _K N=C- _{TMC278}
Methods				
MP2/6-				
31G(d,p):B3LYP/631G(d,p):PM3	2.83	3.38	2.97	3.60
X-ray	2.70	3.21	3.03	3.70

^{*}Hydrogen bond distances of (-C=O_K----H-N_{TMC278}) and (-N-H_K---N=C_{TMC278}) are in Å

The mutations in the L100I/K103N enzyme leads to a reduction in the stabilization energy of the complex and induces destabilization in the cavity by reducing contact between K101 and TMC278. This corresponds with increased hydrogen bond distances between TMC 288 and K101 (Table 9). The hydrogen bond distances between TMC278 and K101 from MP2/6-31G(d,p):B3LYP/6-31G(d,p):PM3 calculations correspond well with the X-ray structure data (Table 9). TMC278 shows higher inhibitory affinities with the wild-type compared to the double mutation L100I/K103N enzyme.

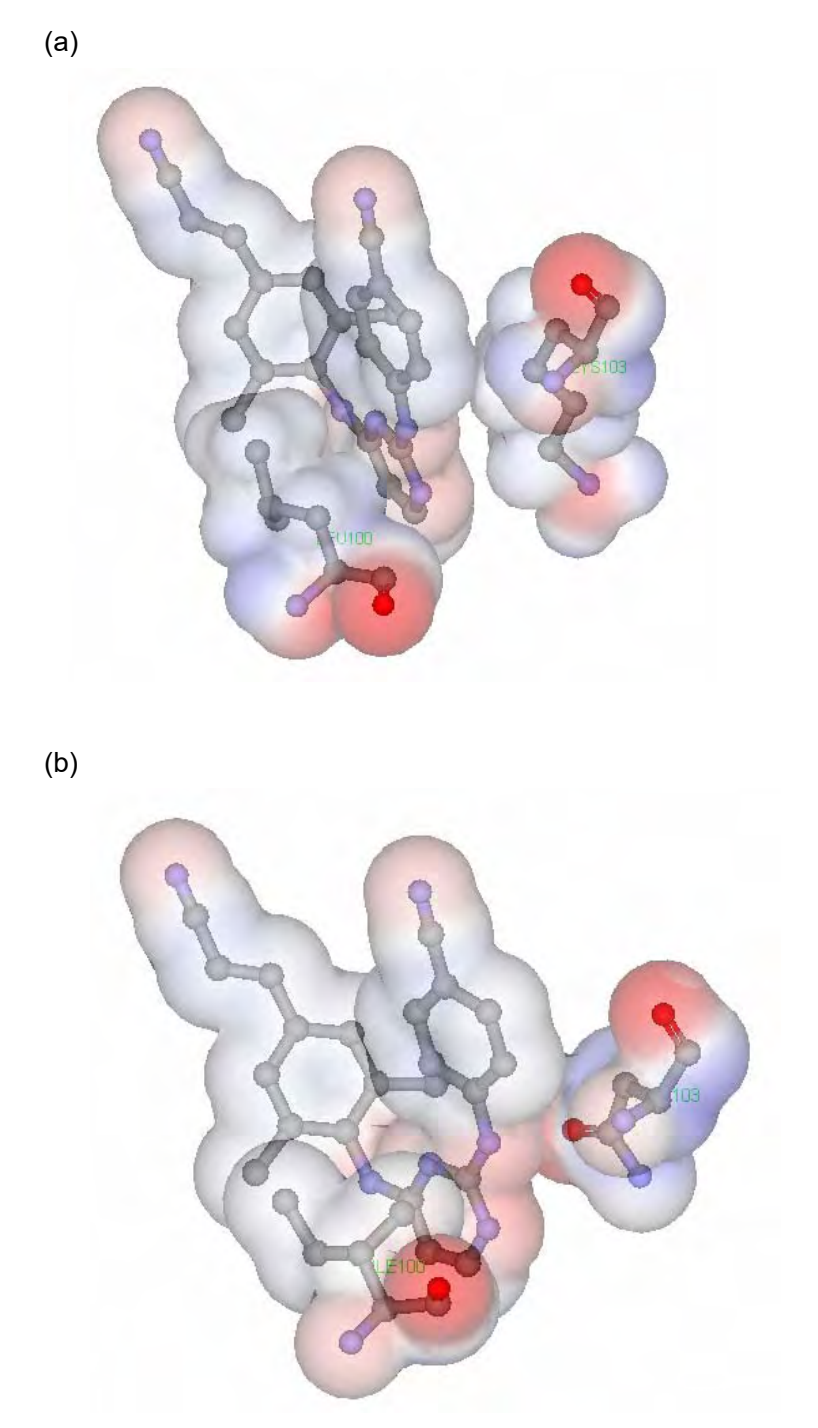


Figure11. The electrostatic potential is shown on the VDW accessible surface with red for negative and blue for positive values for (a) TMC278 interacting with L100 and K103, and (b) TMC278 interacting with I100 and N103.

Conclusion

The ONIOM method method has been applied to determine the binding energies of TMC278 to L100I/K103N and K103N/Y181C enzymes as compared with the wild-type RT. The calculated binding energy for TMC278/K103N/Y181C HIV-1 RT complex is -27.31 kcal/mol by using MP2/6-31G(d,p):B3LYP/6-31G(d,p):PM3 method which is similar to the TMC278/wild-type complex (28.29 kcal/mol). Moreover, it was found that interaction energies calculated at MP2/6-31G(d,p) level between TMC278 and each individual residues of the binding pocket for both wild-type and K103N/Y181C HIV-1 RT are not significantly different except for C181. The interaction between K101 and TMC278 for both wild-type and K103N/Y181C enzymes was found to be the major component, typically -8 kcal/mol. These results are consistent with the observation that TMC278 shows high inhibitory affinities against for both wild-type and K103N/Y181C enzymes, and that TMC278 has a higher inhibitory affinity for the K103N/Y181C enzyme than other DAPY and second generation drugs such as efavirenz. Consequently, the influence of X spacer connecting the left phenyl ring and the pyrimidine was investigated to determine binding energy of compound 2 (O-linker) and compound 3(Slinker) to a double mutant (K103N/Y181C) enzyme compared with TMC278. Binding energies of compound 2 and 3(11.92 and 11.64 kcal/mol, respectively) were less than TMC278 ((-28.31 kcal/mol). These results indicate that the NH- group of TMC278 as the most appropriate spacer to achieve high-level potency on double mutant K103N/Y181C. Therefore, NH- linker of TMC278 was used to study the effect of the substituent at position 2 and 6 on the left phenyl A ring. The binding energy of mono-substituted derivative 4 is less than TMC278 2 for both wild-type and K103N/Y181C enzymes, with the difference of -2.66 and -2.03, respectively. Moreover, it was found that binding energies of compound 5 (non-2,6-substituent on phenyl A-ring of TMC278) is less than that TMC278 for both wild-type and K103N/Y181C enzymes, with the greatest difference of -5.81 and -5.11 kcal/mol, respectively. It is clearly that the substituent at position 2 and 6 on the left phenyl A ring of TMC278 is necessity maintained to achieve a high level of inhibition on wild type and K103N/Y181C enzymes. Furthermore, it point out that the other functionalities including electron-donating group (-OMe) and electron-withdrawing group (-Cl) for compound 6 can replace the methyl group in TMC278 without loss of activity of this drug. This data can support further development of TMC278 derivatives.

With the L100I/K103N enzyme, the two mutations L100I and K103N eliminate favourable contacts of the hydrocarbon side chain of L100 and K103 with TMC278 leading to reduce the stabilization energy of the complex. It was observed that this then leads to more repulsive interactions between TMC278 with residues of the binding pocket of the L100I/K103N enzyme compared to the wild-type and K103N/Y181C enzymes. The binding energy for TMC278/L100I/K103N HIV-1 RT complex was calculated to be -9.71 kcal/mol less than that of the wild-type complex (-20.29 kcal/mol). In the binding pocket of L100I/K103N enzyme, hydrogen bonding between TMC278 and K101 was disturbed, and N103 in the binding pocket of L100I/K103N enzyme creates a repulsive interaction with TMC278. This is consistent with the observation that TMC278 shows lower inhibitory affinities against L100I/K103N HIV-1 RT than wild-type and K103N/Y181C HIV-1 RT. The understanding interactions involved in binding within the pocket, and the structural changes that occur, can be useful for the design of higher potency inhibitors specific to double mutant enzyme target.

Reference

- Béthune, M. 2010. Non-nucleoside reverse transcriptase inhibitors (NNRTIs), their discovery, development, and use in the treatment of HIV-1 infection: A review of the last 20 years (1989–2009). **Antiviral Research**.85: 75–90.
- Dapprich, S. I., Komaromi, K.S. Byun, K. Morokuma and M.J. Frisch. 1999. A new ONIOM implementation in Guassian98. part I. The calculation of energies, gradients, vibrational frequencies and electric field derivatives. **Journal of Molecular Structure (Theochem).** 1-21: 461-462
- Das, K., J. Ding, Y. Hsiou, A.D. Clark, H. Moereels, L. Koymans, K. Andries, R. Pauwels,
 P.A.J. Janssen, P.L. Boyer, P. Clark, R.H. Smith, M.B.K. Smith, C.J. Michejda S.
 H. Hughes and E. Arnold. 1996. Crystal structures of 8-Cl and 9-Cl TIBO complexed with wild-type HIV-1 RT and 8-Cl TIBO complexed with the Tyr181Cys
 HIV-1 RT drug-resistant mutant. Journal of Molecular Biology. 264: 1085–1100.
- Das, Kalyan., Sarafianos, S. G., Clark, A. D., Boyer, P. L., Hughes, S. H., & Arnold, E. (2007). Crystal Structures of Clinically Relevant Lys103Asn/Tyr181Cys Double Mutant HIV-1 Reverse Transcriptase in Complexes with ATP and Non-nucleoside Inhibitor HBY 097. J. Mol. Biol. 365: 77–89
- Das, K., Bauman, J. D., Clark, A.D., Frenkel, Y. V., Lewi, P. J., Shatkin, A. J., Hughes, S. H., and Arnold, E. 2008. High-resolution structures of HIV-1 reverse transcriptase/TMC278 complexes: Strategic flexibility explains potency against resistance mutations. PNAS. 105(5): 1466-1471
- De Clercq, E. 1994. HIV resistance to reverse transcriptase inhibitors. **Biochemical Pharmacology.** 47: 155-169.
- _____. 1995a. Antiviral therapy for human immunodeficiency virus infections.

 Clinical Microbiology Reviews. 8: 200-239.

_____. 1995b. Toward improved anti-HIV chemotherapy: therapeutic strategies for intervention with HIV-1 infections. **Journal Medicinal Chemistry.** 38: 2491-2517.

- Frisch, M.J., G.W. Trucks, H.B. Schlegel, G.E. Scuseria, M.A. Robb, J.R. Cheeseman, J.A. Montgomery, T. Vreven, K.N. Kudin, J.C. Burant, J.M. Millam, S.S. Iyengar, J. Tomasi, V. Barone, B. Mennucci, M. Cossi, G. Scalmani, N. Rega, G.A. Petersson, H. Nakatsuji, M. Hada, M. Ehara, K. Toyota, R. Fukuda, J. Hasegawa, M. Ishida, T. Nakajima, Y. Honda, O. Kitao, H. Nakai, M. Klene, X. Li, J.E. Knox, H.P. Hratchian, J.B. Cross, C. Adamo, J. Jaramillo, R. Gomperts, R.E. Stratmann, O. Yazyev, A.J. Austin, R. Cammi, C. Pomelli, J.W. Ochterski, P.Y. Ayala, K. Morokuma, G.A. Voth, P. Salvador, J.J. Dannenberg, V.G. Zakrzewski, S. Dapprich, A.D. Daniels, M.C. Strain, O. Farkas, D.K. Malick, A.D. Rabuck, K. Raghavachari, J.B. Foresman, J.V. Ortiz, Q. Cui, A.G. Baboul, S. Clifford, J. Cioslowski, B.B. Stefanov, G. Liu, A. Liashenko, P. Piskorz, I. Komaromi, R.L. Martin, D.J. Fox, T. Keith, M.A. Al-Laham, C.Y. Peng, A. Nanayakkara, M. Challacombe, P.M.W. Gill, B. Johnson, W. Chen, M.W. Wong, C. Gonzalez, J.A. Pople. 2003. Gaussian 03, revision B.05; Gaussian, Inc.: Pittsburgh.
- Gyseghem, E. V., Pendela, M., Baert, L., Rosier, J., Klooster, G. V., Manf, H., Bouche, M., P., Schueller, L., Remoortere, P. V., Wigerinck, P., Adams, E., Hoogmartens, J., Mooter, G. V. (2008). Powder for reconstitution of the anti-HIV-1 drug TMC278 Formulation development, stability and animal studies. **European Journal of Pharmaceutics and Biopharmaceutics.** 70: 853–860.
- Hannongbua, S., K. Nivesanond, L. Lawtrakul, P. Pungpo and P. Wolschann. 2001. 3D-Quantitative Structure-Activity Relationships of HEPT Derivatives as HIV-1 Reverse Transcriptase Inhibitors, Based on *Ab Initio* Calculations. Journal of Chemical Information and Modeling. 41: 848-855.

- Hsiou, Y., J. Ding, K. Das, A.D. Clark, P.L. Boyer, P. Lewi, P.A.J. Janssen, M. Rosner, S.H.
 Hughes and E. Arnold. 2001. The Lys103Asn Mutation of HIV-1 RT: A Novel mechanism of drug resistance. Journal of Molecular Biology. 309: 437-445.
- Jacobo-Molina, A. and E. Arnold. 1991. HIV reverse transcriptase structure function relationships. **Biochemistry.** 30: 6351-6361.
- Karadakov, P.B. and K. Morokuma. 2000. ONIOM as an efficient tool for calculating NMR chemical shielding constants in large molecules. **Chemical Physics Letters**. 317: 589–596.
- Kuno, M., S. Hannongbua and K. Morokuma. 2003. Theoretical investigation on and HIV-1 reverse transcriptase binding site interaction, based on ONIOM method.Chemical Physics Letters. 380: 456–463.
- Lindberg, J., S. Sigurðsson, S. Lowgren, H..O. Andersson, C. Sahlberg, R. Noreen, H. Zhang and T. Unge. 2002. Structural basis for the inhibitory efficacy of efavirenz (DMP-266), MSC194 and PNU142721 towards the HIV-1 RT K103N mutant. **European Journal of Biochemistry**. 269: 1670-1677.
- Mei, Y., X. He, Y. Xiang, D.W. Zhang, J.Z.H. Zhang. 2005. Quantum Study of Mutational Effect in Binding of Efavirenz to HIV-1 RT. **PROTEINS: Structure, Function, and Bioinformatics.** *59*: 489–495
- Morokuma K. 2002. New challenges in quantum chemistry: quests for accurate calculations for large molecular systems. **Philosophical Transactions of the Royal Society of London Series A.** 360: 1149–1164.
- Morokuma, K. 2003. ONIOM and its applications to material chemistry and catalyses. **Bulletin of the Korean Chemical Society.** 24(6): 797-801.

- Morokuma, K., Q. Wang and T. Vreven. 2006. Performance Evaluation of the Three-layer ONIOM method: Case study for a zwitterionic peptide. **Journal of chemical theory and computation.** 2(5): 1317-1324.
- Mulholland, A.J. 2005. Modelling enzyme reaction mechanisms, specificity and catalysis. **Drug discovery today.** 10: 1393-1402.
- Mordant, C., Schmitt, B., Pasquier, E., Demestre, C., Queguiner, L., Masungi, C., Peeters, A., Smeulders, L., Bettens, E., Hertogs, K., Heeres, J., Lewi, P., & Guillemont, J. (2007). Synthesis of novel diarylpyrimidine analogues of TMC278 and their antiviral activity against HIV-1 wild-type and mutant strains. **European Journal of Medicinal Chemistry.** 42: 567- 579.
- Ren, J., R. Esnouf, E. German, D. Somers, C. Ross, I. Kirby, J. Keeling, G. Darby, Y.
 Jones, D.I. Stuart and D. K. Stammers. 1995. High resolution structures of HIV-1
 RT from four RT- inhibitor complexes. Nature Structure Biology. 2: 293-302.
- Ren, J., J. Milton, K.L. Weaver, S.A. Short, D.I. Stuart and D.K. Stammers. 2000.

 Structural basis for the resilience of efavirenz (DMP-266) to drug resistance mutations in HIV-1 reverse transcriptase. **Structure.** 8: 1089–1094.
- Ren, J., C. Nichols, L. Bird, P. Chamberlain, K. Weaver, S. Short, D.I. Stuart and D.K. Stammers. 2001. Structural mechanisms of drug resistance for mutations at codons 181 and 188 in HIV-1 reverse transcriptase and the improved resilience of second generation non-nucleoside inhibitors. Journal of Molecular Biology. 312: 795-805.
- Ren , J., C.E. Nichol, P.P. Chamberlain, K.L. Weaver, S.A. Short and D.K Stammers. 2004. Crystal structures of HIV-1 reverse transcriptases mutated at codons 100, 106 and 108 and mechanisms of resistance to non-nucleoside inhibitors. Journal of Molecular Biology. 336: 569–578.

- Richman, D.D., D. Havlir, J. Corbeil, D. Looney, C. Ignacio, S.A. Spector and J. Sullivan.

 1994. Nevirapine resistance mutations of human immunodeficiency virus type 1 selected during therapy. **Journal of Virology**. 68: 1660–1666.
- Ridder, L and A.J. Mulholland. 2003. Modeling biotransformation reactions by combined quantum mechanical/molecular mechanical approaches: from structure to activity.

 Current Topics Medicinal Chemistry. 3: 1241-1256.
- Saen-oon, S. 2003. **Thesis**: Structural Conformational Analysis of 8-Cl and 9-Cl *TIBO* and Investigation on the HIV-1 RT/*TIBO*s Interactions, Based on Quantum Chemical Calculations. 205 pages.
- Saen-oon, S., M. Kuno and S. Hannongbua. 2005. Binding Energy Analysis for Wild-Type and Y181C Mutant HIV-1 RT/8-Cl *TIBO* Complex Structures: Quantum Chemical Calculations Based on the ONIOM Method. **PROTEINS: Structure, Function, and Bioinformatics.** 61: 859–869.
- Schinazi, R.F., B.A. Larder and J.W. Mellors. 1997. Mutations in retroviral genes associated with drug resistance. **International Antiviral News.** 5: 129-135.
- Svensson, M., S. Humbel, R.D.J. Froese, T. Matsubara, S. Sieber and K. Morokuma 1996. ONIOM: A multilayered integrated MO + MM method for geometry optimizations and single point energy predictions. A test for Diels-Alder Reactions and Pt(P(t-Bu)₃)₂ + H₂ oxidative addition. **Journal of Physical Chemistry.** 100: 19357-19363.
- Tantillo, C., J. Ding, A. Jacobo-Molina, R.G. Nanni, P.L. Booyer, S.H. Hughes, R. Pauwels, K. Andries, P.A.J. Janssen and E. Arnold. 1994. Locaton of anti-AIDS drug binding seetes and resistance mutations in the three-dimensional structure of HIV-1 reverse transcriptase. Journal of Molecular Biology. 243: 369-387.

- Tian, X., Qin, B., Lu, H., Lai, W., Jiang, S., Lee K. H., Chen, C. H. & Xie, L.2009.
 Discovery of diarylpyridine derivatives as novel non-nucleoside HIV-1 reverse transcriptase inhibitors. Bioorganic & Medicinal Chemistry Letters. 19: 5482–5485.
- Tsuzuki, S. and H.P. Luthi. 2001. Interaction energies of van der Waals and hydrogen bonded systems calculated using density functional theory: assessing the PW91 model. **Journal of Chemicals Physics**. 114: 3949.
- Wang, D.P., R.C. Rizzo, J.T. Rives and W.L. Jorgensen. 2001. Antiviral Drug Design: Computational analyses of the effects of the L100I mutation for HIV-RT on the binding of NNRTIs. Bioorganic & Medicinal Chemistry Letters. 11: 2799–2802.
- Whitcomb, J.M. and S.H. Hughes. 1992. Retroviral reverse transcription and integration: progress and problems. **Annual Review Cell Biology.** 8: 275-306.

Output จากโครงการวิจัยที่ได้รับทุนจาก สกอ. และ สกว.

1. การเสนอผลงานในที่ประชุมวิชาการ

- 1.1 นำเสนอผลงานในรูปโพสเตอร์ ในงานสัปดาห์วิทยาศาสตร์ คณะวิทยาศาสตร์และ เทคโนโลยี มหาวิทยาลัยเทคโนโลยีราชมงคลศรีวิชัย วิทยาเขตนครศรีธรรมราช ระหว่างวันที่ 25-29 กันยายน 2552 เรื่อง "Investigation on the Interaction between DAPY Inhibitors and Mutant HIV-1 RT (K103N/Y181C), Based on Quantum Mechanical Methods"
- 1.2 นำเสนอผลงานในรูปโพสเตอร์ ที่ประชุมวิชาการ Pure and Applied Chemistry International Conference (PACCON2011) ระหว่างวันที่ 5-7 มกราคม 2553 ณ Miracle Grand Hotel Bangkok, Thailand. เรื่อง "Theoretical Investigation on wild type and L100I/K103N HIV-1 Reverse Transcriptase Complexed with TMC278, Based on Quantum Mechanical Methods"
- 1.3 นำเสนอผลงานในรูปโพสเตอร์ การประชุมวิชาการและเสนอผลงานวิจัย/สร้างสรรค์ ระดับชาติและนานาชาติ "ศิลปากรวิจัยและสร้างสรรค์ ครั้งที่ 5 : บูรณาการศาสตร์และศิลป์" ระหว่าง วันที่ 25-27 มกราคม 2555 ณ ศูนย์ศิลปวัฒนธรรมเฉลิมพระเกียรติ 6 รอบ พระชนมพรรษา มหาวิทยาลัยศิลปากร วิทยาเขตพระราชวังสนามจันทร์ เรื่อง Analysis of interaction of TMC278 inhibitor to Double Mutant HIV-1 Reverse Transcriptases K103N/Y181C and L100I/K103N as compared with wild type based on Quantum Mechanical calculations.
- 1.4 นำเสนอผลงานในรูปโพสเตอร์ การประชุมวิชาการม.อ. ภูเก็ตวิจัย ครั้งที่ 4 (2554) สหวิทยาการเพื่อการพัฒนาอย่างยั่งยืน ระหว่างวันที่ 16-18 พฤศจิกายน 2555 ณ มหาวิทยาลัยสงขลานครินทร์ วิทยาเขตภูเก็ต เรื่อง Investigation on the Interaction between TMC278 inhibitors and Mutant HIV-1 Reverse Transcriptase (K103N/ Y181C), Based on ONIOM2 method

2. ผลงานตีพิมพ์ในวารสารวิชาการนานาชาติ

- 2.1 Quantum Mechanical Investigation of the Binding Stabilities of TMC278 inhibitor to Double Mutant HIV-1 Reverse Transcriptases K103N/Y181C and L100I/K103N, will be submitted.
- 2.2 Binding stabilities of DAPY inhibitors to Double Mutant HIV-1 Reverse Transcriptase (K103N/ Y181C), Based on ONIOM Methods, will be submitted.

3. Proceedings

- 3.1 Pensri Srivub, Pongtep Nokkaew and Supa Hannongbua. Theoretical Investigation on wild type and L100I/K103N HIV-1 Reverse Transcriptase Complexed with TMC278, Based on Quantum Mechanical Methods. Proceeding in Pure and Applied Chemistry International Conference (PACCON2011), January 5-7, 2011, Miracle Grand Convention Hotel Bangkok, Thailand.
- 3.2 Analysis of interaction of TMC278 inhibitor to Double Mutant HIV-1 Reverse Transcriptases K103N/Y181C and L100I/K103N as compared with wild type based on Quantum Mechanical calculations. Submitting in proceeding "Asian Wisdom Conferences", January 25-27, 2011. Silpakron University.
- 3.3 Investigation on the Interaction between TMC278 inhibitors and Mutant HIV-1 Reverse Transcriptase (K103N/ Y181C), Based on ONIOM2 method Submitting in proceeding in the 4th Annual PSU Phuket Research Conference 2011, November 16-18, Prince of Songkla University, Phuket Campus.

ภาคผนวก

1. การเสนอผลงานในที่ประชุมวิชาการ

1.1 นำเสนอผลงานในรูปโพสเตอร์ ในงานสัปดาห์วิทยาศาสตร์ คณะวิทยาศาสตร์และเทคโนโลยี มหาวิทยาลัยเทคโนโลยีราชมงคลศรีวิชัย วิทยาเขตนครศรีธรรมราช ระหว่างวันที่ 25-29 กันยายน 2552 เรื่อง "Investigation on the Interaction between DAPY Inhibitors and Mutant HIV-1 RT (K103N/Y181C), Based on Quantum Mechanical Methods"

ศึกษาอันตรีกิริยาระหว่าง DAPY inhibitors และ Mutant HIV-I Reverse Transcriptase (K103N/ Y181C).







Based on Quantum Mechanical Methods

ผส.ลรมพัญศรี สรีวัย", หายพงศ์เพพ นคนด้ว" เพะ วส.ลร.สุลา พารพนองยัว[‡]

"สาขาวิทยาสาสทร์ เจยะวิทยาสาสทร์และพากโนโลยี, มหาวิทยาลัยพากโนโลยีราชมมาลสรีวิจัย วิทยาพกามกาสาริธรรมราช +66-75-773131-2 +66-75-325887 E-mall :pendr_artvub@hommil.com ³ภากวิชาหนี กละวิทยาสาสาร์ มหาวิทยาลัยทยงาสาสาร์ วิทยายงบายขน กรุมทานทานกร Tel.: +66-2-9428900 ext 217; Fax : +66-2-9428900 ext 218; E-mail : Include Ska.ac.th.



רוביייים

ปัจจุบันโรงเซลที่ (Aququired Immune Deficiency Syndrome) ซึ่งเป็นปัญหาใหญ่ของทุกประกาศทั่วโดก โรงเฉลา์ พิลกาศโรรัสรเมิลหนึ่งที่เรียกว่า Human Immunodeficiency View (HIV) สังษณะพิเศษของไรรัสระโลนีก็อยามารถ น่าเอาส่วนของ gene ของตัวสันเข้าใช่แผ่งเป็นส่วนหนึ่งของ gene ของกา โดยอาศัยเอนใชม์ที่ก็เยือว่า Revers aw Enzyme (RT) เป็นตัวกระหุ้น ดันนั้นอนใชม์ HIV-1 RT เป็นอนใชม์เป็วหมากรัวหนึ่งที่มีความสำคัญ พ่อกรรรักษาโรกเอลล์ ยาโบกลุ่ม non-nucleoade RT inhibitor (NNRTI) มีประสิทธิกาหกรรยับยังการประชาย BIV-1 RT ได้ดี กล่งังเดิดล้องติดการคือยเรริงมาก ยาราสารได้ไรรักกติดการคลายพันธุ์ (motation) อย่างรวดเริง การ างหรับรู้ส่งเกลขน่างมากต่อการแลกงกับมันตกาพของทา โดยเฉพระอย่างนึ่งการกลายพันธุ์ของกาคอะมีในบริเวณ โพรงจับที่ดำแหน่ง Y181C และ K103N ทำให้ประสิทธิภาพของพาทมิลนี้อุดลงอย่างรวดเร็ว ดังนั้นจึงมีความ จำเป็นต้องพัฒนาการออกเบเนโมเอกุลแปลมีเพาะดับหายปลมที่มีประสิทธิภาพการออกฤทธิ์สูง เพื่อด้านประสาของสำ ในแท่งการการวงพระเกลียว อเพลิพซ้ามาช่วยในการที่เพารีลัย จึงเป็นวิธีที่สามารถทางแบบสิ่นกับ รายกับไร กับกุม การทำงานวิธีที่ให้สุรมายและให้เมที่สองกล้องกับการทรงอง พากราวพยยยายในการทัพยายกย่างต่อเลื่องเพื่อ ทัปัญหาการลื้อสาล่ออลเรียม์ HIV-1 RT หมว่ายาโนกลุ่ม NSRTI» เป็นสารที่ออกฤทธิ์สัมสังคมโชม์ไล้ลืมากทั้งใน ของสุดเกตรากอยากของคระสามาราชสามาราชสามารถสามารถสามารถสามารถสามารถสามารถสามารถสามารถสามารถสามารถสามารถสามารถสา เพื่อที่ไม่มีการกลามารถสามารถสามารถสามารถสามารถสามารถสามารถสามารถสามารถสามารถสามารถสามารถสามารถสามารถสามารถสาม ทัมร์ แต่จะวัติเการที่จอยไม่อารถสามารถสามารถสามารถสามารถสามารถสามารถสามารถสามารถสามารถสามารถสามารถสามารถสามารถ YISIC/KIOSN ขณะที่ Etavla-ax ที่เป็นแท่ที่นี่ประสิทธิกาหการออกฤทธิ์ได้ในเรื่อที่ไม่มีการกลามกันย์ และการกลาม ก็เห็ต่ายหน่งเดียว Y181C แต่อะเกิดการถื้อยาในหากลายพันธ์การกลายพันธ์ต่ายหน่งเดียว K103N และกลายพันธ์ ของกำหากส่ง YISIC/KIOSN ดังนั้นอื่อสืดาวทัดนายากคุ่ม NNRTI» อย่างก่อเนื่อง สืออุบันยากคุ่มของ DAPY เส็นยา ตัวใหม่ในการวัดมาโรกเอกส์ได้ลีทั้งกรณีในเรื่อที่ให้มีการกอบเท้นผู้ การกอบเท้นผู้หนึ่งตำแหน่ง เช่น VISIC หรือ K103N และกลามทับผู้สองคำแหน่ง เพิ่ม Y181C/K103N สาวกลุ่ม DAPY เพิ่ม TMC278 มีประสิทธิภาพการออกฤทธิ์ ดีกว่า Neviropiae และ Efevireux ดเราะโลรงสร้างของตา TMC278 มีความถึกหญ่นสูง ซึ่งสามารถปรับโครงสร้างให้ ดามสดาวะโพรงการจับของ HIV-1 RT ที่เปลี่ยนแปลงไปเพื่อมีการตัดการทอบทันธุ์ โครงสร้างของมา TMC27 เกษลังรูปที่เ



วูปที่1. โกรเครื่องของการMC278

เริ่มกับงานวิจัยขึ้นที่จึงมีเป้าหมายที่จะสึกษาการจับของยา TMC278 ในเชื้อที่ไม่มีการกลายกับผู้และเชื้อที่การกลายกับธ์ อองตำแหน่ง (doable matant, YISIC/KION) และสึกษาอันตรกิริยาระหว่างสารกับยังตั้งกล่าวกับหรืเวลประราชารกับ ของอเปี ยที่ HIV-1 RT ด้วยวิธีการกานวยทางอเดิกวอนกับ ซึ่งเอการศึกษาวิจัยในกรั้งนี้จะกามาวอนไปปกินข้อมูล ที่แลานในการออกแบบดัวยับนั้วที่ดียิ่งนี้แต่อไป อีกทั้งมีภา ให้เซ็าในนิ้มการดิดอันกาทีวิตาระหว่างตัวยับนั้งและเอนไขม่ (inhibitor-enzyme interaction)

วัดถประสงค์

- 1. พรียมโกรงตร้างการจับตัวของยากกุ่ม TMC278 กับกาลอะมิโหในโพรงการจับของเอนใชม์ HIV-1 RT กาลีที่ในมีการกลายพันธุ์เกละเพื่อที่การกลายพันธ์สองศัพเหน่ง (double mutant, Y181C/K103N) โดย น่าโกรงกร้างมาจาก X-ray crystallography
- เพื่อกำนวณกากำหลังงานการกิลย์แตรกิริยาระหว่างตัวยา TMC278 กับกาลอะมีโนเพ่กะหัวในโพรง. การจับของเอนใชม์ HIV-t RT ด้วยการถ่านวณด้วยระเบียบวิธีทางกาอนดัม
- ร. เพื่อเปรียบเทียบพถังงานอ่าหลังงานการเกิดอันตรกิริยาระหว่างตัวยา TMC278 ในเชื้อที่ให้มีการกลาย ทับรุ่นฉะเชื้อที่การกลายทับร์สองท่ายหนึ่ง (double mutant, Y181C/K103N) ของ HIV-1 RT ด้วยการ กานวณด้วยระเบียมวิธีทางกวอนตัม

จะเบียบวิธีการวิจัย

1. กร้างแบบจำกองโครงกร้างของเอนใชม์ HIV-1 RT/ TMC278 complex ทั้งหนิดที่ไม่มีคาวดถายทันธุ์ เพราะนิดที่มีการกกายพันธุ์ที่ตำแหน่ง Y181C/K103N จากโกรงสร้าง X-ray crystallography

- นาโกรงสร้างที่ได้ มาตัดเอาส่วนของกรดอะมิโนในโพรงการจับของเอนใหม่ HIV-1 RT ท่างจาก กูนย์กลางของตัวยับยั้งประมาณ 7 A จะใต้เกมสำกองโลรงสร้างของเอนใชม์ HIV-1 RT/ 278 comple
- . 3. จากน้ำเปิดปกายพงกาลตะมีโนที่ถูกกัด เพะทำโครงตรึงปกัตมมูรณ์โดยการเติมไปเดาเจนเข้าไป และ เพื่อทำโห้สมเกม่งของไปโดรเอมดูกต้องและเกมาะตม นำโครงตรัรงที่ได้ optimize จะต่อมของไปโดรเจม ด้วยระเบียบวิธี semi-empirical PM3
- ทำโกรงสร้างที่ใส่จากข้อ 3.4 ถ้าแวดหาคำหลังงานการเกิดฉันตรกิริยาระหว่างตัวยากลุ่ม DAPY ถับ กรดอะมิโนเพ่นะตัวในโพรงการจับของเอนใจที่ HIV-t RT โดยการกำหวดตัวยระเบียบวิธีทางกวองตัน

กิดดีกรรมประกาศ

สำหัดงานของๆและรับสะทุนการวิจัย ร่วมกับสำหัดงานกายของระหวรจุดเผลิกเล

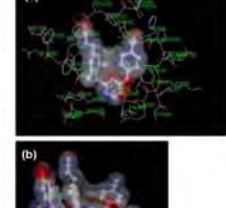
- กาลวิชเหลนี กละวิทยาลากเรียนาวิทยาลัยกาลากเรา กายกรี กรุ เยยเมษาเพลา
- ดายวัทยาสากร์ คละวิทยาสากหว่าคะเหลโนโกมี มหาวิทยาลัยเหลโนโลยีราชสาลคลรีวิธัยวิทยาเบตผลาสรีธรรมราช

ผลการคำนวณ

ทรวงที่ 1. Interaction energier Wes Individual residues (in keal/nos) สำหวด โลกระเบียบวิธี MP2/6-51g(d) level of theory

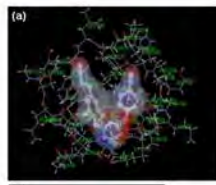
B. 11. 000	Interaction energy (kcal/mol)			
Residue(X ₁)	Wild type	K103N/Y181C	Δε	
PRO95	-0.46	-0.39	-0.06	
GLY99	-0.13	-0.16	0.02	
LEU100	1.86	-3.27	1.42	
LYS101	-8.15	-7.76	-0.39	
LY\$102	-0.13	0.22	0.09	
LY8103 (ASN)	-1.80	(-2.28)	6.48	
VAL 106	-0.39	-0.21	-0.13	
GLU138	-2.95	-2.44	-0.51	
ILE180	-0.92	-L11	0.19	
TYR181(CV#)	-4.52	-0.98	-2.93	
GLN182	-0.37	6.03	-0.40	
TYR183	-0.55	-1.38	0.83	
TYR188	-2.24	-1.33	-0.91	
VAL 189	-0.26	0.36	0.09	
GLY190	-0.72	-0.87	0.15	
PRO225	-1.52	-1.19	-0.33	
PRO226	-0.60	-1.19	0.59	
PHE227	-3.09	-2.43	-0.66	
LEU228	0.46	6.61	-0.15	
TRF229	-5.46	-5.51	0.05	
LEU234	-0.94	-1.02	0.08	
PRO236	2.18	-2.98	0.80	
ASP237	1.50	:2.44	0.94	
TYR318	-1.50	-1.44	-0.06	
Total Energy	~41.76	-41.36	-0.82	

INT inhibitor Xi = E inhibitor Xi + E inhibitor - Exi



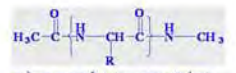


rdiff2, (as ferra saffrancia a TMC218 la banding pocket with ld type (b) Electrostatic potential laudinaries dues intellis eliminariellus positive values voi tentiant for Low 100 une Tyritt





olita, ca averagifyman TMC2W lis blodies backet pants (0,000) HIV-1 RT (b) Electrodate potential โดยสัยกายแลง negative values และสีน้ำเป็นแสดงหนึ่น poultve values ของกับคริสินีกระหว่างมากับ Aut (0) และ



าปที่4 การตัดกับ ะใชโดงเกระหว่าเก TMC278ลัย Lyder

apharieralarreisanles

จากการศึกษากวามแพลต่างของอันตรกิริยาระหว่าง wild type HIV-1 RT และ K103N/V181C mutan HIV-1 RT กับมา TMC 278 กำหวดโดยระเบียนวิธี MP2-6-31G(d.p.) level กำหลังงานอังตรกิริมาที่มีกำ มากที่ถูกประมาณ 8 kcm/mol ทั้งกรณีเนื้อที่ไม่มีการกถานกันทุ้นแะกรณีเชื้อที่มีการกถายกันทุ้ ถือ แรงคึงดูค าะหว่าง TMC278 กับ Lys101 เป็นผถเนื่องมาลากมีพันธะใชโดวเลน แกดงดังรูปที่3 เพะนอกลากนี้หมว่าค่า พลังงานยันตรกิริยารวม ทั้งกรณี พลิส type และ K103N/V181C HIV-1 RT แตลงว่า TMC278 เป็นยา ที่ สามารถออกฤทธิ์ได้ดีในเชื้อที่ไม่มีการกกายพันธุ์และเชื้อที่มีการกลายพับธุ์สองตาแหน่ง (K103N/YISIC) เพ่งม่าสำรักกามหนว่าการที่ที่เพื่อมีการกามพันธุ์ส่งผลให้ หลังงานอันตารกิรินาระหว่างมา TMC278 และCys 181 ลดลงประมาณ 3 kademot เมื่อเยียมกับเพื่อที่ไม่มีการกลายทันธุ์ ข้อมูตที่ได้เป็นข้อมูกพื้นฐานในการ ออกแบบตัวยับยั้งที่ดียิ่งขึ้นค่อไป อีกทั้งยังทำให้เข้าใจถึงกาวเกิดอันตรกิริยาระหว่างตัวยับยั้งและเอนใชม์ (inhibitor-enzyme interaction)

เอกสารข้างอิง

- Kimo, M., Hannongbus, S. and Morokuma, K., Theoretical Investigation on Nevirapine and HIV-Reverse Transcriptuse Binding Site Interaction, Based on ONIOM Method Chem. Phy. Lett. 380 (2003) 456
- Nunrhum, P., Kuno, M., Saen-oon, S. and Hannongbua, S., Particular Interaction between Effvirong and the HIV-1 RT binding site as explained by the ONIOM2 method, Chem. Phy. Lett. 405 (2005) 198.
- Saen-oon, S., Kuno, M., and Hannongbua, S., Binding Energy Analysis for Wild type and Y181C Mutan HIV-1 RT/8-Cl TIBO Complex Structures; Quantum Chemical Calculations, Based on ONIOM Method, PROTEINS, (2005), inpress.

1.2 นำเสนอผลงานในรูปโพสเตอร์ ที่ประชุมวิชาการ Pure and Applied Chemistry International Conference (PACCON2011) ระหว่างวันที่ 5-7 มกราคม 2553 ณ Miracle Grand Hotel Bangkok, Thailand เรื่อง "Theoretical Investigation on wild type and L100I/K103N HIV-1 Reverse Transcriptase Complexed with TMC278, Based on Quantum Mechanical Methods"



THEORETICAL INVESTIGATION ON WILD TYPE AND L100I/K103N HIV-1 RT COMPLEXED WITH TMC278, BASED ON QUANTUM MECHANICAL METHODS



Pensri Srivub^{1*}, Pongtep Nokkaew¹ and Supa Hannongbua²

Faculty of Science and Technology, Rajamangala University of Technology Srivijaya, Nakronsri Thammat, Thailand. ²Center of Nanotechnology and NANOTECH Center of Excellence Kasatsart University, Bangkok 10900 Thailand.



The interactions between TMC278 and allosteric binding site of HIV-1 reverse transcriptase of wildtype, and with double mutation L1001/K100N were investigated by using three-layered ONIOM
calculations. Binding energies were determined and compared to describe the loss of activity of
TMC278 with double mutation L1001/K100N HIV-1 RT binding pockets as compared with wild type.
The binding energy for the TMC278-L1001/K103N HIV-1 RT complex is less than that of the wildtype complex by approximately 9.71 kcalmon. This lead to specific interactions between TMC278 and
key residues in the two complex structures being investigated. It was found that the attractive
interactions between TMC278 and K101, K103 and W229 were reduced compared to the wild-type by
5.92, -4.69 and 3.21 kcalmon, respectively. It is important to note that hydrogen bonding occurring
between TMC278 and K101 was also disturbed. Moreover, N103 in the binding pocket of the
L1001/K100N enzyme creates a repulsive interaction with the inhibitor. This confirmed that TMC278
shows higher inhibitory affinities against wild-type than L1001/K100N enzyme. Understanding these
particular structural interactions can be useful for the design of inhibitors which are specific to HIV-1
RT allosteric site and with greater potency against mutant types.

INTRODUCTION

Human immunodeficiency virus type I reverse transcriptase (HIV-1 RT) is one of the most important enzymes in the HIV-1 life cycle for the development of new anti-AIDS drugs to treat HIV-1 infections, permitting dramatic reduction in viral loads and restoration of the immune system. However, treatments of drug do not eliminate the infection and treatment must be life-long. Drug closely to prolonged drug can be lead to the emergence of drug-resistant mutant virus that is the key problem to develop new anti-AIDS drugs. Nevirapine fails to treat the V181C mutation[1]. The K103N mutation confers resistance to efavirenz. The L1001 mutation and combined two mutations such as K103NY181C and L1001K103N were fully resistant to almost all NNRTis drugs including nevirapine, efavirenz[2] and delavirdine. New series of NNRTIs was discover that belong to the diarylpy rimidine(DAPY) family. DAPY compounds, with TMC278 and them derivatives were more potent than efavirenz, nevirapine and delavirdine. Moreover, TMC278 and some them derivatives demonstrated high potency on wild type, single and the double mutant strains as compared with to marked drugs. The wiggling and jiggling of TMC278 compounds help them to retain their potency against mutant HIV-1 viruses. In an attempt to understand the different binding stability of TMC278 to wild type and double mutant L1001K103N at a molecular level, the ONIOM computational approach[5] was employed, it has not been clearly understood inhibitory effect of TMC278 to the double mutant L1001K103N. This understanding will be helpful in the design of new hinibitors especially active against double mutant HIV-1, and thus better anti-AIDs agents. Thus, the understanding of the molecular mechanism of drug resistance can help in the design of new hinibitors especially active against double mutant HIV-1 (ra) and the behavior of the design of new hinibitors especially active against double mutant HIV-1 (ra) and the behavior of the molecular mechanism of drug resistance can help in the design of new h

COMPUTATIONAL METHODS

The starting models for calculations were obtained from the X-ray structures of TMC278 bound to HIV-1 RT for the wild-type and L1001/K103N enzymes, listed in the Protein Data Bank with PDB entry codes 2ZD1 and 2ZE2 respectively [4]. The studied binding pocket included residues surrounding the non-nucleoside inhibitor binding pocket (NMBP) with at least one atom interacting with any of the atoms of the TMC278 inhibitor within the interatomic distance of 7.0 Å. These residues of the studied system are Pro95, Leat00(He100), Lys101, Lys102, Lys103, Val106, Val179, He180, Tyr181, Gl182, Tyr181, Tyr188, Val189, Cyly90, Pro225, Pro226, Pre427, he227, Fre220, Lea234, Pro236, Asp237 and Tyr318 from the p66 domain of RT, and Gl138(b) from the St domain of RT (Figure1). All residues were assumed to be in their neutral form. The N- and C-terminal ends of cut residues were capped with an acetyl group (CH3CCO) and a methyl amino group (NHCH3), respectively [H3C-C(C90-[NH-CHG-F-CH3])]. The hydrogen atoms then were added to generate the complete structures and their positions were optimized by the semi-empirical PM3 method as available in the GAUSSIAN 03 program running in Linux on a Pentium IV 3.2 GHz PC. The optimizations were carried out with fixed heavy atoms and the final structures produced were used as the starting geometries for all subsequent calculations. The interaction energies, Ergang-may, between TMC278 and individual residues, Xi. were calculated at the MP2/6-31G(d,p) levels of theory using the gonoticy described above. Three layer Oxford calculations were performed to determine the binding energy of TMC278 bound to the double mutant L1001/K103N HIV-1 RT as compared to the wild-type. All calculations were carried out using the GAUSSIAN 03 package.

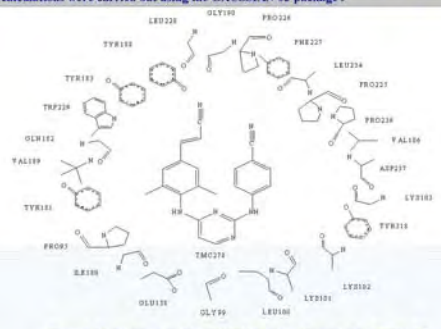


Figure 1. Model system used for TMC278 bound to allosteric site of HIV-1 RT consisting of 24 residues wild-type HIV-1 RT NNIBP.

HESULUS AND DESEUSSION

Table1 The calculated interaction of TMC278 with individual residues (Xi) from MP2/6 31G(d,p) methods

Interaction energy (kraluna)

	Interaction energy (kcal/mol)		o D
Residue(X _i)	Wild type	L1001/K103N	ΔE
PRO95	-0.46	-0.19	-0.27
GLY99	+0.13	-0.67	0.54
LEU100	-1.86	-0.08	-1.78
LYS101	-8.15	-2.23	-5.92
LYS102	-0.13	-0.20	0.07
LYS103 (A5N)	-1.80	(7.89)	4.69
VALI06	-0.39	-1.55	1.16
II.E180	-0.92	-0.55	-0.37
TYRISI CVS	-4.52	4.16	0.49
GLN182	-0.37	-0.16	-0.21
TYR183	-0.55	-1.35	0.8
TYR188	-2.24	-434	2.1
VAL189	-0.26	-0.40	0.14
GLY190	-0.72	-0.41	-0.31
PR-0225	-1.52	-1.19	-0.33
PR0226	-0.60	-0.80	0.2
PHE227	-3.09	-3.78	0.69
LEU228	0.46	0.76	-0.3
TRP229	-5.46	-2.25	-3.21
LEU234	-0.94	1.22	-2.16
PR-0236	-2.18	-1.07	1.11
ASP237	-1.50	-0.11	-1.39
TYR318	-1.50	-1.21	-0.29
GLU138	-2.95	-2.44	-0.51
TYP318	-1.50	-1.44	-0.06
Total Energy	41.76	41.36	-0.82

Table2. Binding energy for the wild type and L1001/K103N mutant HIV-1 RT complexed with TMC278 using ONIOM3[MP2/6-31G(d,p):B3LYP/6-31G(d,p):PM3].

HIV-1 RT	Binding Energy (kcal/mol)	ΔE
Wild-type	-20.29	-10.58
1100L/K103N	-9.71	



with largest interactions in the binding pocket of wild-type HIV-1 RT

INT inhibitor +Xi = Einhibitor +Xi + Einhibitor -Exi

In wild type RT, the main contributions to the interactions with TMC278 come from K101, Y181, F227 and W229 which produce attractive interactions greater than 3 kcal/mol, calculated at MP2/6-31G(d,p) level. Considered in greater detail (Figure 2), TMC278 can be flexible to bind to HIV-1 RT and interacts with aromatic side chains of Y181 and W229 via H-x interaction. The repulsive interactions between TMC278 and residues of the binding pocket for the L1001/K103N enzyme is more than in wild-type. Also, the attractive interactions between TMC278 and K101, K103 and W229 in the L1001/K103N enzyme were reduced to 502, 4.69 and 3.21 kcal/mol, respectively (&E in Table 1, MP2/6-31G(d,p) method), compared to the wild type RT. These results indicate that the mutated residues (L1001 and K103N) not only reduce binding stability of TMC278, but also induce destabilization in the cavity leading W229 residue to loose contact with the inhibitor. Table 2 shows the binding energies for the wild type and L1001/K103N complexes using three-layer ON1OM calculations. It can be seen that the difference in binding energy between wild type and L1001/K103N enzymes is far more significant (10.58 kcal/mol with the MP2/6-31G(d,p):PM3 method). The mutations in the L1001/K103N enzyme leads to a reduction in the stabilization energy of the mutations in the L1001/K103N enzyme leads to a reduction in the stabilization energy of the complex and induces destabilization in the cavity by reducing contact between K101 and TMC278. TMC278 shows higher inhibitory affinities with the wild type compared to the double mutation L1001/K103N enzyme.

CONCLUSION

The binding energy for the TMC278-L1001/K103N HIV-1 RT complex is less than that of the wild-type complex by approximately 9.71 kcal/mol. This lead to specific interactions between TMC278 and key residues in the two complex structures being investigated. It was found that the attractive interactions between TMC278 and K101, K103 and W229 were reduced compared to the wild-type by 5.92, -4.69 and 3.21 kcal/mol, respectively. It is important to note that hydrogen bounding occurring between TMC278 and K101 was also disturbed. Moreover, 103 in the binding pocket of the L1001/K103N enzyme creates a repulsive interaction with the inhibitor. This confirmed that TMC278 shows higher inhibitory affinities against wild-type than L1001/K103N enzyme. Understanding these particular structural interactions can be useful for the design of inhibitors which are specific to HIV-1 RT allosteric site and with greater potency against mutant types.

- M. Kuno, S. Hannongbua, K. Morokuma, Chem, Phy. Lett. 2003, 380, 456-463.
 P. Srivab and S. Hannongbua, ChemMedChem 2008, 3, 1-10.
 K. Morokuma, Philos. Transact. A Math. Phys. Eng. Sci. 2002, 360, 1149-1164.

- K. Das, J.D. Bauman, A.D. Clark, Y.V. Frenkel, P.J. Lewi, A.J. Shatkin, S.H. Hughes, and E. Arnold, PNAS, 2008, 105(5), 1466-1471.

ACKNOWLEDGMENT

- The Thailand Research Fund.
- The Commission on Higher Education, Ministry of Education.
- · Faculty of Science and Technology, Rajamangala University of Technology Srivijaya.

2. ผลงานตีพิมพ์ในวารสารวิชาการนานาชาติ

- 2.1 Quantum Mechanical Investigation of the Binding Stabilities of TMC278 inhibitor to Double Mutant HIV-1 Reverse Transcriptases K103N/Y181C and L100I/K103N, will be submitted.
- 2.3 Binding stabilities of DAPY inhibitors to Double Mutant HIV-1 Reverse Transcriptase (K103N/ Y181C), Based on ONIOM Methods, will be submitted.

Manuscript will be submitted in topic:

Quantum Mechanical Investigation of the Binding Stabilities of TMC278 inhibitor to Double Mutant HIV-1 Reverse Transcriptases K103N/Y181C and L100l/K103N.

Pensri Srivub [a]*. Pongtep Nokkaew and Supa Hannongbua [b]

^[a]Faculty of Science and Technology, Rajamangala University of Technology Srivijaya, Nakronsri Thammarat, 80110 Thailand

^[b]Center of Nanotechnology and *NANOTECH,* Center of Excellence, Kasatsart University, Bangkok 10900 THAILAND.

* Corresponding Author: pensri srivub@yahoo.com

ABSTRACT

The interactions between TMC278 and the allosteric binding site of HIV-1 reverse transcriptase of wild-type, and with double mutations L100I/K103N or K103N/Y181C, were investigated using three-layered ONIOM calculations. Binding energies were determined and used to describe the loss of activity of TMC278 with the double mutation binding sites. The calculated binding energy for the TMC278-K103N/Y181C HIV-1 RT complex is -28.31 kcal/mol using the MP2/6-31G(d,p):B3LYP/6-31G(d,p):PM3 method. This is not significantly different from the wild-type complex binding energy of -30.01 kcal/mol. In contrast, the binding energy for TMC278-L100I/K103N HIV-1 RT complex is less than that of the wild-type complex by 9.71 kcal/mol. This lead to the specific interactions between TMC278 and key residues in the three complex structures being investigated. It was found that interaction energies calculated at MP2/6-31G(d,p) level between TMC278 and individual residues surrounding the binding pocket for both wild-type and K103N/Y181C HIV-1 RT are not significantly different excepted for mutated residue C181. In the L100I/K103N enzyme, the attractive interactions between TMC278 and K101, K103 and W229 were reduced compared to the wild-type by 5.92, -4.69 and 3.21 kcal/mol, respectively. It is important to note that hydrogen bonding occurring between TMC278 and K101 was also disturbed. Moreover, N103 in the binding pocket of the L100I/K103N enzyme creates a repulsive interaction with the inhibitor. This confirmed that TMC278 shows higher inhibitory affinities against wild-type and K103N/Y181C enzymes than L100I/K103N enzyme, and shows the structural changes responsible. Understanding

these particular structural interactions can be useful for the design of inhibitors which are specific to HIV-1 RT allosteric site and with greater potency against mutant types.

Keywords: Binding energy, HIV-1 RT, Interaction energy, inhibitor-enzyme interactions, DAPY inhibitors, TMC278, ONIOM

Introduction

Human immunodeficiency virus type 1 reverse transcriptase (HIV-1 RT) is one of the most important enzymes in the HIV-1 life cycle targeted for the development of new anti-AIDS drugs to treat HIV-1 infections, as its inhibition results in a dramatic reduction in viral loads and restoration of the immune system [1]. However, treatment does not eliminate the infection and must be life-long. Drug toxicity and prolonged drug use can lead to the emergence of drug-resistant mutant virus, and this is a key problem to developing new anti-AIDS drugs. Nevirapine fails to treat the Y181C mutation, while the K103N mutation confers resistance to efavirenz. The L100I mutation and combined dual mutations such as K103N/Y181C and L100I/K103N are fully resistant to almost all NNRTIs drugs including nevirapine, efavirenz and delavirdine. A new series of NNRTIs was discovered that belongs to the diarylpyrimidine (DAPY) family. DAPY compounds, with TMC278 and its derivatives, are more potent than efavirenz, nevirapine and delavirdine[2]. Moreover, they demonstrated high potency against wild-type, single and the double mutant strains compared to marked drugs [3]. The motion and flexibility of TMC278 compounds help them to retain their potency against mutant HIV-1 viruses [4].

In order to understand the binding stabilities of TMC278 to double mutation such as K103N/Y181C or L100I/K103N at a molecular level, the ONIOM computational approach was employed to calculate binding energy of TMC278. This approach was useful in previous studies to demonstrate the particular interactions between the NNRTIs TIBO [5], nevirapine [6] and efavirenz [7], and amino acids in the non-nucleoside inhibitor binding pocket (NNIBP) with wild-type, single mutant HIV-1 RT and K103N/Y181C. This understanding will be helpful in the design of new inhibitors especially active against double mutant HIV-1 RT, thus providing better anti-AIDs agents.

The three-layer ONIOM (ONIOM3) method was used to study the interaction between efavirenz and residues in the binding pocket for K103N/Y181C double mutation

HIV-1 RT as compared with wild-type. The results showed the calculated binding energy for the efavirenz-K103N/Y181C HIV-1 RT complex is less than that with the wild-type complex by approximately 8 kcal/mol [8]. The inhibitory effect of TMC278 on the double mutant strain such as K103N/Y181C or L100I/K103N has not been clearly understood. The following work describes the binding interaction of TMC278 to the double mutant K103N/Y181C or L100I/K103N.

Computational Methods

System studied

The starting models for calculations were obtained from the X-ray structures of TMC278 bound to HIV-1 RT for the wild-type, K103N/Y181C and L100I/K103N enzymes, listed in the Protein Data Bank with PDB entry codes 2ZD1, 3GBR and 2ZE2 respectively [2]. The studied binding pocket included residues surrounding the non-nucleoside inhibitor binding pocket (NNIBP) with at least one atom interacting with any of the atoms of the TMC278 inhibitor within an interatomic distance of 7.0 Å These residues of the studied system are Pro95, Leu100(Ile100), Lys101, Lys102, Lys103(Asn103), Val106, Val179, Ile180, Tyr181(Cys181), Gln182, Tyr183, Tyr188, Val189, Gly190, Pro225, Pro226, Phe227, Leu228, Trp229, Leu234, Pro236, Asp237 and Tyr318 from the p66 domain of RT, and Glu138(b) from the 51 domain of RT (Figure1). All residues were assumed to be in their neutral form. The N- and C-terminal ends of cut residues were capped with an acetyl group (CH₃CO-) and a methyl amino group (-NHCH₃), respectively $[(H_3C-C(=O)-\{NH-CH(-R)-C(=O)\}_n-NH-CH_3)]$. Hydrogen atoms were added to generate the complete structures and their positions were optimized by the semi-empirical PM3 method available in the GAUSSIAN 03 program running in Linux on a Pentium IV 3.2 GHz PC [10]. The optimizations were carried out with fixed heavy atoms and the final structures produced were used as the starting geometries for all subsequent calculations.

Figure 1 Model system used for TMC278 bound to the allosteric site, NNIBP, of HIV-1 RT consisting of 24 residues. Wild-type HIV-1 RT shown.

Interaction energy calculations

The interaction energies, $E_{(TMC278+Xi)}$, between TMC278 and individual residues, X_i , were calculated at the MP2/6-31G(d,p) levels of theory using the geometry described above. The total interaction energy, INT, can be expressed as: [5]

$$INT_{(EFZ+Xi)} = E_{(EFZ+Xi)} - E_{(EFZ)} - E_{(Xi)},$$

$$\tag{1}$$

where $E_{(TMC278)}$ and $E_{(Xi)}$ are energies of TMC278 and each individual residue, respectively.

Binding energy calculations

Three layer ONIOM calculations were performed to determine the binding energy of TMC278 bound to the double mutant L100I/K103N or K103N/Y181C HIV-1 RT as compared to the wild-type. The total ONIOM energy of the entire system was obtained from five independent energy calculations in the ONIOM3 methods as shown in the equations (2) [9].

 $\Delta E^{ONIOM3} = E [Cpx]_{opt} - E[P]_{opt} - E[L]_{opt}$ $= \Delta E (High, A) + [\Delta E (Mid, AB) - \Delta E (Mid, A)] + [\Delta E (Low, ABC) - \Delta E (Low, AB)]$ $= \Delta E (High, A) + [\Delta \Delta E (Mid, AB-A)] + [\Delta \Delta E (Low, ABC-AB)] (2)$

Where $E[Cpx]_{opt}$ is the total optimized energy of the TMC278-binding pocket complex, Cpx; $E[P]_{opt}$ is the optimized energy of binding pocket; and $E[L]_{opt}$ is the optimized energy of the TMC278 ligand. Also, ΔE (High, A) is the interaction energy in the region A which is treated at the high level of theory, $\Delta \Delta E$ (Mid, AB-A) is the interaction energy from interactions between the regions A and B and is evaluated at the medium level of theory, and $\Delta \Delta E$ (low, ABC-AB) is the interaction energy from interactions between the regions AB and C which is evaluated at the low level of theory.

Comparing binding energy calculations between wild-type and K103N/Y181C enzymes, The inner layer (region A) including TMC278 and Y181 or C181 was treated at the MP2/6-31G(d,p) and The medium layer (region B) including K101 and K103 was treated at the B3LYP/6-31G(d,p) methods. The remainder of the residues was taken as the outer layer (region C) which was treated at the PM3 level. For this study, the following models were generated:

ONIOM3 calculation: MP2/6-31G(d,p)[TMC278+(Y181 or C181)]:B3LYP/6-31G(d,p) [K101+K103 or N103]:PM3[real]

Comparing binding energy calculations between wild-type and L100l/K103N enzymes, The inner layer or interaction region including the TMC278 and L100 or I100 was treated by the MP2/6-31G(d,p) methods. The medium layer including K101 and either K103 or N103 were treated by the B3LYP/6-31G(d,p) method. The remainder of the residues was taken as the outer layer which was treated by the PM3 method. For this study, the following models were generated:

ONIOM3 calculation: MP2/6-31G(d,p)[TMC278+(L100I or I100)]:B3LYP/6-31G(d,p)

[K101+(K103 or N103)]:PM3[real]

Results and discussion

1. Interaction energy of TMC278 with individual residues of the HIV-1 RT binding pocket

The interaction energies between TMC278 and the individual residues (Xi) of HIV-1 RT binding pocket for wild-type, L100I/K103N or K103N/Y181C enzymes were calculated at MP2/6-31G(d,p) levels of theory and are shown in Table 1. As the MP2 method includes the dispersion interactions, it is expected to give more accurate interaction energies than B3LYP [11]. In wild-type RT, the main contributions to the interactions with TMC278 come from K101, Y181, F227 and W229 which produce attractive interactions greater than 3 kcal/mol, calculated at MP2/6-31G(d,p) level. Considered in greater detail (Figure 2), hydrogen bonding between a linker nitrogen atom of TMC278 (Figure 3) and the mainchain carbonyl oxygen of K101 causes the strongest interaction, 8.15 kcal/mol at the MP2/6-31G(d,p) level, and is conserved in the binding of many NNRTIs. The cyanovinyl group is positioned to fit into a hydrophobic tunnel formed by the side chains of amino acid residues F227 and W229 that may explain why TMC278 is the most potent of DAPY analogues. TMC278 can be flexible to bind to HIV-1 RT and interacts with aromatic side chains of Y181 and W229 via H- π interactions. Comparing the wild-type RT and K103N/Y181C RT at the MP2/6-31G(d,p) method shows no significant difference between the interactions, except for the mutated residue C181. The attractive interactions between TMC278 and C181 in the K103N/Y181C enzyme were reduced by 2.93 kcal/mol.

The repulsive interactions between TMC278 and residues of the binding pocket for the L100I/K103N RT are greater than in wild-type RT and K103N/Y181C RT. Also, the attractive interactions between TMC278 and K101, K103 and W229 in the L100I/K103N RT were reduced to 5.92, 4.69 and 3.21 kcal/mol, respectively ($^b\Delta$ E in Table 1, MP2/6-31G(d,p) method), compared to the wild-type RT. These results indicate that the mutated residues L100I and K103N not only reduce the binding stability of TMC278, but actually destabilize the cavity, leading the W229 residue to lose contact with the inhibitor.

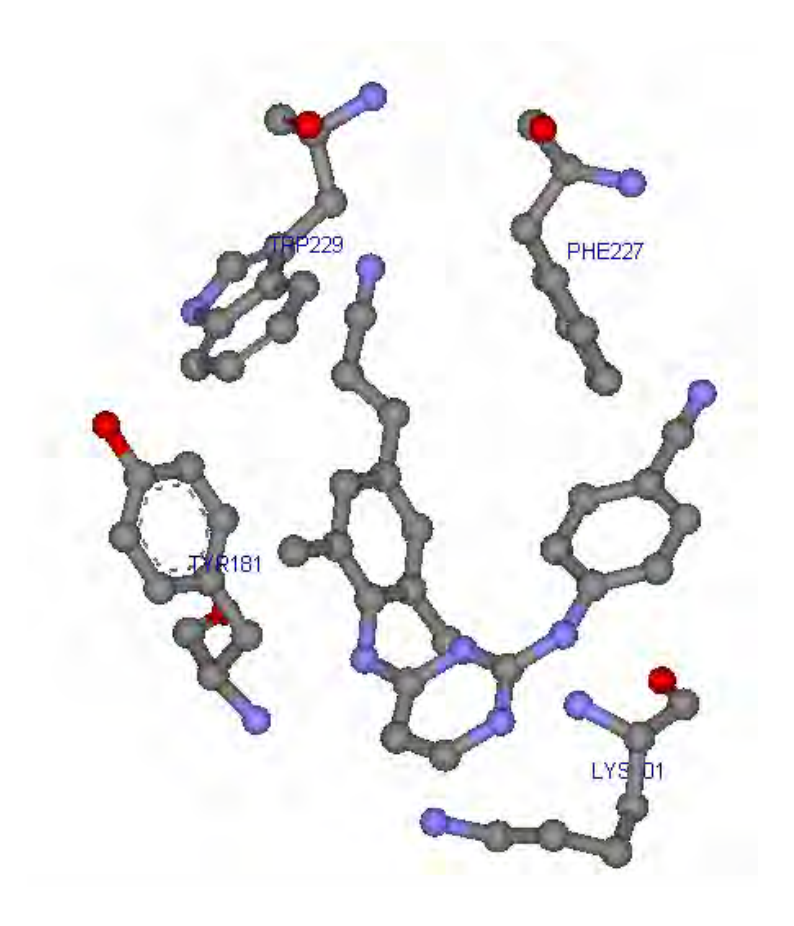


Figure 2 Orientation of TMC278 and the residues with the largest interactions in the binding pocket of wild-type HIV-1 RT.

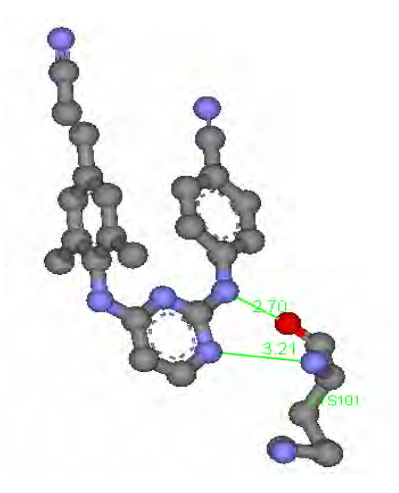


Figure 3 Hydrogen bonding between K101 and TMC278

Table 1 The calculated interactions between TMC278 and individual residues (X_i) from the MP2/6-31G(d,p) method.

Residue(X _i)	Interaction energy (kcal/mol)				
	Wild-type	K103N/Y181C	L100/I/K103N	ΔE_a	ΔE_b
PRO95	-0.46	-0.39	-0.19	-0.06	-0.27
GLY99	-0.13	-0.16	-0.67	0.02	0.54
LEU100	-1.86	-3.27	-0.08	1.42	-1.78
LYS101	-8.15	-7.76	-2.23	-0.39	-5.92
LYS102	-0.13	-0.22	-0.20	0.09	0.07
LYS103 (ASN)	-1.80	-2.28	2.89	0.48	-4.69
VAL106	-0.39	-0.21	-1.55	-0.18	1.16
ILE180	-0.92	-1.11	-0.55	0.19	-0.37
TYR181(CYS)	-4.52	-1.60	-4.03	-2.93	-0.49
GLN182	-0.37	0.03	-0.16	-0.40	-0.21
TYR183	-0.55	-1.38	-1.35	0.83	0.8
TYR188	-2.24	-1.33	-4.34	-0.91	2.1
VAL189	-0.26	-0.36	-0.40	0.09	0.14
GLY190	-0.72	-0.87	-0.41	0.15	-0.31
PRO225	-1.52	-1.19	-1.19	-0.33	-0.33
PRO226	-0.60	-1.19	-0.80	0.59	0.2
PHE227	-3.09	-2.43	-3.78	-0.66	0.69
LEU228	0.46	0.61	0.76	-0.15	-0.3
TRP229	-5.46	-5.51	-2.25	0.05	-3.21
LEU234	-0.94	-1.02	1.22	0.08	-2.16
PRO236	-2.18	-2.98	-1.07	0.80	-1.11
ASP237	-1.50	-2.44	-0.11	0.94	-1.39
TYR318	-1.50	-1.44	-1.21	-0.06	-0.29
GLU138	-2.95	-2.44	-0.68	-0.51	-2.27
Total Energy	-41.76	-41.36	-22.36	-0.82	-19.42

 $\Delta E_a = E_{wild- type} - E_{K103N/Y181C mutant}$

 $\Delta E_b = E_{wild-type} - E_{L100I/K103N mutant}$

Binding energy calculations

Comparing binding energy calculations between wild-type RT and K103N/Y181C RT.

K103N and Y181C are the two drug-resistant mutations most frequently observed in patients treated with NNRTIs, and viruses carrying these mutations show high levels of resistance to existing NNRTIs. However, TMC278 inhibits K103N/Y181C RT and K103N/Y181C RT mutants at an EC $_{50}$ < 1 nM [2]. From Table 1, it can be seen that the K101 residue has the strongest interaction with TMC278. The interaction energies between TMC278 and each residue of both the wild-type RT and K103N/Y181C RT are similar excepted for the mutated position C181. The mutated Y181C has less contact between TMC278 and C181 because TMC278 interacts with Y181 via hydrogen atoms of its dimethylphenyl ring with the aromatic ring of the residue. For better accuracy, the MP2 method was used in ONIOM3 calculations to include these dispersion interactions. With all the ONIOM methods used, it was found that the binding energy differences (Table2) between wild-type RT and K103N/Y181C RT are small, with 1.48 kcal/mol from MP2/6-31G(d,p):B3LYP/6-31G(d,p):PM3 calculations being the greatest difference.

With the ONIOM3 method (Table2), binding energy of TMC278 is determined from three terms: (i) the interaction energy in region A [Δ E (High, A)], (ii) interaction between the regions A and B [$\Delta\Delta$ E (Mid, AB-A)], and (iii) the interaction energy between the regions A+B and C [$\Delta\Delta$ E (Iow, ABC-AB)]. The main contributions come from both the interaction energy between regions A and B (-14.25 kcal/mol for wild-type RT and -13.58 kcal/mol for K103N/Y181C RT). The calculated interaction energy in region A of the K103N/Y181C RT is less attractive than that in region A of the wild-type by 1.70 kcal/mol, indicating that change from an aromatic side chain of Y181 to a non-aromatic side chain of C181 leads to a reduction of contact between TMC278 and this residue. However, the main contribution to binding energy from K101 is not changed. Moreover, residues in outer layer of binding pocket, such as Y183, Leu100, Pro236 and Asp237, help to compensated for the loss of interactions caused by C181 mutation. This mode of compensatory interaction is different from that observed for other NNRTI such as HBY097. Thus it can be concluded that TMC278 shows similar high inhibitory affinities for both wild-type and Y181C enzymes.

Table 2 Binding energy for the wild-type RT and K103N/Y181C mutant HIV-1 RT complexed with TMC278 by ONIOM3 methods [MP2/6-31G(d,p):B3LYP/6-31G(d,p):PM3].

Calculated energies (kcal/mol)	Wild-Type	K103N/Y181C mutant
Δ E (high, A)	-5.89	-4.19
$[\Delta\Delta$ E (M, AB-A)]	-14.25	-13.58
[$\Delta\Delta$ E (Low, ABC-C]	-8.15	-9.04
Binding Energy (kcal/mol)	-28.29	-27.31
$^{ extsf{a}}\DeltaE$	-1.4	8

 $^{^{\}rm a}\Delta{\rm E}$ = BE $_{\rm wild-type}$ - BE $_{\rm K103N/Y181C~mutant}$

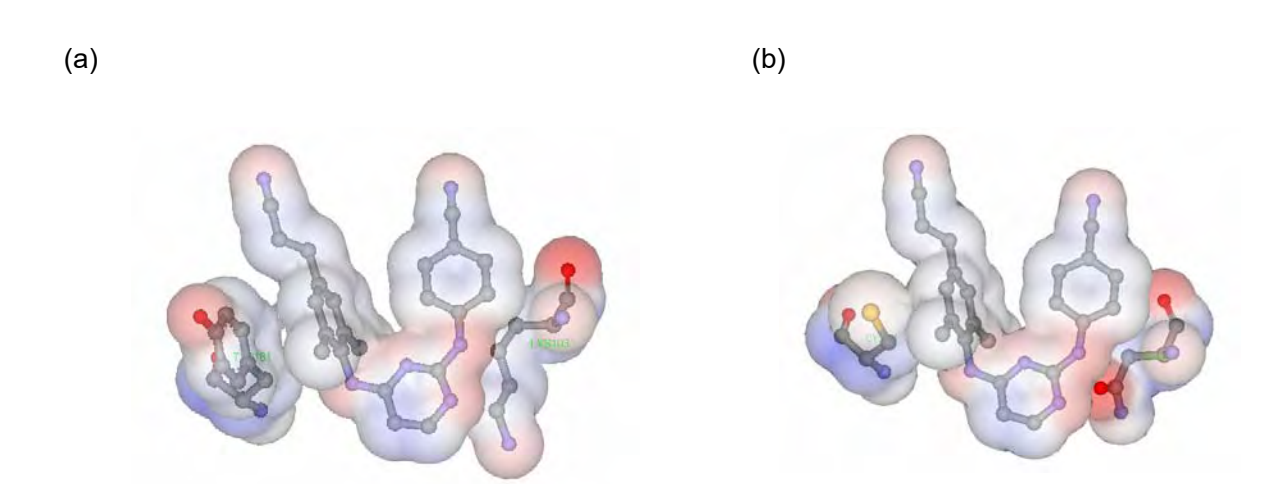


Figure 4 The electrostatic potential is shown on the VDW (van der Waals) accessible surface with red for negative and blue for positive values for (a) TMC278 interacting with K103 and Y181 for wild-type RT and (b) TMC278 interacting with N103 and C181 for K103N/Y181C mutant RT

2.2 Comparing binding energy calculations between wild-type RT and L100l/K103N RT

Among the known NNRT-resistance mutations, the L100I/K103N double mutation has the greatest effect on the potency of TMC278. However, TMC278 still inhibits the double mutant at \sim 8 nM EC₅₀ [2]. In the wild-type RT/TMC278 structure, L100 is near the centre of the pocket and primarily interacts with the central pyrimidine ring of TMC278, while K103 is located on the other side of the pyrimidine ring of TMC278. Comparison of structures of the L100I/K103N mutant RT/TMC278 and wild-

type RT/TMC278 complexes (Figure 5) shows that β -branching of I100 in the L100I mutant lead to steric conflict with the inhibitor TMC278. To avoid this steric conflict, TMC278 shifts away from the I100 and towards the N103. However, NNRTIs do not have the ability to flex and move, to "wiggle and jiggle", and adapt their shape to the various pockets found in the NNRTI-resistant. RTs fail against the known mutants because their binding is susceptible to steric hindrance, as they lose key hydrophobic interactions, or mutation K103N interferes with entry of the NNRTIs into the pocket [2].

From Table 1, the double mutations L100I and K103N lead to the loss of contact between TMC278 and K101, N103 and W229, with the interaction energies to these residues reduced by 5.92, 4.69 and 3.21 kcal/mol, respectively, as compared with the wild-type RT. Table 5 shows the binding energies for the wild-type and L100I/K103N complexes using three-layer ONIOM calculations. It can be seen that the difference in binding energy between wild-type and L100I/K103N enzymes is far more significant (10.58 kcal/mol with the MP2/6-31G(d,p):B3LYP/6-31G(d,p):PM3 method). The interaction energy in region A and the interaction energy between regions AB and C of the L100I/K103N enzyme are less than wild-type by 4.47 and 8.94 kcal/mol, respectively. This indicates that the double mutation L100l/K103N causes a large reduction in attractive interactions between TMC278 and residues in core regions (mutated residue, I100) and in region B (K101 and N103). The mutation L100l introduces a significant distortion in the NNRTI-binding pocket that causes a loss of contact between TMC278 and I100 leading to a weakly attractive interaction in region A (-0.38 kcal/mol at MP2/6-31G(d,p):B3LYP/6-31G(d,p):PM3 calculations). The mutation K103N interferes with entry of the NNRTIs into the pocket. N103 creates repulsive interactions with TMC278 (Table 1) when compared with the interaction between K103 and TMC278. The mutation in the L100I/K103N enzyme leads to a reduction in the stabilization energy of the complex and induces destabilization in the cavity by reducing contact between K101 and TMC278. TMC278 shows higher inhibitory affinities with the wild-type compared to the double mutation K103N/Y181C enzyme.

Table3 Binding energy for the wild-type and L100I/K103N mutant HIV-1 RT complexed with
TMC278 using ONIOM3[MP2/6-31G(d,p):B3LYP/6-31G(d,p):PM3].

Calculated energies (kcal/mol)	Wild-Type	I100L/K103N mutant
Δ E (high, A)	-4.85	-0.38
$[\Delta\Delta$ E (M, AB-A)]	-9.27	-0.33
[$\Delta\Delta$ E (Low, ABC-C]	-6.17	-6.04
Binding Energy,BE(kcal/mol)	-20.29	-9.71
$^{ t a}\Delta$ E		-10.58

 $^{^{}a}\Delta$ E = BE_{wild-type} - BE_{I100L/K103N mutant}

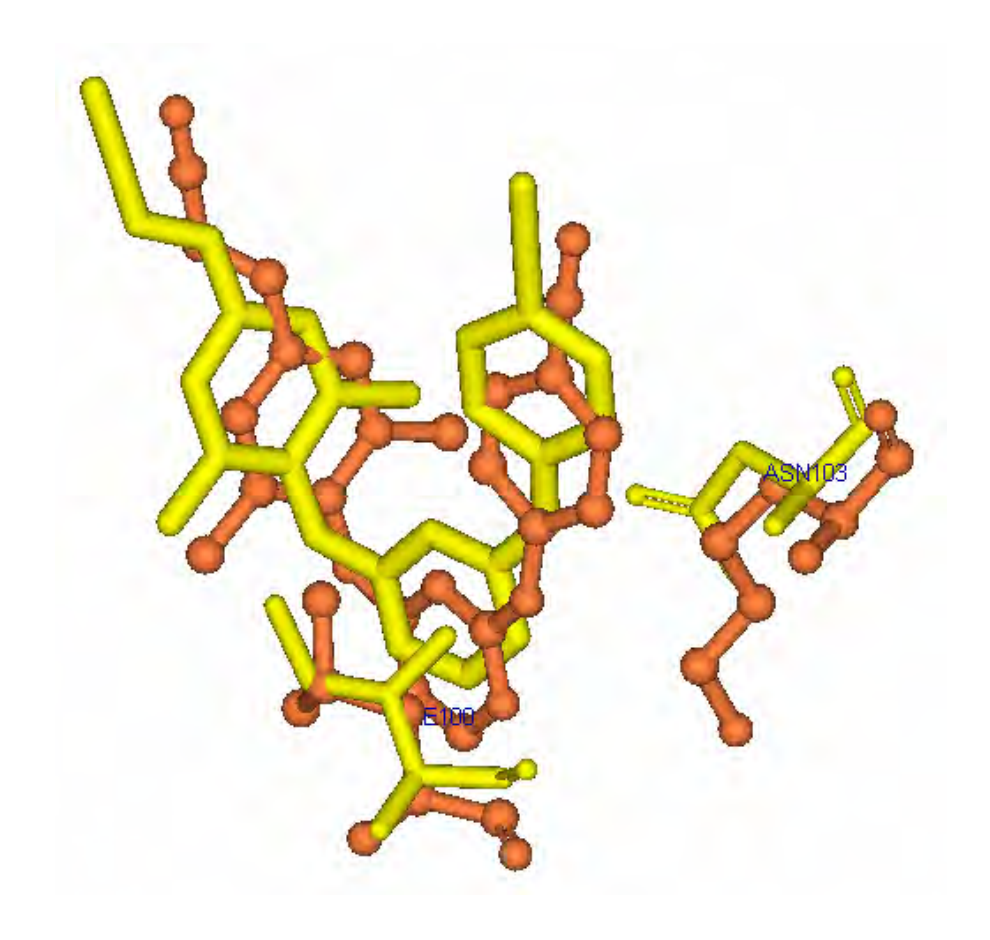


Figure 5 Comparison of structures of TMC278 and mutated residues in the n L100I/K103N mutant RT (orange colour) as compared with wild-type.

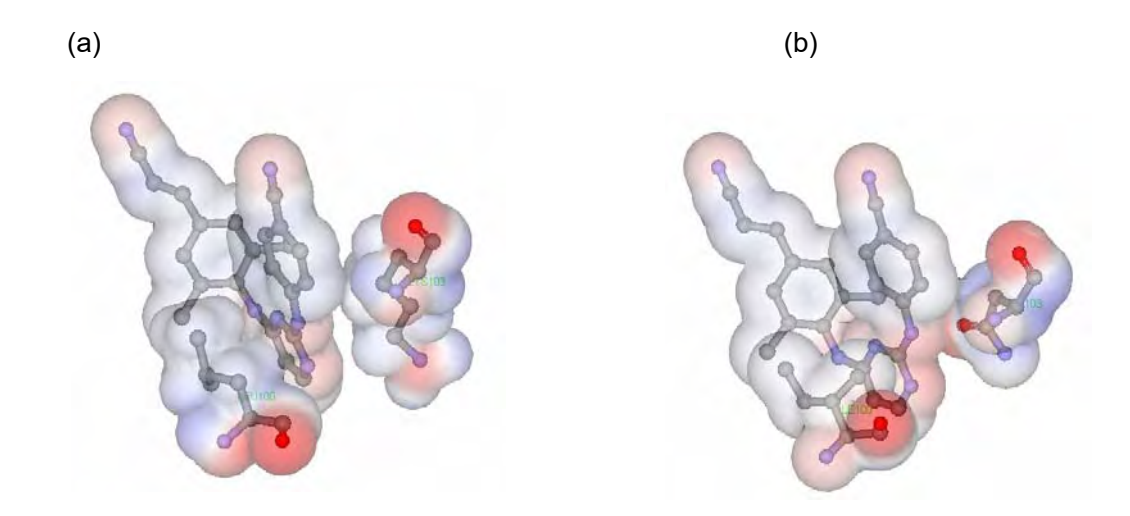


Figure 6 The electrostatic potential is shown on the VDW accessible surface with red for negative and blue for positive values for (a) TMC278 interacting with L100 and K103, and (b) TMC278 interacting with I100 and N103.

CONCLUSION

Three-layer ONIOM method has been applied to determine the binding energies of TMC278 to L100I/K103N and K103N/Y181C enzymes as compared with the wild-type RT. The calculated binding energy for TMC278/K103N/Y181C HIV-1 RT complex is -27.31 kcal/mol by using MP2/6-31G(d,p):B3LYP/6-31G(d,p):PM3 method which is similar to the TMC278/wild-type complex (28.29 kcal/mol). Moreover, it was found that interaction energies calculated at MP2/6-31G(d,p) level between TMC278 and each individual residues of the binding pocket for both wild-type and K103N/Y181C HIV-1 RT are not significantly different except for C181. The interaction between K101 and TMC278 for both wild-type and K103N/Y181C enzymes was found to be the major component, typically -8 kcal/mol. These results are consistent with the observation that TMC278 shows high inhibitory affinities against for both wild-type and K103N/Y181C enzymes, and that TMC278 has a higher inhibitory affinity for the K103N/Y181C enzyme than other DAPY and second generation drugs such as efavirenz.

With the L100I/K103N enzyme, the two mutations L100I and K103N eliminate favourable contacts of the hydrocarbon side chain of L100 and K103 with TMC278 leading to reduce the stabilization energy of the complex. It was observed that this then leads to more repulsive interactions between TMC278 with residues of the binding pocket of the

L100I/K103N enzyme compared to the wild-type and K103N/Y181C enzymes. The binding energy for TMC278/L100I/K103N HIV-1 RT complex was calculated to be -9.71 kcal/mol less than that of the wild-type complex (-20.29 kcal/mol). In the binding pocket of L100I/K103N enzyme, hydrogen bonding between TMC278 and K101 was disturbed, and N103 in the binding pocket of L100I/K103N enzyme creates a repulsive interaction with TMC278. This is consistent with the observation that TMC278 shows lower inhibitory affinities against L100I/K103N HIV-1 RT than wild-type and K103N/Y181C HIV-1 RT. The understanding interactions involved in binding within the pocket, and the structural changes that occur, can be useful for the design of higher potency inhibitors specific to double mutant enzyme target.

ACKNOWLEDGMENTS

This work was supported with grants from the Thailand Research Fund (MRG5280214). The Commission on Higher Education, Ministry of Education; the Faculty of Science and Technology, Rajamangala University of Technology Srivijayaare; the National Nanotechnology Center (NANOTEC); and the Ministry of Science and Technology, Thailand, through its program of Center of Excellence Network, are gratefully acknowledged for partial financial support.

Reference

- [1] A Jacobo-Molina, E. Arnold, Biochemistry 1991, 30, 6351-6361.
- [2] K. Das, J.D. Bauman, A.D. Clark, Y.V. Frenkel, P.J. Lewi, A.J. Shatkin. S.H. Hughes, and E. Arnold, PNAS, 2008, 105(5), 1466-1471.
- [3] C. Mordant, B. Schmitt, E. Pasquier, C. Demestre, L. Quequiner, C. Masungi, A. Peeters, L. Smeulders, E. Bettens, K. Hertogs, J. Heeres, P. Lewi, and J. Guillemont, European Journal of Medicinal Chemistry 2007, 42, 567-579.
- [4] E.V. Gyseghen, M. Pendela, L. Baert, J. Rosier, G.V. Klooster, H.D. Man, M.P. Bouche, L.Schueller, P.V. Remoortere, P. Wigerinck, E. Adams, J. Hoogmartens, G V. Mooter, European Journal of Pharmaceutics and Biopharmaceutics 2008, 70, 853-860.
- [5] S. Saen-oon, M. Kuno, S. Hannongbua, Proteins Struct. Funt. Genet, 2005, 61, 859-869.
- [6] M. Kuno, S. Hannongbua, K. Morokuma, Chem, Phy. Lett. 2003, 380, 456-463.
- [7] P. Nunrium, M. Kuno, S. Saen-oon, S. Hannongbua, Chem. Phys. Lett. 2005, 405, 198-202.
- [8] P. Srivab and S. Hannongbua, ChemMedChem 2008, 3, 1-10.
- [9] K. Morokuma, Philos. Transact. A Math. Phys. Eng. Sci. 2002, 360, 1149-1164.
- [10] M. J. Frisch, G. W. Trucks, H. B. Schlegel, G. E. Scuseria, M. A. Robb, J. R. Cheeseman, J. A. Jr. Montgomery, T. Vreven, K. N. Kudin, J. C. Burant, J. M. Millam, S. S. Iyengar, J. Tomasi, V. Barone, B. Mennucci, M. Cossi, G. Scalmani, N. Rega, G. A. Petersson, H. Nakatsuji, M. Hada, M. Ehara, K. Toyota, R. Fukuda, J. Hasegawa, M. Ishida, T. Nakajima, Y. Honda, O. Kitao, H. Nakai, M. Klene, X. Li, J. E. Knox, H. P. Hratchian, J. B. Cross, C. Adamo, J. Jaramillo, R. Gomperts, R. E. Stratmann, O. Yazyev, A. J. Austin, R. Cammi, C. Pomelli, J. W. Ochterski, P. Y. Ayala, K. Morokuma, G. A. Voth, P. Salvador, J. J. Dannenberg, V. G. Zakrzewski, S. Dapprich, A. D. Daniels, M. C. Strain, O. Farkas, D. K. Malick, A. D. Rabuck, K. Raghavachari, J. B. Foresman, J. V. Ortiz, Q. Cui, A. G. Baboul, S. Clifford, J. Cioslowski, B. B. Stefanov, G. Liu, A. Liashenko, P. Piskorz, I. Komaromi, R. L. Martin, D. J. Fox, T. Keith, M. A. Al-Laham, C. Y. Peng, A. Nanayakkara, M. Challacombe, P. M. W. Gill, B. Johnson, W. Chen, M. W. Wong, C. Gonzalez, J. A. Pople, Gaussian O3, revision B.05;Gaussian, Inc.: Pittsburgh, 2003.
- [11] S. Kristya, P. Pulay, Chem. Phys. Lett . 1994, 229, 175-180;

- [12] S. Tsuzuki, H. P. Luthi, J. Chem. Phys. 2001, 114, 3949.
- [13] J. Ren, et al. *J. Mol. Biol.* 2004, 336, 569-578.

Manuscript will be submitted in topic:

Binding stabilities of DAPY inhibitors to Double Mutant HIV-1 Reverse

Transcriptase (K103N/ Y181C), Based on ONIOM Methods,

Pensri Srivub^[a] and Supa Hannongbua^[b]

^[a]Faculty of Science and Technology, Rajamangala University of Technology Srivijaya

^[b]Center of Nanotechnology and NANOTECH Center of Excellence Kasatsart University,

Bangkok 10900 (Thailand).

ABSTRACT

The effect of the substituent at position 2 and 6 on the left phenyl A of TMC278 for

wild type and double mutant K103N/Y181C was investigated. The calculated binding

energy of mono-substituted derivative 4 using ONIOM2 method (B3LYP/6-31(q,d):PM3) is

less than TMC278 2 for both wild-type and K103N/Y181C enzymes, with the difference of -2.66

and -2.03, respectively. Moreover, it was found that binding energies of compound 5 (non-

2,6-substituent on phenyl A-ring of TMC278) is less than that TMC278 for both wild-type

and K103N/Y181C enzymes, with the greatest difference of -5.81 and -5.11 kcal/mol,

respectively. It is clearly that the substituent at position 2 and 6 on the left phenyl A ring of

TMC278 is necessity maintained to achieve a high level of inhibition on wild type and

K103N/Y181C enzymes. Furthermore, it point out that the other functionalities including

electron-donating group (-OMe) and electron-withdrawing group (-CI) for compound 6 can

replace the methyl group in TMC278 without loss of activity of this drug. This data can

support further development of TMC278 derivatives.

Keywords: Binding energy, HIV-1 RT, DAPY inhibitors, TMC278, ONIOM

Introduction

Human immunodeficiency virus type 1 reverse transcriptase (HIV-1 RT) is one of the most important enzymes in the HIV- 1 life cycle for the development of new anti-AIDS drugs to treat HIV-1 infections, permitting dramatic reduction in viral loads and restoration of the immune system [1]. However, treatments of drug do not eliminate the infection and treatment must be life-long. Drug toxicity and prolonged drug can be lead to the emergence of drug-resistant mutant virus that is the key problem to develop new anti-AIDS drugs. Nevirapine fails to treat the Y181C mutation. The K103N mutation confers resistance to efavirenz. The K103N mutation and combined two mutations such as K103N/Y181C was fully resistant to almost all NNRTIs drugs including nevirapine, efavirenz and delavirdine. New series of NNRTIs was discover that belong to the diarylpyrimidine(DAPY) family. DAPY compounds, with TMC278 and them derivatives were more potent than efavirenz, nevirapine and delavirdine[2]. Moreover, TMC278 and some them derivatives demonstrated high potency on wild type, single and the double mutant strains as compared with to marked drugs [3]. The wiggling and jiggling of TMC278 compounds help them to retain their potency against mutant HIV-1 viruses [4]. In order to understand the binding stabilities of TMC278 and its derivatives to double mutant K103N/Y181C as compared with wild type at a molecular level, the ONIOM computational approach was employed to calculate binding energy of TMC278 and its derivative to double mutant K103N/Y181C as compared with wild type.

Recently, the ONIOM method was successfully used to calculated the interaction energies and the binding energies TIBO[5], nevirapine [6] and efavirenz [7] in the HIV-1 RT binding pocket. The three-layer ONIOM (ONIOM3) method was performed to study the interaction between efavirenz and residues in the binding pocket for K103N/Y181C double mutation HIV-1 RT as compared with wild type. The results showed the calculated binding energy for the efavirenz-K103N/Y181C HIV-1 RT complex is less than that with the wild type complex by approximately 8 kcal/mol [8]. In an attempt to understand the different binding stability of TMC278 and its derivatives to double mutant K103N/Y181C HIV-1 RT at a molecular level, the ONIOM computational approach was employed [9]. It has not been clearly understood inhibitory effect of TMC278 and its derivatives to the double mutant K103N/Y181C HIV-1 RT. The following work describes how the binding interaction of

TMC278 and its derivatives to the double mutant K103N/Y181C. This understanding will be helpful in the design of new inhibitors especially active against double mutant HIV-1 RT, and thus better anti-AIDs agents.

Figure 1 Structure of DAPY inhibitors

Computational Methods

System studied

The structural complex of the wild-type and K103N/Y181C HIV-1 RT/other DAPY (compound 2-4) was prepared by a docking method. Compound 2-4 were docked into the binding pocket of wild-type (PDB code: 2ZD1) and K103N/Y181C (PDB code:3GBR) HIV-1 RT using Autodock 3.05. The studied binding pocket included residues surrounding the non-nucleoside inhibitor binding pocket (NNIBP) with at least one atom interacting with any of the atoms of the DAPY inhibitors within the interatomic distance of 7.0 Å These residues of the studied system are Pro95, Leu100(Ile100), Lys101, Lys102, Lys103(Asn103), Val106, Val179, Ile180, Tyr181(Cys181), Gln182, Tyr183, Tyr188, Val189, Gly190, Pro225, Pro226, Phe227, Leu228, Trp229, Leu234, Pro236, Asp237 and Tyr318 from the p66 domain of RT, and Glu138(b) from the 51 domain of RT (Figure2). All residues were assumed to be in their neutral form. The N- and C-terminal ends of cut

residues were capped with an acetyl group (CH_3CO -) and a methyl amino group (- $NHCH_3$), respectively [(H_3C -C(=O)-{NH-CH(-R)-C(=O)}_n-NH- CH_3)]. The hydrogen atoms then were added to generate the complete structures and their positions were optimized by the semi-empirical PM3 method as available in the GAUSSIAN 03 program running in Linux on a Pentium IV 3.2 GHz PC [10]. The optimizations were carried out with fixed heavy atoms and the final structures produced were used as the starting geometries for all subsequent calculations.

Binding energy of DAPY inhibitors bound to the allosteric pocket of wild type and K103N /Y181 HIV-1 RT

The two layer ONIOM calculations were performed to determine the binding energy of DAPY inhibitors bound to the mutant K103N/Y181C HIV-1 RT as compared to the wild-type. The total ONIOM energy of the entire system was obtained from five independent energy calculations in ONIOM3 methods as shown in equations (2) [9]. All calculations were carried out using the GAUSSIAN 03 package [10]. More precisely, the binding energy of DAPY inhibitors bound to the allosteric pocket of HIV-1 RT was determined using equations (2) for the ONIOM2 methods[6].

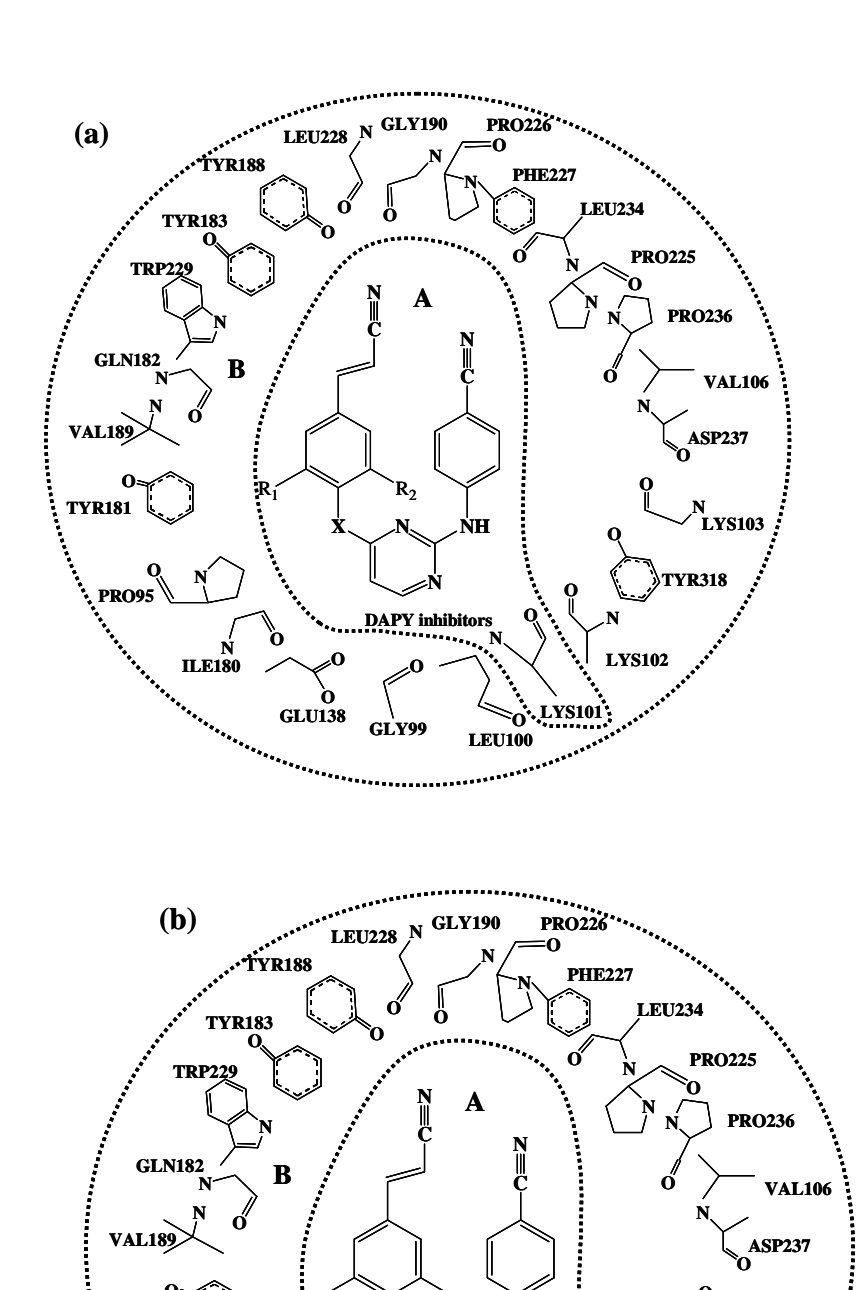
$$\Delta E^{ONIOM2} = E[Cpx]_{opt} - E[P]_{opt} - E[L]_{opt}$$

$$= \Delta E \text{ (High, A+B)} + [\Delta E \text{ (Low, ABC)} - \Delta E \text{ (Low, AB)}]$$

$$= \Delta E \text{ (High, A+B)} + [\Delta \Delta E \text{ (Low, ABC-AB)}]$$
(2)

Where $E[Cpx]_{opt}$ is the total optimized energy of the TMC278 and some them derivative-binding pocket complex, Cpx; $E[P]_{opt}$ is the optimized energy of binding pocket; and $E[L]_{opt}$ is the optimized energy of the DAPY inhibitors ligand. Also, ΔE (High, A) is the interaction energy in the region A which is treated at the high level of theory and $\Delta\Delta E$ (low, AB-A) is the interaction energy from interactions between the regions AB and C which is evaluated at the low level of theory. The inner layer or interaction region including the DAPY inhibitors and K101 was treated by the B3LYP/6-31G(d,p) method. The remainder of the residues were taken as the outer layer which was treated by the PM3 method. For this study, the following models were generated:

ONIOM2 calculation: B3LYP/6-31G(d,p) [TMC278+ K101]:PM3[real]



TYR181

PRO95

ILE180

GLU138

Figure 6 Model system used for TMC278 bound to allosteric site of HIV-1 RT consisting of 24residues; (a) wild-type HIV-1 RT NNIBP, and (b) K103N/Y181C HIV-1 RT NNIBP.

ILE100

GLY99

ASN103

Results and discussion

The effect of the left phenyl A-ring 2, 6-disubstitution of TMC278 on wild type and K103N/Y181C enzymes was investigate. Binding energy of other DAPY inhibitors (compound 4, 5 and 6) as compared TMC278 to describe the activity of these drugs with wild-type and the K103N/Y181C enzymes. The strongest interaction between TMC278 and K101, exhibiting moderate hydrogen bond (Fig.) was considered as part of the interacting core for ONIOM2 calculation. The inner layer or interacting core (Figure, region A) including DAPY inhibitors and K101 was treated by the B3LYP/6-31G(d,p) methods. The outer layer (Figure 7, region B) was treated at the PM3 method. The calculated binding energy of TMC278 (-11.69 kcal/mol) on K103N/Y181C enzyme was slightly decreased as compared with wild-type (-9.21 kcal/mol) which agrees well with the experimentally observed $E_{50} = 0.1$ nM for K103N/Y181C enzyme and E_{50} = 3.2 nM for K103N/Y181C enzyme. Only the interaction energy between region A and B [$\Delta\Delta$ E (Low, AB-A)] of K103N/Y181C enzyme (-2.53 kcal/mol) is less than that in the wild type (-4.59 kcal/mol), with the difference of -2.06 kcal/mol. This indicates the mutation, K103N/Y181C induce a slight loss of contact of residues in region B with TMC 278 and eliminate favorable contacts of the aromatic ring of the Y181 with TMC278 leading to reduce contact between mutate residues Tyr 181. However, the main contribution to binding energy from K101 is not much changed, which corresponds well with the little change in hydrogen bonding distance between TMC278 and the carbonyl (-C=O) and amino (-NH) groups of K101 (Table 3). This also agrees with the X-ray structure data (Table 3). Noticeably, the differences in binding energy between wild-type and K103N/Y181C enzymes for the other DAPY drugs (compound 4-6) is similar trend with TMC278. The left phenyl A-ring of TMC278 shows π - π main interactions with residues Tyr181 and Tyr 188 of binding pocket. 2,6-dimethyl on phenyl A ring of TMC278 prevent great conformational shift and limit the resulting in the conformation favoring this specific interaction[...]. rotational freedom Consequently, the binding energy of mono-substituted derivative 4 is less than TMC278 2 for both wild-type and K103N/Y181C enzymes, with the difference of -2.66 and -2.03, respectively (table). Moreover, it was found that binding energies of compound 5 (non-2,6-substituent on phenyl A-ring of TMC278) is less than that TMC278 for both wild-type K103N/Y181C enzymes, with the greatest difference of -5.81 and -5.11 kcal/mol, respectively. This indicates that removal of 6- or 2,6- substituent on phenyl A-ring of TMC278 might

increase the conformational degrees of freedom and weaken π - π main interactions between compound 4 or 5, with residues Tyr181 and Tyr 188[] in binding pocket of wild-type and K103N/Y181C enzymes. At position 2 and 6 on phenyl A-ring of TMC278 was substituted with –OMe as electron-donating and –Cl as electron-withdrawing group (compound 6). The calculated binding energy of compound 6 is similar to the TMC278 on wild-type and K103N/Y181C enzymes. It is point out that the dimethyl groups on phenyl A ring of TMC278 could be replaced by electron-donating and electron-withdrawing group without loss of binding of compound 6 to wild-type and K103N/Y181C enzymes. This data could support further development of the DAPY inhibitors. This concluded that maintain a 2,6-disubstitution on phenyl A ring of DAPY to achieve a high level of inhibition on wild-type and K103N/Y181C enzymes. These calculated binding energies of TMC278, compound 4, 5 and 6 for double mutant K103N/Y181C HIV-1 RT using ONIOM2 method (B3LYP 6-31g(d,p):PM3) agree well with the experimentally observed E₅₀ = 3.2, 89.6, 3952 and 2.2 nM, respectively (Mordant *et al.* 2007).

Table 3 Calculated distances of the hydrogen bonds (Å) between TMC278 and the backbone carbonyl oxygen (-C=O) and backbone amino hydrogen (-NH) of K101, based on X-ray structure, ONIOM3 methods for wild-type and K103N/Y181C mutant.*

	Wild-type		K103N/Y181C mutant		
	-C=O _K H	-N _{TMC} : -N-H _K N=C- _{TMC278}	-C=O _K H-N _{TMC278}	-N-H _K N=C-	
Methods					
MP2/6-31G(d,p):B3LYP/631G(d,p):PM3	2.80	3.41	2.93	3.38	
X-ray	2.87	3.32	2.82	3.30	

^{*}Hydrogen bond distances of (-C=O_K----H-N_{TMC278}) and (-N-H_K---N=C_{TMC278}) are in \square

Table 2 Binding energy for the wild-type RT and K103N/Y181C mutant HIV-1 RT complexed with DAPY inhibitors by ONIOM2 methods [B3LYP/6-31G(d,p):PM3].

Compounds	Cal	culated energies (k	cal/mol)
	ΔΕ	Δ E (High, A)	$\Delta\Delta$ E (Low, AB-A)
Compound 1 (TMC278)			
Wild-type	-11.69	-7.10	-4.59
K103N /Y181 mutant	-9.21	-6.68	-2.53
$^{ t a}\!\DeltaE$	-2.48	-0.42	-2.06
Compound 2			
Wild-type	-9.03	-6.72	-2.31
K103N /Y181 mutant t	-7.18	-6.62	-0.56
$^{ t a}\!\DeltaE$	-1.85	-0.10	-1.75
$^{ t b}\!\Delta$ E	-2.66	-0.38	-2.28
$^{\circ}\Delta$ E	-2.03	-0.06	-1.97
Compound 3			
Wild-type	-5.88	-3.61	-2.26
K103N /Y181 mutant	-4.10	-3.53	-0.57
$^{ extsf{a}}\DeltaE$	-1.78	-0.081.69	-1.69
$^{ t b}\!\Delta$ E	-5.81	-3.49	-2.33
$^{\circ}\Delta$ E	-5.11	-3.15	-1.96
Compound 4			
Wild-type	-11.96	-7.05	-4.91
K103N /Y181 mutant	-9.46	-6.50	-2.96
$^{a}\!\DeltaE$	-2.50	-0.55	-1.95
$^{ t b}\!\Delta$ E	0.27	-0.05	0.32
° ∆ E	0.25	-0.18	0.43

 $^{^{\}rm a}\Delta$ E = E_{wild-type} - E _{K103N /Y181 mutant}

 $^{^{\}mathrm{b}}\Delta\mathrm{E}$ = BE $_{\mathrm{TMC278}}$, wild-type - BE derivative of TMC27, wild- type

 $^{^{\}rm c}\Delta$ E = BE_{TMC278}, K103N /Y181 mutant - BE derivative of TMC27, K103N /Y181 mutant

CONCLUSION

Three-layer ONIOM method has been applied to determine the binding energies and to describe the effect of the substituent at position 2 and 6 on the left phenyl A ring of TMC278 for double mutant K103N/Y181C enzymes as compared with the wild type RT. The binding energy of mono-substituted derivative 4 is less than TMC278 2 for both wild-type and K103N/Y181C enzymes, with the difference of -2.66 and -2.03, respectively. Moreover, it was found that binding energies of compound 5 (non-2,6-substituent on phenyl A-ring of TMC278) is less than that TMC278 for both wild-type and K103N/Y181C enzymes, with the greatest difference of -5.81 and -5.11 kcal/mol, respectively. It is clearly that the substituent at position 2 and 6 on the left phenyl A ring of TMC278 is necessity maintained to achieve a high level of inhibition on wild type and K103N/Y181C enzymes. Furthermore, it point out that the other functionalities including electron-donating group (-OMe) and electron-withdrawing group (-CI) for compound 6 can replace the methyl group in TMC278 without loss of activity of this drug. This data can support further development of TMC278 derivatives.

ACKNOWLEDGMENT

This work was supported with grants from the Thailand Research Fund (MRG5280214). The Commission on Higher Education, Ministry of Education and Faculty of Science and Technology, Rajamangala University of Technology Srivijaya are acknowledged for partial financial support. Partial supporting by National Nanotechnology Center (NANOTEC), Ministry of Science and Technology, Thailand, through its program of Center of Excellence Network is grateful.

Reference

- [1] A Jacobo-Molina, E. Arnold, Biochemistry 1991, 30, 6351-6361.
- [2] K. Das, J.D. Bauman, A.D. Clark, Y.V. Frenkel, P.J. Lewi, A.J. Shatkin. S.H. Hughes, and E. Arnold, PNAS, 2008, 105(5), 1466-1471.
- [3] C. Mordant, B. Schmitt, E. Pasquier, C. Demestre, L. Quequiner, C. Masungi, A. Peeters, L. Smeulders, E. Bettens, K. Hertogs, J. Heeres, P. Lewi, and J. Guillemont, European Journal of Medicinal Chemistry 2007, 42, 567-579.
- [4] E.V. Gyseghen, M. Pendela, L. Baert, J. Rosier, G.V. Klooster, H.D. Man, M.P. Bouche, L.Schueller, P.V. Remoortere, P. Wigerinck, E. Adams, J. Hoogmartens, G V. Mooter, European Journal of Pharmaceutics and Biopharmaceutics 2008, 70, 853-860.
- [5] S. Saen-oon, M. Kuno, S. Hannongbua, Proteins Struct. Funt. Genet, 2005, 61, 859-869.
- [6] M. Kuno, S. Hannongbua, K. Morokuma, Chem, Phy. Lett. 2003, 380, 456-463.
- [7] P. Nunrium, M. Kuno, S. Saen-oon, S. Hannongbua, Chem. Phys. Lett. 2005, 405, 198-202.
- [8] P. Srivab and S. Hannongbua, ChemMedChem 2008, 3, 1-10.
- [9] K. Morokuma, Philos. Transact. A Math. Phys. Eng. Sci. 2002, 360, 1149-1164.
- [10] M. J. Frisch, G. W. Trucks, H. B. Schlegel, G. E. Scuseria, M. A. Robb, J. R. Cheeseman, J. A. Jr. Montgomery, T. Vreven, K. N. Kudin, J. C. Burant, J. M. Millam, S. S. Iyengar, J. Tomasi, V. Barone, B. Mennucci, M. Cossi, G. Scalmani, N. Rega, G. A. Petersson, H. Nakatsuji, M. Hada, M. Ehara, K. Toyota, R. Fukuda, J. Hasegawa, M. Ishida, T. Nakajima, Y. Honda, O. Kitao, H. Nakai, M. Klene, X. Li, J. E. Knox, H. P. Hratchian, J. B. Cross, C. Adamo, J. Jaramillo, R. Gomperts, R. E. Stratmann, O. Yazyev, A. J. Austin, R. Cammi, C. Pomelli, J. W. Ochterski, P. Y. Ayala, K. Morokuma, G. A. Voth, P. Salvador, J. J. Dannenberg, V. G. Zakrzewski, S. Dapprich, A. D. Daniels, M. C. Strain, O. Farkas, D. K. Malick, A. D. Rabuck, K. Raghavachari, J. B. Foresman, J. V. Ortiz, Q. Cui, A. G. Baboul, S. Clifford, J. Cioslowski, B. B. Stefanov, G. Liu, A. Liashenko, P. Piskorz, I. Komaromi, R. L. Martin, D. J. Fox, T. Keith, M. A. Al-Laham, C. Y. Peng, A. Nanayakkara, M. Challacombe, P. M. W. Gill, B. Johnson, W. Chen, M. W. Wong, C. Gonzalez, J. A. Pople, *Gaussian* 03, revision B.05; Gaussian, Inc.: Pittsburgh, 2003.

- [11] S. Kristya, P. Pulay, Chem. Phys. Lett . 1994, 229, 175–180;
- [12] S. Tsuzuki, H. P. Luthi, J. Chem. Phys. 2001, 114, 3949.
- [13] J. Ren, et al. J. Mol. Biol. 2004, 336, 569-578.
- [14] G.M. Morris, D.S. Goodsell, A.J. Olson, The Scripps Research Institute, AutoDock 3.05, 2000.

3. Proceedings

- 3.1 Pensri Srivub, Pongtep Nokkaew and Supa Hannongbua. Theoretical Investigation on wild type and L100I/K103N HIV-1 Reverse Transcriptase Complexed with TMC278, Based on Quantum Mechanical Methods. Proceeding in Pure and Applied Chemistry International Conference (PACCON2011), January 5-7, 2011, Miracle Grand Convention Hotel Bangkok, Thailand.
- 3.2 Analysis of interaction of TMC278 inhibitor to Double Mutant HIV-1 Reverse Transcriptases K103N/Y181C and L100I/K103N as compared with wild type based on Quantum Mechanical calculations. Submitting in proceeding "Asian Wisdom Conferences", January 25-27, 2011. Silpakron University.
- 3.3 Investigation on the Interaction between TMC278 inhibitors and Mutant HIV-1 Reverse Transcriptase (K103N/ Y181C), Based on ONIOM2 method Submitting in proceeding in the 4th Annual PSU Phuket Research Conference 2011, November 16-18, Prince of Songkla University, Phuket Campus.

Manuscript will be submitted in proceeding

Analysis of interaction of TMC278 inhibitor to Double Mutant HIV-1 Reverse Transcriptases K103N/Y181C and L100l/K103N as compared with wild type based on Quantum Mechanical calculations.

Pensri Srivub^{1*} and Supa Hannongbua²

¹Faculty of Science and Technology, Rajamangala University of Technology Srivijaya,

Nakronsri Thammarat, 80110 Thailand

²Center of Nanotechnology and *NANOTECH*, Center of Excellence, Kasatsart University,

Bangkok 10900 THAILAND.

Corresponding Author: pensir srivub@hotmail.com

Abstract

K103N/Y181C and L100I/K103N mutation are fully resistant to almost all NNRTIs drugs including nevirapine, efavirenz and delavirdine. A new series of NNRTIs was discovered that belongs to the diarylpyrimidine (DAPY) family. DAPY compounds, with TMC278 and its derivatives, are more potent than efavirenz, nevirapine and delavirdine. In the study, the specific interactions between TMC278 and key residues in the three complex structures including wild type, K103N/Y181C and L100I/K103N HIV-1 RT were investigated. It was found that interaction energies calculated at MP2/6-31G(d,p) level between TMC278 and individual residues surrounding the binding pocket for both wild-type and K103N/Y181C HIV-1 RT are not significantly different excepted for mutated residue C181. In the L100I/K103N enzyme, the attractive interactions between TMC278 and K101, K103 and W229 were reduced compared to the wild-type by 5.92, -4.69 and 3.21 kcal/mol, respectively. It is important to note that hydrogen bonding occurring between TMC278 and K101 was also disturbed. Moreover, N103 in the binding pocket of the L100I/K103N enzyme creates a repulsive interaction with the inhibitor. This confirmed that TMC278 shows higher inhibitory affinities against wild-type and K103N/Y181C enzymes than L100I/K103N enzyme, and shows the structural changes responsible. It is expected that this understanding will be

helpful in the design of new inhibitors especially active against double mutant HIV-1 RT, and thus better anti AIDs agents.

Keywords: HIV-1 RT, Interaction energy, inhibitor-enzyme interactions, TMC278 Quantum mechanical calculations

Introduction

Human immunodeficiency virus type 1 reverse transcriptase (HIV-1 RT) is one of the most important enzymes in the HIV-1 life cycle targeted for the development of new anti-AIDS drugs to treat HIV-1 infections, as its inhibition results in a dramatic reduction in viral loads and restoration of the immune system [1]. However, treatment does not eliminate the infection and must be life-long. Drug toxicity and prolonged drug use can lead to the emergence of drug-resistant mutant virus, and this is a key problem to developing new anti-AIDS drugs. Nevirapine fails to treat the Y181C mutation, while the K103N mutation confers resistance to efavirenz. The L100I mutation and combined dual mutations such as K103N/Y181C and L100I/K103N are fully resistant to almost all NNRTIs drugs including nevirapine, efavirenz and delavirdine. A new series of NNRTIs was discovered that belongs to the diarylpyrimidine (DAPY) family. DAPY compounds, with TMC278 and its derivatives, are more potent than efavirenz, nevirapine and delavirdine[2]. Moreover, they demonstrated high potency against wild-type, single and the double mutant strains compared to marked drugs [3]. The motion and flexibility of TMC278 compounds help them to retain their potency against mutant HIV-1 viruses [4].

In order to understand the binding stabilities of TMC278 to double mutation such as K103N/Y181C or L100I/K103N at a molecular level, the quantum mechanical calculations[5-6] was employed to calculate interaction energy of TMC278. As the MP2 method [7] that includes the dispersion interactions, it is expected to give more accurate interaction energies than B3LYP. This approach was useful in previous studies to demonstrate the particular interactions between the NNRTIs TIBO [8], nevirapine [9] and efavirenz [10], and amino acids in the non-nucleoside inhibitor binding pocket (NNIBP) with wild-type, single mutant HIV-1 RT and K103N/Y181C. In this report, we employed the MP2/6.-31G(d,p) level of theory to calculate the interaction energy of individual pair of the system. The studied system included the HIV-1RT wild type and double mutant L100I/K103N and

K103N/Y181C. It is expected that this understanding will be helpful in the design of new inhibitors especially active against double mutant HIV-1 RT, and thus better anti AIDs agents.

Computational methods

System studied

The starting models for calculations were obtained from the X-ray structures of TMC278 bound to HIV-1 RT for the wild-type, K103N/Y181C and L100I/K103N enzymes, listed in the Protein Data Bank with PDB entry codes 2ZD1, 3GBR and 2ZE2 respectively [2]. The studied binding pocket included residues surrounding the non-nucleoside inhibitor binding pocket (NNIBP) with at least one atom interacting with any of the atoms of the TMC278 inhibitor within an interatomic distance of 7.0 Å These residues of the studied system are Pro95, Leu100(Ile100), Lys101, Lys102, Lys103(Asn103), Val106, Val179, Ile180, Tyr181(Cys181), Gln182, Tyr183, Tyr188, Val189, Gly190, Pro225, Pro226, Phe227, Leu228, Trp229, Leu234, Pro236, Asp237 and Tyr318 from the p66 domain of RT, and Glu138(b) from the 51 domain of RT (Figure1). All residues were assumed to be in their neutral form. The N- and C-terminal ends of cut residues were capped with an acetyl group (CH₃CO-) and a methyl amino group $(-NHCH_3)$, respectively $[(H_3C-C(=O)-\{NH-CH(-R)-C(=O)\}_n-NH-CH_3)]$. Hydrogen atoms were added to generate the complete structures and their positions were optimized by the semi-empirical PM3 method available in the GAUSSIAN 03 program running in Linux on a Pentium IV 3.2 GHz PC [11]. The optimizations were carried out with fixed heavy atoms and the final structures produced were used as the starting geometries for all subsequent calculations.

Figure 1 Model system used for TMC278 bound to the allosteric site, NNIBP, of HIV-1 RT consisting of 24 residues.

Interaction energy calculations

The interaction energies, $E_{(TMC278+Xi)}$, between TMC278 and individual residues, X_i , were calculated at the MP2/6-31G(d,p) levels of theory using the geometry described above. The total interaction energy, INT, can be expressed as: [8]

$$INT_{(TMC278+Xi)} = E_{(TMC278+Xi)} - E_{(EFZ)} - E_{(Xi)},$$
(1)

where $E_{(TMC278)}$ and $E_{(Xi)}$ are energies of TMC278 and each individual residue, respectively.

Results and discussion

Interaction energy of TMC278 with individual residues of the HIV-1 RT binding pocket

The interaction energies between TMC278 and the individual residues (Xi) of HIV-1 RT binding pocket for wild-type, L100I/K103N or K103N/Y181C enzymes were calculated at MP2/6-31G(d,p) levels of theory and are shown in Table 1. As the MP2 method includes the dispersion interactions, it is expected to give more accurate interaction energies than B3LYP [7]. In wild-type RT, the main contributions to the interactions with TMC278 come from K101, Y181, F227 and W229 which produce attractive interactions greater than 3

kcal/mol, calculated at MP2/6-31G(d,p) level. Considered in greater detail, hydrogen bonding between a linker nitrogen atom of TMC278 (Figure 1) and the main-chain carbonyl oxygen of K101 causes the strongest interaction, 8.15 kcal/mol at the MP2/6-31G(d,p) level, and is conserved in the binding of many NNRTIs. The cyanovinyl group is positioned to fit into a hydrophobic tunnel formed by the side chains of amino acid residues F227 and W229 that may explain why TMC278 is the most potent of DAPY analogues. TMC278 can be flexible to bind to HIV-1 RT and interacts with aromatic side chains of Y181 and W229 via H- π interactions. Comparing the wild-type RT and K103N/Y181C RT at the MP2/6-31G(d,p) method shows no significant difference between the interactions, except for the mutated residue C181. The attractive interactions between TMC278 and C181 in the K103N/Y181C enzyme were reduced by 2.93 kcal/mol.

The repulsive interactions between TMC278 and residues of the binding pocket for the L100I/K103N RT are greater than in wild-type RT and K103N/Y181C RT. Also, the attractive interactions between TMC278 and K101, K103 and W229 in the L100I/K103N RT were reduced to 5.92, 4.69 and 3.21 kcal/mol, respectively ($^b\Delta$ E in Table 1, MP2/6-31G(d,p) method), compared to the wild-type RT. These results indicate that the mutated residues L100I and K103N not only reduce the binding stability of TMC278, but actually destabilize the cavity, leading the W229 residue to lose contact with the inhibitor.

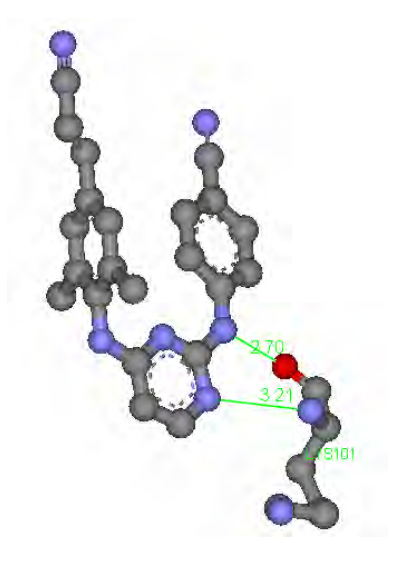


Figure 2 Hydrogen bonding between K101 and TMC278

Table 1. The calculated interactions between TMC278 and individual residues (X_i) from the MP2/6-31G(d,p) method.

	Interaction energy (kcal/mol)				
Residue(X _i)	Wild-type	K103N/Y181C	L100/I/K103N	ΔE_{a}	Δ E _b
PRO95	-0.46	-0.39	-0.19	-0.06	-0.27
GLY99	-0.13	-0.16	-0.67	0.02	0.54
LEU100	-1.86	-3.27	-0.08	1.42	-1.78
LYS101	-8.15	-7.76	-2.23	-0.39	-5.92
LYS102	-0.13	-0.22	-0.20	0.09	0.07
LYS103 (ASN)	-1.80	-2.28	2.89	0.48	-4.69
VAL106	-0.39	-0.21	-1.55	-0.18	1.16
ILE180	-0.92	-1.11	-0.55	0.19	-0.37
TYR181(CYS)	-4.52	-1.60	-4.03	-2.93	-0.49
GLN182	-0.37	0.03	-0.16	-0.40	-0.21
TYR183	-0.55	-1.38	-1.35	0.83	0.8
TYR188	-2.24	-1.33	-4.34	-0.91	2.1
VAL189	-0.26	-0.36	-0.40	0.09	0.14
GLY190	-0.72	-0.87	-0.41	0.15	-0.31
PRO225	-1.52	-1.19	-1.19	-0.33	-0.33
PRO226	-0.60	-1.19	-0.80	0.59	0.2
PHE227	-3.09	-2.43	-3.78	-0.66	0.69
LEU228	0.46	0.61	0.76	-0.15	-0.3
TRP229	-5.46	-5.51	-2.25	0.05	-3.21
LEU234	-0.94	-1.02	1.22	0.08	-2.16
PRO236	-2.18	-2.98	-1.07	0.80	-1.11
ASP237	-1.50	-2.44	-0.11	0.94	-1.39
TYR318	-1.50	-1.44	-1.21	-0.06	-0.29
GLU138	-2.95	-2.44	-0.68	-0.51	-2.27
Total Energy	-41.76	-41.36	-22.36	-0.82	-19.42

 $\Delta E_a = E_{wild-type} - E_{K103N/Y181C mutant}$

 $\Delta \mathsf{E}_\mathsf{b} = \mathsf{E}_\mathsf{wild\text{-type}} - \mathsf{E}_\mathsf{L100I/K103N\ mutant}$

The mutations in the L100I/K103N enzyme leads to a reduction in the stabilization energy of the complex and induces destabilization in the cavity by reducing contact between K101 and TMC278. TMC278 shows higher inhibitory affinities with the wild-type compared to the double mutation K103N/Y181C enzyme.

Conclusion

MP2/6-31G(d,p) level of calculation was applied to determine the binding energies of TMC278 to L100I/K103N and K103N/Y181C enzymes as compared with the wild-type RT. It was found that interaction energies calculated at MP2/6-31G(d,p) level between TMC278 and each individual residues of the binding pocket for both wild-type and K103N/Y181C HIV-1 RT are not significantly different except for C181. The interaction between K101 and TMC278 for both wild-type and K103N/Y181C enzymes was found to be the major component, typically -8 kcal/mol. These results are consistent with the observation that TMC278 shows high inhibitory affinities against for both wild-type and K103N/Y181C enzymes, and that TMC278 has a higher inhibitory affinity for the K103N/Y181C enzyme than second generation drugs such as efavirenz. With the L100l/K103N enzyme, the two mutations L100I and K103N eliminate favourable contacts of the hydrocarbon side chain of L100 and K103 with TMC278 leading to reduce the stabilization energy of the complex. In the L100I/K103N enzyme, the attractive interactions between TMC278 and K101, K103 and W229 were reduced compared to the wild-type by 5.92, -4.69 and 3.21 kcal/mol, respectively. It is important to note that hydrogen bonding occurring between TMC278 and K101 was also disturbed. Moreover, N103 in the binding pocket of the L100I/K103N enzyme creates a repulsive interaction with the inhibitor. This confirmed that TMC278 shows higher inhibitory affinities against wild-type and K103N/Y181C enzymes than L100I/K103N enzyme, and shows the structural changes responsible. Understanding these particular structural interactions can be useful for the design of inhibitors which are specific to HIV-1 RT allosteric site and with greater potency against mutant types.

Acknowledgments

This work was supported with grants from the Thailand Research Fund (MRG MRG5280214). The Commission on Higher Education, Ministry of Education; the Faculty of Science and Technology, Rajamangala University of Technology Srivijayaare; the National Nanotechnology Center (NANOTEC); and the Ministry of Science and Technology, Thailand, through its program of Center of Excellence Network, are gratefully acknowledged for partial financial support.

Reference

- [1] A Jacobo-Molina, E. Arnold, Biochemistry **1991**, *30*, 6351-6361.
- [2] K. Das, J.D. Bauman, A.D. Clark, Y.V. Frenkel, P.J. Lewi, A.J. Shatkin. S.H. Hughes, and E. Arnold, PNAS, **2008**, *105*(5), 1466-1471.
- [3] C. Mordant, B. Schmitt, E. Pasquier, C. Demestre, L. Quequiner, C. Masungi, A. Peeters, L. Smeulders, E. Bettens, K. Hertogs, J. Heeres, P. Lewi, and J. Guillemont, European Journal of Medicinal Chemistry, **2007**, *42*, 567-579.
- [4] E.V. Gyseghen, M. Pendela, L. Baert, J. Rosier, G.V. Klooster, H.D. Man, M.P. Bouche, L.Schueller, P.V. Remoortere, P. Wigerinck, E. Adams, J. Hoogmartens, G V. Mooter, European Journal of Pharmaceutics and Biopharmaceutics 2008, 70, 853-860.
- [5] S. Caratzoulas, D. G. Vlachos, Carbohydrate Research . 2011, 346, 664–672.
- [6] K. Raha, M. B. Peters, B. Wang, N. Yu, A. M. Wollacott, L. M. Westerhoff and K. M. Merz Jr, *Drug Discovery Today.* 2007, 12, 725-731.
- [7] S. Kristya, P. Pulay, Chem. Phys. Lett. 1994, 229, 175-180.
- [8] S. Saen-oon, M. Kuno, S. Hannongbua, Proteins Struct. Funt. Genet, 2005, 61, 859-869.
- [9] M. Kuno, S. Hannongbua, K. Morokuma, Chem, Phy. Lett. 2003, 380, 456-463.
- [10] P. Nunrium, M. Kuno, S. Saen-oon, S. Hannongbua, Chem. Phys. Lett. 2005, 405, 198-202.
- [8] P. Srivab and S. Hannongbua, ChemMedChem, 2008, 3, 1-10.
- [9] K. Morokuma, Philos. Transact. A Math. Phys. Eng. Sci. 2002, 360, 1149-1164.
- [10] M. J. Frisch, G. W. Trucks, H. B. Schlegel, G. E. Scuseria, M. A. Robb, J. R. Cheeseman, J. A. Jr. Montgomery, T. Vreven, K. N. Kudin, J. C. Burant, J. M.

Millam, S. S. Iyengar, J. Tomasi, V. Barone, B. Mennucci, M. Cossi, G. Scalmani, N. Rega, G. A. Petersson, H. Nakatsuji, M. Hada, M. Ehara, K. Toyota, R. Fukuda, J. Hasegawa, M. Ishida, T. Nakajima, Y. Honda, O. Kitao, H. Nakai, M. Klene, X. Li, J. E. Knox, H. P. Hratchian, J. B. Cross, C. Adamo, J. Jaramillo, R. Gomperts, R. E. Stratmann, O. Yazyev, A. J. Austin, R. Cammi, C. Pomelli, J. W. Ochterski, P. Y. Ayala, K. Morokuma, G. A. Voth, P. Salvador, J. J. Dannenberg, V. G. Zakrzewski, S. Dapprich, A. D. Daniels, M. C. Strain, O. Farkas, D. K. Malick, A. D. Rabuck, K. Raghavachari, J. B. Foresman, J. V. Ortiz, Q. Cui, A. G. Baboul, S. Clifford, J. Cioslowski, B. B. Stefanov, G. Liu, A. Liashenko, P. Piskorz, I. Komaromi, R. L. Martin, D. J. Fox, T. Keith, M. A. Al-Laham, C. Y. Peng, A. Nanayakkara, M. Challacombe, P. M. W. Gill, B. Johnson, W. Chen, M. W. Wong, C. Gonzalez, J. A. Pople, *Gaussian 03*, revision B.05;Gaussian, Inc.: Pittsburgh, 2003.

- [12] S. Tsuzuki, H. P. Luthi, J. Chem. Phys. 2001, 114, 3949.
- [13] J. Ren, et al. J. Mol. Biol. **2004**, 336, 569-578.

Physical and Theoretical Chemistry

Theoretical Study of Ring-Opening Polymerization of ε-Caprolactone Initiated by Tin(II) Methoxide: Mechanism and Kinetics

C. Sattayanon¹, W. Punyodom^{1,2}, P. Meepowpan^{1,2} and N. Kungwan^{1,2*}

* E-mail: naweekung@gmail.com

Abstract: The ring-opening polymerization (ROP) mechanism of \(\epsilon\)-caprolactone (CL) with tin(II) methoxide initiator, Sn(OMe)2, was investigated using quantum chemical calculation. Geometry optimization was calculated using density functional theory (DFT) at B3LYP level with mixed basis set. Our calculation results support a coordination-insertion mechanism initiated by tin(II) methoxide with two transition states prior to the ROP. The relative energies of all investigated stationary points along the reaction profile were calculated from potential energy surface. From the energy profile, tin(II) methoxide initiator demonstrated exothermic reaction and the rate determining step was the nucleophilic attack of the methoxide on the carbonyl carbon of the CL monomer at the first transition state (TS1). The electronic and structural information of transition state structures along the reaction pathway was employed to obtain the thermal rate constant using the transition state theory with TheRATE program.

Introduction

Currently, there has been increasing interest in materials derived from bio-renewable resources as environmentally sustainable alternatives petrochemical-derived products. Among the most prominent examples are poly(lactic acid) (PLA) and poly(ε-caprolactone) (PCL) have been studied intensively due to their biodegradability, biocompatibility and permeable properties and have shown their potential applications in a variety of field such as biomedical and pharmaceutical industries as a resorbable implant material and a vehicle for controlled drug delivery [1-3]. A convenient synthetic route to PLA and PCL is ring-opening polymerization (ROP) of corresponding cyclic ester monomers [1,4,

ROP has been widely studied and many efficient initiators have been developed. Three methods of ROP mechanism are cationic, anionic and coordination-insertion [6]. The coordination-insertion is the best method due to its advantages such as easy control of the molecular weight (MW), the lower risk of side reactions and the higher molecular weight obtained [7].

The most common catalyst used in coordinationinsertion is metal alkoxides, such as tin, aluminium, trivalent lanthanide, magnesium, zinc derivatives, group IV metals and iron [8-11]. These metal alkoxides have been reported to be effective initiators that initiate ROP of cyclic esters. Among them, tin alkoxide is suitable for the ROP catalyst because of its solubility and ease of handling. In particular, tin(II) 2ethylhexanoate, commonly known as stannous octoate (SnOct₂), is the most widely used in both scientific research and industrial production. It is the catalyst that has been accepted by the U.S. Food and Drug Administration (FDA) [12]. The polymerization mechanism with this initiator is rather complex and several mechanisms have been proposed in the past [13-16]. In the polymerization process, SnOct₂ acts as an initiator in the presence of an alcohol (ROH) coinitiator before carrying to actual initiating species. So, SnOct₂ is not the true initiator. For this reason, true initiators were developed by Winita et al. [17] and the new mechanism was also proposed as shown in Scheme 1. From their experiment, the synthesis was achieved on several tin(II) alkoxides initiators. These new initiators can completely control the ROP polymerization of CL and give the high MW polymers. Their kinetic study from dilatometry method at 120 °C of ROP polymerization showed very interesting results. All initiators performed high reactivity and fast reaction as a first order rate respected to monomer concentration. However, a clear description of this ROP mechanism is still ambiguous.

For more understanding of this mechanism, the theoretical calculations by means of quantum chemical calculation and transition state theory (TST) [18] will be used to investigate the reaction mechanism and reaction rate constant [2, 19-23]. Furthermore, the calculated rate constant will be compared with experimental data [18].

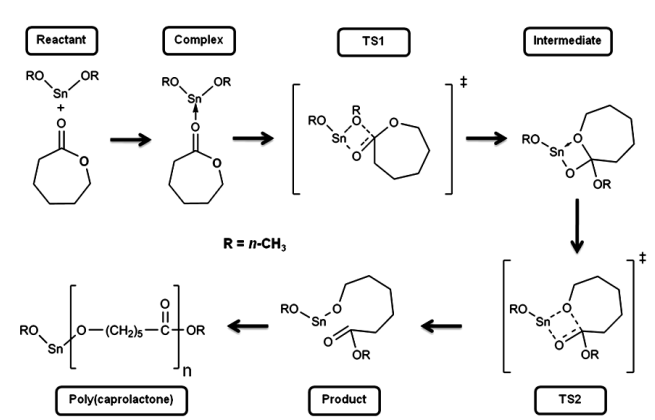
Computational Details

Theoretical study by means of quantum chemical calculation was used to investigate the ROP mechanism of CL initiated by tin(II) methoxide, Sn(OCH₃)₂ initiator. Geometries, energies and vibrational frequencies of all stationary points (reactant, complex, transition state, intermediate and product) along with reaction profiles were computed using the hybrid density functional theory (DFT) at

¹ Center of Excellence for Innovation in Chemistry, Department of Chemistry, Faculty of Science, Chiang Mai University, Chiang Mai, Thailand 50200

² Biomedical Polymers Technology Unit, Department of Chemistry, Faculty of Science, Chiang Mai University, Chiang Mai, Thailand 50200

B3LYP level [24]. For metal atom, a doublet-ζvalence quality basis set LANLD2Z was assigned for Sn atom. A relativistic electron core potential (ECP) developed by Hay and Wadt replaced the Sn core electron [25, 26]. For non-metal atom, a valence triple zeta with polarization function (VTZ2P) at cc-pVTZ was assigned for C, H, and O atoms. This popular and computationally cheap method predicted reliable geometries and energetic as reported in previous works [21, 18]. The character of intermediates and transition states was confirmed by performing frequency calculations [19, 21]. The energy barrier heights of all reactions were corrected by including the zero-point energy corrections [27]. All calculations were performed with the Gaussian03 software package [28]. The information obtained from quantum chemical calculation was employed to determine the thermal rate constant of the reaction. The thermal rate constant at temperature 120 °C was calculated using the conventional transition state theory (TST) [18] method implemented in TheRATE program by University of Utah's web-based kinetics module within the Computational Science and Engineering Online suite (CSEOnline) [29]. Finally, the calculated rate constants will be compared with the available experimental data.



Scheme 1. Proposed mechanism for ring-opening polymerization of ϵ -caprolactone initiated by tin(II) alkoxide

Results and Discussion

The tin(II) methoxide assisted ROP coordination-insertion mechanism for monomer of CL was investigated by DFT(B3LYP) with mix basis set method. The corresponding DFT based optimized structures and energies of each step followed Scheme 1 are depicted in Figure 1. The exo-carbonyl group of CL coordinates the Sn metal (Complex) with O¹ in the cis position, resulting in a Sn-O² distance of 2.58 Å. The energy of Complex formation is -7.03 kcal mol⁻¹. The transformation of Complex into TS1 involves addition of the Sn-O³ onto the C¹-O² double bond and a corresponding rotation of the O¹-C¹-O² plane 90° forming a planar four-membered ring (TS1) having sp²-sp³ hybridized C¹ which is located above that O²-C¹-O¹ plane. This process lengthens the Sn-O³ and

shortens the Sn-O² (Figure 1). This process requires moderate energy (14.01 kcal mol⁻¹) and the supported DFT with only one negative imaginary frequency is confirmed. The nature bond orbital (NBO) charges along the reaction pathway on Sn and C¹ slightly increase and on O³ also increase but those on O¹ and O¹ decrease (Figure 2).

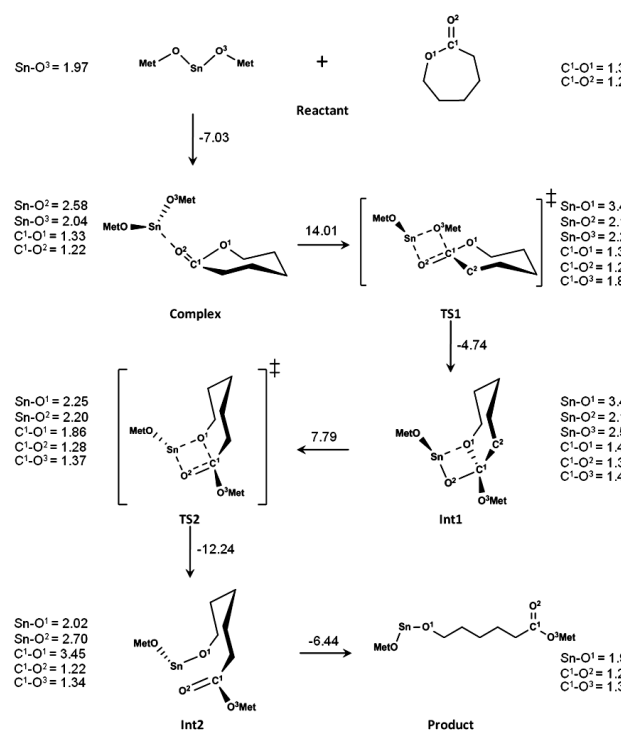


Figure 1. ROP mechanism of CL initiated with Sn(OMet)₂. Bond lengths are in Å and energies are in kcal mol⁻¹

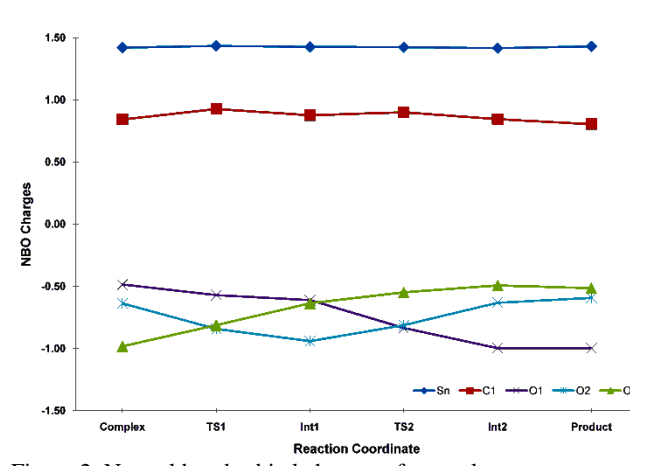


Figure 2. Natural bond orbital charges of several atoms involved in the reaction intermediates in the polymerization of CL initiated by $Sn(OMe)_2$

The conversion of **TS1** to intermediate1 (**Int1**) involves rotation of CL ring around the C¹-O² bond resulting in a decrease and increase in the Sn-O³ and Sn-O¹ distances respectively (Figure 1). The Sn-O¹ distance is about 3.40 Å which is not a bond between but only attractive force between the two atoms. The energy of **Int1** formation is -4.73 kcal mol⁻¹ above the **Complex**. The optimized transition state 2, **TS2**,

shows a four-membered ring with nearly equal Sn-O¹ and Sn-O² distance and a sp³ hybridized C¹ atom with C^1 - O^1 , C^1 - O^2 and C^1 - O^3 bond lengths between 1.28 and 1.86 Å. This step is completely attained when the bond of Sn-O¹ is created. The **TS2** structure is confirmed by an imaginary frequency and intrinsic reaction coordination (IRC) calculation indicating that saddle point along the reaction pathway is exists. This TS2 eventually ruptures to intermediate2 (Int2) and then form **Product** with increasing bond length of C¹-O¹. Our DFT based calculation gave two transition state formation steps with the TS1 being as the ratedetermining step. Our calculated results based on proposed mechanism in Scheme 1 of tin(II) methoxide with CL is found similar to the proposed ROP mechanism of SnMe₃OMe with 1,5-dioxepan-2-one (DXO) reported by von Schenck and co-workers [21]. This may be due to the similarity of coordinate stability for Sn both in tetravalent and divalent forms. The overall reaction is exothermic.

The relative energies of all investigated stationary points (Reactant, Complex, TS1, Int1, TS2, Int2 and **Product**) along the reaction profile for ROP mechanism of CL initiated by tin(II) methoxide are showed in Figure 3. From energy profile, the **Reactant** energy is assigned to be 0.00 kcal mol⁻¹. The **Complex** energy is lower than the **Reactant** energy about -7.03 kcal mol⁻¹. For **TS1**, the barrier height energy of this step is 14.01 kcal mol⁻¹ and the **TS1** energy is 6.98 kcal mol⁻¹ above **Reactant** energy. For the intermediate 1 (Int1), the energy is found to be 2.24 kcal mol⁻¹ above the **Reactant** energy. The apparent barrier height of **TS2** step is 7.78 kcal mol⁻¹ when compared with Int1. From the energy profile, the first transition state formation (TS1) is a rate determining step of this reaction.

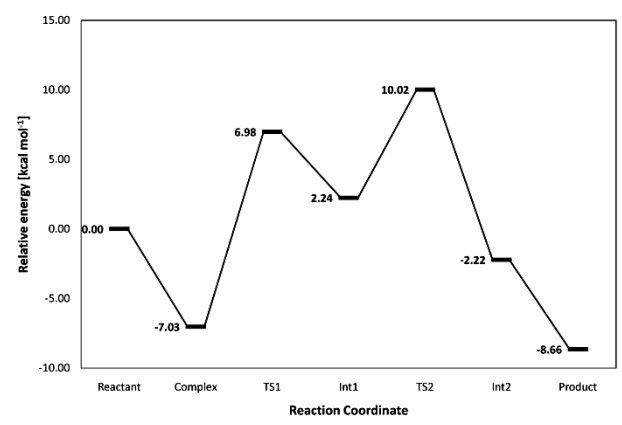


Figure 3. Relative energy profile for ROP mechanism of CL initiated by tin(II)-methoxide, calculated at B3LYP method

The thermal rate constant at 120 °C was calculated to be 357.4 L mol⁻¹ min⁻¹ (shown in Table 1) using information from the quantum calculation with TST implemented in TheRATE program. The calculated value is in a good agreement within a factor of two compared with experimental data.

Table 1 The theoretical and experimental rate coefficient of tin(II) methoxide initiator

Sn(OP)	Temperature _	Rate coefficient (L mol ⁻¹ min ⁻¹)		
Sn(OR) ₂	(°C)	Experiment ^a	Theory b	
Met	120	712.2	357.4	

^a Calculated by dilatometry's measurement of Winita's group [17]. ^bCalculated by TheRATE program of university of Utah [29].

Conclusions

The ring-opening polymerization of ε -caprolactone with tin(II) methoxide initiator has been carried out using density functional method. The reaction proceeds via coordination-insertion mechanism initiated by tin(II) methoxide. The relative energy profile of tin(II) methoxide is calculated and showed in the Figure 3. The overall reaction is exothermic. The barrier heights are 14.01 kcal mol⁻¹ and 7.8 kcal mol⁻¹ for TS1 and TS2, respectively. The rate-determining step is the nucleophilic attack (TS1 formation step) of the tin(II) methoxide on the exo-ring carbonyl carbon of e-caprolactone. The rate constant obtained from TST is a factor of two compared with available experimental data indicating that TST can be further used to predict the rate constant of other tin(II) alkoxide initiators.

Acknowledgements

C. Sattayanon gratefully thanks to the Center of Excellent for Innovation in Chemistry (PERCH-CIC) for financial support. This work is also supported by National Research University Project under Commission on Higher Education, Thailand and Biomedical Polymers Technology Unit, Department of Chemistry, Faculty of Science, Chiang Mai University. Finally, The Graduate School of Chiang Mai University is also acknowledged.

References

- Albertsson, A.-C.; Varma, I. K., Biomacromolecules, 2003, 4, 1466.
- [2] Dove, A. P.;Gibson, V. C.;Marshall, E. L.;Rzepa, H. S.;White, A. J. P.;Williams, D. J., Journal of the American Chemical Society, 2006, 128, 9834.
- [3] Chen, H.-Y.; Huang, B.-H.; Lin, C.-C., Macromolecules, 2005, 38, 5400.
- [4] Hormnirun, P.;Marshall, E. L.;Gibson, V. C.;Pugh, R. I.;White, A. J. P., Proc. Natl. Acad. Sci. U. S. A., Oct, 2006, 103, 15343
- [5] Storey, R. F.;Mullen, B. D.;Desai, G. S.;Sherman, J. W.;Tang, C. N., Journal of Polymer Science Part A: Polymer Chemistry, 2002, 40, 3434.
- [6] Edlund, U.; Albertsson, A. C., Degradable Aliphatic Polyesters; Springer-Verlag Berlin: Berlin, 2002, 157, 67
- [7] Kricheldorf, H. R., Chemosphere, 2001, 43, 49.

- [8] Yu, T.-L.; Wu, C.-C.; Chen, C.-C.; Huang, B.-H.; Wu, J.; Lin, C.-C., Polymer, 2005, 46, 5909.
- [9] Ling, J.; Shen, J.; Hogen-Esch, T. E., Polymer, 2009, 50, 3575.
- [10] Li, P.;Zerroukhi, A.;Chen, J.;Chalamet, Y.;Jeanmaire, T.;Xia, Z., Polymer, 2009, 50, 1109.
- [11] Liu, J.;Ling, J.;Li, X.;Shen, Z., Journal of Molecular Catalysis A: Chemical, 2009, 300, 59.
- [12] Gilding, D. K.; Reed, A. M., Polymer, 1979, 20, 1459.
- [13] Leenslag, J. W.; Pennings, A. J., Die Makromolekulare Chemie, 1987, 188, 1809.
- [14] Du, Y. J.; Lemstra, P. J.; Nijenhuis, A. J.; van Aert, H. A. M.; Bastiaansen, C., Macromolecules, 1995, 28, 2124.
- [15] Duda, A.; Penczek, S.; Kowalski, A.; Libiszowski, J., Macromolecular Symposia, 2000, 153, 41.
- [16] Kowalski, A.; Duda, A.; Penczek, S., Macromolecules, 2000, 33, 689.
- [17] Dumklang, M.;Pattawong, N.;Punyodom, W.;Meepowpan, P.;Molloy, R.;Hoffman, M., Chiang Mai Journal of Science, 2009, 36, 136.
- [18] Khanna, A.;Sudha, Y.;Pillai, S.;Rath, S., Journal of Molecular Modeling, 2008, 14, 367.
- [19] Eguiburu, J. L.; Fernandez-Berridi, M. J.; Cossio, F. P.; Roman, J. S., Macromolecules, 1999, 32, 8252.
- [20] Ryner, M.; Stridsberg, K.; Albertsson, A.-C.; von Schenck, H.; Svensson, M., Macromolecules, 2001, 34, 3877.
- [21] von Schenck, H.;Ryner, M.;Albertsson, A.-C.;Svensson, M., Macromolecules, 2002, 35, 1556.
- [22] Marshall, E. L.; Gibson, V. C.; Rzepa, H. S., Journal of the American Chemical Society, 2005, 127, 6048.
- [23] Wang, Q.; Zhang, J., Yingyong Huaxue, 1994, 11, 76.
- [24] Stevens, P. J.; Devlin, F. J.; Chablowski, C. F.; Frisch, M. J., The Journal of Physical Chemistry 1994, 98, 11623.
- [25] Hay, P. J.; Wadt, W. R., The Journal of Chemical Physics, 1985, 82, 299.
- [26] Wadt, W. R.; Hay, P. J., The Journal of Chemical Physics, 1985, 82, 284.
- [27] Zhu, R.; Wang, R.; Zhang, D.; Liu, C., Australian Journal of Chemistry, 2009, 62, 157.
- [28] M. J. Frisch, G. W. T., H. B. Schlegel, G. E. Scuseria, M. A. Robb, J. R. Cheeseman, J. A. Montgomery, Jr., T. Vreven, K. N. Kudin, J. C. Burant, J. M. Millam, S. S. Iyengar, J. Tomasi, V. Barone, B. Mennucci, M. Cossi, G. Scalmani, N. Rega, G. A. Petersson, H. Nakatsuji, M. Hada, M. Ehara, K. Toyota, R. Fukuda, J. Hasegawa, M. Ishida, T. Nakajima, Y. Honda, O. Kitao, H. Nakai, M. Klene, X. Li, J. E. Knox, H. P. Hratchian, J. B. Cross, V. Bakken, C. Adamo, J. Jaramillo, R. Gomperts, R. E. Stratmann, O. Yazyev, A. J. Austin, R. Cammi, C. Pomelli, J. W. Ochterski, P. Y. Ayala, K. Morokuma, G. A. Voth, P. Salvador, J. J. Dannenberg, V. G. Zakrzewski, S. Dapprich, A. D. Daniels, M. C. Strain, O. Farkas, D. K. Malick, A. D. Rabuck, K. Raghavachari, J. B. Foresman, J. V. Ortiz, Q. Cui, A. G. Baboul, S. Clifford, J. Cioslowski, B. B. Stefanov, G. Liu, A. Liashenko, P. Piskorz, I. Komaromi, R. L. Martin, D. J. Fox, T. Keith, M. A. Al-Laham, C. Y. Peng, A. Nanayakkara, M. Challacombe, P. M. W. Gill, B. Johnson, W. Chen, M. W. Wong, C. Gonzalez, and J. A. Pople Gaussian 03 (Revision E.01), Gaussian, Inc.: Wallingford CT, 2004.
- [29] Truong, T. N.; Zhang, S. VKLab version 1.0, University of Utah: Salt Lake, UT, 2001.

A Theoretical Study on the Electronic Structures and Optical Properties of Organic Dyes with Double Electron Donor for Dye-Sensitized Solar Cell

R. Tarsang, T. Khan-asa, V. Promarak, T. Sudyoadsuk, T. Kaewin, S. Saengsuwan and S. Jungsuttiwong*

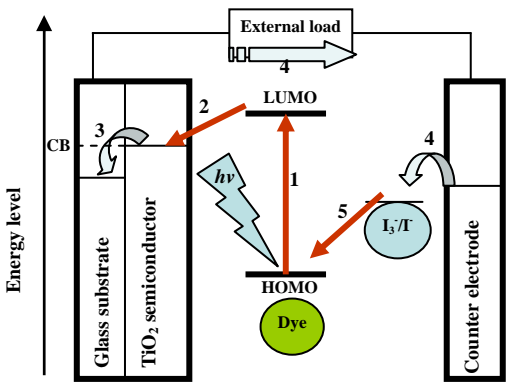
Center for Organic Electronics and Alternative Energy, Department of Chemistry and Center of Excellence for Innovation in Chemistry, Faculty of Science, Ubon Ratchathani University, Warinchamrap, Ubon Ratchathani, 34190, Thailand

* E-mail: jungsuttiwong@hotmail.com

Abstract: We designed and theoretically investigated novel organic dyes of double electron donor type based on carbazole connected to triphenvlamine moiety as photosensitizers for the dye-sensitized solar cell (DSC). The density functional theory (DFT) and time-dependent density functional theory (TD-DFT) calculations were used to estimate the structures and optical properties of the dyes in the design stage. The ground-state geometries for a series of CTT_nA (n = 1-3) were optimized at the B3LYP/6-31G (d,p) level. By means of the TD-DFT method, the absorption spectra were calculated based on the optimized ground-state geometries. According to calculated results, we found that dihedral angle between carbazole-triphenylamine units on the ground-state conformations were twisted about 53° which have significant steric hindrance leading to preventing unfavorable dye aggregation. The influence of the oligothiophene length as a spacer of CTT_nA dyes on the absorption spectra was studied. We observed that the dyes with longer spacer length exhibit higher maximum absorption wavelength. It is interesting to note that these CTT_nA dyes show very broad absorption peaks over the UV-visible to near IR region in high molar coefficients, the results obtained by TD-DFT calculation were corresponding to experimental observation. Therefore, our new organic dves can be effectively used as dve for Dye Sensitized Solar Cell (DSC).

Introduction

Since the first developed and reported by M. Grätzel et al in the 1991, Dye-sensitized Solar Cell (DSC) have attracted a great deal of interest rapidly in the attenion of many research groups during the recent years.^{1,2} This DSC technology has certain advantages over the traditional silicon solar cell because of DSC shown distinguished advantages i.e. their high optical absorption extinction coefficient, adjustable spectral wavelength response, low cost materials, and their environmental friendly.^{3,4} The mechanism of DSC is based on the injection of electrons from dye molecules into the conduction band of TiO₂ (schem 1.), so far, to achive high power efficiency is depended on to design new dye with good properties. Actually, Ruthenium dyes in DSC was recorded of the highest efficiency coded as N3 dye about 11% but the Ru dye are limited with the problem of manufacturing cost and toxicity issues.⁵ Therefore, many organic dyes have been used



Schem 1. Principle operations of DSC: (1) photon excitation; (2) electron injection; (3) collection; (4) transportation; (5) recombination.

in DSC, such as, coumarin⁶, indoline⁷, triarylamine⁸ and perylene⁹ derivatives. The efficiencies of DSC with organic dyes are in range of 5-9% that lower than the Ru dyes. One choice for increasing the efficiency organic dye is the design with Donor- π conjugated-Acceptor (D- π -A) system. ¹⁰ In addition, the absorption spectra of organic dye must be broaded and red-shifted for efficient performance. In order to rationalize the experimentally observed properties of known materials as well as predict and design those of unknown efficient-dyes, theoretical studies using accurate quantum mechanical methods are very essential to provide the energetic properties and geometry of the target dye molecules. At present, numbers of papers have been proposed in the theoretical studies of organic dyes for dye-sensitized solar cell.¹¹ In this study, we reported organic dyes with double electron donor, D-D- π -A dyes, (CTT₁A, CTT₂A, and CTT₃A) dyes which have been synthesized by our group. Carbazole connected to triphenylamine acts as electron donor and cyanoacrylic acid as electron acceptor linked by thiophene units as π -spacer. The photophysical properties of dyes i.e. structures, and electronic properties, in term of HOMO, LUMO involve the absorption spectra were studied to reveal mechanism of electron transfer and discuss about the efficiency of these dyes. In addition, excitation states

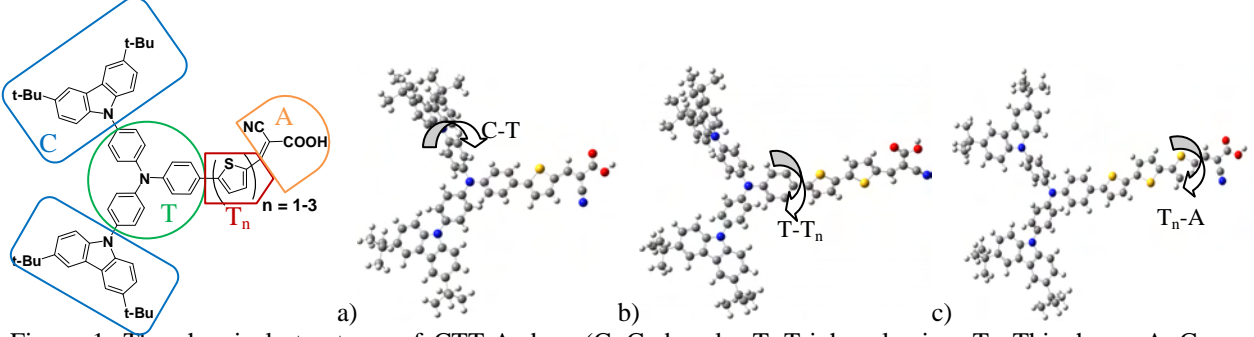


Figure 1. The chemical structures of CTT_nA dyes (C=Carbazole, T=Triphenylamine, T_n=Thiophene, A=Cyanoacrylic acid) and optimized conformation of CTT₁A (a), CTT₂A (b) and CTT₃A (c).

and frontier molecular orbitals of dyes were also analyzed.

Materials and Methods

Computational details. All of organic dyes, CTT₁A, CTT₂A, and CTT₃A, have been performed using the Guassian 03 program package. The groundstate geometries were fully optimized using Density Functional Theory (DFT) method combined with Becke's three-parameter hybrid functional and Lee-Yang-Parr's gradient-corrected correlation functional (B3LYP) at 6-31G(d,p) level. All calculations were performed without any symmetry constraints only in gas phase. These optimized structures were calculated the first excitation energy (E_g), maximal absorption wavelength and oscillator strengths (f) for the 10 states by using Time-Dependent Density Functional Theory (TD-DFT). To investigate the affect of hybrid functional on the E_g, TD-DFT with B3LYP and BHandHLYP hybrid functional were calculated at 6-31G(d,p) level. Subsequently, the TD-DFT results were entried in to the SWizard program for the simulation of absorption spectra of these dyes. Furthermore, these results are also discussed on electronic transition and its character which related to the absorption wavelength. These calculated results were compared with the experimental data in our group.

Results and Discussion

1) Optimal ground-state electronic structures. The calculated molecular structures on ground-state of four CTT_nA organic dyes with DFT method are shown in Figure 1. and the selected dihedral angles are summarized in Table 1. A major factor for the low conversion efficiency of many organic dyes in the DSC is the formation of dye aggregates on the semiconductor surface.¹² Therefore, we designed carbarzole connected to triphenylamine moiety as donor to perform steric hindrance part of molecules. It was found that dihedral angle between carbazoletriphenylamine units, (C-T) column, of all three dyes were twisted about 52.587, 53.095 and 52.637 degree for CTT₁A, CTT₂A and CTT₃A, respectively. These results show that nonplanar conformation due to steric hindrance in dye molecule can prevent unfavourable dye aggregation. In addition, dihedral angle between π-spacer and anchoring group, T_n-A column, are nearby 0 degree indicating that the injection of excited

Table 1. The calculated dihedral angle (degree).

Dihedral angle (°)					
Dye	C-T	$T-T_1$	T_1 - T_2	T_2 - T_3	T _n -A
CTT ₁ A	52.587	20.516	-	-	0.690
CTT_2A	53.095	22.467	5.872	-	0.510
CTT_3A	52.637	23.21	11.871	4.533	0.175

electron from thiophene unit into the neighboring cyanoacrylic acid group are provided conveniently leading to be considered as an intramolecular charge transfer (ICT).

2) Effect of intramolecular charge transfer (ICT). The molecular orbitals contribution is very important in determining the charge-separated states of organic dyes. To create an efficient charge-separated state, HOMO must be localized on the donor subunit, and LUMO on the acceptor subunit.¹³ In order to obtain ICT effect, density of state (DOS) was performed, the molecular orbitals contribution of three dyes were shown in Table2. and the contour plots of HOMO and LUMO and other molecar orbitals of these dyes are displayed in Figure 2. As listed in Table 2., we devided the dye molecule into 4 parts, C=carbazole part, T=triphenylamine part, T_n=thiophene part and A=cyanoacrylic acid part. Electron density of the HOMO were located over the carbazole and triphenylamine parts which to be 95%(C+T), 90%(C+T) and calculated for CTT₁A, CTT₂A, and CTT₃A, 85%(C+T) respectively, this results showed the electron density of HOMO remains delocalized on the donor part. Whereas, the electron density of LUMO were located mainly across the thiophene part as π -system and cyanoacrylic acid part as anchoring group which are calculated to be $38\%(T_n)$, 50%(A) for CTT_1A , $36\%(\pi)$, 60%(A) for CTT₂A and 52%(π), 47%(A) for CTT₃A. As shown in Figure 2., the molecular orbitals analysis couter plotted confirmed that the HOMO of all dyes was delocalized over carbazole and the triphenylamine and the LUMO was delocalized across the π -system and anchoring group. This distribution of the HOMO and LUMO is separated in the molecule, indicating that the HOMO-LUMO transition can be considered as an intramolecular charge-transfer (ICT) transitions. In addition, the orbitals energies of LUMO are -1.65, -1.83 and -1.86 eV for CTT₁A, CTT₂A and CTT₃A, respectively. These energies level are located above the conduction band (CB) of TiO_2 (-2.77 eV)¹⁴

Table 2. Molecular orbitals contribution of 3 highest occupied and 3 lowest unoccupied molecular orbitals of D-D- π -A type dyes.

Dye	Electronic level	Orbital	The percent contribution (%)			
	levei	energies	C	T	T_n	Α
CTT_1A	LUMO	-1.65	0	12	38	50
	HOMO	-6.03	50	45	4	1
	HOMO-3	-6.62	58	27	10	4
	HOMO-4	-6.63	83	11	4	2
CTT_2A	LUMO	-1.83	0	4	36	60
	HOMO	-5.97	42	48	6	4
	HOMO-2	-6.48	40	21	24	15
	HOMO-5	-7.05	15	38	25	22
CTT_3A	LUMO	-1.86	0	1	52	47
	HOMO	-5.89	36	49	11	4
	HOMO-2	-6.33	37	10	38	15
	HOMO-5	-6.84	24	40	24	12

C=Carbazole, T=Triphenylamine, T_n=Thiophene, A=Cyanoacrylic acid

which indicated a good property of dye-sensitizer. Therefore, these CCT_nA organic dyes have sufficient driving force for electron injection into CB of TiO₂.

3) Absorption spectra. To gain insight into the excited states giving rise to the absorption spectra of CTT_nA organic dyes, TD-DFT calculations were employed with the B3LYP/6-31G(d,p) level in gas phase. It is well known that the failure of TD-DFT/B3LYP in highly delocalized/CT molecules is attributed to the fact that the exchange-correlation potentials generated by the current approximate exchange-correlation function decay too rapidly in the asymptotic region. 15 Therefore, the BHandHLYP functional has been employed to correct asymptotic behavior of the charge transfer (CT) states. The maximal absorption wavelengths from computational results are listed in Table 3. The TD-DFT results were entried into the SWizard program for the simulation of absorption spectra as show in Figure 3. These calculated results compared were with experimental data in our group. As shown in Table 3. Absorption maximal wavelength of CTT₁A and CTT₃A dye using B3LYP functional are located at 358.2 and 524.3 nm, respectively. While, the calculated results of the BHandHLYP functional show that the absorption spectra were located at 386.0 and 425.8 for CTT₁A and CTT₃A, respectively, which closely agree with the experimental results are 459 and 464 nm for CTT₁A and CTT₃A, respectively. Whereas, the maximal absorption wavelength of CTT₂A dye is same different shifted with experimental results. However, the B3LYP tended to overestimate the experimental absorption wavelength BHandHLYP can reasonably improve the calculated results to be more accurate. It has been found that BHandHLYP results are in excellent agreement with the experimental data compared with B3LYP results.

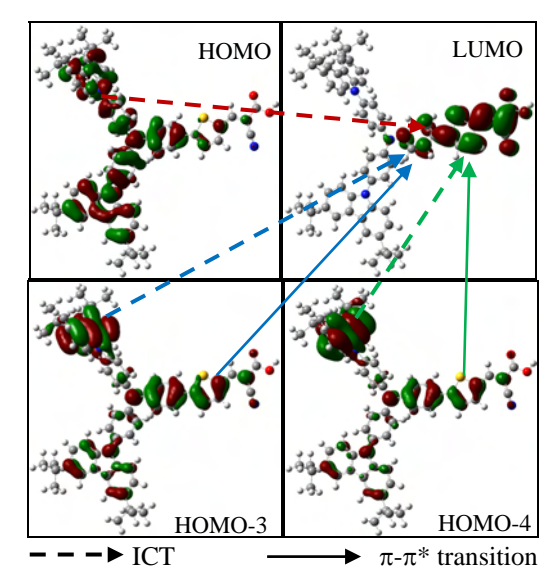
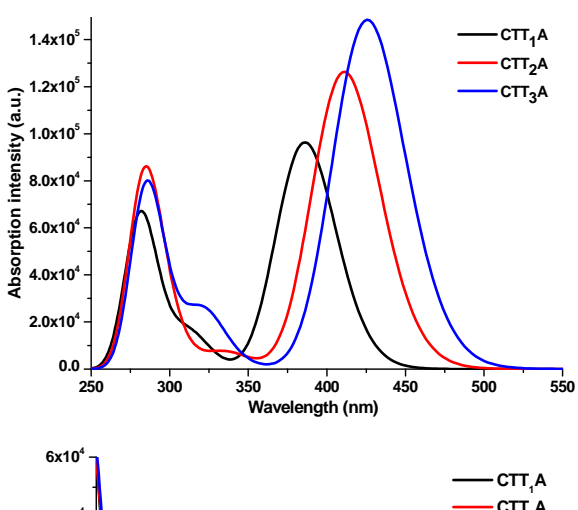


Figure 2. The couter plotted of HOMO, LUMO and others molecular orbitals of CTT₁A dyes.

Table 3. Computational and experimental absorption maxima wavelength (nm).

Dye	Ca	Experiment	
Dye	B3LYP	BHandHLYP	Experiment
CTT ₁ A	358.2	386.0	459
CTT_2A	490.3	411.2	454
CTT_3A	524.3	425.8	464



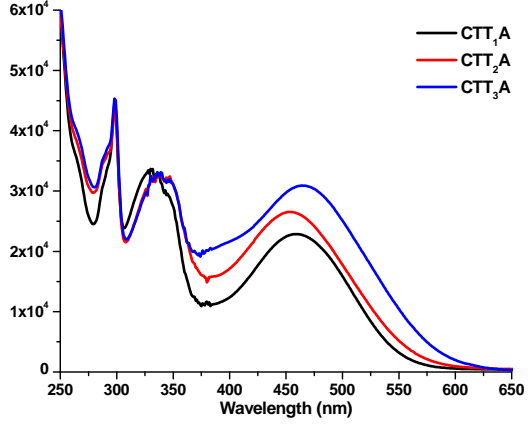


Figure 3. Computational with TD-DFT/ BHandHLYP (graph top) and experimental absorption spectra (graph down).

Table 4. Calculated TD-DFT excitation energies (E_g), oscillator strengths (f), and electronic properties of CTT_nA

organic dyes by TD-DFT/BHandHLYP at 6-31G(d,p).

Dye	State	Excitation energy (eV, nm)	Oscillator strength (f)	Assignment	Character
CTT_1A	\mathbf{S}_1	3.21 (386.0)	1.3297	H-0→L+0 (+55%)	ICT
				H-3→L+0 (+16%)	ICT
				H-4→L+0 (+11%)	ICT
CTT_2A	S_1	3.02 (411.2)	1.7435	H-0→L+0 (+42%)	ICT
				H-2→L+0 (+34%)	ICT, π-π*
				H-5→L+0 (+8%)	ICT, π-π*
CTT_3A	S_1	2.91 (425.8)	2.0483	H-0→L+0 (+39%)	ICT
				H-2→L+0 (+32%)	ICT, π-π*
				H-5→L+0 (+9%)	ICT, π-π*

H=HOMO, L=LUMO, H-3=HOMO-3 etc.

So that, we choose the BHandHLYP functional results for simulation the absorption spectra. As shown in Figure 3, the calculated absorption spectra show two main peak and a shudder peak. The similar trend has been found in the experimental absorption peak but shudder peak is become the three main peak for the experiment. The number of thiophene unit were increased in Figure 3, It has been shown that when increasing thiophene up to 3 units the adsorption wavelength were red-shifted.the increasing of the molar extinction coefficient were found due to the π conjugated system were extended. The TD-DFT calculated results are summarizes in Table 4. In addition, we can characterized the electronic transition character by consider the counter plotted in Figure 2. We found that all of excitation from HOMO→LUMO is intramolecular charge transfer (ICT) process. The orientation of charge transfer is from carbazole ane triphenylamine as donor units to thiophene and cyanoacrylic acid as π -spacer and acceptor unit. There are π - π * transition over the other molecular orbitals except the HOMO-LUMO transition.

Conclusions

In summary, we presented the theoretical study of organic D-D- π -A dyes. To gain a better understanding of the role of its electronic structure, absorption and electron transport properties, we performed DFT and TD-DFT calculation. From the present study, we can infer that CTT_nA dye showed the appropriate donor steric hindrance and coplanarity between π -spacer and acceptor group. It also exhibited the best absorption characteristics with highest molar extinction coefficient as well as, performing a good ICT character. This theoretical CTT_nA results show that it could greatly possible to use as potential sensitizer for highly efficient Dye-Sensitized solar cell (DSC). Furthermore, we found that making use of functional using a larger percentage of exact exchange (BHandHLYP) provided

better results for highly delocalized/CT molecules compared to the hybrid B3LYP density functional which tends to overestimate the transition energies.

References

- [1] D. Kim, M. Kang, K. Song, S. Kang, J. Ko, *Tetrahedron* **64** (2008), pp. 10417–10424.
- [2] R. Ma, P. Guo, H. Cui, X. Zhang, M.K. Nazeeruddin, M. Grätzel, J. Phys. Chem. A 113 (2009), pp. 10119-10124.
- [3] M. Grätzel, Nature 414 (2001), pp. 338-344.
- [4] M.P. Balanay, D.H. Kim, *Phys. Chem. Chem. Phys.* **10** (2008), pp. 5121-5127.
- [5] M. Grätzel, J. Photochem. Photobiol. C 4 (2003), pp. 145-153.
- [6] K. Hara, Z.S. Wang, T. Sato, A. Furube, R. Katho, K. Sugihara, Y. Dan-oh, C. Kasada, A. Shinpo, S. Suga, J. Phys. Chem. B 109 (2005), pp. 15476-15482.
- [7] T. Horiuchi, H. Miura, K. Sumioka, S. Ushida, *J. Am. Chem. Soc.* **126** (2004), pp. 12218-12219.
- [8] G. Li, K.J. Jiang, Y.F. Li, S.L. Li, L.M. Yang, *J. Phys. Chem. C* **112** (2008), pp. 11591-11599.
- [9] Y. Shibano, T. Umeyama, Y. Matano, H. Imahori, Org. Lett. 9 (2007), pp. 1971-1974.
- [10] L. Zhang, Y. Liu, Z. Wang, M. Liang, Z. Sun, S. Xue, *Tetrahedron* **66** (2010), pp. 3318-3325.
- [11] R. Ma, P. Guo, L. Yang, L. Guo, Q. Zeng, G. Lui, X. J. Zhang, Mol. Str. Theochem 942 (2010), pp. 131-136.
- [12] S.E. Ela, M. Marszalek, S. Tekoglu, M. Can, S. Icli, Curr. Appl. Phys. 10 (2010), pp. 749-756.
- [13] Y. Tachinaba, S.A. Haque, I.P. Mercer, J.R. Durrant, D.R. Klug, *J. Phys. Chem. B* 104 (2000), pp. 1198-1205.
- [14] H.W. Ham, Y.S. Kim, *Thin Solid Films* **518** (2010), pp. 6558-6563.
- [15] K. Srinivas, K. Yesudas, K. Bhanuprakash, V.J. Roa, L. Giribabu, J. Phys. Chem. C 113 (2009), pp. 20117-20126.

The Adsorbed Hydrogen Molecules in Cof-105 Doping with Lithium Alkoxide: an Ab initio Study

P. Ariyageadsakul¹ and C. Kritayakornupong^{1,*}

¹Department of Chemistry, Faculty of Science, King Mongkut's University of Technology Thonburi, Bangkok, 10140.

*chinapong.kri@kmutt.ac.th

Abstract: To enhance hydrogen storage ability, lithium alkoxide (LiO) was doped on the Covalent Organic Frameworks (COFs). 1-4 hydrogen molecules adsorbed at the binding site of the COF-LiO structure were studied using the B3LYP/6-311G(d,p) method. The results show that the first and second H_2 molecules were adsorbed at Li atom, while the third and fourth hydrogen molecules were bound at oxygen atom of the lithium alkoxide. The interaction energy of -2.5 kcal/mol was obtained from the H_2 -COF-LiO structure, which is weaker than that evaluated from dihydrogen molecules (-4.5 kcal/mol). The highest interaction energy of -6.1 kcal/mol was calculated for 4 hydrogen molecules, while the corresponding value of -5.4 kcal/mol was elucidated for 3 hydrogen molecules.

Introduction

Recently, a new class of hydrogen storage materials so call Covalent Organic Frameworks (COFs) has been characterized and synthesized [1, 2]. The COFs are composed of light elements (B, C, Si and O) that are linked by strong covalent bonds (B-O, C-C, B-C, and C-Si) [3]. The COFs have a high thermal stability (up to 400–500 °C), high porosity (4210 m²/g for COF-103), and extremely low crystal density (0.17 g cm⁻³ for COF-108) [4-6]. The hydrogen storage capacities in COFs have been reported, showing that the capacities in 3-D COFs are higher than 2-D COFs about 2.5-3 times [3, 5].

In previous work, the MOF doping with lithium atom revealed the significant higher hydrogen storage ability at the ambient temperature [7-9], proving that hydrogen molecules were bound with the lithium atom by quadrupole moment contribution. In this study, the nH₂ molecules (n=1-4) binding to COF-105 doping with lithium alkoxide (COF-LiO) were investigated using the quantum mechanical calculations. The aim of this study is that the COF doping with LiO could improve its hydrogen storage capabilities.

Computational details

The density functional theory (DFT) in conjunction with the Becke's three-parameter hybrid exchange functional and the Lee-Yang-Parr correlation functional (B3LYP) was used. The 6-311G(d,p) basis sets were applied for all atoms. The simplest model of COF-105 doping with lithium alkoxide was evaluated by B3LYP/6-311G(d,p) level of theory for obtaining the optimized position of LiO functional group located in the COF-105 structure (Figure 1.).

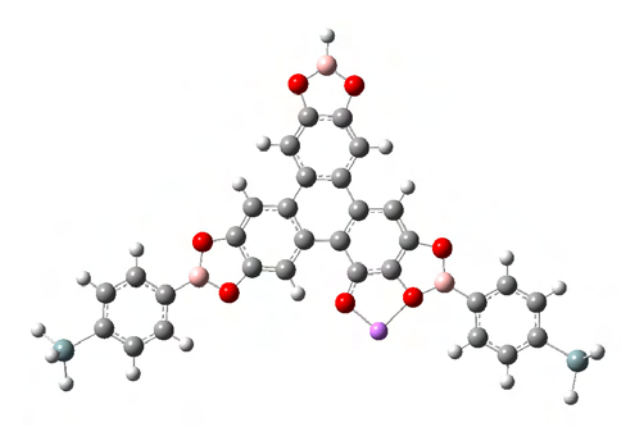


Figure 1. Structure of COF-LiO; carbon, oxygen, boron, hydrogen, silicon and lithium atoms were shown as grey, red, pink, white, green and purple colors, respectively.

The interaction energies between hydrogen molecules and COF-LiO were defined as

$$\Delta E_B = E_{(Complex)} - (E_{(COF\text{-LiO})} + E_{(nH_2)})$$

where $E_{(Complex)}$, $E_{(COF\text{-}LiO)}$, and $E_{(nH_2)}$ are the total energy of multiple adsorbed hydrogen molecules in COF-LiO, the intrinsic COF-LiO with frozen geometry taken from the nH_2 -COF-LiO complex, and nH_2 cluster, respectively.

Finally, the geometrical properties of the COF-LiO adsorbed with H_2 molecules were evaluated in terms

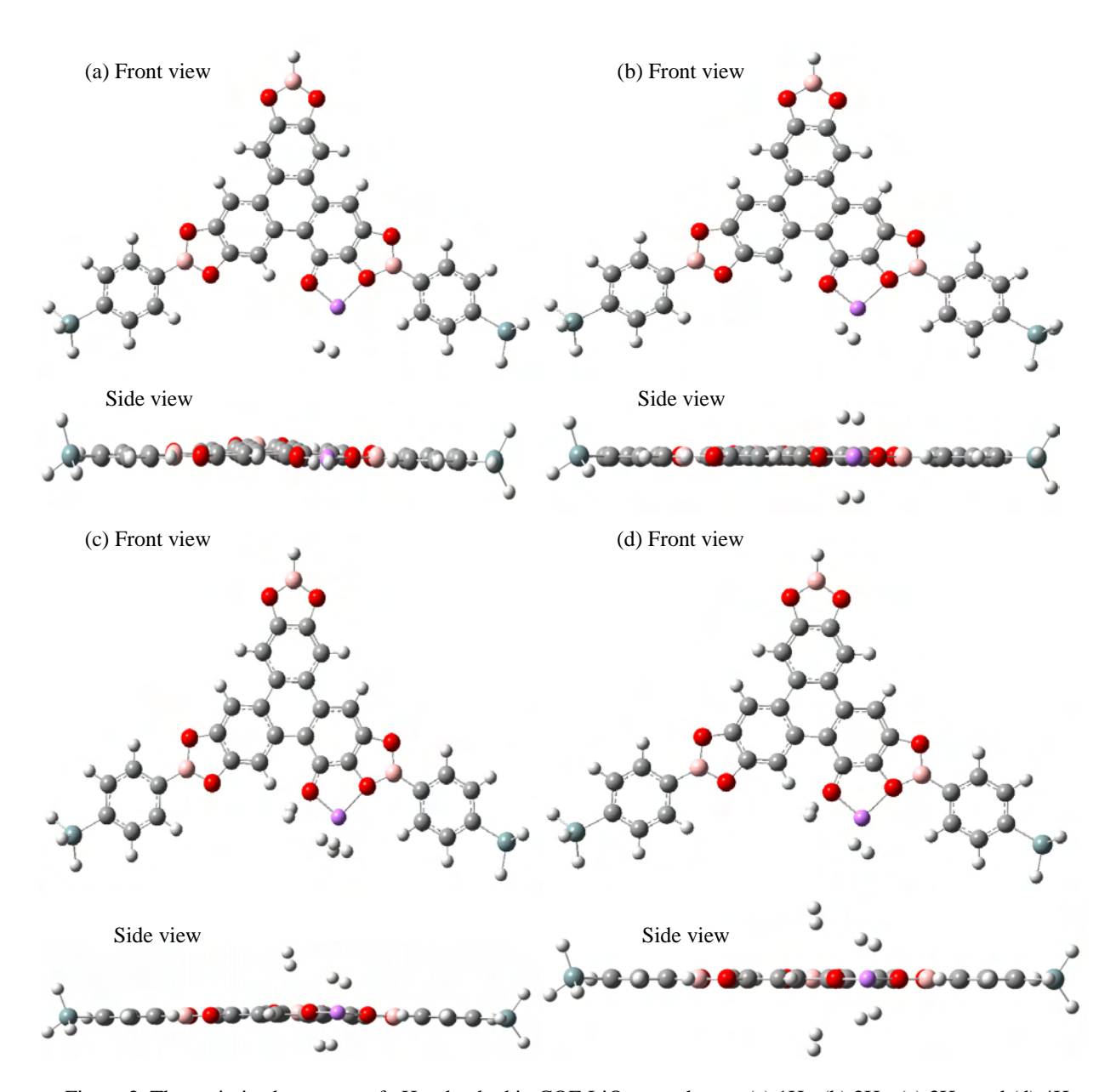


Figure 2. The optimized structure of nH₂ adsorbed in COF-LiO were shown; (a) 1H₂, (b) 2H₂, (c) 3H₂, and (d) 4H₂.

of distances between center of mass of hydrogen molecules and their adsorption sites. All calculations were performed using the Gaussian 03 program [10].

Results and Discussion

The results show that the lithium atom was located at middle of the two neighbor oxygen atoms and lying within the COF-105 plane as shown in Figure 1.

The Li-O_(alkoxide) and Li-O_(C2O2B ring) bond lengths are 1.76 and 1.94 Å, respectively, while the $O_{(C2O2B ring)}$ -Li-O_(alkoxide) angle is 96.8°. It was found that Li and O_(alkoxide) atoms were characterized as the binding sites of the hydrogen molecules. The optimized structures of nH₂ complexed with COF-LiO are depicted in Figure 2. As shown in Figure 2, the first and second H₂ molecules are located at the Li site, while the third and fourth H₂

molecules are adsorbed at the $O_{(alkoxide)}$ atom. The average distances between the center of mass of H_2 molecules and their binding sites of COF-LiO are summarized in Table 1.

Table 1. The average distance between the center of mass of H_2 and the binding sites of COF-105.

	Distance (Å)				
_	H ₂ -Li	H ₂ -O(alkoxide)			
$1H_2$	2.06	=			
$2H_2$	2.10	=			
$3H_2$	2.11	3.00			
$4H_2$	2.11	3.03			

For 1H₂ molecule, the hydrogen molecule was bound at the lithium site and lying within the plane of COF-LiO with the Li-H₂ distance of 2.06 Å. As shown in Figure 2(b), the orientation of two hydrogen molecules coordinated at Li atom are parallel to the Li-O bonds, presenting the average distances of 2.10 Å. In the cases of three and four hydrogen molecules, the O_(alkoxide) was also found to be an alternative adsorption site of the COF-LiO complex. Two hydrogen molecules were interacted with the Li atom with the distance of 2.11 Å, while the third and the fourth of hydrogen molecule were adsorbed at O(alkoxide) site, showing the distances of 3.00 and 3.03 Å for the third and the fourth hydrogen molecules, respectively. However, our findings are in contrast with those evaluated from the RI-PBE/def2-TZVPP method [9] in which the third and fourth hydrogen molecules were attached to the Li site.

Table2. The interaction energy (kcal/mol) between nH_2 and COF-LiO obtained from B3LYP/6-311G(d,p) method.

,	Interaction Energy
	(kcal/mol)
$1H_2$	-2.5
$2H_2$	-4.5
$3H_2$	-5.4
4H ₂	-6.1

The interaction energies between nH_2 and COF-LiO obtained from B3LYP/6-311G(d,p) method were listed in Table 2. The coordination of one hydrogen molecule at the lithium site of the COF-LiO

structure is -2.5 kcal/mol, which is weaker than the value of -4.5 kcal/mol evaluated for 2H₂. In the case of 3H₂, the corresponding energy of -5.4 kcal/mol was evaluated, while the highest adsorption energy of -6.1 kcal/mol was obtained 4 hydrogen molecules complexed with the COF-LiO structure.

Conclusion

It can be concluded that the hydrogen storage capabilities of the COF structure is increased by doping of the lithium alkoxide group. The Li and $O_{(alkoxide)}$ atoms are found to be the adsorption sites in the COF-LiO structure.

References

- A. Cote', A. Benin, N. Ockwig, M. O'Keeffe, A. Matzger and O. M. Yaghi, *Science* 310 (2005), pp. 1166.
- [2] H. El-Kaderi, J. Hunt, J. Mendoza-Corte's, A. Cote', R. Taylor, M. O'Keeffe and O. M. Yaghi, *Science* 316 (2007), pp. 316,268.
- [3] H. Furukawa and O. M. Yaghi, J. Am. Chem. Soc. 131 (2009), pp. 8875-8873.
- [4] E. Klontzas, E. Tylianakis and E. George, J. Phys. Chem. C 112 (2008), pp. 9095-9098.
- [5] S. Han, H. Furukawa, O. M. Yaghi and W. Goddard, J. Am. Chem. Soc. 130 (2008), pp. 11580-11581.
- [6] G. Garberoglio, Langmuir 23 (2007), pp. 12154-12158.
- [7] A. Mavrandonakis, E. Tylianakis, A. K. Stubos and G. E. Froudakis, J. Phys. Chem. C 112 (2008), pp. 7290-7294
- [8] A. Mavrandonakis, E. Klontzas, E. Tylianakis and G. E. Froudakis, J. Am. Chem. Soc. 131 (2009), pp.13410-13414
- [9] E. Klontzas, E. Tylianakis and G. E. Froudakis, J. Phys. Chem. C 113 (2009), pp. 21253-21257.
- [10] M.J. Frisch, G. W. Trucks, H. B. Schlegel, G. E. Scuseria, M. A. Robb, J. R. Cheeseman, J. A. Montgomery, Jr., T. Vreven, N. Kudin, J. C. Burant, J. M. Millam, S. S. Iyengar, J. Tomasi, V. Barone, B. Mennucci, M. Cossi, G. Scalmani, N. Rega, G. A. Petersson, H. Nakatsuji, M. Hada, M. Ehara, K. Toyota, R. Fukuda, J. Hasegawa, M. Ishida, T. Nakajima, Y. Honda, O. Kitao, H. Nakai, M. Klene, X. Li, J. E. Knox, H. P. Hratchian, J. B. Cross, C. Adamo, J. Jaramillo, R. Gomperts, R. E. Stratmann, O. Yazyev, A. J. Austin, R. Cammi, C. Pomelli, J. W. Ochterski, P. Y. Ayala, K. Morokuma, G. A. Voth, P. Salvador, J. J. Dannenberg, V. G. Zakrzewski, S. Dapprich, A. D. Daniels, M. C. Strain, O. Farkas, D. K. Malick, A. D. Rabuck, K. Raghavachari, J. B. Foresman, J. V. Ortiz, Q. Cui, A. G. Baboul, S. Clifford, J. Cioslowski, B. B. Stefanov, G. Liu, A. Liashenko, P. Piskorz, I. Komaromi, R. L. Martin, D. J. Fox, T. Keith, M. A. Al-Laham, C. Y. Peng, A. Nanayakkara, M. Challacombe, P. M. W. Gill, B. Johnson, W. Chen, M. W. Wong, C. Gonzalez, and J. A. Pople, Gaussian Inc., Pittsburgh PA, 2003.

Photocatalytic Degradation of Sodium Dodecylbenzene Sulfonate in the Presence of Zno Suspensions

R. Thianchutima¹, S. Chinsarot¹ and <u>B. Sangchakr^{1*}</u>

¹Department of Chemistry, Faculty of Science, King Mongkut's University of Technology Thonburi, Bangmod, Rasburana, Bangkok, Thailand 10140

*E-mail: benchang.san@ kmutt.ac.th, Tel: +66-2-470-8843 ext 8965

Abstract: Photocatalytic degradation of sodium dodecyl benzene sulfonate (SDBS, $C_{18}H_{29}SO_3Na$) was studied under irradiation of a high pressure mercury lamp using ZnO as the catalyst. The photodegradation activity was followed by periodically monitoring residual concentration of the dye using UV-visible spectrometer. The results showed that the photodegradation kinetics of SDBS on ZnO follows the pseudo-first order rate according to the Langmuir-Hinshelwood equation with the rate constant (k), and the adsorption constant (K) of 4.02 mgl⁻¹min⁻¹ and 0.01 lmg⁻¹, respectively. It was also found that the photodegradation was enhanced by adding Fe²⁺ or H_2O_2 .

Introduction

Linear alkylbenzene sulfonates, the anionic surfactants, are widely used in various industrial process such as in cosmetics, food processings, etc. After use surfactants are usually discharged along with wastewater, causing pollution problems. Although biological treatment can be used to decontaminate surfactants but the degradation is slow and there are such problems as enhanced foam formation, and retarded biodegradation of the accompanying pollutants [1, 2]. Photocatalytic oxidation is an advance oxidation process (AOP) to solve these problems. The advantage of photocatalytic process is its mild operating conditions and it can be activated by sunlight, thus reducing the elective power required and therefore the operating cost [3].

Titanium dioxide (TiO₂) is generally considered to be the best photocatalysts, and has the ability to mineralize wastewater [4, 5]. However widespread use of TiO2 is uneconomical for large scale water treatment, thereby interest has been drawn towards the search for suitable alternatives to TiO2. Many attempts have been made to study photocatalytic activity of different semiconductors such as SnO2, CdS and ZnO [6, 7]. Our present study provides results describing the photocatalytic degradation and mineralization of sodium dodecylbenzene sulfonate (SDBS), important anionic surfactant frequently used in industry, over ZnO powders under experimental conditions.

Materials and Methods

Materials

Sodium dodecylbenzene sulfonate (C₁₈H₂₉SO₃Na) and ZnO were purchased from Fluka (Switzerland) and were used without further purification. Solutions were prepared by dissolving appropriate amount of the SDBS in deionized water.

Photoreactor

All experiments were carried out in a 100 ml Pyrex glass bottle. The radiation source was a 200W high pressure mercury lamp (Applied Photophysics, England), which was placed about 20 cm behind a Pyrex glass bottle.

Procedure

For the photodegradation of SDBS, a solution containing known concentration of the SDBS and ZnO was prepared and the solution was stirred during irradiation. Irradiation was carried for a specific period. Subsequently, the suspension was filtered through 0.45µm Millipore membrane to remove the particles before analyzed.

Analysis

The degradation was monitored by measuring the absorbance on a UV-VIS spectrophotometer at 224nm. The degradation efficiency (%) has been calculated as:

$$Efficiency(\%) = \frac{C_0 - C}{C_0} \times 100$$

where C_0 is the initial concentration of SDBS and C is the concentration of SDBS after photoirradiation.

Results and Disscusion

Effect of UV Irradiation and ZnO

The change in the SDBS concentration versus time during the photocatalytic degradation of SDBS is shown in Figure 1. The removal of SDBS was negligible in the absence of ZnO. It can be seen from the figure that in the presence of ZnO and light, about 90% of SDBS degraded within 120 min of irradiation

time. These results reveal that both UV light and photocatalyst, such as ZnO, were needed for the effective destruction of SDBS. When ZnO is exposed to UV radiation, an electron-hole pair is produced [8].

$$ZnO + hv \longrightarrow e_{cb} + h_{vb}^{+}$$
 (i)

where, e^-_{cb} and h^+_{vb} are the electrons in the conduction band and valence band holes, respectively. The photogenerated holes can react easily with surface bound H_2O to produce hydroxyl radicals, whereas, e^-_{cb} can react with O_2 to produce superoxide radical anion.

$$e_{cb} + O_2 \longrightarrow O_2^{\bullet}$$
 (ii)

$$h^{+}_{vb} + H_2O \longrightarrow {}^{\bullet}OH + H^{+}$$
 (iii)

$$O_2^{\bullet} + H_2O + H^+ \longrightarrow H_2O_2 + O_2$$
 (iv)

$$H_2O_2 \longrightarrow 2 \circ OH$$
 (v)

The hydroxyl radical is extremely strong oxidant that leads degradation of organic pollutants [9].

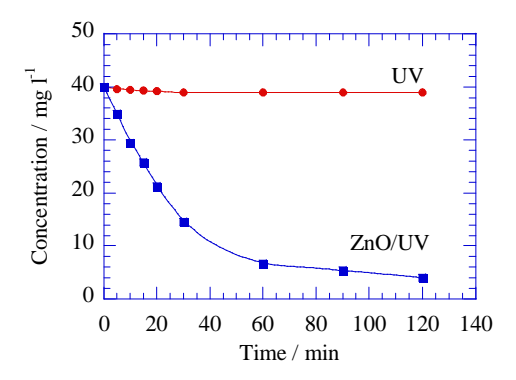


Figure 1. Effect of UV light and ZnO on photocatalytic degradation of SDBS. [SDBS] $_0 = 40 \text{ mg}\Gamma^1$; [ZnO] = $1 \text{ g}\Gamma^1$.

Effect of the Amount of ZnO

The effect of the varying the quantity of ZnO on the degradation of SDBS is presented in Figure 2. As the ZnO concentration increases the initial rate (r_0) of photodegradation increases. The increase in the amount of catalyst enhances the number of active sites on the photocatalyst surface, thus causing an increase

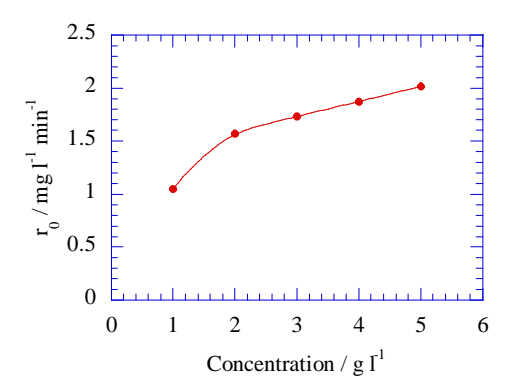


Figure 2. Dependence of r_0 on the concentration of ZnO for constant SDBS concentration (40mgl^{-1}).

in the number of hydroxyl radicals which can take part in the photodegradation of the SDBS.

Effect of Initial SDBS Concentration

The effect of the initial SDBS concentration on the photocatalytic degradation is an important aspect of the study. The photodegradation of various initial concentrations of SDBS in the presence of 1 gl⁻¹ ZnO is illustrated in Figure 3. The effect of altering the initial concentration of SDBS (C₀) on the initial rate of photodegradation is shown Figure 4. The rate of photodegradation first increases sharply and then nearly reaches saturation value at high concentration of SDBS. This may be due to the fact that as the initial concentration of SDBS increases, the solution becomes more intense which presents penetration of light to the surface of the catalyst. Therefore, less hydroxyl radicals are formed, thus causing a decrease in the degradation.

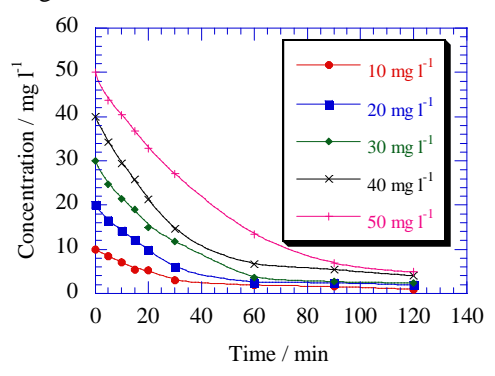


Figure 3. Plot of the photodegradation of SDBS versus irradiation time, at various initial concentrations for constant concentration of ZnO 1 gl⁻¹

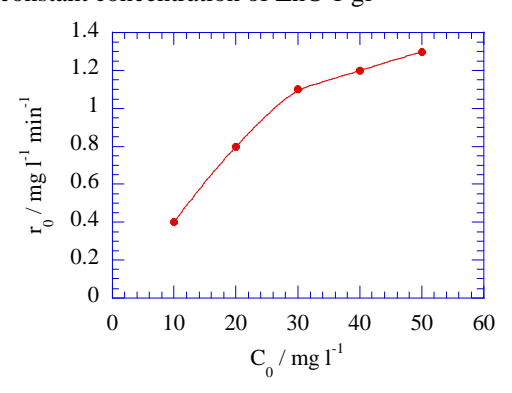


Figure 4. Plot of r_0 vs. C_0 for SDBs at constant constant concentration of ZnO 1 gl⁻¹

Kinetics of Photocatalytic Degradation of SDBS

The influence of the initial concentration of the solute to the photocatalytic degradation rate of most organic compounds is described by a pseudo-first kinetic order according to the Langmuir-Hinshelwood model, modified to a reaction occurring at solid-liquid interface [10].

$$1/r_0 = 1/k + 1/(kKC_0)$$

where k is the rate constant and K is the adsorption coefficient. The dependence of r_0^{-1} values on the

respective inverse initial concentrations of SDBS for constant concentration of ZnO at 1 gl⁻¹ is shown in Figure 5. The k and K values were calculated from the slope and the intercept of the straight line, respectively. The values were $k=4.02~\text{mgl}^{-1}\text{min}^{-1}$ and $K=0.01~\text{lmg}^{-1}$.

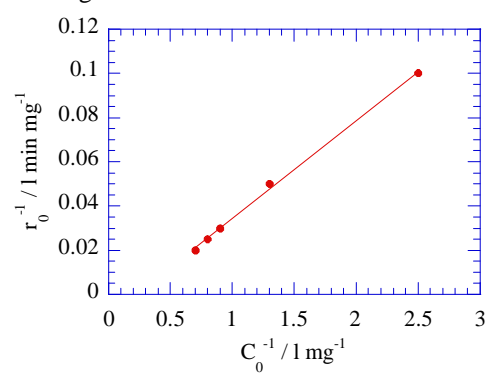


Figure 5. Plot of ${r_0}^{\text{-1}}$ versus ${C_0}^{\text{-1}}$ for photocatalytic degradation of SDBS. [ZnO] = 1 gl⁻¹

Effect of Addition of Fe2+

The change in SDBS degradation in the presence of Fe^{2+} is shown in Figure 6. It was observed that small amount of Fe^{2+} enhanced the photocatalytic degradation of SDBS. Since H_2O_2 is produced in the photocatalytic process, adding Fe^{2+} thus simulating a Fenton process (Fe^{2+}/H_2O_2). In this process, Fe^{2+} will catalyze the decomposition of H_2O_2 to produce hydroxyl radicals. The another reason may be due to Fe^{2+} can react with h^+_{vb} thus reducing the recombination of e^-_{cb} and h^+_{vb} . Hence, the generation of the hydroxyl radicals on the surface of catalyst increases [11].

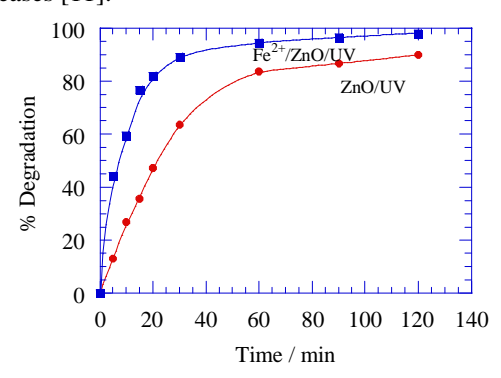


Figure 6. Effect of Fe^{2+} on photodegradation of SDBS. $[SDBS]_0 = 40 \text{ mgl}^{-1}$; $[ZnO] = 1 \text{ gl}^{-1}$; $[Fe^{2+}] = 2 \text{ mgl}^{-1}$.

Effect of Addition of H₂O₂

The change in SDBS degradation in the presence of H_2O_2 is shown in Figure 7. It was also observed that adding H_2O_2 enhanced the photocatalytic degradation of SDBS. Since H_2O_2 is an electron acceptor, it enhances the formation of hydroxyl radicals and also inhibits the (e^-/h^+) pair recombination [12]. This result showed that hydroxyl radicals play a major role in the UV/ZnO process.

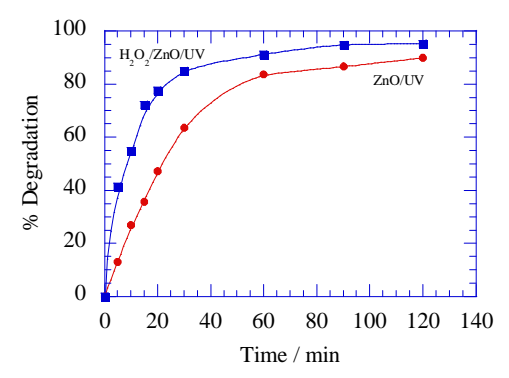


Figure 7. Effect of H_2O_2 on photodegradation of SDBS. [SDBS]₀ = 40 mgl⁻¹; [ZnO] =1 gl⁻¹; [H_2O_2] = 50mgl⁻¹.

Conclusions

Effective degradation of SDBS, an anionic surfactant, is possible by photocatalysis in the presence of ZnO suspension and UV light. The kinetics of the photocatalytic degradation follows the Langmuir-Hinshelwood model. Addition of Fe^{2+} or H_2O_2 can enhance the photodegradation of SDBS.

Acknowledgements

The authors thank the Chemistry Department, King Mongkut's University of Technology Thonburi for financial and other supports.

References

- [1] H. Hidaka, H. Kubota, M. Gratzel, E. Pelizzetti and N. Serpone, *J. Photochem.* **35** (1986), pp. 219-230.
- [2] A.M. Amat, A. Arques, M.A. Miranda and S. Sequi, Solar Energy **77** (2004), pp. 559-566.
- [3] D.Y. Goswami, Advance in Solar Energy 10 (1995), pp. 165-209.
- [4] I. Poulios and I. Aetopoulou, Environ. Technol. 20 (1999), pp. 479-487.
- [5] J. Saien, and A.R. Soleymani, J. Hazard. Mater. 144 (2007), pp. 506-512.
- [6] S.K. Kansal, M. Singh and D. Sud, J. Hazard. Mater. 141 (2007), pp. 581-590.
- [7] X. Wang, B.Q. Xu, J. Zhao, B. Mai, P. Peng, G. Sheng and J. Fu, J. Photochem. Photobiol. A: Chem. 168 (2004), pp. 47-52.
- [8] M.A. Rauf, S.B. Bukallah, A. Hammadi, A. Soliman, and F. Hammadi, *Chem. Eng. J.* 129 (2007), pp. 167-172.
- [9] N.M. Mahmoodi, M. Arami, N.Y. Limaee, and N.S. Tabrizi, J. Colloid Interface Sci. 295 (2006), pp. 159-164
- [10] H. Al-Ekabi and N. Serpone, J. Phys. Chem. 92 (1982), pp. 5726-5731.
- [11]M.I. Litter, Appll. Catal. B: Environ. 23 (1999), pp. 89-114.
- [12] C.C. Chen, A.J. Chaudhary and S.M. Grimes, *Dyes and Pigments* 73 (2005), pp.55-58.

Adsorption of Sodium Polyacrylate on Ceramic Glaze

A. Terdputtakun and O. Arquero*

Department of Chemistry and Center of Excellence for Innovation in Chemistry, Faculty of Science, Chiang Mai University, Chiang Mai, Thailand 50200

* E-mail: noi2495@hotmail.com

Abstract: The problematic which mostly found in ceramic glaze is the dispersion instability that resulted in solid flocculation and inhomogeneity of glaze slip. Through the addition of polyelectrolyte, the dispersion stability was achieved by surface modification of adsorption of polyelectrolyte on ceramic glaze. Optimum amount of the added polyelectrolyte resulted in good dispersion. The adsorption of anionic polyelectrolyte (sodium polyacrylate, NaPA) onto a celadon ceramic glaze mixture composed of limestone, kaolin, quartz and feldspar was studied. The adsorption isotherm was investigated in order to understand the dispersion stability as a function of anionic polyelectrolyte concentration. It was found that the adsorbed amount of increased with the increasing polyelectrolyte concentration. The adsorption data of NaPA was correlated with the Langmuir and Freundlich isotherms. The maximum adsorbed amount of NaPA was 13.72 mg/g, evaluated by using Langmuir isotherm.

Introduction

Many processing steps in the manufacture of ceramic products need to be controlled in order to prevent defect formation and to achieve desirable products. Generally, ceramic production consists of 5 steps which are preparation of raw materials, formulation of body mixture, forming, glazing and firing. Glazing is one of the steps that a ceramic surface being coated to make the piece more impervious to water and enhance its appearance. This process involves applying a glaze on the ceramic body and firing with at temperature, usually about 1100 – 1300 °C. Glaze will fuse and a thin glassy layer is formed on the surface of the ceramic body.

Raw glazes are combination of natural and synthetic materials such as clays, quartz, feldspars, carbonates and oxides of suitable composition to produce the final glaze [1]. Glaze is usually applied in aqueous suspension but the dispersion of glaze mixture in the water was not stable. The particles tend to settle quickly. This is a quite problem because when glaze settle out, some ingredients of the glaze may settle to the bottom of the container. Coating the ceramic body with this settled glaze could provide some defects in the products because the missing of some ingredients. To prevent such problem, it is necessary to produce a stable dispersion of the glaze suspension.

The ceramic particles in solution tend to attract each other due to van der Waals attractive forces [2]. To mitigate this force, one approach is to generate repulsive forces between particles. Particles may possibly become dispersed in a repulsive manner by the forces developed at the particles surfaces. Addition of additives to glaze suspension can produce the dispersion stability [3-6]. One of the additives used is polyelectrolyte.

Polyelectrolytes are charged polymers. polymer chains contain a large number of dissociative functional groups. The polyelectrolytes widespread applications in many industrial processes and in numerous products due to their ability to adsorb at solid/liquid interfaces and to modify surface properties. They are frequently used to control the stability of dispersed systems such as pigments, pharmaceuticals, paper cosmetics. etc Polyelectrolytes will be adsorbed on the particles surfaces and increase interparticle repulsive forces through electrical charge and/or sterically hindering the close approach of neighboring particles [4]. Thus, studies on adsorption of polyelectroytes on the particles are important to an understanding of the stability of colloidal suspension. The adsorption process must be carefully controlled to produce a satisfactory process system.

Materials and Methods

Materials: All ceramic glaze raw materials were sourced in Thailand: the limestone (97%) from Sara Buri, the kaolin (85%) from Ranong, the feldspar (99%) and quartz (>99%) from Tak. The components were ground and size adjusted by sieving and mixed by dry ball milling to homogeneous. The basic compositions of the ceramic glaze were 28 wt.% limestone, 27 wt.% kaolin, 25 wt.% feldspar and 20 wt.% quartz. The average particle size (d_{4,3}) of the ceramic glaze particles, measured by laser diffraction (LD) with a Masterizer S (Malvern, UK), was 16.25 um. The specific surface area for glaze powder was 6.65 m²/g determined by nitrogen adsorption (BET) at 77 K (Quantachrome). The anionic polyelectrolyte – sodium polyacrylate (NaPA), produced by Aldrich was used in this study. The average molecular weight of the NaPA is 2100 g/mol. Its structure was shown in Figure 1. Deionized water was used for the preparation of suspension.

Adsorption equilibrium determination: Adsorption equilibrium determination provides data about the rate of polyelectrolyte adsorption on the ceramic glaze raw

Figure 1. Structure of sodium polyacrylate

material surface. The experiments were carried out at 30 °C. Ceramic glaze suspensions were prepared by adding 0.1 g of glaze powder into the Erlenmeyer flask which contained 100 mL of NaPA solutions (50 and 250 mg/L). The obtained suspensions were shaken continuously. Aliquots were removed at predetermined times and centrifuged for 30 minutes. The supernatants were taken to determine the concentration of remaining NaPA using a spectrophotometer (Lambda 25 UV/Vis Spectrometer). The used wavelength was 199 nm. The amount of NaPA adsorbed on the particles was evaluated from the difference between the initial concentration and the NaPA equilibrium concentration in the supernatant. Aliquots were removed until no further adsorption was observed indicating that equilibrium was achieved.

Adsorption isotherms: The adsorption measurements were made in the NaPA concentration range 25-400 mg/L. 0.1 g of ceramic glaze powder was added to 100 mL of NaPA solution of known concentration. The suspensions were shaken at 30 °C for 2 hours, the time required to reach adsorption equilibrium indicated by the adsorption equilibrium studies. After equilibrium took place, the mixtures were centrifuged for 20 minutes. The supernatants were separated in order to determine the amount of non-adsorbed NaPA according to the method described above.

The amount of NaPA uptake per unit of adsorbent (q_e) was calculated using the following equations:

$$q_e = (C_i - C_e) \times V/m \tag{1}$$

where C_i is the initial NaPA concentration (mg/L), C_e is the NaPA concentration at the adsorption equilibrium (mg/L), V is the volume of NaPA solution (L), and m is the weight of the ceramic glaze powder (g).

Results and Discussion

The results of the adsorption equilibrium determination of NaPA on ceramic glaze are illustrated in Figure 2. The adsorption rate was fast under all solution concentrations and no change was observed in the maximum adsorption after 1 hour. In order to be sure that the equilibrium was reached, 2 hours was used for all adsorption experiments.

Adsorption isotherm was obtained by plotting the adsorbed amount of NaPA per ceramic glaze unit mass as a function of NaPA equilibrium concentration. The

adsorption isotherm of NaPA on ceramic glaze at 30 °C is shown in Figure 3. The result shows that the

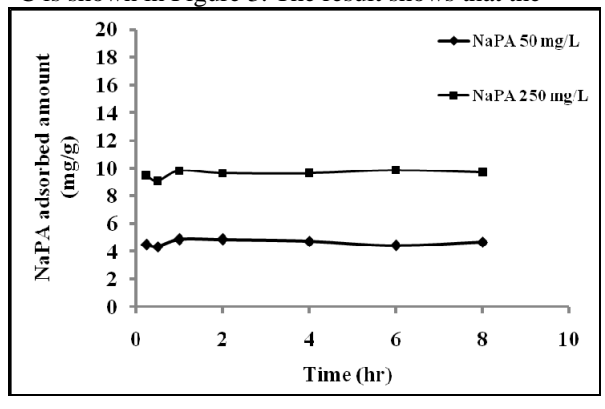


Figure 2. Adsorption of NaPA on ceramic glaze as a function of time under different NaPA concentrations

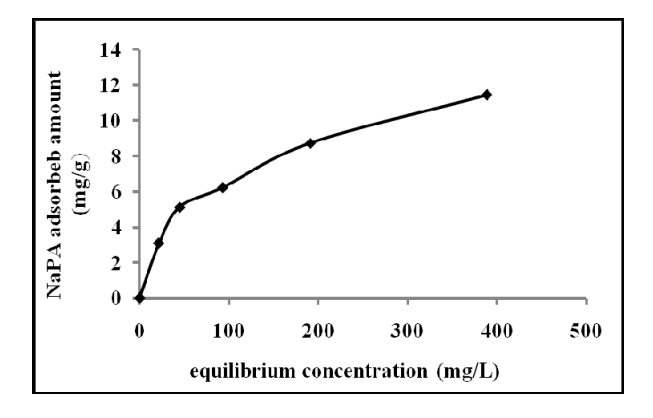


Figure 3. Adsorption isotherm for NaPA on ceramic glaze at 30 $^{\circ}\text{C}$

adsorbed amount increases with increasing the NaPA concentration.

The Langmuir isotherm is expressed by the following empirical equation:

$$C_e/q_e = C_e/q_{max} + 1/q_{max}b$$
 (2)

where C_e is the equilibrium concentration of adsorbate (mg/L); q_e is the amount of adsorbate adsorbed (mg/g); q_{max} is Langmuir constant (maximum adsorption capacity) (mg/g); b is Langmuir constant (L/mg).

The linear form of Freundlich model is

$$\log q_e = \log K_F + (1/n) \log C_e \tag{3}$$

where K_F and n are Frendlich constants related to adsorption capacity and adsorption intensity.

Plots of adsorption data in linear form of Langmuir and Freundlich isotherms are shown in Figures 4 and 5, respectively. The linearity of these plots is an indication of the applicability of the Langmuir and Freundlich adsorption isotherms equation in the concentration range studied. From these plots, the Langmuir values, q_{max} and b, and Freundlich values, K_F and n, were then calculated. The results are shown in Table 1.

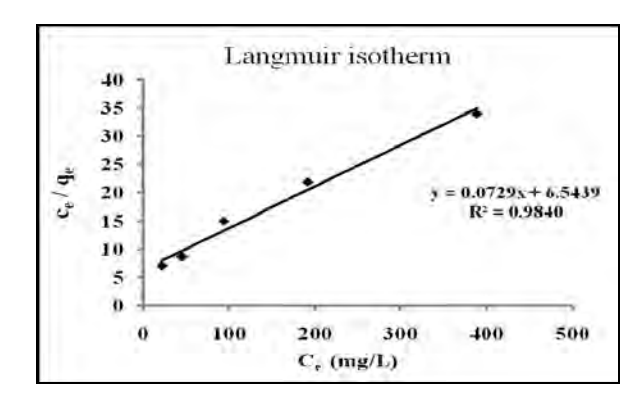


Figure 4. Langmuir linear regression plot

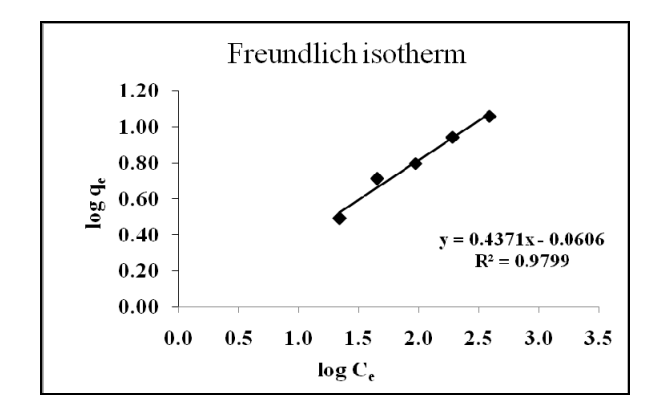


Figure 5. Freundlich linear regression plot

Table 1 Langmuir and Freundlich constants

	Langmuir			Freundlich		
NaPA	q_{max}	b	\mathbf{r}^2	K_{F}	n	\mathbf{r}^2
Ivai A	(mg/g)	(L/mg)				
	13.72	0.011	0.9840	0.87	2.3	0.9799

From the Langmuir plot, the maximum adsorbed amount of NaPA on the ceramic glaze is 13.72 mg/g.

Conclusions

Adsorption equilibrium as a function of time and adsorption isotherm of NaPA on ceramic glaze at 30°C have been investigated. The adsorbed amount of NaPA on ceramic glaze increases with the increasing of concentration. Adsorption of NaPA on ceramic glaze fit to both Langmuir and Freundlich adsorption isotherms. The maximum adsorbed amount is 13.72 mg/g.

Acknowledgments

The authors would like to thank the National Research University, and the Center of Excellence for Innovation in Chemistry: PERCH-CIC, Thailand, for partial finacial support of this research.

References

[1] D.J. Shanefield, *Organic Additives and Ceramic Processing*, Kluwer Academic Publishers, Boston, USA (1998).

- [2] B.P. Singh, R. Menchavez, C. Takai, M. Fuji and M. Takahashi, J. Colloid Interface Sci. 291 (2005), pp. 181-186
- [3] P. Panya, O. Arquero, G.V. Franks and E.J. Wanless, *J. Colloid Interface Sci.* **279** (2004), pp. 23-35.
- [4] S. Schwarz, K. Lunkwitz, B. Spiegler, E. Killmann and W. Jaeger, *Colloid Surf. A: Physicochem. Eng. Aspects.* 163 (2000), pp. 17-27.
- [5] S. Farrokhpay, G. Morris, D. Fornasiero and P. Self, Progr. Colloid Polym. Sci. 128 (2004), pp. 216-220.
- [6] J. Chen, T. He, W. Wu, D. Cao, J. Yun and C.K. Tan, Colloids surf. A: Physicochem. Eng. Aspects. 232 (2004), pp. 163-168.
- [7] S. Luifu, H. xiao and Y. Li, J. Colloid Interface Sci. 281 (2005), pp. 155-163.
- [8] P. Marco and J. Llorens, J. Eur. Ceram. Soc. 29 (2009), pp. 559-564.
- [9] M. Sjöberg, L. Bergström, A. Larsson and E. Sjöström, *Colloids surf. A: Physicochem. Eng. Aspects.* 159 (1999), pp. 197-208.

An Influence of Silver Nanoparticles on Double Proton-Transfer Process in Guanine-Cytosine Base Pair

J. Wicheandee¹, K. Kunsutha¹ and C. Kritayakornupong^{1*}

Department of Chemistry, Faculty of Science, King Mongkut's University of Technology Thonburi, Bangkok, Thailand 10140

*E-mail: chinapong.kri@kmutt.ac.th

Abstract: Characteristics of Ag_n clusters (n=1, 2, and 4) complexed with guanine-cytosine (G:C) Watson-Crick DNA base pairs and their double proton-transfer processes were determined using the Density Functional Theory (DFT). A combination of Becke's threeparameter hybrid exchange functional and the Lee-Yang-Parr correlation functional (B3LYP) was used. The Los Alamos effective core potential (LANL2DZ ECP) basis set was applied for silver atoms, while the rest was calculated using the 6-31+G(d,p) basis set. The strongest hydrogen bonding interaction of -25.5 kcal/mol was obtained from the G:C-Ag₄ complex in which a pair of silver atoms is coordinated at N7 and N3 sites of guanine, while the G:C-Ag and G:C-Ag2 predict the corresponding values of -23.4 and -23.6 kcal/mol, respectively. For double proton-transfer processes, the activation energy was decreased as increasing silver nanoparticles. The lowest activation energy of 11.2 kcal/mol was observed for the G:C-Ag₄ structure, which is much lower than that determined from the GC base pair. It can be concluded that double proton-transfer processes in the G:C-Ag_n complexes are more favourable in comparison with the isolated G:C base pair.

Introduction

The double proton-transfer process in DNA base pair plays an important role in formation of these rare tautomers and the mutation of biological.[1-2] The N7 and N3 sites of purine base are preferred as targets for metal ion binding in DNA base pair by experimental.[3] The N7 site is exposed in the major groove and the N3 site is found to be the minor groove within DNA.[4] In the present work, the complexes of silver nanoparticles located near the N7 and/or N3 site of guanine in DNA base pair were studied using an ab initio quantum mechanical calculation to investigate the influence of nanoparticles in double proton-transfer reactions of G:C base pair.

Materials and Methods

The geometries of silver (Ag_n) cluster (n=1, 2, and 4) complexed with guanine-cytosine (G:C) Watson-Crick base pairs, their double proton-transfer (DPT) processes and model of the transition state (TS) have been fully optimized by using the density functional theory (DFT). Becke's three-parameter hybrid exchange functional and the Lee-Yang-Parr correlation functional (B3LYP) was used. The 6-

31+G(d,p) basis set was employed for all atoms except silver nanoparticles. The Los Alomos effective core potential (LAN2DZ ECP) was used for Ag_n clusters, which coordinated at the N3 and/or N7 site of guanine in DNA base pair. The DPT processes in G:C base pair may occur between the deprotonation from the N4 site of cytosine to the O6 site of guanine, and the proton transfer from the N1 site of guanine to N3 site cytosine. The silver nanoparticles attached sites with one, two (e.g., the silver clusters located near the N3 site of guanine in DNA base pair: the Ag-N3(G):C and Ag₂-N3(G):C complexes, respectively), and four atoms (i.e., the N3 and N7 sites in guanine complexed with Ag₂: the Ag₂-N3 Ag₂-N7(G):C structure). All calculations were performed using the Gaussian 03 program.[5]

Results and Discussion

Table 1: Optimized bond distances for G:C base pair complexed with silver clusters $(Ag_{1,2,4})$ in Watson-Crick base pair and DPT reactions.

	G:C (Å)	
O6-N4	N1-N3	N2-O2
2.79	2.95	2.93
2.81	2.94	2.90
2.81	2.93	2.92
2.82	2.93	2.88
2.82	2.93	2.90
2.84	2.91	2.86
	DPT (Å)	
O6-N4	N1-N3	N2-O2
2.69	2.90	3.00
2.67	2.90	2.99
2.66	2.89	3.01
2.67	2.90	2.99
2.65	2.89	2.99
2.62	2.88	3.00
	2.79 2.81 2.81 2.82 2.82 2.84 2.69 2.67 2.66 2.67 2.65	2.79 2.95 2.81 2.94 2.81 2.93 2.82 2.93 2.82 2.93 2.84 2.91 DPT (Å) 06-N4 N1-N3 2.69 2.90 2.67 2.90 2.66 2.89 2.67 2.90 2.65 2.89

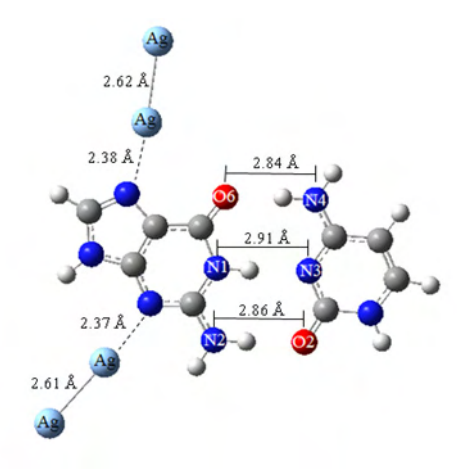
Structural properties of silver clusters coordinated at the N3 and/or N7 site of guanine in Watson-Crick base pair and DPT processes evaluated from the B3LYP/6-31+G(d,p) level of theory are shown in the Table 1. The interatomic distances of O6-O4, N1-N3, and N2-O2 bonds obtained from the G:C Watson-Crick base pair are 2.79, 2.95, and 2.93 Å, respectively. The Ag-N3(G):C and Ag-N7(G):C

complexes reveal the similar value of the O6-N4 bond distances (2.81 Å), which are slightly larger than the G:C Watson-Crick. By adding Ag₂ clusters, the O6-N4 and N1-N3 bond distances were found to be 2.82 and 2.93 Å, respectively, which are slightly longer than those observed for the G:C base pair complexed with a silver atom. The N1-N3 and N2-O2 bond distances of the increasing silver nanoparticles complexes are generally decreased for all complexes, while the O6-N4 bond distances are all increased. The O6-O4, N1-N3, and N2-O2 bonds evaluated from the Ag₂-N3_Ag₂-N7(G):C complex are 2.84, 2.91, and 2.86 Å, respectively. For the DPT complexes, the O6-O4 and N1-N3 bond distances are all decreased with respect to the corresponding bond distances in G:C Watson-Crick base pair. The similar value of the O6-N4, N1-N3, and N2-O2 bond distances in the cases of one and two silver atoms coordinated at the N3 site of G:C base pairs were pronounced with the values of 2.67, 2.90, and 2.99 Å, respectively. The Ag-N7(G):C, Ag₂-N7(G):C, and Ag_2 -N3_ Ag_2 -N7(G):C show the corresponding values of 2.66, 2.65, and 2.62 Å, respectively. The N1-N3 distance was found to be decreased by ~0.02 Å. In addition, the N2-O2 bond distance of the Ag-N7(G):C complex (3.01 Å) is slightly longer than those evaluated from the G:C Watson-Crick base pair and the Ag₂-N3_Ag₂-N7(G):C complexes (3.00 Å), while the Ag-N3(G):C and Ag₂-N7(G):C complexes reveal the similar N2-O2 bond distance of 2.99 Å. These results indicate that the hydrogen bond lengths in the G:C base pair are increased or decreased due to their complexation with silver nanoparticles

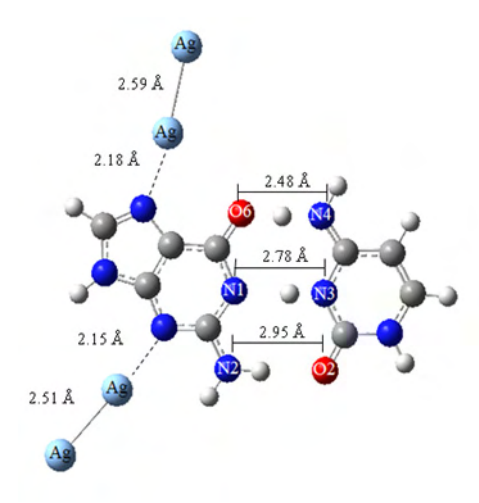
Table 2: Binding energies and activation energy (E_a) of G:C base pair complexed with silver clusters in Watson-Crick base pair and DPT processes obtained from the B3LYP/6-31+G(d,p) method.

Complex	Binding energy (kcal/mol)		E _a (kcal/
	G:C	DPT	mol)
G:C	-26.2	-18.8	14.9
Ag-N3(G):C	-23.0	-15.1	13.9
Ag-N7(G):C	-23.4	-14.4	14.0
Ag_2 -N3(G):C	-23.6	-15.5	13.3
Ag_2 -N7(G):C	-23.6	-16.0	13.3
$Ag_2-N3_Ag_2-N7(G):C$	-25.5	-17.4	11.2

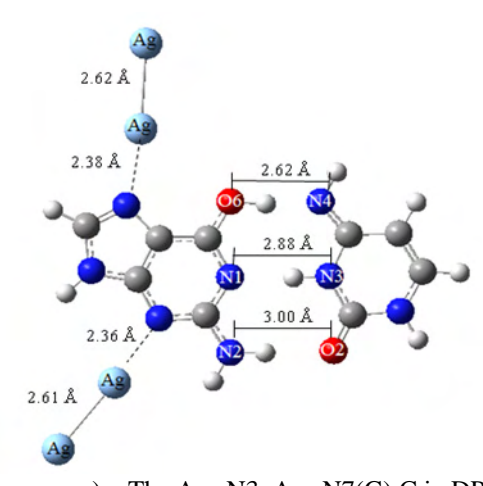
Table 2 presents the binding energy and activation energy of G:C base pair coordinated with silver clusters obtained from the B3LYP/6-31+G(d,p) method. The binding energy of -26.2 kcal/mol was evaluated for the G:C Watson-Crick base pair, while the value of -18.8 kcal/mol was calculated from the DPT process in G:C base pair with the reaction barrier of 14.9 kcal/mol. The binding energies of one and two silver atoms attached at the N3 or N7 sites of G:C base pairs were found to be decreased by ~3 kcal/mol in comparison with the G:C Watson-Crick form. Similar trend was also observed in the cases of DPT processes.



a) The Ag_2 -N3_ Ag_2 -N7(G):C in Watson-Crick



b) The Ag_2 -N3_ Ag_2 -N7(G):C in TS



c) The Ag_2 -N3_ Ag_2 -N7(G):C in DPT

Figure 1. The complexes Ag₂-N3_Ag₂-N7(G):C in a) Watson-Crick base pair, b) transition state (TS), and c) double proton-transfer (DPT) reaction.

The binding energies of the DPT reaction in G:C base pair complexed with one and two silver nanoparticles were decreased by 2.8-4.4 kcal/mol. The lowest reaction barrier of 11.2 kcal/mol was predicted from the Ag₂-N3_Ag₂-N7(G):C complex, while the reaction barriers of 13.9, 14.0, 13.3, and 13.3 kcal/mol were

resulted from the Ag-N3(G):C, Ag₂-N3(G):C, Ag-N7(G):C, Ag₂-N7(G):C, and Ag₂-N3_Ag₂-N7(G):C complexes, respectively. These observations indicate that the DPT processes in G:C base pair complexed with silver nanoparticles are more favorable compared with the isolated G:C base pair.

Conclusions

Characteristics of silver nanoparticles with the G:C Watson-Crick base pair and their DPT reaction were elucidated using the B3LYP/6-31+G(d,p)ULANL2DZ method. Our calculated data suggest that the activation energy of the DPT processes in G:C base pair is decreased by attaching the silver clusters at N3 and/or N7 sites of the G:C base pair.

- [1] G. Villani, G. Chem. Phys. **324** (2006), pp. 438-446.
- [2] C.F. Guerra, F.M. Bickelhaupt, J.G. Snijders, and E.J. Baerends, J. Am. Chem. Soc. 122 (2000), pp. 4117-4128
- [3] M.M. Cerda, D. Amantia, B. Costisella, A. Houlton, and B. Lippert, *Dalton Trans.* 32 (2006), pp. 3894-3899
- [4] H. Sigel, Pure Appl. Chem. **76** (2004), pp. 1869–1886.
- [5] M. J. Frisch, G. W. Trucks, H. B. Schlegel, G. E. Scuseria, M. A. Robb, J. R. Cheeseman, J. A. Montgomery, Jr., T. Vreven, K. N. Kudin, J. C. Burant, J. M. Millam, S. S. Iyengar, J. Tomasi, V. Barone, B. Mennucci, M. Cossi, G. Scalmani, N. Rega, G. A. Petersson, H. Nakatsuji, M. Hada, M. Ehara, K. Toyota, R. Fukuda, J. Hasegawa, M. Ishida, T. Nakajima, Y. Honda, O. Kitao, H. Nakai, M. Klene, X. Li, J. E. Knox, H. P. Hratchian, J. B. Cross, C. Adamo, J. Jaramillo, R. Gomperts, R. E. Stratmann, O. Yazyev, A. J. Austin, R. Cammi, C. Pomelli, J. W. Ochterski, P. Y. Ayala, K. Morokuma, G. A. Voth, P. Salvador, J. J. Dannenberg, V. G. Zakrzewski, S. Dapprich, A. D. Daniels, M. C. Strain, O. Farkas, D. K. Malick, A. D. Rabuck, K. Raghavachari, J. B. Foresman, J. V. Ortiz, Q. Cui, A. G. Baboul, S. Clifford, J. Cioslowski, B. B. Stefanov, G. Liu, A. Liashenko, P. Piskorz, I. Komaromi, R. L. Martin, D. J. Fox, T. Keith, M. A. Al-Laham, C. Y. Peng, A. Nanayakkara, M. Challacombe, P. M. W. Gill, B. Johnson, W. Chen, M. W. Wong, C. Gonzalez, and J. A. Pople, Gaussian, Inc., Pittsburgh PA, 2003.

Theoretical Study on the stabilities of Be Ion and Small Be Cluster in Sapphire

C. Sukyoo, P. Phintasiri and A. Saksaengwijit*

Department of Chemistry, Faculty of Science, King Mongkut's University of Technology Thonburi, Bangkok, Thailand

*E-mail:aimorn.sak@kmutt.ac.th

Abstract: In gem industrial, the heat treatment together with some chemicals (Be²⁺,Fe³⁺,...) is a well-known process to improve the gem appearance. Since the value of gem depends on its appearance, it is important to understand how these chemicals improve the optical and physical properties of gems. In this work, we attempt to gain the information on the electronic structure of α - Al_2O_3 (or sapphire) doped with Be^{2+} ion (or Be cluster) by means of the computational simulation. The Density-Functional Theory (DFT) with the Goedecker normconserving pseudopotentials implemented in the CPMD program is used to perform all calculations. The stabilities of Be2+ and small Be cluster at many possible positions in Al₂O₃ structure were studied. We found that Be²⁺ ion is too small to stay stably in the octahedral hole. In contrast, it gains a lot binding energy when it is added in the tetrahedral hole. Moreover, adding either Be²⁺ or Be cluster to the aluminum defect position can stabilize the Al₂O₃ structure. The cohesive and rearrangement energies are also reported.

Introduction

In the crystalline state, the most widespread and important phase of aluminum oxide (α-Al₂O₃) is corundum. The presence of impurities in corundum can influence its mechanical, semiconducting and optical properties [1-2]. Over the past five years a new technique to improve the corundum appearence was introduced in gem-industrial. An annealing or using a heat-treatment together with some chemicals (beryllium, chromium, borax, lead, tantalum) can completely change the color of corundum [3]. The dramatic results from this technique encourages many gemologists and scientists to find out the precise cause of the change in color. One famous product from this process is treated pink-orange sapphire, which can be prepared by annealing a pale or blue sapphire together with some beryllium compound at high temperature. Many hypothesis have been proposed from the gem community [3-4], however it is seem to sattle on theory about bulk-diffusion or lattice-diffusion. It suggests the cause of the change in color might be from the diffusion of the chemical into corundum. However, this issue is still on a debate.

From the physical adjudement no one can separate the treated corundum and the natural one apart. Only some advance spectroscopic techniques (exp. SIMS & LA-ICP-MS) [3] can give the accurate result. However, these techniques offer us only an amount of added chemicals in corundum. The knowledge on the nature of added impurities, the local electronic structures around them and their stabilities in corundum is still lacked. In a few decades, the computational simulation has been proved to be an

effective technique to study chemical and physics of materials on atomic level [5-6]. In the present work, we have performed some computational simulations based on quantum chemistry approaches to study the electronic structures and the stabilities of beryllium ion (Be²⁺) and beryllium cluster (Be-Be) in α -Al₂O₃

Materials and Methods

We have investigated the electronic structures of the doped aluminum oxide with Be²⁺ and beryllium cluster, Be:Al₂O₃. The smallest beryllium-cluster consists of two beryllium atoms (Be-Be) is chosen. The stabilities of Be²⁺ and Be-Be cluster in the crystal structure of α-Al₂O₃ are studied in both structural and energetic aspects. The cohesive energy for adding Be²⁺ and the corresponding rearrangement energy for any doping are calculated. In the previous works [5], doping an impurity ion (exp. Mn³⁺, Fe³⁺, Cr³⁺) in corundum structure had been done only in an octahedral site or substituting at the Al³⁺ position. Since the ionic radius of Be2+ is much smaller than Al³⁺, it might be possible to fill in a tetrahedral site of corundum as well. To examine these possible sites we doped a Be2+ ion in both empty tetrahedral and octahedral sites and also doped it in an Al3+ defect site. For the case of defect-Al₂O₃, we also calculate the formation energy in order to check the possibility to substitute Be²⁺ and Al³⁺ (at the defect site). For a case of Be-Be cluster we doped it in two empty nearbyoctahedral sites or at the defect site next to an empty octahedral site (see the doped positions from the optimized structures in figure 1&2).

In the present work we have carried out the first principle calculation of Be:Al₂O₃ based on the Density Functional Theory (DFT) in the Kohn–Sham (KS) formulation as implemented in the Car-Parrinello molecular dynamics (CPMD) parallel code version 3.11.1 [7]. The CPMD method has been successfully used for the study of the stability of impurity ion in both amorphous and crystal systems [8]. The interactions of the ion cores with the valence electrons were described by Goedecker norm-conserving pseudo-potentials in the Kleinman-Bylander form. The electronic wave functions were expanded in a planewave basis set with an energy cutoff of 160 Ryd. The local density approximation (LDA) is used in all calculations. The generalized gradient approximation (GGA) is not used in this simulation since it had been reported that it does not improve geometries for this case [9]. The periodic crystal structure is taken into account by using the periodic boundary conditions at the unit cell boundaries.

The structural model of plain aluminium oxide (\$\alpha\$-Al\$_{2}O_{3}\$) is constructed by using the lattice parameters received from the Inorganic Crystal Structure Database (ICSD). The X-ray data was published by Maslen *et al.* The crystal of Al\$_{2}O_{3}\$ belongs to the space group R3c. A model of hexagonal supercell box has parameters a = b = 9.520 Å, c = 12.990 Å and \$\alpha\$ = \$\beta\$ = 90°, \$\gamma\$ = \$120°, which contains 48 six-coordinated Al atoms and 72 four-coordinated O atoms. After fully relaxation, the optimized structure of pure-Al\$_{2}O_{3}\$ was received. The starting structure of Be:Al\$_{2}O_{3}\$ was constructed by doping Be\$^{2^+}\$ and Be-Be cluster in the optimized pure-Al\$_{2}O_{3}\$ optimized structures were performed with relaxation of all atomic positions by the preconditioned conjugate gradient (PCG) method.

Results and Discussion

The crystal structure of Al_2O_3 has hexagonal symmetry. Naturally, oxygen ions form a framework of tetrahedral and octahedral holes, which Al^{3+} ions fill in only 2/3 of octahedral holes. The filled octahedron is distorted due to asymmetry space around it. The distortion causes an asymmetric trigonal bipyramid in octahedron unit. The following notation O1 and O2 are used to classify neighbouring oxygen ions formed a trigonal bipyramid for reasons of structure analysis. Three neighboring oxygen ions, which are closed to the ion in an octahedral site are labeled O1, while the others in octahedron unit are denoted O2. This nomenclature also applies to all Be: Al_2O_3 .

In this section, we first focus on the $Be:Al_2O_3$ doped with one Be^{2+} ion per supercell. Three proposed possible sites to fill Be^{2+} ion are (a) in a tetrahedron, (b) in an empty octahedron, and (c) at an Al^{3+} defect site. Three proposed models are fully relaxed all atomic positions and shown in figure 1. For a case of non-defect Al_2O_3 , doping Be^{2+} ion in an empty octahedral site does not affect any significant change in Al_2O_3 structure. This seems to lack of strong interaction between Be^{2+} ion and octahedral oxygens

Table 1: Some geometric properties of Be: $Al_2O_3^*$.% Δ is the percent difference between the corresponding properties of Be: Al_2O_3 and the ones of pure Al_2O_3 .

Be:Al ₂ O ₃	QBe_1O_1	%Δ	$O_2Be_1O_2$ (degree)	%Δ	d_{BeO}	%Δ
	(degree)		(degree)		(Å)	
Be ²⁺ :tetrahedron	-	-	-	-	1.73	11**
Be2+:octahedron	92.6	-	92.6	-	2.03	-
Be ²⁺ :defect	101.67	+0.4	79.29	-0.6	2.02	+0.2
	Q_1XQ	%Δ	O_2XO_2	%Δ	$d_{{\scriptscriptstyle BeB\epsilon}}$	$\%\Delta^{\pm}$
	(degree)		(degree)		(Å)	
Be-Be:2octahedrons (X=Al)	75.80	-28	102.42	+28	1.64	-31
Be-Be:defect+octa- Hedron (X=Be)	78.39	-22	99.51	+24	1.99	-16

^{*}The value is averaged over all sides of the trigonal pyramid.

around it. In contrast, doping a Be^{2+} ion in tetrahedral site affects a lot change in oxygen geometry around it. Be^{2+} ion relaxes itself by moving close to three of tetrahedral oxygens. Note that the Be-O bond length (1.73 Å) in this structure is longer than the Be-O bond length (1.33 Å) in a tetrahedral unit in BeO crystal.

The last case for doping Be^{2+} ion is to dope Be^{2+} at the Al^{3+} defect site. Since Be^{2+} ion is about 1.5 times smaller than Al^{3+} ion, it moves itself close to three of octahedral oxygens (O1). This results of the stronger distortion in a trigonal bipyramid (i.e. the wider O1BeO1 angle and the narrower O2BeO2 angle). It is agreed with the influence of some transition metals on the Al_2O_3 structure reported in the previous work [5].

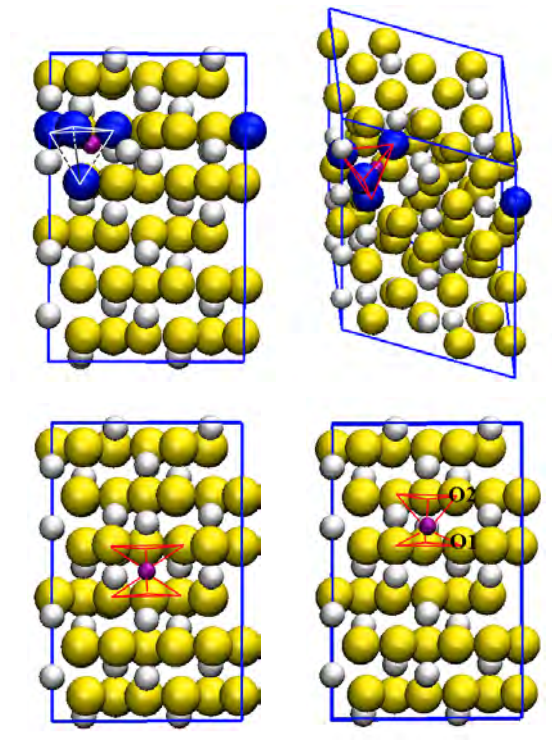


Figure 1. The electronic structures of Be:Al₂O₃. The largest, middle and the smallest spheres represent O, Al and Be²⁺, respectively. (a) & (b) Be²⁺ doped in tetrahedral site. Only tetrahedral oxygens at the doped site are shaded. (c) Be²⁺ doped in an empty octahedral site. (d) Be²⁺ doped at Al³⁺ defect site. The sketchs shows a distorted octahedron and tetrahedral sites.

Next, we consider the Be:Al₂O₃ doped with one Be-Be cluster per supercell. In the present work only two proposed possible cases are studied. The first-case is to fill a Be-Be cluster along two nearby empty octahedrons in z-axis. Its optimized structure is shown in figure 2a. As expected, the repulsion of the Be-Be cluster causes some geometric constraints on the above and below filled octahedron. This results of the wider O2AlO2 angle and the narrower O1AlO1 in the next-layer octahedrons. The second case is to fill a Be-Be cluster into an Al³⁺ defect position which is next to an empty octahedron along z-axis (see figure 2b). The oxygen geometry around Be²⁺ at the defect site changes a bit. The repulsion of Be-Be cluster in this Be:Al₂O₃ is not strong as the previous case.

^{**}Comparison with the value of the initial configuration

[±] Comparison with d_{Be-Be} in free Be cluster.

Some geometric properties of the electronic structure of all Be: Al_2O_3 are summarized in table 1.

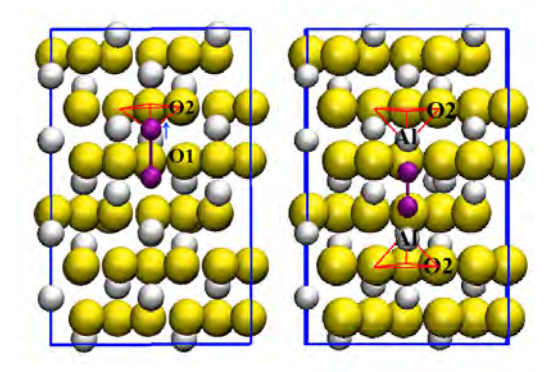


Figure 2. The electronic structures of Be: Al_2O_3 . (a) Be-Be cluster doped in two empty octahedral. (b) Be-Be cluster doped in one Al^{3+} defect site next to an empty octahedron. The notations for all spheres are same as ones in the previous figure.

In order to study the stability of Be^{2+} , which is doped in an empty site (tetrahedron or octahedron) of non-defect Al_2O_3 , the corresponding cohesive energy was calculated by the following expression.

$$E_{cohesive\;for\;1\;Be^{2+}} = E_{BeAl2O3,\;opt} - E_{Al2O3,sp} - E_{Be^{2+}} \label{eq:energy}$$

, which $E_{BeAl2O3, \, opt}$ = total energy of $Be:Al_2O_3$ $E_{Al2O3, sp}$ = single point energy of Al_2O_3 E_{Be2+} = total energy of Be^{2+} ion.

Generally, the cohesive energy is an amount of interaction energy (attraction energy) for holding all ions together to form the crystal, which can be determined by the difference between the energy of bulk crystal and the total energy of all free ions. In order to calculate an amount of energy, which is corresponding only for adding one Be²⁺ into the Al₂O₃ crystal, we defined the corresponding cohesive energy as described above. Interestingly, the cohesive energy for adding Be²⁺ in an octahedral site is positive, while one for the other site (tetrahedral site) is negative. This means that adding Be²⁺ in an empty octahedral site causes some higher energy to Al_2O_3 crystal. Therefore, from energetic aspect Be2+ should not stay stably in an empty octahedral site. On the other hand it suggests that Be²⁺ could stay in a tetrahedral site in Al₂O₃ crystal. However, from the structural point of view adding Be²⁺ in tetrahedral site affects a lot changes in Al₂O₃ structure. The rearrangement energy involved for this process can be calculated as

$$E_{\text{rearrangement}} = E_{\text{Al2O3, opt}} - E_{\text{Al2O3, sp}}$$

, which $E_{Al2O3, opt} = total energy of pure Al₂O₃.$

The rearrangement energy for this case is about 5.5 eV or 130 kcal/mol. This amount of energy can be achieved easily during annealing (~ 1800 K) in the gem apparent-enhancement process. The formation and rearrangement energies for all case are listed in table 2.

Table 2 Some energetic properties of Be:Al₂O₃

Be:Al ₂ O ₃	E _{cohesive} (eV)	$E_{rearragement}$ (eV)
Be ²⁺ :tetrahedron	-2.72	5.5
Be ²⁺ :octahedron	2.95	2.43
Be-Be:2octahedrons	-1.32	8.85

Usually, the defect site is filled by an ion with equal charge (isovalent ion). According to charge-compensation mechanism in defect chemistry, it is still possible to add a mismatch-charge ion at the defect site. In this work, Be^{2+} is used to fill at an Al^{3+} defect site (see figure 1d). The formation energy E_f of ${\rm Be}^{2+}$ substituting for Al^{3+} in a bulk Al_2O_3 crystal is obtained by

$$E_{\rm f} = E_{\rm Be:Al2O3} + \mu_{\rm Al} - E_{\rm Al2O3} - \mu_{\rm Be} + qE_{\rm F},$$

where $E_{Be:Al2O3}$ and E_{Al2O3} are total energies for $Be:Al_2O_3$ and corresponding Al_2O_3 . μ_{Al} and μ_{Be} are chemical potential for Al^{3+} and Be^{2+} . E_F is the Fermi energy, which is set to zero at the valence-band maximum.

The formation energy E_f described above is the difference in the total crystal energy before and after substitute Al^{3+} with Be^{2+} . The calculated E_f in this work is -0.28 eV. The small E_f suggests that it is possible to substitute Al^{3+} with Be^{2+} in Al_2O_3 crystal.

Conclusions

In summary, we have studied some structural properties of the $Be:Al_2O_3$ crystal and the stabilities of doped Be^{2+} and a small Be-Be cluster in pure aluminum oxide. In case of adding a Be^{2+} ion in an empty site of Al_2O_3 , from the energetic aspects it suggests that Be^{2+} cannot stay stably in octahedral site while it is possible to be in tetrahedral site if there is enough energy to rearrange the Al_2O_3 structure.

- [1] T. Hirata, S. Ota and T. Morimoto , *J. Euro. Ceram. Soc.*, **23** (2003), pp 91-97.
- [2] Yu. N. Novikov, V. A. Gritsenko, and K. A. Nasyrov, JETP Lett., 98 (2009), pp 506-509.
- [3] J. L. Emmett and T. R. Douthit, Gems & Gemology, Vol. 29, No. 4, pp. 250–272 (1993)
- [4] V. Pisutha-Arnond, T. Haeger, P. Wathanakul and W. Atichat, Gems & Gemology, Summer 2003, pp 84-135
- [5] E. Gaudry, D. Cabaret, P. Sainctavit, C. Brouder, F. Mauri, J. Phys.: Condens. Matter, 17 (2005) 5467–5480
- [6] O. M. Lo.vvik, S. M. Opalka, H. W. Brinks and B. C. Hauback, *Phys. Rev. B*, **69**(2004), pp 134117.
- [7] CPMD V3.13 Copyright IBM Corp. 1990-2008, Copyright MPI fuer Festkoerperforschung Stuttgart 1997-2001.
- [8] W. Hayami, T. Tanaka, S. Otani, J. Phys. Chem. A, 109(2005), pp 11975-11979.
- [9] I. Frank, D. Marx, and M. Parrinello, J. Chem. Phys. 104 (1996), pp 8143.

Finding Out the Potential Binding Mode of Calanolide a Derivatives in WT HIV-1 RT Based on Molecular Modelling

A. Kumkong¹, A. Punkvang¹, P. Khamsri¹, P. Saparpakorn², S. Hannongbua², P. Wolschann³, G. Liu⁴ and P. Pungpo^{1*}

¹Department of Chemistry, Faculty of Science, Ubon Ratchathani University, Ubon Ratchathani, Thailand
 ²Department of Chemistry, Faculty of Science, Kasetsart University, Chatuchak, Bangkok, Thailand
 ³Institute for Theoretical Chemistry, University of Vienna, Vienna, Austria
 ⁴Department of Synthetic Medicinal Chemistry, Institute of Materia Medica, Chinese Academy of Medical Sciences & Peking Union Medical College, Beijing, China

* E-mail: pornpan_ubu@yahoo.com

Abstract: (+)-Calanolide A was described as the first natural product that inhibits HIV-1 reverse transcriptase (HIV-1 RT). Calanolide A derivatives show extremely high potency against several single mutations of HIV-1, especially Y181C mutation. However, the binding mode of calanolide A derivative in HIV-1 RT binding site has not been clarified. The docking calculations and MD simulations using GROMACS were employed to model the potential binding mode of a calanolide A derivative in the WT HIV-1 RT binding site. The obtained results show that a calanolide A derivative is bound in the same binding site with nevirapine. However, there are new arrangement of resides in HIV-1 RT binding site to accommodate the binding of a calanolide A derivative. The positions of Tyr181, Tyr183, Tyr188, Pro225, Pro226, Trp229, Leu234, His235, Pro236, Tyr318 and Glu138 are significantly changed as compared with those of nevirapine binding site. Additionally, Thr139 of HIV-1 RT chain B is participated in the binding of a calanolide A derivative. This result is correlated with the experimental data that the mutation of Thr139 affects on the inhibition activities of calanolide derivatives more than that of nevirapine. Based on the molecular modelling results, the reasonable binding mode of a calanolide A derivative in WT HIV-1 RT was proposed. These results should provide the better understanding the binding mechanism of calanolide A derivatives in WT HIV-1 RT.

Introduction

Highly active antiretroviral therapy (HAARTa) has been very effective for treatment of HIV-1. However, several limitations of this medication are presented such as the rapid emergence of drug-resistant mutant strains due to the narrow range of chemical structure of the cocktail components. Accordingly, HIV-1 treatment remains a great need to discover novel antivirals, especially ones that function nonnucleoside reverse transcriptase inhibitors (NNRTIs). (+)-Calanolide A was described as the first natural product that inhibits HIV-1 reverse transcriptase (HIV-1 RT) [1-2]. Calanolide A derivatives show extremely high potency against several single mutations of HIV-1, especially Y181C mutation. However, the binding mode of calanolide A

derivative in HIV-1 RT binding site has not been clarified. In this present study, the docking calculations and molecular dynamics (MD) simulations using GROMACS were employed to model the potential binding mode of a calanolide A derivative in the wild type (WT) HIV-1 RT binding site.

Figure 1. The chemical structure of (+)-Calanolide A

Materials and Methods

Calanolide/WT HIV-1 RT structure: The X-ray crystal structure of nevirapine complexed with WT HIV-1 RT (pdb code of 1VRT) was taken for this study. Calanolide derivatives were docked into the nevirapine binding site using Autodock 3.05 program. The complexed structure of calanolide derivatives obtained from docking calculations was served as the initial structure for MD simulations.

Force Fields: GROMOS96 53a6 force field was applied for MD simulation. Because of no such standard force field for calanolide derivatives, ACPYPI program was employed to calculate force field for these compounds.

Molecular simulation: GROMACS 4.0.4 software package was used for MD simulations. The calanolide/HIV-1 RT complex was immersed in a box that extends at 12 Å from all atoms of this complex and it was then solvated by SPC216 water molecules. To treat the electroneutrality condition, 9 Cl-

counterions were added by replacing 9 water molecules in the system. The energy minimization with 2000 steps using the steepest descent algorithm was performed for this system with all bonds constrained. After energy minimization, 200 ps position restraining simulation of this system was performed to relieve close contacts before the actual simulation. Then, full MD simulation with time step of 0.002 ps was performed with the simulation time of 10 ns. The leapfrog algorithm in the NVT ensemble at 300 K was used for simulation. The V-rescale temperature coupling was used to keep the system in a stable environment. All bonds were constrained LINCS algorithm. During MD simulation, the particle mesh Ewald (PME) method was used to calculate long-range electrostatics. 10 Å cutoff for Lennard-Jones and short-range Coulomb interaction was employed. Coordinates and energy of system were saved at every 2 ps.

Results and Discussion

Root mean square deviation

The root mean square deviations (RMSD) of backbone atoms of HIV-1 RT compared with initial coordinates as a function of the simulation time were examined to reveal the stability of the system. HIV-1 RT reaches equilibrium after 500 ps of simulation time as shown in Figure 2. However, HIV-1 RT shows more flexibility with RMSD in range of 2.5-4.0 Å. In case of calanolide inhibitor, it reaches equilibrium at the early simulation time. Based on RMSD, calanolide shows two binding modes in WT HIV-1 RT. Two binding modes of calanolide are shown in Figure 3.

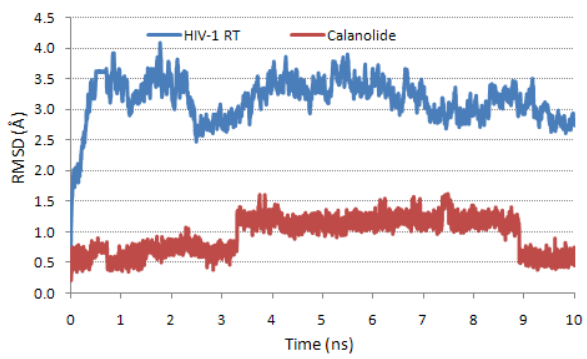


Figure 2. RMSDs of backbone atoms of HIV-1 RT and all atoms of a calanolide derivative

Interactions of calanolide A derivative in HIV-1 RT

Although a calanolide A derivative shows two binding modes in HIV-1 RT binding site, their interactions are similar. This result may be resulted from the high flexibility of HIV-1 RT. A calanolide A derivative is bound in the same binding site with nevirapine as shown in Figure 4. However, there are new arrangement of resides in HIV-1 RT binding site to accommodate the binding of a calanolide A

derivative. The positions of Tyr181, Tyr183, Tyr188, Pro225, Pro226, Trp229, Leu234, His235, Pro236, Tyr318 and Glu138 are significantly changed as compared with those of nevirapine binding site. Additionally, Thr139 of HIV-1 RT chain B is participated in the binding of a calanolide A derivative which is correlated with the experimental data that the mutation of Thr139 affects on the inhibition activities of calanolide derivatives more than that of nevirapine [1]. This result implies the reasonable binding mode of a calanolide A derivative in WT HIV-1 RT obtained from MD simulation.

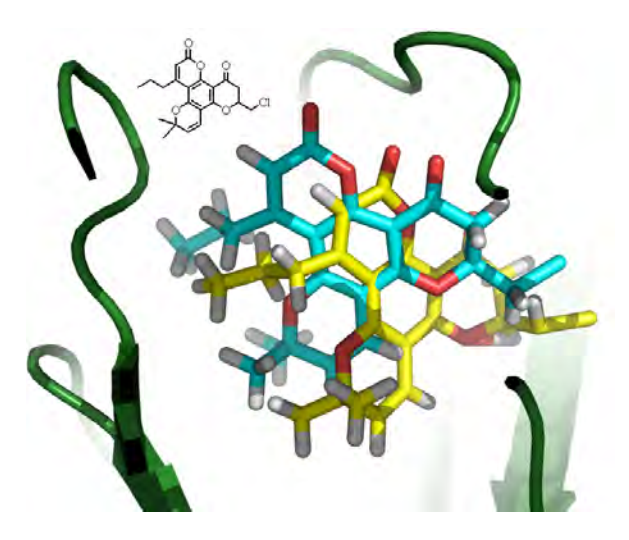


Figure 3. The binding modes of calanolide A derivative at 2 ns (cyan) and 8 ns (yellow) in HIV-1 RT

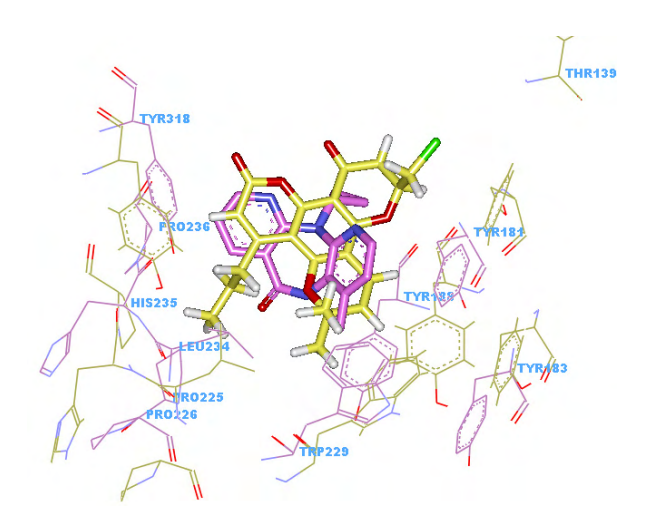


Figure 4. The binding modes of calanolide A derivative (yellow) and nevirapine (pink) in HIV-1 RTs.

A calanolide A derivative could form a hydrogen bond interaction with Lys103 as shown in Figure 5. Moreover, the hydrophobic interaction of this compound with Val179, Tyr181, Tyr188, Phe227, Trp229, Leu234, Pro236 and Tyr318 could be observed.

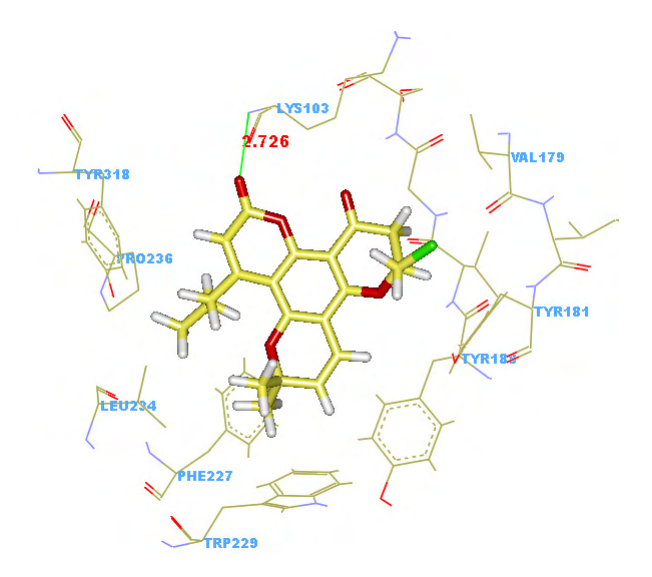


Figure 5. The binding mode of calanolide A derivative in HIV-1 RT obtained from MD simulation

Conclusions

The docking calculations and MD simulation using GROMACS are nicely to simulate the reasonable binding mode of a calanolide A derivative in the WT HIV-1 RT binding site. A calanolide A derivative is bound in the same binding site with nevirapine. Moreover, the important interactions for binding of a calanolide A inhibitor in HIV-1 RT were elucidated. Consequently, our results should provide the better understanding the binding mechanism and dynamics behavior of calanolide A derivatives in WT HIV-1 RT. These results could benefit for designing novel anti-HIV agent with high inhibitory activity.

- [1] H. Xue, X. Lu, P. Zheng, L. Liu, C. Han, J. Hu, Z. Liu, T. Ma, Y. Li, L. Wang, Z. Chen and G. Liu. *J. Med. Chem.* 53 (2010), pp. 1397–1401.
- [2] T. Ma, Q. Gao, Z. Chen, L. Wang and G. Liu. Bioor. Med. Chem. Lett. 18 (2008), pp. 1079–108

Investigation of Inhibition Mechanism of Arylamide Inhibitors as an Antitubercular Agent on InhA Using MD Simulations

A. Punkvang¹, P. Saparpakorn², S. Hannongbua², H. A. Wahab⁴, P. Wolschann³ and P. Pungpo^{1*}

¹Department of Chemistry, Faculty of Science, Ubonratchathani University, Ubonratchathani, Thailand
²Department of Chemistry, Faculty of Science, Kasetsart University, Chatuchak, Bangkok, Thailand
³Institute for Theoretical Chemistry, University of Vienna, A-1090 Vienna, Austria
⁴Pharmaceutical Design and Simulation Laboratory, School of Pharmaceutical Sciences, Universiti Sains Malaysia, Malaysia

*E-mail: pornpan_ubu@yahoo.com

Abstract: Arylamide derivatives as an antitubular agent have been introduced to overcome the resistance of isoniazid (INH) associated with mutations in the KatG enzyme. The enoyl acyl carrier protein reductase (InhA) from M. tuberculosis has been identified as the target enzyme of arylamide derivatives. InhA catalyzes the NADH-specific reduction of 2-trans-enoyl-ACP substrate. Arylamide derivatives could bind to both of InhA-NADH and InhA-NAD+ forms. In order to examine which form of the enzyme arylamides prefer, molecular dynamics (MD) simulations of an arylamide derivative bound to both of InhA-NADH and InhA-NAD+ were performed. Moreover, MM-PBSA method was employed to calculate the binding free energy of this compound. The results reveal that an arylamide derivative bound to InhA-NAD+ shows more flexible than that bound to InhA-NADH. Based on the calculated binding free energies, an arylamide inhibitor complexed with InhA-NAD+ represents the binding free energy higher than that complexed with InhA-NADH, -11.83 and -17.59 kcal/mol, respectively. Therefore, our results should provide the better understanding on the inhibition mechanism of arylamide derivatives which is the important information for designing novel antitubular agent.

Introduction

Many compounds functioning as direct InhA inhibitors have been discovered and identified [1-2] to overcome the INH resistance associated with mutations in the KatG enzyme. A series of arylamides is one of the novel classes of potent InhA inhibitors that circumvent the resistance mechanism to INH prodrug [3]. The enoyl acyl carrier protein reductase (InhA) from M. tuberculosis has been identified as the target enzyme of arylamide derivatives. InhA participates in the elongation cycle of the mycolic acid biosynthesis. This enzyme utilizes NADH to reduce the trans double bond between positions C2 and C3 of a fatty acyl chain linked to the acyl carrier protein as shown in Figure 1. Arylamide derivatives are possible to bind to both of InhA-NADH and InhA-NAD+ forms. In order to examine which form of the enzyme arylamides more prefer, molecular dynamics (MD) simulations of an arylamide derivative bound to both of InhA-NADH and InhA-NAD+ were performed. The

obtained results should provide the better understanding on the inhibition mechanism of arylamide derivatives leading to design the novel antitubular agent.

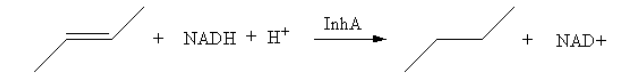


Figure 1. Enzyme reaction of InhA

Materials and Methods

Model setup: Two X-ray structures of InhA complexed with arylamide and substrate with pdb codes of 1P44 and 1BVR, respectively, were taken as the starting structures for MD simulations. Amber03 force field was used for InhA and Gaff force field was used for substrate, arylamide P3, NADH and NAD+. Whole system was solvated by TIP3P water using a truncated octahedron periodic box with a spacing distance of 10 Å around the molecule. Na counter ions were added to neutralize the charge.

Minimization and MD simulation: Molecular dynamic simulations were performed using AMBER10. A steepest descents energy minimization with position restraint was performed using the Sander program to relieve bad steric interactions. Non-bonded cutoff was set at 8 Å. The force of 500.0 kcal/mol was used to restrain the atom positions. Then whole system without restraint condition was minimized. Then, the system was heat from 0 K to 100 K with 10 ps simulation time and then this system was heat from 100 K to 200 using the same simulation time. The system was heat from 200 K to 300 K with 10 ps simulation time. Finally, production run was carried out for 3 ns at 300 K under constant volume condition.

MM-PBSA: MM-PBSA method was employed to calculate the binding free energy of system. All energetic analysis were done using a single trajectory approach. All water molecules and ions were removed before MM-PBSA was calculated. Snapshots of 1.5-3 ns were taken for MM-PBSA calculations.

Figure 2. The chemical structure of arylamide P3

Results and Discussion

Structural stability during MD simulations

The root mean square deviations (RMSD) of all atoms of InhA in two complexes, InhA/NADH/P3 and InhA/NAD+/P3 reach the plateau characteristic at the early time. Compound P3 complexed with InhA/NAD+ show more flexible than that complexed with InhA/NADH as shown in Figure 3.

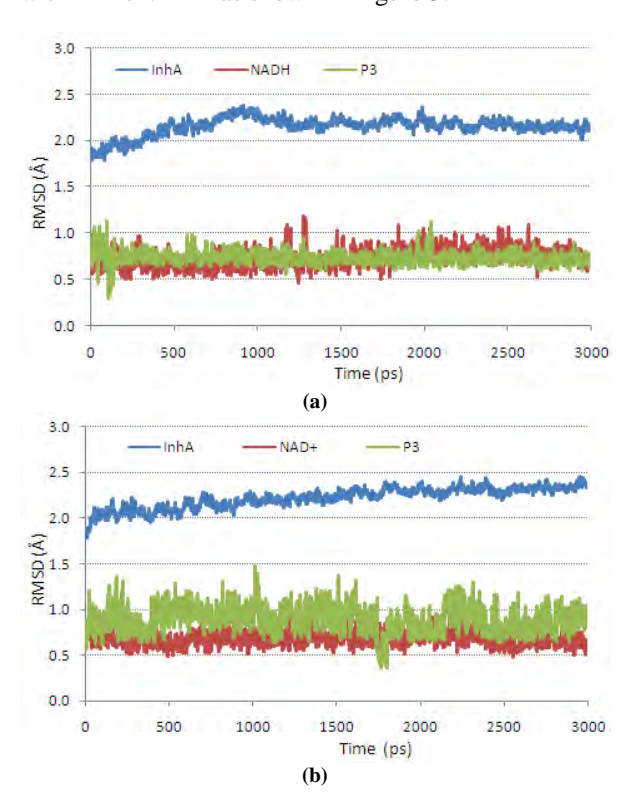


Figure 3. RMSD of all atoms of each molecule in complexes of InhA/NADH/P3 (a), InhA/NAD+/P3 (b)

The complexed structure

The MD structures of InhA/NADH/P3 and InhA/NAD+/P3 are shown in Figure 4. The binding modes of arylamide P3 in both structures are similar. However, two main hydrogen bond distances of arylamide P3 in InhA/NADH are longer than that in InhA/NAD+ as shown in Figure 5.

The binding free energy

The estimate binding free energies of two systems of InhA/NADH/P3 and InhA/NAD+/P3 were calculated by MM-PBSA method (Table 1). The

calculated binding energies of arylamide P3 in InhA/NADH and InhA/NAD+ complexes are -11.83 and -17.59 kcal/mol, respectively. This result indicates that arylamide P3 more prefers to bind in InhA/NAD+ form than InhA/NAD+ form. According to enzyme reaction of InhA in Figure 1, arylamide P3 should bind InhA after InhA catalyzed the reduction of 2-transenoyl-ACP substrate.

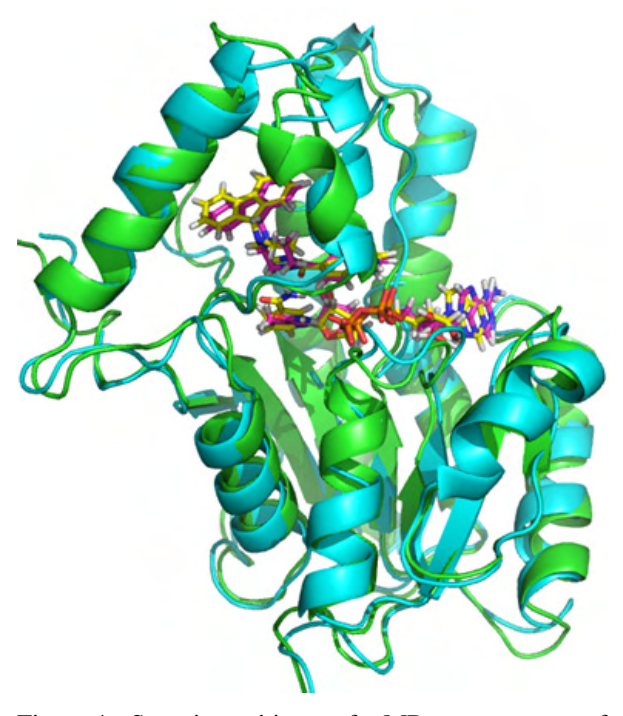


Figure 4. Superimposition of MD structures of InhA/NADH/P3 (cyan) and InhA/NAD+/P3 (green)

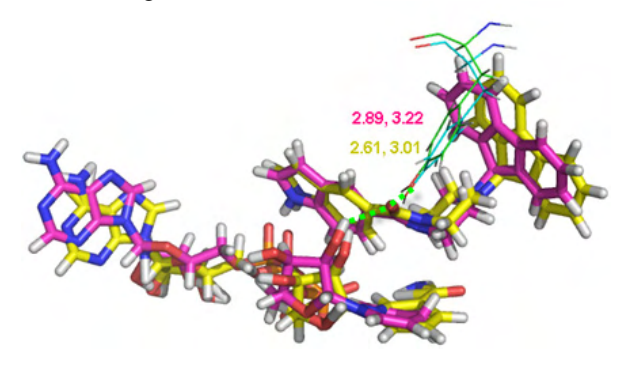


Figure 5. Two main hydrogen bond distances of arylamide P3 in InhA/NADH (pink) and InhA/NAD+ (yellow)

Table 1: The calculated binding free energy obtained from MM-PBSA method

System	Binding free energy (kcal/mol)
InhA/NADH/P3	-11.83
InhA/NAD+/P3	-17.59

Conclusions

MD simulations with AMBER program are successfully to simulate the binding mode of arylamide P3 in both forms of InhA/NADH and InhA/NADH. Based on MM-PBSA method, an arylamide derivative complexed with InhA/NAD+ represents the binding free energy higher than that complexed with InhA/NADH. This result indicates that arylamide inhibitors prefer to bind with InhA/NAD+ form. Therefore, the obtained results provide insights into the inhibition mechanism of arylamide inhibitors on InhA function which may be useful for rational drug design of antituberculosis agent.

- [1] J.S. Freundlich, F. Wang, C. Vilchèze, G. Gulten, R. Langley, G.A. Schiehser, D.P. Jacobus, W.R. Jacobs Jr, J.C. Sacchettini. *Chem. Med. Chem.* 4 (2009), pp. 241-248.
- [2] C.W. am Ende, S.E. Knudson, N. Liu, J. Childs, T.J. Sullivan, M. Boyne, H. Xu, Y. Gegina, D.L. Knudson, F. Johnson, C.A. Peloquin, R.A. Slayden, P.J. Tonge. *Bioorg. Med. Chem. Lett.* 18 (2008), pp. 3029-3033.
- [3] X. He, A. Alian, P.R. Ortiz de Montellano. *Bioorg. Med. Chem.* **15** (2007), pp. 6649–665.

Study on the Binding Mode of Azanaphthoquinone Annelated Pyrrole Derivatives as Anti-Cancer Agent in DNA Duplex Using MD Simulations

P. Pungpo¹*, A. Punkvang¹, A. Kumkong¹, P. Khamsri¹, P. Saparpakorn², N. Pongprom¹, P. Wolschann³ and S. Hannongbua²

¹Department of Chemistry, Faculty of Science, Ubonratchathani University, Ubonratchathani, Thailand ²Department of Chemistry, Faculty of Science, Kasetsart University, Chatuchak, Bangkok, Thailand ³Institute for Theoretical Chemistry, University of Vienna, Vienna, Austria

* *E-mail: pornpan_ubu@yahoo.com

pyrrole Abstract: Azanaphthoquinone annelated derivatives, a class of the synthetic DNA intercalating agent, exhibit cytotoxic activity against tumor cell lines. However, the binding modes of these anti-cancer agents have not been established. In order to predict the potential binding modes of these compounds in DNA binding site, molecular dynamics (MD) simulations with AMBER program were performed. Moreover, MM-PBSA method was employed to calculate the binding free energy of azanaphthoquinone annelated pyrrole derivatives in DNA binding site. Based on MD simulations, azanaphthoquinone annelated pyrrole scaffolds of azanaphthoquinone annelated pyrrole derivatives are inserted into two base pair steps of cytosine (C) and guanine (G). These scaffolds form π - π interactions with base pairs of C and G. The hydrogen bond donor group at the R substituent could form hydrogen bond interactions with carbonyl oxygens and nitrogen atoms of C and G. Based on the calculated binding free energy, the hydrogen bond interaction of R substituent could enhance the binding affinity of azanaphthoquinone annelated pyrrole derivatives in DNA duplex. Moreover, the long sidechain of R substituents reinforces the binding of these compounds. Therefore, the obtained results from this study should be helpful for understanding the binding modes and the crucial interactions of azanaphthoquinone annelated pyrrole derivatives in DNA binding site.

Introduction

Azanaphthoquinone annelated pyrrole derivatives act as the synthetic DNA intercalating agent [1-2]. They were synthesized and screened for cytotoxic activity against at least four different cell lines KB/HeLa, NCI-H460, SKOV-3 and SF-268. They exhibit promising cytotocity. However, the binding modes of these anti-cancer agents have not been established. In order to predict the potential binding modes of these compounds in DNA binding site, molecular dynamics (MD) simulations with AMBER program were performed. Moreover, MM-PBSA method was employed to calculate the binding free energy of azanaphthoquinone annelated pyrrole derivatives in DNA binding site.

Materials and Methods

Material: The X-ray crystal structure of anti-cancer complexed with DNA duplex (pdb code of 2BG9) was taken for this study. Azanaphthoquinone annelated pyrrole derivatives complexed with DNA obtained from docking calculations was served as the initial structure. The chemical structures and inhibition activities of azanaphthoquinone annelated pyrrole derivatives are shown in Table 1.

Table 1: The chemical structures and inhibition activities of azanaphthoquinone annelated pyrrole derivatives

Cpd.	Structure	KB (IC ₅₀)
	N O	N R
1	$R = -CH_2CH_2N(CH_3)_2$	11.04
	R O N O N O H ₃ G	N-CH ₃
2	$R = -CH_2CH_2OH$	0.66

Minimization and MD simulation: Amber03 and Gaff force fields were used for DNA and anti-cancer, respectively. Whole system was solvated by TIP3P water using a truncated octahedron periodic box with a spacing distance of 10 Å around the molecule. 10 Na+counter ions were added to neutralize the charge. A steepest descents energy minimization with position restraint was performed using the Sander program to relieve bad steric interactions. Non-bonded cutoff was set at 8 Å. The force of 500.0 kcal/mol was used to restrain the atom positions. Then whole system

without restraint condition was minimized. The system was heat from 0 K to 100 K, 100 K to 200 and 200 K to 300 K with time step of 10 ps. The production run was carried out at 300 K under constant volume condition.

MM-PBSA: MM-PBSA method was employed to calculate the binding free energy of system. All energetic analysis were done using a single trajectory approach. All water molecules and ions were removed before MM-PBSA was calculated. Snapshots of 2 ns were taken for MM-PBSA calculations.

Results and Discussion

Structural stability during MD simulations

10 ns MD simulations compounds 1, 2 and 3 were performed. The root mean square deviations (RMSD) as a function of the simulation time of each complex with respect to the starting structure were analyzed and are shown in Figures 1 and 2. The RMSD curves of DNA complexed with compounds 1 and 2 become flat in the early time, indicating that these systems reach equilibrium. However, both of ligand and DNA structures show more flexibility.

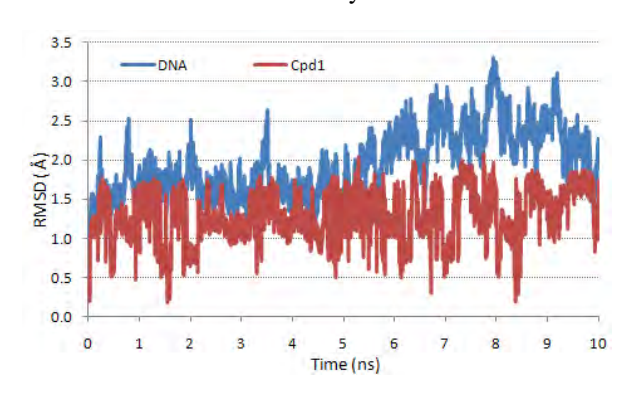


Figure 1. RMSD of DNA and compound 1

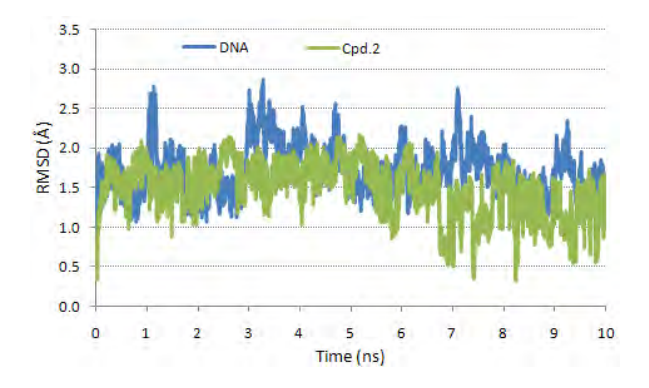


Figure 2. RMSD of DNA and compound 2

The binding modes of anti-cancer obtained from MD simulations

The binding modes of compounds 1 and 2 are shown in Figures 3 and 4, respectively. The azanaphthoquinone annelated pyrrole scaffolds of compounds 1 and 2 form π - π interactions with base pair of C and G. Two hydrogen bonds of the R substituent of compound 2 with base C and sugar of

base C could be observed, whereas those interactions could not be found in compound 1.

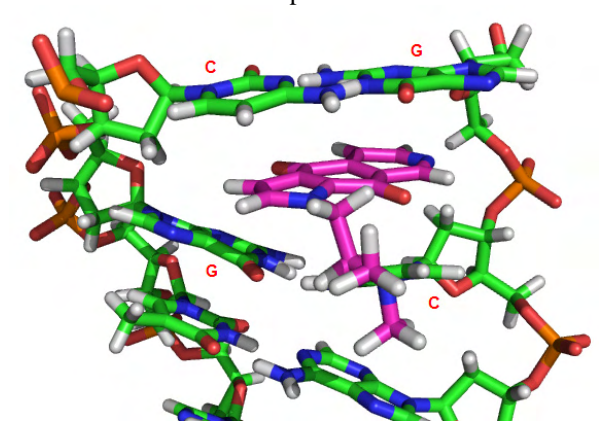


Figure 3. The binding mode of compound 1 in DNA duplex obtained from MD simulation

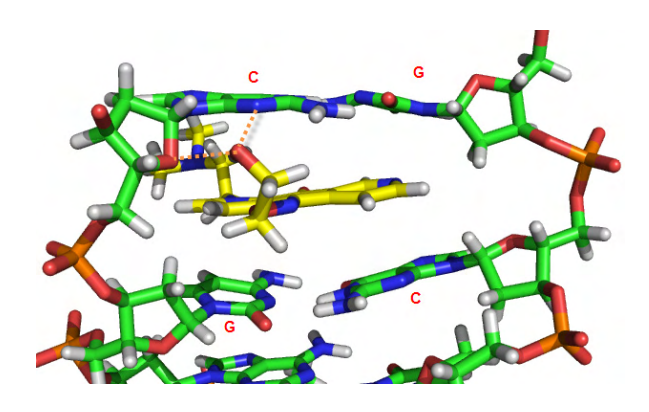


Figure 4. The binding mode of compound 2 in DNA duplex obtained from MD simulation

The binding free energy

The binding free energies of all compounds calculated using MM-PBSA method are shown Table 2. Compound 2 shows the binding free energy higher than that of compound 1 which correlate with their activities. This result suggests that the hydrogen bond interactions of the R substituent could enhance the binding affinity of azanaphthoquinone annelated pyrrole derivatives.

Table 2. The binding free energy calculated by MM-PBSA method

System	ΔG (kcal/mol)
Cpd. 1	-9.35
Cpd. 2	-11.55

Conclusions

The potential binding modes of azanaphthoquinone annelated pyrrole derivatives in DNA binding site are successfully carried out by MD simulation. The azanaphthoquinone annelated pyrrole scaffolds of

azanaphthoquinone annelated pyrrole derivatives are inserted into two base pair steps of cytosine (C) and guanine (G) and form $\pi\text{-}\pi$ interactions with these base pairs. The hydrogen bond interactions of R substituent could enhance the binding affinity of azanaphthoquinone annelated pyrrole derivatives in DNA duplex which lead to increase the biological activity. Therefore, the obtained results are fruitful information for designing new and more cytotoxic activity anti-cancer agents.

- [1] N. Pongprom, G. M ller, P. Schmidt, W. Holzer, H. Spreitzer, Monatsh Chem. **140** (2009), pp.309–313.
- [2] K. Shanab, N. Pongprom, E. Wulz, W. Holzer, H. Spreitzer, P. Schmidt, B. Aicher, G. Muller, E. Guntherb, Bio. Med. Chem. Lett., 17 (2007), pp.6091–6095

MD-ONIOM2 of Amines in DMSO for Full QM-Like Predictions Without the Full QM Cost

V. Vailikhit^{1*}, W. J. Holzschuh¹, P. Akayothin¹, S. Nithakorn¹ and S. Hannongbua²

¹ Faculty of Liberal Arts and Science, Kasetsart University Kamphaeng Saen, Nakhon Pathom THAILAND 73140

² Department of Chemistry, Faculty of Science, Kasetsart University Jatuchak, Bangkok, THAILAND 10900

*Corresponding Author: veeramol.v@ku.ac.th

Abstract: MD-ONIOM2 is compared to full quantum mechanical modelling for different amines in solution with the aprotic, highly polar solvent DMSO. This involves hydrogen bonding which complicates the system and causes significant deshielding of the amine hydrogen atoms and strongly affects their 1H-NMR chemical shifts. Initially, the anti-HIV drug nevirapine in DMSO was modelled as a real-world test-case. Subsequently, four amines, aniline, N-methylaniline, acetamide and valerolactam, were also modelled to show that MD-ONIOM2 is more generally applicable.

Tested against experimental results, it was found that full quantum mechanical "gas-phase" modelling gave good predictions for all protons except acidic amine hydrogen atoms. MD-ONIOM2 is shown to use a very good compromise in that it predicts all the hydrogen 1H-NMR chemical shifts well, but is computationally cheap enough to run in a reasonable time on a standard PC because the solvation shell is treated at a low level of theory.

MD-ONIOM2 also has the advantage of modelling dynamic systems, allowing the solvent molecules to break and form hydrogen bonds constantly, and even to exchange solvent molecules over time. This helps to define the solvation shell around the solute molecule, the amine, that is the basis for the different levels of theory in ONIOM. As a bonus, the IR spectra of the five compounds were also predicted and showed the expected shift in the N-H stretching bands to lower wavenumber in the DMSO solution.

Introduction

Computer modelling is an indispensible tool of modern science, and in chemistry has many uses in understanding and interpreting real systems and experimental data [1,2]. One fundamental use is the modelling of spectra, in particular NMR and infrared spectra, which may have complicated forms but are especially useful for analysis of functional groups and bonds in molecules. Modelling helps in the interpretation of complex absorption peaks, assisting in the assignment to the appropriate functional groups, bonds or atoms.

Conversely, measured spectra can be used to check the accuracy of models and the predictions they make. Obviously, if there is a significant discrepancy between an experimentally measured spectrum and a modelled one, the model is to be considered to be inaccurate or inadequate.

Modelling must often balance accuracy and detail in a system against the computational cost of calculations. That is, better modelling results require more computer resources and/or more time to produce. The researcher usually has to decide what level of accuracy is acceptable for the study being undertaken and choose the appropriate level of detail in the model.

A common problem in modelling chemical systems is the effect of hydrogen bonding. In spectra, this can be seen as extra deshielding causing ¹H-NMR shifts to significantly higher ppm values for the affected hydrogen atoms, and IR shifts to lower wavenumber for the vibrational modes of the bonds associated with the same hydrogen atom [3,4].

In the popular Gaussian03 software package, the basic model used to generate spectra is the "gas-phase" model. This is an isolate molecule treated with a high level of quantum mechanical (QM) theory. However, previous work has shown that, while this model generates acceptable ¹H-NMR spectra predictions for most hydrogen atoms, the NMR shifts of any hydrogen atoms involved in hydrogen bonding are significantly underestimated. This model, for example, may be adequate for a compound dissolved in a non-polar solvent such as chloroform as there is minimal interaction between solute and solvent molecules, and the solute molecule can be considered to be effectively isolated.

However, for a compound with acidic hydrogen atoms in a polar solvent such as DMSO, there is significant interaction with the formation of hydrogen bonds and subsequent extra deshielding that the standard gas-phase model does not incorporate. This deficiency can be overcome by including solvent molecules in the model.

In the work reported here, one solute molecule of interest is added to a box of solvent molecules and molecular dynamics (MD) used to model the interactions between them. This shows the effective solvation shell which is used to determine the cut-off for selecting solvent molecules to include in the subsequent QM calculations. Again, this uses the gasphase option of Gaussian03 but with Our own *N*-layered Integrated molecular Orbital and Molecular

mechanics, with N=2, (ONIOM2). This method applies the same high level of quantum theory to the solute molecule as the standard gas-phase. However, as shown in Figure 1, the solvent molecules included in the solvation shell are treated at a lower level of theory, minimising the extra time required to complete calculations. The results will show that this gives well simulated ¹H-NMR and IR spectra of several amines in DMSO.

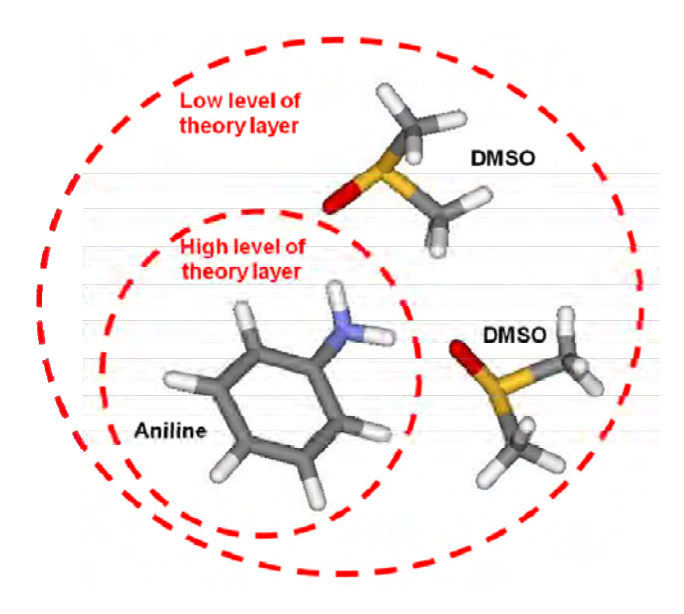


Figure 1. Schematic of ONIOM2 for aniline and its solvation shell. The aniline is treated at a high level of quantum theory, and the bonded DMSO at a low level.

Materials and Methods

Original work [5] on modelling the anti-HIV drug nevirapine in DMSO showed that, compared to the standard gas-phase model, MD-ONIOM2 was able to better predict the NMR shift of the acidic amine hydrogen that forms hydrogen bonds to the polar DMSO solvent. This led to the modelling of four representative, simple amines to show the general applicability of MD-ONIOM2. The amines aniline, N-methylaniline, acetamide and valerolactam were chosen because experimental NMR data are available for them, and they have variously one or two acidic amine hydrogen atoms and different neighbouring functional groups. Also, acetamide has *cis-* and *trans*-acidic hydrogen atoms, due to its resonance structure, which a good model should distinguish.

For the gas-phase model, a single solute molecule as used to generate the $^{1}\text{H-NMR}$ chemical shifts using the Gaussian03 software package at B3LYP/6-311++ G^{**} //B3LYP/6-31 G^{**} , with TMS as the standard NMR reference. The IR spectra were calculated at B3LYP/6-31 G^{*} // B3LYP/6-31 G^{**} .

Modelling of the solute molecules was performed in two stages: first MD of the molecule in a box of solvent molecules, followed by ONIOM2 of sample snapshots from the MD stage to calculate ¹H-NMR

shifts and IR spectra. This was described in detail previously [5] and only a summary is given below.

The AMBER9 software package was used for the MD with this work. Each solute molecule, as DMSO beforehand, was generated with the SYBYL7.0 program [6] and optimised with the Gaussian03 program [7] at B3LYP/6-31G** level. The molecule electrostatic potential (ESP) was generated using single point calculation at HF/6-31G* level with the Merz–Kollman–Shigh charge scheme (MK). The Antechamber module was used to generate the ''prep' input file and atomic charge, using the AMBER force-field parameters [8].

The solute molecule model was placed in a box of DMSO molecules [5] for the MD run and a radial distribution function (RDF) was used to determine the average distribution of DMSO-oxygen atoms around the acidic protons. From the RDF, the solvation shell could be determined and the cut-off set to provide the discrete models for ONIOM2 (Figure 1). Because of the dynamic nature of hydrogen bond formation and breaking, 10 snapshots were taken every 100 ps during the final 1 ns of the production period for the ONIOM2 modelling with the Gaussian03 software B3LYP/6-311++G**//B3LYP/6at 31G**:HF/STO-3G//PM3, using TMS as the standard NMR reference. The predicted 1H NMR shifts from each of the ten snapshots were averaged at the end.

The IR spectra were calculated at $B3LYP/6-31G^*//B3LYP/6-31G^{**}$.

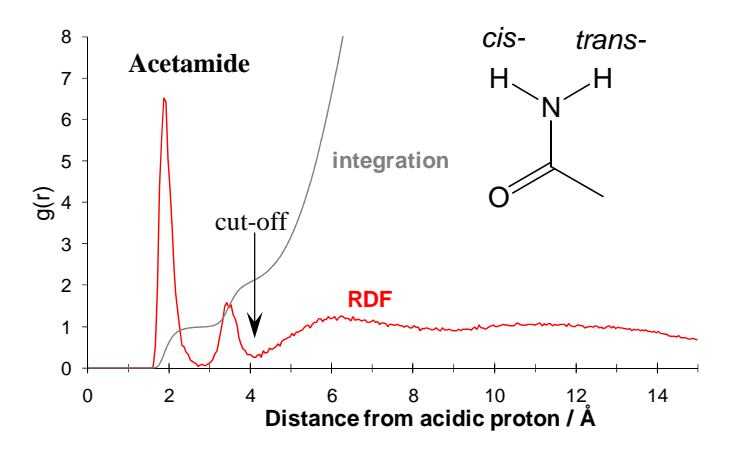


Figure 2. An example of a RDF from a MD simulation. This shows the distribution of DMSO-oxygen atoms around one of the acidic hydrogen atoms in acetamide.

Results and Discussion

The stability of the MD simulations was checked by observing the root mean square deviation (RMSD) of heavy atoms in the solute molecules and the total energy of the system.

For the MD of each solute molecule, the RDF of the DMSO-oxygen atoms around the acidic proton gave the radius of the solvation shell, that is, the distance within which the DMSO is bonded to the proton. This was obvious from peaks in the RDF, and integration of the area under the peaks showed that on average only one DMSO molecule was bonded to each acidic proton. Figure 2 shows the RDF of acetamide as an example. The solvation shell radius was used as the cut-off for the ONIOM2 model with all the DMSO molecules that were completely outside the radius excluded. The cut-off radius was approximately 3Å for the molecules with only one acidic proton, and approximately 4Å for those with two acidic protons.

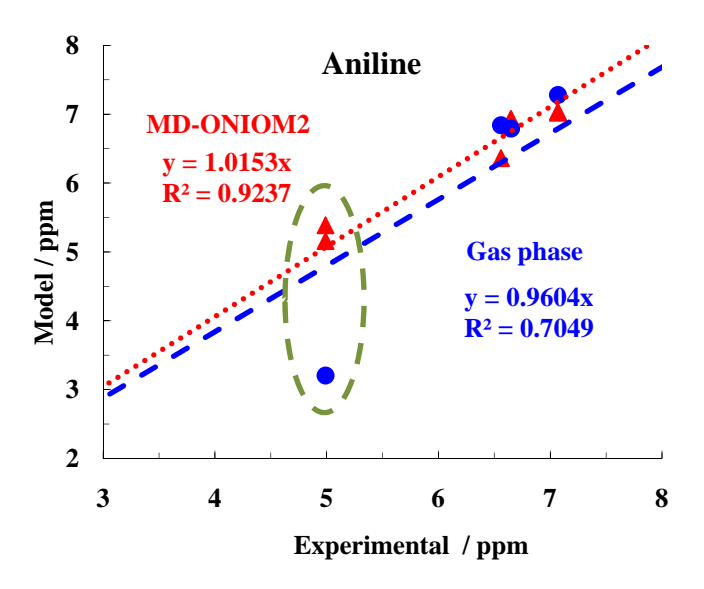


Figure 3. Predicted NMR shifts plotted against experimental values are shown for aniline. The slope and correlation are also given for least squares regression lines which are constrained to go through the origin. The oval highlights the acidic hydrogens.

Table 1. The experimentally measured and the predicted NMR shifts of the acidic hydrogens of the five amine compounds studied. The difference = (experimental value - predicted value) is given for easier comparison.

	Expt.	ONIOM2		gas-phase	
	ppm	ppm	difference	ppm	difference
Nevirapine	9.86	10.93	-1.07	6.43	3.43
N-methylaniline	5.52	5.00	0.52	3.35	2.17
Aniline	4.99 4.99	5.16 5.39	-0.17 -0.40	3.20 3.20	1.79 1.79
Valerolactam	7.34	6.96	0.38	4.62	2.72
Acetamide	6.70 7.30	6.28 6.85	0.42 0.45	4.38 4.74	2.32 2.56

The ONIOM2 calculated NMR shifts for the acidic amine protons can be seen in Table 1. Also seen are the experimental NMR shift values, and the corresponding gas-phase model results. The differences from the experimental value are shown for clarity. The two models give similar predictions of NMR shifts for all the non-acidic protons. However, for the acidic amine protons, the gas-phase model gives the poor predictions and ONIOM2 better ones.

This can be seen in Table 2 which shows the linear correlation between the predicted shifts and the experimentally measured shifts of all the hydrogens. Least squares regression analysis was used to calculate the slope and correlation for a line fitted to each set of points as seen in the example of aniline in Figure 3. The regression line is constrained to go through the origin as both modelled and experimental shifts are relative to TMS with a shift of 0 ppm.

Table 2. For plots of predicted NMR shifts against experimental data, the slope and correlation are shown for least squares regression lines which are constrained to go through the origin, since all shifts are relative to TMS. It can be seen that the MD-ONIOM2 results are very close to the ideal line which would have m = 1 and $R^2 = 1$. (See Figure 3.)

	ONI	OM2	gas-phase	
	m	\mathbb{R}^2	m	\mathbb{R}^2
Nevirapine	1.0002	0.9968	0.9383	0.9239
N-methylaniline	1.0126	0.9847	0.9841	0.8543
Aniline	1.0153	0.9237	0.9604	0.7049
Valerolactam	0.9924	0.9869	0.8145	0.4740
Acetamide	0.9398	0.9997	0.6815	0.8726

For a perfect model, the resultant points would lie on a line with a slope, m=1, and correlation, $R^2=1$. MD-ONIOM2 gives results close to the ideal. The gasphase model consistently gives shifts for the acid hydrogens that are too low. It should also be noted that the *cis*- and *trans*- hydrogens in acetamide are also well modelled by ONIOM2 and different values for each predicted. Additionally, either acidic hydrogen can be chosen as the centre for the RDF as all the bonded DMSO molecules will still be observed and the same snapshots used in ONIOM2

Table 3. Position of N-H stretching for simulated IR spectra showing the shift in ONIOM2 to lower wavenumber.

	ONIOM2 /cm ⁻¹		gas-phase /cm ⁻¹
Nevirapine	3135		3459
N-methylaniline	3558		3670
Aniline	3590	asym.	3778
	3473	sym.	3651
Valerolactam	3481		3601
Acetamide	3602	asym.	3749
	3397	sym.	3616

Comparing the simulated IR spectra of nevirapine to the experimental spectrum of the pure solid (KBr pellet, Bruker FT-IR IF66S/S) shows that the ONIOM2 model predicts the shift to lower wavenumber that is expected for N-H stretching. This is due to the hydrogen bonding interactions present. Table 3 shows the values of N-H stretching for all five

amines. The shift to lower wavenumber is seen in all cases.

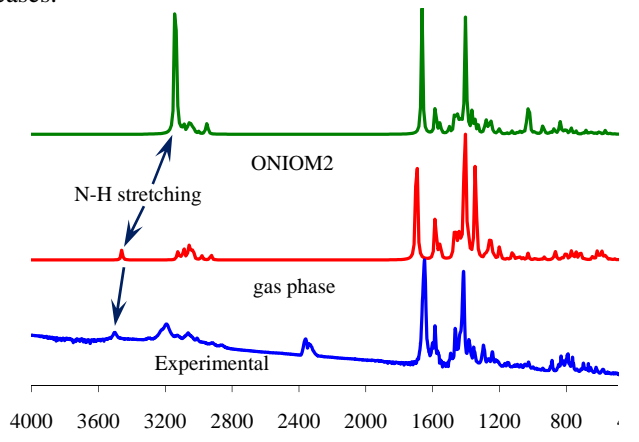


Figure 4. Comparison of IR spectra of nevirapine. Note that the gas-phase matches the experimental spectrum of pure nevirapine well, but ONIOMS shows the shift in N-H stretching expected due to H-bonding.

Conclusions

Using a high level of quantum mechanical theory to model an isolated molecule in the "gas-phase" gives good accuracy, and can generate acceptable ¹H-NMR and IR spectra, if no hydrogen bonding is present in the system.

If hydrogen bonding is present, the resulting model is significantly inaccurate for the acidic hydrogen atoms. However, it was shown that including the hydrogen bonding, for example, using MD to determine the solvation shell around a solute molecule, and using a low level of theory to describe this part gives good accuracy. It particular, the shift in ¹H-NMR and IR spectra are more realistically predicted.

- T Helgaker, M Jaszuński and K Ruud, Chem. Rev. 99 (1999), 293–352.
- [2] S. Saen-Oon, S; Hannongbua, S and P. Wolschann, J Chem Inf Comput Sci 43(5) (2003), 1412 - 1422.
- [3] J. S. Lomas, A. Adenier, C. Cordier and J. C. Lacroix, *J. Chem. Soc.*, *Perkin Trans.* **2** (1998), 2647-2652.
- [4] G. O. Dudek, J. Org. Chem. 30 (1965), 548-552.
- [5] V. Vailikhit, W. Treesuwan and S. Hannongbua, J. Mol. Struct. (THEOCHEM) 806 (2007), 99-104.
- [6] SYBYL 7.0, Tripos Associates Inc., 1699 South Hanely Road, Suite 303, ST. Louis, Missouri 63144, USA.
- [7] M.J. Frisch et al., Gaussian03, Inc., Wallingford CT,
- [8] D.A. Case, T.A. Darden, T.E. Cheatham III, C.L. Simmerling, J. Wang, R.E. Duke, R. Luo, K.M. Merz, D.A. Pearlman, M. Crowley, R.C. Walker, W. Zhang, B. Wang, S. Hayik, A. Roitberg, G. Seabra, K.F. Wong, F. Paesani, X. Wu, S. Brozell, V. Tsui, H. Gohlke, L. Yang, C. Tan, J. Mongan, V. Hornak, G. Cui, P. Beroza, D.H. Mathews, C. Schafmeister, W.S. Ross, P.A. Kollman, AMBER 9, University of California, San Francisco, 2006.

Theoretical Investigation On Wild Type And L100I/K103N HIV-1 RT Complexed with TMC278, Based on Quantum Mechanical Methods

P. Srivub^{1*}, P. Nokkaew¹ and S. Hannongbua²

¹Faculty of Science and Technology, Rajamangala University of Technology Srivijaya, Nakronsri Thammat, Thailand. ²Center of Nanotechnology and *NANOTECH* Center of Excellence Kasatsart University, Bangkok 10900 Thailand.

* Corresponding Author: pensir_srivub@hotmail.com

Abstract: The interactions between TMC278 and allosteric binding site of HIV-1 reverse transcriptase of wild-type, and with double mutation L100I/K103N were investigated by using three-layered ONIOM calculations. Binding energies were determined and compared to describe the loss of activity of TMC278 with double mutation L100I/K103N HIV-1 RT binding pockets as compared with wild type. The binding energy for the TMC278-L100I/K103N HIV-1 RT complex is less than that of the wild-type complex by approximately 9.71 kcal/mol. This lead to specific interactions between TMC278 and key residues in the two complex structures being investigated. It was found that the attractive interactions between TMC278 and K101, K103 and W229 were reduced compared to the wild-type by 5.92, -4.69 and 3.21 kcal/mol, respectively. It is important to note that hydrogen bonding occurring between TMC278 and K101 was also disturbed. Moreover, N103 in the binding pocket of the L100I/K103N enzyme creates a repulsive interaction with the inhibitor. This confirmed that TMC278 shows higher inhibitory affinities against wild-type than L100I/K103N enzyme. Understanding these particular structural interactions can be useful for the design of inhibitors which are specific to HIV-1 RT allosteric site and with greater potency against mutant types.

Introduction

Human immunodeficiency virus type 1 reverse transcriptase (HIV-1 RT) is one of the most important enzymes in the HIV- 1 life cycle for the development of new anti-AIDS drugs to treat HIV-1 infections, permitting dramatic reduction in viral loads and restoration of the immune system [1]. However, treatments of drug do not eliminate the infection and treatment must be life-long. Drug toxicity and prolonged drug can be lead to the emergence of drugresistant mutant virus that is the key problem to develop new anti-AIDS drugs. Nevirapine fails to treat the Y181C mutation. The K103N mutation confers resistance to efavirenz. The L100I mutation and combined two mutations such as K103N/Y181C and L100I/K103N were fully resistant to almost all NNRTIs drugs including nevirapine, efavirenz and delayirdine. New series of NNRTIs was discover that belong to the diarylpyrimidine(DAPY) family. DAPY compounds, with TMC278 and them derivatives were more potent than efavirenz, nevirapine

delayirdine[2]. Moreover, TMC278 and some them derivatives demonstrated high potency on wild type, single and the double mutant strains as compared with to marked drugs [3]. The wiggling and jiggling of TMC278 compounds help them to retain their potency against mutant HIV-1 viruses [4]. In order to understand the binding stabilities of TMC278 to double mutation such as K103N/Y181C L100I/K103N as compared with wild type at a molecular level, the ONIOM computational approach was employed to calculate binding energy of TMC278 to double mutation as compared with wild type. This approach was useful in previous studies to demonstrate the particular interaction between the NNRTIs and amino acids in the non-nucleoside in inhibitor binding pocket (NNIBP) with wild type, single mutant HIV-1 RT and K103N/Y181C. This understanding will be helpful in the design of new inhibitor especially active against double mutant HIV-1 RT and the better anti-AIDs agents.

Recently, the ONIOM method was successfully used to calculated the interaction energies and the binding energies TIBO[5], nevirapine [6] and efavirenz [7] in the HIV-1 RT binding pocket. The three-layer ONIOM (ONIOM3) method was performed to study the interaction between efavirenz and residues in the binding pocket for K103N/Y181C double mutation HIV-1 RT as compared with wild type. The results showed the calculated binding energy for the efavirenz-K103N/Y181C HIV-1 RT complex is less than that with the wild type complex by approximately 8 kcal/mol [8].

In an attempt to understand the different binding stability of TMC278 to wild type and double mutant L100I/K103N at a molecular level, the ONIOM computational approach was employed [9]. It has not been clearly understood inhibitory effect of TMC278 to the double mutant L100I/K103N HIV-1 RT. The following work describes how the binding interaction of TMC278 to the double mutant L100I/K103N. This understanding will be helpful in the design of new inhibitors especially active against double mutant HIV-1 RT, and thus better anti-AIDs agents. Thus, the understanding of the molecular mechanism of drug resistance can help in the design of better inhibitor.

Computational Methods

System studied

The starting models for calculations were obtained from the X-ray structures of TMC278 bound to HIV-1 RT for the wild-type and L100I/K103N enzymes, listed in the Protein Data Bank with PDB entry codes 2ZD1 and 2ZE2 respectively [2]. The studied binding pocket included residues surrounding the non-nucleoside inhibitor binding pocket (NNIBP) with at least one atom interacting with any of the atoms of the TMC278 inhibitor within the interatomic distance of 7.0 Å These residues of the studied system Pro95, Leu100(Ile100), Lys101, Lys102, Lys103(Asn103), Val106, Val179, Ile180, Tyr181, Gln182, Tyr183, Tyr188, Val189, Gly190, Pro225, Pro226, Phe227, Leu228, Trp229, Leu234, Pro236, Asp237 and Tyr318 from the p66 domain of RT, and Glu138(b) from the 51 domain of RT (Figure 1). All residues were assumed to be in their neutral form. The N- and C-terminal ends of cut residues were capped with an acetyl group (CH₃CO-) and a methyl amino group (-NHCH₃), respectively $[(H_3C-C(=O)-\{NH-CH(-R)-C(=O)\}_n-NH-CH_3)].$ The hydrogen atoms then were added to generate the complete structures and their positions were optimized by the semi-empirical PM3 method as available in the GAUSSIAN 03 program running in Linux on a Pentium IV 3.2 GHz PC [10]. The optimizations were carried out with fixed heavy atoms and the final structures produced were used as the starting geometries for all subsequent calculations.

Figure 1. Model system used for TMC278 bound to allosteric site of HIV-1 RT consisting of 24 residues wild-type HIV-1 RT NNIBP.

Interaction energy calculations

The interaction energies, $E_{(TMC278+Xi)}$, between TMC278 and individual residues, X_i , were calculated at the MP2/6-31G(d,p) levels of theory using the geometry described above. The total interaction energy, INT, can be expressed as: [5]

$$INT_{(EFZ+Xi)} = E_{(EFZ+Xi)} - E_{(EFZ)} - E_{(Xi)},$$
 (1)

where $E_{(TMC278)}$ and $E_{(Xi)}$ are energies of TMC278 and each individual residue, respectively.

Binding energy calculations

Three layer ONIOM calculations were performed to determine the binding energy of TMC278 bound to the double mutant L100I/K103N HIV-1 RT as compared to the wild-type. The total ONIOM energy of the entire system was obtained from five independent energy calculations in ONIOM3 methods as shown in equations (2) [9]. All calculations were carried out using the GAUSSIAN 03 package [10].

More precisely, the binding energy of TMC278 bound to the allosteric pocket of HIV-1 RT was determined using equations (2) for the ONIOM3 methods[6].

$$\begin{split} \Delta E^{ONIOM3} &= E \ [Cpx]_{opt} - E[P]_{opt} - E[L]_{opt} \\ &= \Delta E (High, A) + [\Delta E (Mid, AB) - \Delta E (Mid, A)] + \\ [\Delta E (Low, ABC) - \Delta E (Low, AB)] \\ &= \Delta E \ (High, A) + [\ \Delta \Delta E (Mid, AB-A)] + \\ [\Delta \Delta E (Low, ABC-AB)] \end{split}$$

Where $E[Cpx]_{opt}$ is the total optimized energy of the TMC278-binding pocket complex, Cpx; $E[P]_{opt}$ is the optimized energy of binding pocket; and $E[L]_{opt}$ is the optimized energy of the TMC278 ligand. Also, ΔE (High, A) is the interaction energy in the region A which is treated at the high level of theory, $\Delta \Delta E$ (Mid, AB-A) is the interaction energy from interactions between the regions A and B and is evaluated at the medium level of theory, and $\Delta \Delta E$ (low, ABC-AB) is the interaction energy from interactions between the regions AB and C which is evaluated at the low level of theory.

Comparing binding energy calculations between wildtype and L100I/K103N enzymes

With the ONIOM3 method, the inner layer or interaction region including the TMC278 and Y181 or C181 was treated by the MP2/6-31G(d,p) methods. The medium layer including K101, and L100 or I100 were treated by the B3LYP/6-31G(d,p) method. The remainder residues as outer layer was treated by the PM3 method. For this study, the following models were generated:

ONIOM3 calculation: MP2/6-31G(d,p)[TMC278+(L100I or I100)]:B3LYP/6-31G(d,p) [K101+(K103 or N103)]:PM3[real]

Results and discussion

Interaction energy of TMC278 with individual residues of HIV-1 RT binding pocket

The interaction energies between TMC278 and the individual residues (Xi) of HIV-1 RT binding pocket for wild type and L100I/K103N enzymes were calculated at MP2/6-31G(d,p) levels of theory and are shown in Table 1. As the MP2 method includes the dispersion interactions it is expected to give more

accurate interaction energies than B3LYP [11]. In wild type RT, the main contributions to the interactions with TMC278 come from K101, Y181, F227 and W229 which produce attractive interactions greater than 3 kcal/mol, calculated at MP2/6-31G(d,p) level. Considered in greater detail (Figure 2), Hydrogen bond between a linker nitrogen atom of TMC278 (Figure 3) and the main-chain carbonyl oxygen of K101 causing the strongest interaction: 8.15 kcal/mol at the MP2/6-31G(d,p) method is conserved in the binding of many NNRTIs. The cyanovinyl group is positioned to fit into a hydrophobic tunnel formed by the side chains of amino acid residues F227 and W229 that may explain why TMC278 is most potent of DAPY analogs. TMC278 can be flexible to bind to HIV-1 RT and interacts with aromatic side chains of Y181 and W229 via H- π interaction. The repulsive interactions between TMC278 and residues of the binding pocket for the L100I/K103N enzyme is more than in wild-type. Also, the attractive interactions between TMC278 and K101, K103 and W229 in the L100I/K103N enzyme were reduced to 5.92, 4.69 and 3.21 kcal/mol, respectively (^bΔE in Table 1, MP2/6-31G(d,p) method), compared to the wild type RT. These results indicate that the mutated residues (L100I and K103N) not only reduce binding stability of TMC278, but also induce destabilization in the cavity leading W229 residue to loose contact with the inhibitor.

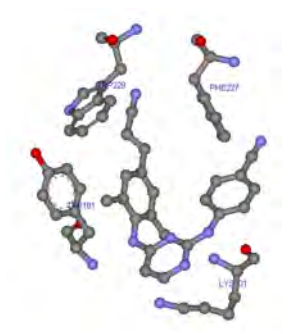


Figure 2. Orientation of TMC278 and residues with largest interactions in the binding pocket of wild-type HIV-1 RT.

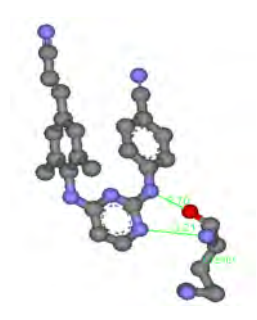


Figure 3. Hydrogen bond between K101 and TMC278

Comparing binding energy calculations between wild type and L100I/K103N enzymes

Among the known NNRT-resistance mutations the L100I/K103N double mutation has the greatest effect on the potency of TMC278. However, TMC278 still inhibits the double mutant at ~ 8 nM EC₅₀ [2]. In the wild type RT/TMC278 structure, L100 is near the center of the pocket and primarily interacts with the central pyrimidine ring of TMC278; K103 is located on the other side of the pyrimidine ring of TMC278 and wild type RT/TMC278 complexes. Comparison of structures of the L100I/K103N mutant RT/TMC278 and wild-type RT/TMC278 complexes (Figure 4) shows that βbranching of I 100 in the L100I mutant lead to steric conflict with the inhibitor if TMC278 were to bind in a conformation similar to that seen in the wild-type RT/TMC278 complex.. To avoid steric conflict with the L100I mutation, TMC278 shift away from I100 and toward N103. In the L100I/K103N complex structure, the amino acid residues in the NNRTIbinding pocket are rearranged to optimize the inhibitor-protein interactions, which contrasts with an earlier proposal that the basis of the effects of the L100I mutation was a loss of interactions with Y181 and Y188[13]. However, analysis of all of the structural results shows that L100I introduces a significant distortion in the NNRTI-binding pocket. NNRTIs that do not have ability to wiggle and jiggle and adapt their shape to the various pockets found in the NNRTI-resistant RTs fail against the known mutants because their binding is susceptible to steric hindrance, because they lose key hydrophobic interactions, or mutations K103N interfere with entry of the NNRTIs into the pocket [2].

From Table 1, the double mutations L100I and K103N lead to the loss of contact between TMC278 and K101, N103 and W229, with the interaction energies between TMC278 and these residues reduced by 5.92, 4.69 and 3.21 kcal/mol, respectively, as compared with the wild-type. Table 2 shows the binding energies for the wild type and L100I/K103N complexes using three-layer ONIOM calculations. It can be seen that the difference in binding energy between wild type and L100I/K103N enzymes is far more significant (10.58 kcal/mol with MP2/6-31G(d,p):B3LYP/6-31G(d,p):PM3 method). The interaction energy in region A and the interaction energy between regions AB and C of the L100I/K103N enzyme are less than wild type by 4.47 and 8.94 kcal/mol, respectively. This indicates that the double mutation L100I/K103N causes a large reduction in attractive interactions between TMC278 and residues in core regions (mutated residue, I100) and in region B (K101 and N103. The mutation L100I introduces a significant distortion in the NNRTI-binding pocket that causes a loss of contact between TMC278 and I100 leading to a weakly attractive interaction in region A (-0.38 kcal/mol MP2/6-31G(d,p):B3LYP/6at 31G(d,p):PM3 calculations)). The mutation K103N interferes with entry of the NNRTIs into the pocket. N103 creates repulsive interactions with TMC278 (Table 1) when compared with the interaction between K103 and TMC278. The mutations in the L100I/K103N enzyme leads to a reduction in the stabilization energy

of the complex and induces destabilization in the cavity by reducing contact between K101 and TMC278. TMC278 shows higher inhibitory affinities with the wild type compared to the double mutation L100I/K103N enzyme.

Table 1. The calculated interaction of TMC278 with individual residues (X_i) from MP2/6-31G(d,p) methods.

		Interaction ener	gy (kcal/mol)
Residue(X _i)	Wild-type	L100/I/K103N	$\Delta \mathrm{E_a}$
PRO95	-0.46	-0.19	-0.27
GLY99	-0.13	-0.67	0.54
LEU100	-1.86	-0.08	-1.78
LYS101	-8.15	-2.23	-5.92
LYS102	-0.13	-0.20	0.07
LYS103 (ASN)	-1.80	2.89	-4.69
VAL106	-0.39	-1.55	1.16
ILE180	-0.92	-0.55	-0.37
TYR181(CYS)	-4.52	-4.03	-0.49
GLN182	-0.37	-0.16	-0.21
TYR183	-0.55	-1.35	0.8
TYR188	-2.24	-4.34	2.1
VAL189	-0.26	-0.40	0.14
GLY190	-0.72	-0.41	-0.31
PRO225	-1.52	-1.19	-0.33
PRO226	-0.60	-0.80	0.2
PHE227	-3.09	-3.78	0.69
LEU228	0.46	0.76	-0.3
TRP229	-5.46	-2.25	-3.21
LEU234	-0.94	1.22	-2.16
PRO236	-2.18	-1.07	-1.11
ASP237	-1.50	-0.11	-1.39
TYR318	-1.50	-1.21	-0.29
GLU138	-2.95	-0.68	-2.27
Total Energy	-41.76	-22.36	-19.42

 $\Delta E_a = E_{wild\text{-type}} - E_{L100I/K103N \; mutant}$

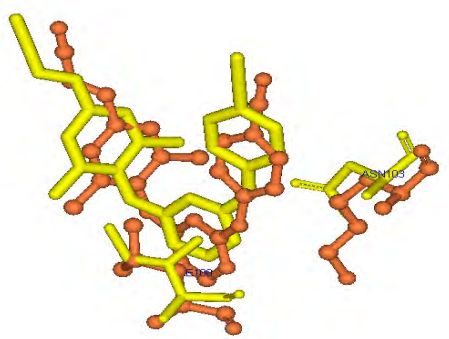


Figure 4. Comparison of structures of TMC278 and mutated residues in the L100I/K103N mutant RT (orange color) as compared with wild-type.

Table 2. Binding energy for the wild type and L100I/K103N mutant HIV-1 RT complexed with TMC278 using

ONIOM3[MP2/6-31G(d,p):B3LYP/6-31G(d,p):PM3].

Energy	Wild-Type	I100L/K103N
ΔE (high, A)	-4.85	-0.38
[ΔΔΕ (M, AB-A)]	-9.27	-0.33
[ΔΔΕ (Low, ABC-C]	-6.17	-6.04
Binding Energy (kcal/mol)	-20.29	-9.71

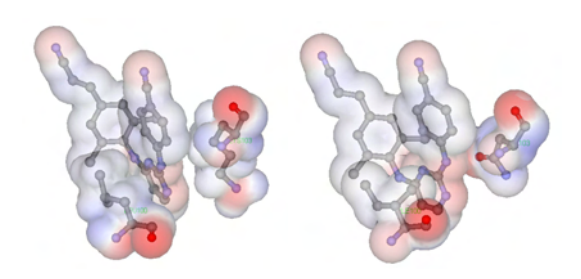


Figure 5. The electrostatic potential is shown on the VDW accessible surface with red for negative and blue for positive values for (a) TMC278 interacting with L100 and K103, and (b) TMC278 interacting with I100 and N103.

Conclusions

Three-layer ONIOM method has been applied to determine the binding energies of TMC278 to L100I/K103N enzyme as compared with the wild type RT. In the L100I/K103N enzyme, the two mutations L100I and K103N eliminate favorable contacts of the hydrocarbon side chain of L100 and K103 with TMC278 leading to reduce the stabilization energy of the complex. It was observed that this then leads to more repulsive interactions between TMC278 with residues of the binding pocket of the L100I/K103N enzyme compared to the wild type. The binding energy for TMC278/L100I/K103N HIV-1 RT complex was calculated to be -9.71 kcal/mol less than that of the wild type complex (-20.29 kcalmol⁻¹). In the binding pocket of L100N/K103N enzyme, hydrogen bonding between TMC278 and K101 was disturbed, and N103 in the binding pocket of L100N/K103N enzyme creates a repulsive interaction with TMC278. This is consistent with the observation that TMC278 shows lower inhibitory affinities against L100I/K103N HIV-1 RT than wild type HIV-1 RT. The understanding interactions involved in binding within the pocket, and the structural changes that occur, can be useful for the design of higher potency inhibitors specific to double mutant enzyme target.

Acknowledgment

This work was supported with grants from the Thailand Research Fund (MRG5280214). The Commission on Higher Education, Ministry of Education and Faculty of Science and Technology, Rajamangala University of Technology Srivijaya are acknowledged for partial financial support. Partial supporting by National Nanotechnology Center (NANOTEC), Ministry of Science and Technology, Thailand, through its program of Center of Excellence Network is grateful.

- [1] A Jacobo-Molina, E. Arnold, *Biochemistry*. **30**(1991), pp. 6351-6361.
- [2] K. Das, J.D. Bauman, A.D. Clark, Y.V. Frenkel, P.J. Lewi, A.J. Shatkin. S.H. Hughes, and E. Arnold, *PNAS*. 105(5)(2008), pp. 1466-1471.
- [3] C. Mordant, B. Schmitt, E. Pasquier, C. Demestre, L. Quequiner, C. Masungi, A. Peeters, L. Smeulders, E. Bettens, K. Hertogs, J. Heeres, P. Lewi, and J. Guillemont, *European Journal of Medicinal Chemistry*. 42 (2007), pp. 567-579.
- [4] E.V. Gyseghen, M. Pendela, L. Baert, J. Rosier, G.V. Klooster, H.D. Man, M.P. Bouche, L.Schueller, P.V. Remoortere, P. Wigerinck, E. Adams, J. Hoogmartens, G V. Mooter, *European Journal of Pharmaceutics and Biopharmaceutics*. 70 (2008), pp. 853-860.
- [5] S. Saen-oon, M. Kuno, S. Hannongbua, *Proteins Struct. Funt. Genet.* **61** (2005), pp. 859-869.
- [6] M. Kuno, S. Hannongbua, K. Morokuma, *Chem, Phy. Lett.* 380 (2003), 456-463.
- [7] P. Nunrium, M. Kuno, S. Saen-oon, S. Hannongbua, Chem. Phys. Lett.. 405 (2005), pp.198-202.
- [8] P. Srivab and S. Hannongbua, *ChemMedChem.* 3 (2008), pp. 1-10.
- [9] K. Morokuma, Philos. Transact. A Math. *Phys. Eng. Sci.* 360 (2002), 1149-1164.
- [10] M. J. Frisch, G. W. Trucks, H. B. Schlegel, G. E. Scuseria, M. A. Robb, J. R. Cheeseman, J. A. Jr. Montgomery, T. Vreven, K. N. Kudin, J. C. Burant, J. M. Millam, S. S. Iyengar, J. Tomasi, V. Barone, B. Mennucci, M. Cossi, G. Scalmani, N. Rega, G. A. Petersson, H. Nakatsuji, M. Hada, M. Ehara, K. Toyota, R. Fukuda, J. Hasegawa, M. Ishida, T. Nakajima, Y. Honda, O. Kitao, H. Nakai, M. Klene, X. Li, J. E. Knox, H. P. Hratchian, J. B. Cross, C. Adamo, J. Jaramillo, R. Gomperts, R. E. Stratmann, O. Yazyev, A. J. Austin, R. Cammi, C. Pomelli, J. W. Ochterski, P. Y. Ayala, K. Morokuma, G. A. Voth, P. Salvador, J. J. Dannenberg, V. G. Zakrzewski, S. Dapprich, A. D. Daniels, M. C. Strain, O. Farkas, D. K. Malick, A. D. Rabuck, K. Raghavachari, J. B. Foresman, J. V. Ortiz, Q. Cui, A. G. Baboul, S. Clifford, J. Cioslowski, B. B. Stefanov, G. Liu, A. Liashenko, P. Piskorz, I. Komaromi, R. L. Martin, D. J. Fox, T. Keith, M. A. Al-Laham, C. Y. Peng, A. Nanayakkara, M. Challacombe, P. M. W. Gill, B. Johnson, W. Chen, M. W. Wong, C. Gonzalez, J. A. Pople, Gaussian 03, revision B.05; Gaussian, Inc.: Pittsburgh, 2003.
- [11] S. Kristya, P. Pulay, Chem. Phys. Lett. 229 (1994), pp. 175–180;
- [12] S. Tsuzuki, H. P. Luthi, J. Chem. Phys. 114(2001), pp. 3949
- [13] J. Ren, et al. J. Mol. Biol. 336(2004), pp. 569-578.

Theoretical Study Of Ethylene Polymerization Catalyzed By The Single-Site Titanium(Iv) Complex Bearing An Asymmetric [ONNO'] Type Salan Ligand

P. Sumrit^{1,2}, T. Nanok^{1,2}, S. Khaubunsongserm³ and P. Hormnirun^{1,2*}

Department of Chemistry, Faculty of Science, Kasetsart University, 50 Phaholyothin Road, Jatuchak, Bangkok 10900, Thailand The Center of Nanotechnology, Kasetsart University, 50 Phaholyothin Road, Jatuchak, Bangkok 10900, Thailand PTT Public Company Limited, PTT Research and Technology Institute, 71 M.2 Paholyothin Road, Sanubtub, Wangnoi, Ayuthaya 13170, Thailand

* Corresponding author. E-mail: fscipph@ku.ac.th

The insertion process of an ethylene monomer into the Ti-methyl bond of the [Ti{(OC₆H₂-4,6-Me₂)NCH₂CH₂-N(OC₆H₂-4,6-Cl₂)}Me]⁺ complex was examined at the density functional B3LYP/6-31G(d,p) level of theory. The results showed that the catalyst investigated was not sidespecific for the first ethylene insertion. The natural bond orbital analyses were performed at the same level of theory to provide insight into the mechanistic details of the propagation insertion and the β -hydrogen transfer reaction. The propagation step was investigated by insertion of the second ethylene monomer. At 298 K, the Gibbs free activation energy for the insertion was estimated to be 7.2 kcal/mol which was considerably lower than that for the β -hydrogen transfer to monomer of 21.2 kcal/mol. The thermodynamically favor of the insertion of the second monomer and the high Gibbs free activation energy of \(\beta\)-hydrogen transfer to monomer suggested that this polymerization system was active and living at ambient temperature.

Introduction

After the discovery of heterogeneous Ziegler-Natta catalysts for olefin polymerization [1,2], the research efforts have concentrated on other classes of homogeneous single-site catalysts (*i.e.* metallocene and post-metellocence) [3-8]. The single-site catalysts have an ability to achieve high stereoselectivity and narrow molecular weight distribution [9]. Their catalytic properties can be controlled by systematic modification of the structure of the catalyst.

In recent years there is a growing interest in Group 4 transition metal catalysts [10-13] and among these, the Group 4 complexes bearing asymmetric [ONNO']-type Salan ligands were recently reported for the olefin polymerization [14,15]. In complement to experimental data, the theoretical studies have extensively played an important role in understanding the mechanistic details of the various steps in the olefin polymerization systems in the past few decades [16-19].

Herein, the mechanistic details of the ethylene insertion and termination steps of the polymerization brought about by an asymmetric [ONNO']-type Salan titanium catalyst was computationally investigated using a density functional theory.

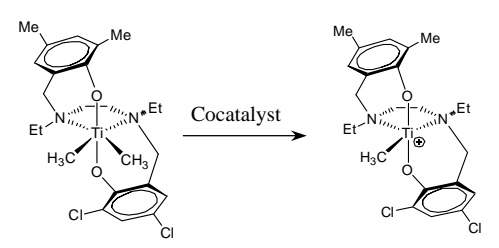


Figure 1. The formation of active species by using the cocatalyst.

Computational Methods

A widely used Becke's three-parameter exchange and Lee, Yang, and Parr's correlation (B3LYP) [20] hybrid density functional theory implemented in the gaussian03 package was applied for the geometry optimization and energy calculation. The Pople style 6-31G(d,p) basis set [21] was assigned to the nonmetal ligand atoms while the titanium transition metal center was treated with the LanL2DZ Hay-Wadt relativistic small-core effective core potential (ECP) and the corresponding split valence double-ζ basis set.[22] The geometry of different stationary points was optimized with no constraints. To verify the nature of the different stationary points, an analytical frequency calculation with a harmonic approximation was carried out at the same level of theory. The thermodynamic Gibbs free energies at 298 K for π complexes, transition states, and products were derived from the harmonic vibrational frequency calculations. Recent theoretical studies showed that solvation had negligible influences on the energetic profile of reaction [23]. These results rationalize our calculations without the solvation corrections.

Results and Discussion

In this study, the catalytic activity of the catalyst after it was activated by the cocatalyst was examined. The effects of the counteranion on the energetic profile were not taken into account. Although the counteraion can play a significant role in the very beginning steps

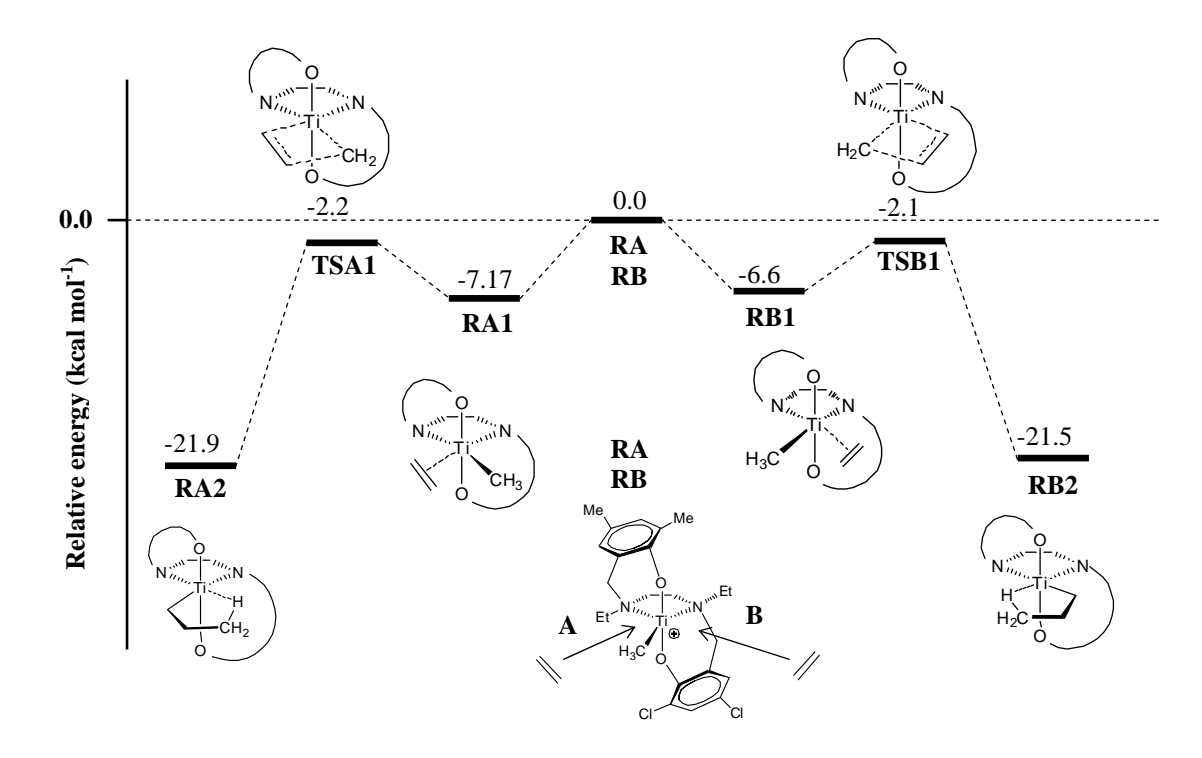


Figure 2. Potential energy profile for the first ethylene insertion incoming from sides A and B.

of ethylene polymerization [23], it is expected to have less important role in the intermediate and long chain propagation steps.

Figure 1 shows the preparation of the coordinatively vacant-site at the titanium metal center of the Ti-ligand complex by the cocatalyst. The generated vacant site will be quickly adsorbed by an ethylene molecule and followed by the insertion into the Ti-methyl bond to regenerate the positively charged vacant site at the titanium metal center. The ongoing insertion of the ethylene monomer into the metal active center will result in the growth in length of polyethylene. However, the uptake of an ethylene molecule may be taken place by the β-hydrogen abstraction instead of the insertion process. As a result, the polymerization reaction will be terminated and the polymer chain will be shortened. Therefore, the computational assessment of the insertion versus the termination competitive processes could provide predictive information on the catalytic activity of the $Ti\{ (OC_6H_2-4,6-Me_2) NCH_2CH_2N (OC_6H_2-4,6-Cl_2) \}$ Me]⁺ complex for ethylene polymerization.

First Ethylene Insertion. The potential energy profile for the first ethylene insertion was illustrated in Figure 2. As can be seen, the positively charged titanium vacant site was taken by an incoming ethylene molecule either from the left-hand side "A" or the right-hand side "B". It was found that the methyl and chloro substituent groups at the *ortho*-positions on the two different phenolate rings had only small effect on the first ethylene insertion. This was reflected by an equivalent in the energy profiles for the ethylene insertion from both sides. The comparable computed binding energies of the π -complex (RA1 and RB1) and the insertion transition state activation

energies (**TSA1** and **TSB1**) indicated that the catalyst was not side-specific for the ethylene insertion. With respect to the isolated ethylene and the active catalyst, the insertion was exothermic and thermodynamically favored. The initiating methyl group was transferred to the coordinated ethylene monomer generating a new initiating propyl group as a corresponding product and resuming a positively charged titanium vacant site. Similar to previous computational studies [24], the terminal C-H bond of the resulting propyl group was oriented in such a way that it was able to form the so called "γ-agostic interaction" with the titanium metal center (**RA2** and **RB2**).

Propagation Insertion versus Termination. From the first insertion study, this catalyst showed no significant side preference for the ethylene uptake. This was also assumed in all other insertion steps along the polymerization pathway. Additionally, to reduce the computational time, the resulting product from the first ethylene insertion was used as a model of the growing short-chain polymer in the propagation step. Although the insertion reaction coordinate favored the formation of the γ -agostic interaction, the more thermodynamically stable β-agostic interaction was adopted as the starting geometry to explore the catalyst efficiency. This structure provided us an equally probabilistic investigation of both the propagation insertion and the β-hydrogen transfer reaction. The roles of the β -agostic interaction in the propagation step were extensively discussed in the literature [24,25].

The optimized geometries together with the natural bond orbitals (NBO) of the π -complex and the transition states for both insertion and termination were depicted in Figure 3. For the π -complex (**RP**),

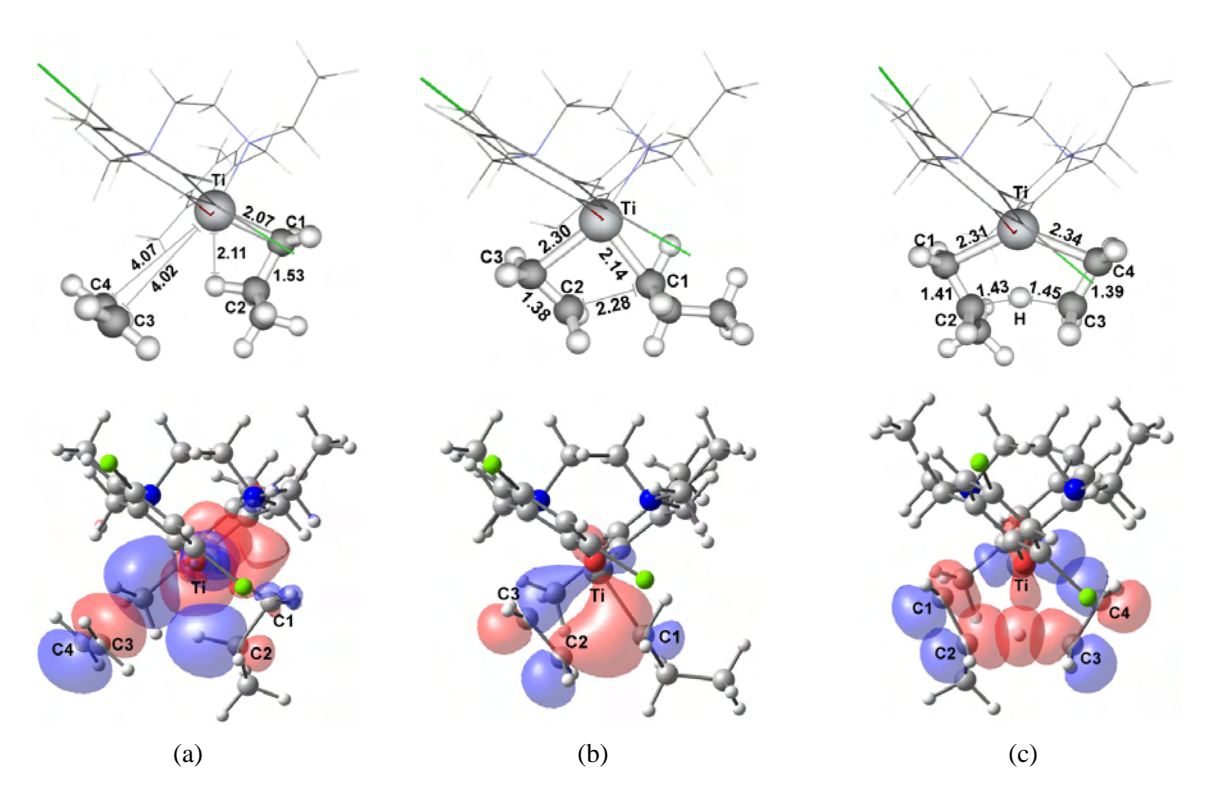


Figure 3. Optimized geometries (top) and natural bond orbitals (bottom) of the π -complex (a) and the transition states for the propagation insertion (b) and the β -hydrogen transfer reaction (c). The signs of the orbital wavefunctions were described by different colors.

the interatomic distances between an ethylene monomer and the titanium metal center were considerably longer than those estimated in the first ethylene insertion (about 3 Å for the Ti---C distances). This was affected by the β -agostic interaction in which the empty d orbitals of the titanium atom were partially filled by electrons from the C-H σ-bonding orbital (see Figure 3a). In the insertion transition state (TSP1), the NBO analysis showed that, while the ethylene π -orbital gave its electrons to the empty d orbitals of the titanium atom, its π^* -orbital was filled by electrons from the Ti-C1 σ -bonding orbital (see Figure 3b). circumstances resulted in the elongation of the Ti-C1 and C2-C3 bond distances and the contact of the C1···C2 and C3···Ti atomic distances. The NBO results of the transition state structure for the β hydrogen transfer reaction (TST1) were rather more complicated than that for the insertion. A number of orbitals that primarily involved in the β-hydrogen transfer were presented in Figure 3c. The overlaps of the orbitals with the same sign (color) wavefunctions from the different atoms resulted in the increase of the electron density between the two atomic centers and the high tendency of the bond formation. It was noted that the β-hydrogen atom was coordinated by three surrounding atoms (Ti, C2, and C3), thus, it could be abstracted by either the ethylene monomer or the metal acceptor. The ethylene C3-C4 bond was lengthened while the propyl C1-C2 bond was shortened. The contact of the Ti···C4 atomic distance and the elongation of Ti...C1 bond length occurred in

a similar fashion to that observed in the insertion transition state.

The catalytic efficiency of the catalyst for ethylene polymerization at ambient temperature was assessed by the relative Gibbs free energy barriers for the ethylene insertion and the β-hydrogen transfer reaction with respect to the π -complex (RP). As shown in Figure 4, the computed Gibbs free energy barrier for the insertion (TSP1) was considerably much lower than that for the β-hydrogen abstraction (TST1). These results revealed that the insertion of the ethylene monomer occurred more favorably over the β-hydrogen transfer process. Thus, polyethylene produced by using this catalyst was expected to have a very high molecular weight, in consistent with the previous experimental achievement of the very high molecular weight poly-1-hexene by using the closely related catalysts [26].

Conclusions

The insertion of ethylene into the titanium complex bearing an asymmetric [ONNO']-type Salan ligand was examined by a density functional theory method. It was found that the catalyst investigated was not side-specific for the ethylene insertion. The propagation insertion was considerably more facile than the β -hydride elimination process. This evidence suggested a living polymerization process and the high molecular weight polyethylene would be produced by this catalyst.

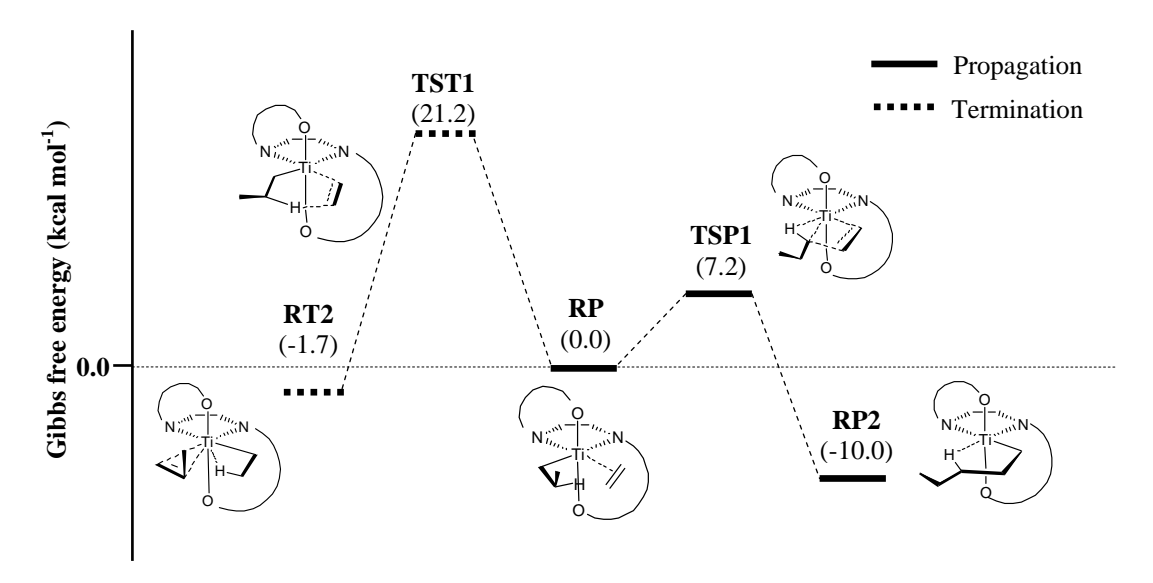


Figure 4. Gibbs free energy profile of propagation versus termination at 298 K.

Acknowledgements

We gratefully acknowledged the Center of Nanotechnology, Kasetsart University for providing the computer facilities. P.S. was financially supported by the Postgraduate Education and Research Program in Petroleum, Petrochemical Technology and Advanced Materials.

- K. Ziegler, E. Holzkamp, H. Breil and H. Martin, *Angew. Chem. Int. Ed.* 67 (1955), pp. 541-547.
- [2] G. Natta, Angew. Chem. Int. Ed. 68 (1956), pp. 393-403
- [3] H.H. Brintzinger, D. Fischer, R. Mülhaupt, B. Rieger and R.M. Waymouth, *Angew. Chem. Int. Ed.* 34 (1995), pp. 1143.-1170.
- [4] W. Kaminsky, J. Chem. Soc., Dalton Trans. (1998), pp. 1413-1418.
- [5] G.G. Hlatky, Coord. Chem. Rev. 181 (1999), pp. 243-296.
- [6] V.C. Gibson and S.K. Spitzmesser, *Chem. Rev.* 103 (2003), pp. 283-315.
- [7] G.J. Domski, J.M. Rose, G.W. Coates, A.D. Bolig and M. Brookhart, *Prog. Polym. Sci.* 32 (2007), pp. 30-92.
- [8] M. Lamberti, M. Mazzeo, D. Pappalardo and C. Pelleccia, Coord. Chem. Rev. 253 (2009), pp. 2082-2097.
- [9] T. Fujita and S. Matsui, *Catalysis Today* 66 (2001) pp. 63-73.
- [10] S. Matsui, M. Mitani, J. Saito, Y.Tohi, H. Makio, N. Matsukawa, Y. Takagi, M. Nitaburu, T. Nakato, H. Tanaka, N. Kashiwa and T. Fujita, J. Am. Chem. Soc. 123 (2001), pp. 6847-6856.
- [11] T. Mastui and T Fujita, Chem. Soc. Rev. 37 (2008), pp. 264-1277.
- [12] C. Capacchione, A. Proto, H. Ebeling, R. Mühaupt, K. Möller, T.P. Spaniol and J. Okuda, *J. Am. Chem. Soc.* 125 (2003), pp. 4964-4965.
- [13] K. Beckerle, R. Manivannan, T.P. Spaniol and J. Okuda, *Organometallics* **25** (2006), pp. 3019-3026.
- [14] A. Cohen, A.Yeori, J. Kopilov, I, Goldberg, and M. Kol, *Chem. Commun.* (2008), pp. 2149-2151.

- [15] A. Cohen, J. Kopilov, I. Goldberg and M. Kol, Organometallics 28 (2009), pp. 1391-1405.
- [16] K. Vanka, Z. Xu and T. Ziegler, Organometallics 23 (2004), pp. 2900-2910.
- [17] M.S.W. Chan and T. Ziegler, Organometallics 19 (2000), pp. 5182-5189.
- [18] T.K. Woo, P.M. Margl and T. Ziegler, *Organometallics* **16** (1997), pp. 3454-3468.
- [19] A. Laine, M. Lonnolahti, T.A. Pakkanen, J.R. Severn, E. Kokko and A. Pakkanen, *Organometallics* 29 (2010), pp. 1541-1550.
- [20] C. Lee, W. Yang and R.G. Paar, *Phys. Rev. B* 37 (1988), pp. 785-789.
- [21] P.C. Hariharan and J.A. Pople, *Theoret. Chimica Acta* **28** (1973), pp.213-222.
- [22] P.J. Hay and W.R. Wadt, J. Chem. Phys. 82 (1985), pp. 299-310.
- [23] A. Motta, I.L. Fragalà and T.J. Marks, *J. Am. Chem. Soc.* **129** (2007), pp. 7327-7338.
- [24] H.A.D. Abreua, W.B.D. Almeidaa, H.A. Duartea, G. Fischerb, T.Heineb, G. Merinob and G. Seifertb, J. Mol. Struct. (THEOCHEM) 762 (2006), pp. 9-15.
- [25] V.L. Cruz, J. Ramos, J.M. Salazar, S.G. Oliva and A.T. Labbé, *Organometallics* 28 (2009), pp. 5889-5895.
- [26] A. Cohen, A. Yeori, J. Kopilov, I. Goldberg and M. Kol, *Chem. Comm.* (2008), pp. 2149-2151.

Encapsulation of Thai Basil Essential Oil by Beta-Cyclodextrins: Molecular Inclusion Complexes Investigation

L. Sitthikornkul, P. Purpiriyapan, S. Tuntisuk and L. Lawtrakul*

School of Bio-Chemical Engineering and Technology, Sirindhorn International Institute of Technology, Thammasat University, 99 Moo 18, Klong Luang, Pathum Thani 12121, Thailand

*E-mail: luckhana@siit.tu.ac.th

Molecular docking technique is used to dock eight aroma compositions, which are found in basil essential oils, into the β -cyclodextrin cavity. The nature of inclusion complexes interactions are studied at a molecular level according to the characteristics of the aroma molecules. One hundred docking runs were performed per structure within the calculations. The model with the lowest energy assigned by molecular docking calculation was selected to further be investigated in details by quantum chemistry calculation at HF/3-21G level. The molecular interactions and binding energies indicated that β -cyclodextrin encapsulates efficiently all of eight flavors in a 1:1 molar ratio.

Introduction

Basil (Ocimum basilicum L.) also known as "horapa" in Thai, is a well known medicinal herb in traditional Thai cuisine. Basil essential oil has many advantages of property which microorganism, anti-free radical, anti-carcinogen, antiinflammation, decrease cholesterol and plague in blood stream, and peptic ulcer treatment [1-2]. Thai basil essential oil contains high amount of estragole and linalool together with anethole, caryophylene, eucalyptol, eugenol, methyl cinnamate, and methyl eugenol [3], their chemical structures are shown in Figure 1. These chemical compositions are effective to the effects of light, oxygen, humidity, and high temperature. For these reasons, encapsulation of flavor is essential to entrap a sensitive substance in cyclodextrin molecule to enhance stability and retention of these compounds. β-cyclodextrin (BCD) is a cyclic oligosaccharide composed with 7 glucopyranose units with a hydrophobic cavity while the rims of the surrounding walls are hydrophilic. BCD is able to form inclusion complex with various hydrophobic with suitable size molecules and then alter physical, chemical, and biological properties of the encapsulated guest molecules. BCDs are natural, nontoxic and slowly biodegradable molecules which are extensively used in pharmaceutical, food, and cosmetics industries [4]. The aim of this work is to study the possibility to use BCD encapsulation of basil essential oils to reduce oxidation, light-induced decomposition, and volatility leading to extended product shelf-life.

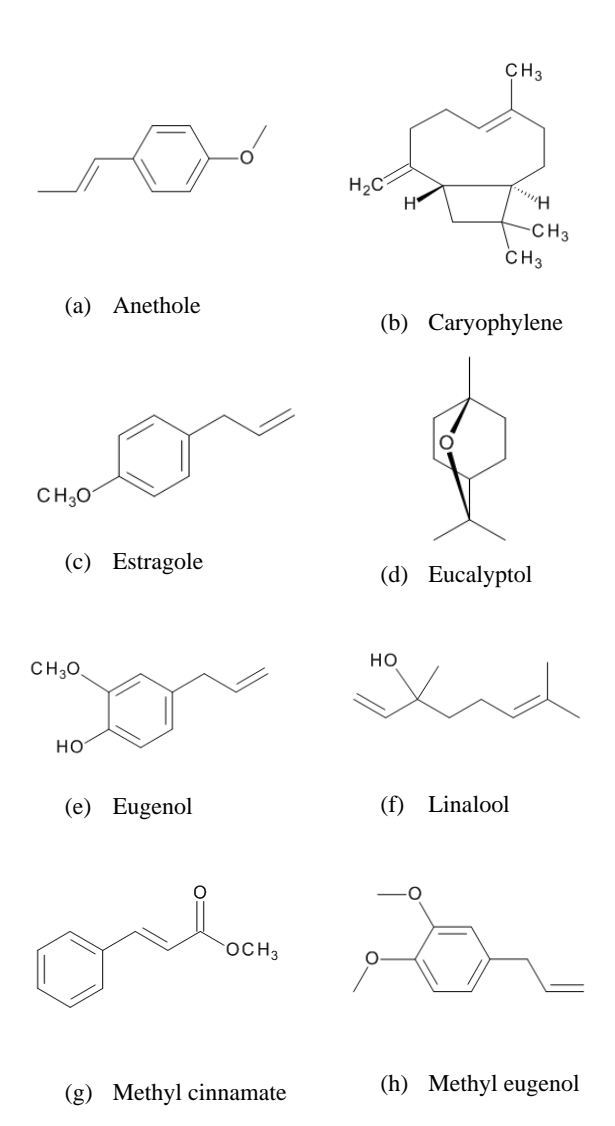


Figure 1. Chemical structures of essential oil that be selected in this study: (a) Anethole: 1-methoxy-4-(1-propenyl)benzene; (b) Caryophylene: 4,11,11-trimethyl-8-methylene-bicyclo[7.2.0]undec-4-ene; (c) Estragole: 1-allyl-4-methoxybenzene; (d) Eucalyptol: 1,3,3-trimethyl- 2-oxabicyclo[2,2,2]octane (e) Eugenol: 4-Allyl-2-methoxyphenol; (f) Linalool: 3,7-dimethylocta-1,6-dien-3-ol; (g) Methyl cinnamate: Methyl (*E*)-3-Phenylprop-2-enoate; (h) Methyl eugenol: 1,2-dimethoxy-4-(2-propenyl)benzene.

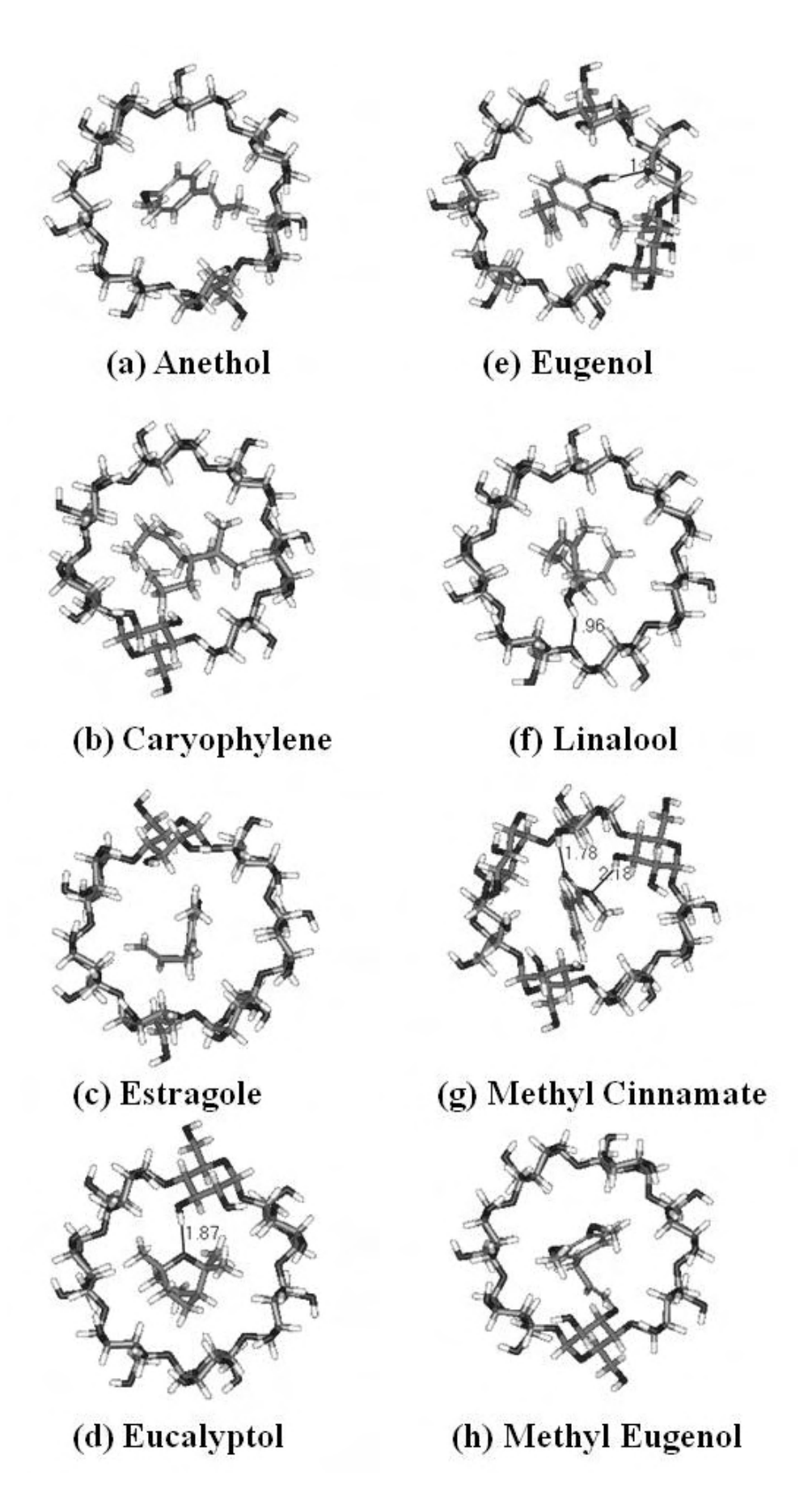


Figure 2. The predicted geometry of basil essential oils and β -cyclodextrins inclusion complexes calculated by using HF/3-21G

Methodology

The BCD structure with C7 symmetry was obtained from the calculations of Wolschann's group [5]. This structure was fully geometry optimized with symmetry restriction with the density functional B3LYP/6-31G(d,p) calculation Gaussian03 program package [6]. The obtained geometry was taken for further modeling of the inclusion complexes with basil essential oils. The structure of eight basil essential oils are constructed by using Gaussian View program and fully optimize the structures by using basis set HF/3-21G. AutoDock 4.2 program [7] was used to calculate the inclusion complex of BCD and flavor compounds. One hundred docking runs were performed per structure within the calculations. The model with the lowest energy assigned by molecular docking calculation was selected to further be investigated in details by quantum chemistry calculation at HF/3-21G level.

Results and Discussion

The energies of BCD/essential oils inclusion complexes from the molecular docking calculations are given in Table 1. The energies of the prediction inclusion complex models and conformations which fully optimized by HF/3-21G are shown in Table 2 and Figure 2, respectively. The structures comparison of the basil essential oils which obtain from HF/3-21G calculations before and after encapsulated by BCD are shown in Figure 3.

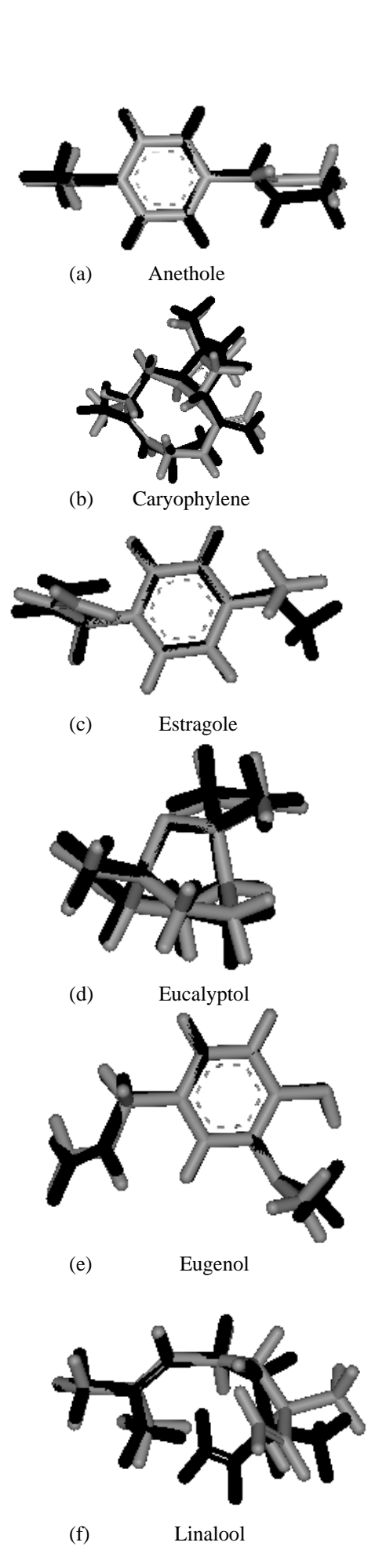
The obtained data indicate the formation of a 1:1 inclusion complex between BCD and these basil essential oils, and additionally provide information regarding conformation and interactions between atoms forming the complexes.

Table 1. The energy of inclusion complexes from molecular docking calculations

Essential oils	Er	nergy (kcal/m	ol)
Essential ons	Lowest	Highest	Average
Anethole	-3.32	-3.20	-3.08
Caryophyllene	-6.04	-5.99	-6.03
Estragole	-3.36	-3.26	-3.31
Eucalyptol	-4.50	-4.47	-4.49
Eugenol	-3.69	-3.33	-3.52
Linalool	-3.70	-3.32	-3.46
Methyl Cinnamate	-3.33	-3.24	-3.29
Methyl Eugenol	-3.45	-3.28	-3.37

Table 2. The energy of inclusion complexes calculated by HF/3-21G

tarearated of Till to 210	
Essential oil	Energy (kcal/mol)
Anethole	-2.94 x 10 ⁶
Caryophylene	-3.02×10^6
Estragole	-2.94×10^6
Eucalyptol	-2.94×10^6
Eugenol	-2.99×10^6
Linalool	-2.94×10^6
Methyl Cinnamate	-2.99×10^6
Methyl Eugenol	-3.01 x 10 ⁶



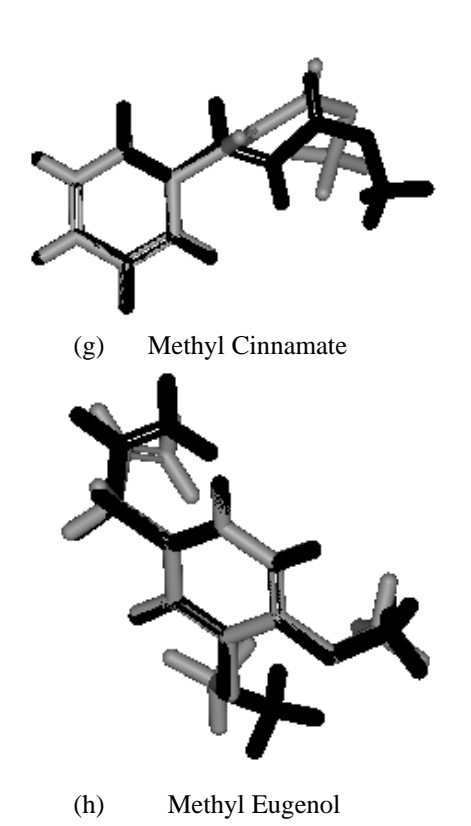


Figure 3. Lowest energy conformation of compound (HF/3-21G,black) superimposed with the structure of compound in the inclusion complex with BCD (gray)

The computer simulated automated docking studies were performed using AutoDock 4.2 program where the BCD is assigned to be a rigid host conformation, the essensial oils are assigned to be a flexible guest conformation. The inclusion complex conformation that has minimum binding energy was further fully optimized using basis set HF/3-21G to obtain the global minimum energy and observed the host-guest interaction. Therefore the energies of inclusion complex which obtain from HF/3-21G (Table 2) are much higher than the energies which obtain from docking simulation (Table 1).

The predictive capabilities of the methods could provide considerate satisfactory, even though they are not well established in the accuracy of the BCD's mobility and the solution effect. However the results from this work could provide the possibility of using BCD encapsulation method in order to increase the stabilizing and the solubility of these basil essential oil components.

Acknowledgments

The financial support of the Thailand Research Fund is gratefully acknowledged.

- [1] J.Janick (ED.), J.E. Simon, M.R. Morales, W.B. Phippen, R.F. Vieira and Z. Hao, *Basil: A Source of Aroma Compounds and a Popular Culinary and Ornamental Herb*, ASHS Press, Alexandria, 1999.
- [2] L.C. Chiang, L.T. Ng, P.W. Cheng, W. Chiang, C.C. Lin, *Antiviral activities of extracts and selected pure constituents of Ocimum basilicum*, Clin. Exp. Pharmacol. Physiol. **32** (2005), pp. 811–6.
- [3] Y. Hasegawa, K. Tajima, N. Toi, Y.Sugimura, Characteristic Components Found in the Essential Oil of Ocimum basilicum L., Flavour Fragr J, 12 (1997), pp. 195-200.
- [4] L. Szente, J. Szejtli, Cyclodextrins as food ingredients, Trends in Food Science & Technology, 15 (2004), pp. 137-42.
- [5] W. Snor, E. L., P. Weiss-Greiler, A. Karpfen, H. Viernstein, P. Wolschann On the structure of anhydrous β-cyclodextrin Chem. Phys. Lett, 441 (2007), pp.159-62.
- [6] M.J. Frisch, G.W. Trucks, H.B. Schlegel, G.E. Scuseria, M.A. Robb, J.R. Cheeseman, J.A. Montgomery, Jr., T. Vreven, K.N. Kudin, J.C. Burant, J.M. Millam, S.S. Iyengar, J. Tomasi, V. Barone, B. Mennucci, M. Cossi, G. Scalmani, N. Rega, G.A. Petersson, H. Nakatsuji, M. Hada, M. Ehara, K. Toyota, R. Fukuda, J. Hasegawa, M. Ishida, T. Nakajima, Y. Honda, O. Kitao, H. Nakai, M. Klene, X. Li, J.E. Knox, H.P. Hratchian, J.B. Cross, V. Bakken, C. Adamo, J. Jaramillo, R. Gomperts, R.E. Stratmann, O. Yazyev, A.J. Austin, R. Cammi, C. Pomelli, J.W. Ochterski, P.Y. Ayala, K. Morokuma, G.A. Voth, P. Salvador, J.J. Dannenberg, V.G. Zakrzewski, S. Dapprich, A.D. Daniels, M.C. Strain, O. Farkas, D.K. Malick, A.D. Rabuck, K. Raghavachari, J.B. Foresman, J.V. Ortiz, Q. Cui, A.G. Baboul, S. Clifford, J. Cioslowski, B.B. Stefanov, G. Liu, A. Liashenko, P. Piskorz, I. Komaromi, R.L. Martin, D.J. Fox, T. Keith, M.A. Al-Laham, C.Y. Peng, A. Nanayakkara, M. Challacombe, P.M.W. Gill, B. Johnson, W. Chen, M.W. Wong, C. Gonzalez, and J.A. Pople, Gaussian 03, Revision C.02, Gaussian, Inc., Wallingford CT, 2004.
- [7] G.M. Morris, R. Huey, W. Lindstrom, M.F. Sanner, R.K. Belew, D.S. Goodsell, A.J. Olson, *J. Comput. Chem.* 30 (2009), pp. 2785-2791.

Preparation of Adsorbent Material from Mixture of Bottom Ash and FGD Gypsum for Dye Adsorption

W. Sittinang¹, O. Arquero¹* and S. Thiansem²

*E-mail: noi2495@hotmail.com, Tel: +66-6-586-5472

Abstract: Utilization of bottom ash and flue gas desulfurization gypsum, which are waste materials produced from the production of power through combustion of coal at the Mae Moh power plant in Lampang province, mixed with paddy soil and sawdust for production of adsorbent material, was studied in this research. The compositions of raw materials used for production of adsorbent material were 22% bottom ash, 7% FGD gypsum and 45% soil followed by the addition of 26% sawdust. The temperature of oxidation firing was studied at 850 °C for 3 hours, with increasing rate of 3 C/minute. This prepared fired adsorbent material (FGD) did not slake after soaking in water. It had good dye absorption, slightly basic pH value and light weight. The analysis by laser particle size analyzer indicated the average size was around 50.26 micrometer.

Introduction

Recently, dye is used in many industries such as food, paper, carpets, rubbers, plastics, cosmetics, and textiles. The discharge of colored wastewater from these industries causes many significant environmental problems. Methyl orange is a representative contamination in industrial wastewater and shows poor biodegradability. Many physical-chemical methods have been tested to remove the dye from aqueous solutions, and adsorption is considered superior to other techniques.

It is difficult to degrade dye materials because they are very stable to light and oxidation reactions [3]. For the removal of dye materials from contaminated water, several methods such as physical, chemical and biological methods have been investigated [1,3]. Among the proposed methods, removal of dyes by adsorption technologies is regarded as one of the competitive methods because of high efficiency, economic feasibility and simplicity of design/operation [3,4]. Moreover, adsorption of dyes on inorganic supports like silica is important to produce pigments.

Methyl orange (MO) is one of the well-known acidic/anionic dyes, and has been widely used in textile, printing, paper, food and pharmaceutical industries and research laboratories [2]. The structures of MO is shown in Scheme 1 and the removal of MO an from water is very important

due to their toxicity [2–4]. MO for the reasons stated above was selected in this study as a representative acidic (anionic) dye.

Bottom ash and FGD-gypsum, which are wastes from electric power plant can be used as main raw materials for production of adsorbent material

The aim of the present work is to produce fired adsorbent material from bottom ash and FGDgypsum, which are residues from Mae Moh electric power plant in Lampang province, mixed with clay to replace the use of commercial adsorbent materials and to investigate the possibility of using this adsorbent material (AM) for the adsorptive removal of methyl orange (MO) from aqueous solution. MO serves as a model compound for common dyes which are widely used in chemical, textile and paper industries. These dves are particularly harmful to the environment. The adsorption efficiency of MO was studied by optimizing experimental variables such as initial MO concentration. The properties of AM were characterized by XRF, lazer particle size and BET surface area.

$$(CH_3)_2N$$
— $N=N$ — SO_3Na

Figure 1. Methyl orange

Materials and Methods

Materials: Bottom ash and flue gas desulfurization (FGD) gypsum, which are waste materials produced from the production of power through combustion of coal at the Mae Moh power plant in Lampang province, were mixed with clay and sawdust for production of adsorbing material. The mixture was fired at 850 °C. It was dried and sieved by using a sieve to mesh size 100 Mesh and stored in separate desiccators. Analytical grade methyl orange (C₁₄H₁₄N₃NaO₃S; molecular weight 327.33) was obtained from Merck and was used as received. The dye solutions were prepared at the desired concentrations using DI-water.

¹ Department of Chemistry and Center of Excellence for Innovation in Chemistry, Faculty of Science, Chiang Mai University, Chiang Mai, Thailand, 50200

² Department of Industrial Chemistry, Faculty of Science, Chiang Mai University, Chiang Mai, Thailand, 50200

Characterization of AM: The composition of AM was determined on a Horiba/MESA-500w X-ray fluorescence spectrometer, and determination of particle size distribution of AM is 50.26 μm by particle size analyzer, diff. Mastersizer, Malvern Instrument Limited. The specific surface area of the AM is 4.81 m²/g measured by using the Brunauer–Emmet–Teller (BET) method. The results were obtained by means of the N₂ adsorption at 77±0.5K using a Quantachrome Autosorb-1 analyzer. Prior to analysis, all samples were degassed under vacuum at 120 °C for 3.77 h.

Adsorbtion studies: Batch technique was employed at temperatures 30 °C. A suitable amount of the adsorbent of the chosen particle size was added to 100 ml of the MO solutions of various initial concentrations (2-14 ppm) in each flask and the mixture was shaken in temperature-controlled water bath shaker till equilibrium was achieved. The solutions were now filtered with filter membrane (0.2 μ) and uptake of dye was analyzed spectrophotmetrically at λ_{max} 465 nm..

The concentration of MO was determined spectrophotometrically using a UV–visible spectrophotometer (model 6400, UK) by taking measurements at the absorbance maximum (465 nm). A calibration curve was plotted between the absorbance and the concentration of the MO solution to obtain the absorbance–concentration profile. The amount of MO uptake per unit of adsorbent (q_e) was calculated using the following equations:

$$q_e = (C_i - C_e) \times V/m \tag{1}$$

where C_i is the initial MO concentration (mg/L), C_e is the MO concentration at the adsorption equilibrium (mg/L), V is the volume of MO solution (L), and m is the weight of the AM (g).

Results and discussion

Characterization of AM: The physico-chemical properties of AM are shown in Table 1 SiO₂ and Al₂O₃ are the major constituents of the AM. The image shows that AM particles are soft clumps that are mainly composed of irregular and porous particles. X-ray Fluorescence (XRF) can be used to determine the bulk structure of a material.

Adsorbtion studies: The studies involving different contact time helps in determining the uptake capacities of the dye at varying time intervals keeping the amount of the adsorbents fixed at temperatures 30 °C. It was established that in case of adsorbent material (0.5 g), 140 min of contact time was found sufficient to acquire equilibrium. Figure 2 illustrates the adsorption of

methyl orange onto AM at various contact times. The amount of methyl orange uptake, q (mg/g), increases with contact time on AM. Methyl orange uptake is rapid in the first 80 min, then proceeds at a slower rate, and finally reaches equilibrium when contact time is around 140 min.

Table 1: Physical and chemical properties of Adsorbent Material.

Compound	wt%
SiO_2	49.87
Al_2O_3	15.00
SO_3	4.42
K_2O	3.58
CaO	12.72
TiO_2	1.72
Mn_2O_3	0.24
Fe_2O_3	12.83
ZrO_2	0.06

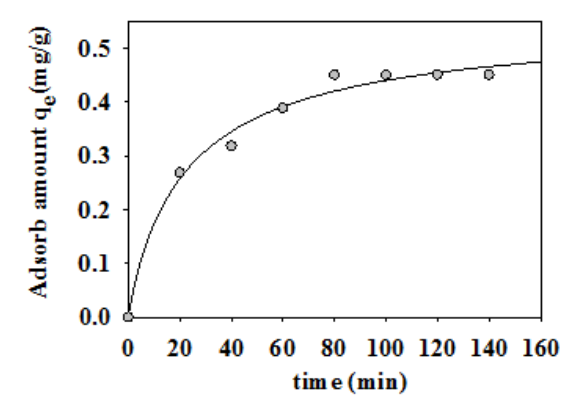


Figure 2: Effect of contact time on adsorption amount of methyl orange onto AM

Various concentrations ranging from 2 to 14 ppm of methyl orange were investigated with fixed amount of adsorbents at temperatures 30 °C. The study reveals that the increase in concentration of methyl orange increases the extent of adsorption (Figure 3).

In the study of adsorption isotherm, the Langmuir isotherm was applied to understand the dye-AM interaction. The heterogeneity arises from the presence of different functional groups on the surface and from the various adsorbent-adsorbate interactions. The Langmuir isotherm is expressed by the following empirical equation:

$$C_e/q_e = C_e/q_{max} + 1/q_{max}b$$
 (2)

where C_e : equilibrium concentration of adsorbate (mg/L); q_e : the amount of adsorbate adsorbed (mg/g); q_{max} : Langmuir constant (maximum

adsorption capacity) (mg/g); b: Langmuir constant (L/mg). Therefore, the q_{max} can be obtained from the reciprocal of the slope of a plot of C_e/q_e against C_e as shown in Figure 4.

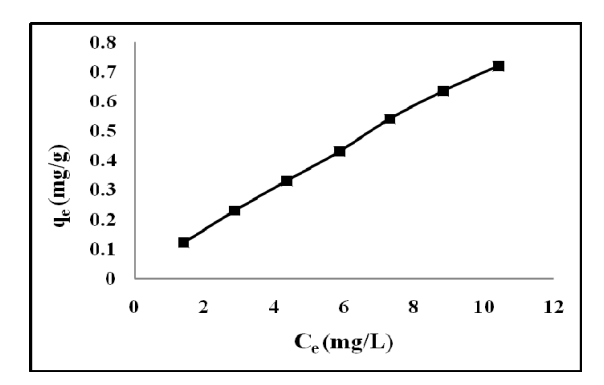


Figure 3: Adsorption isotherm for methyl orange on AM at 30 $^{\circ}\text{C}$

The adsorption data of methyl orange was correlated with the Langmuir isotherm in equilibrium concentration range from 1 to 10 mg/L. From the plot, the Langmuir values, q_{max} and b, were then calculated and are shown in Table 1.

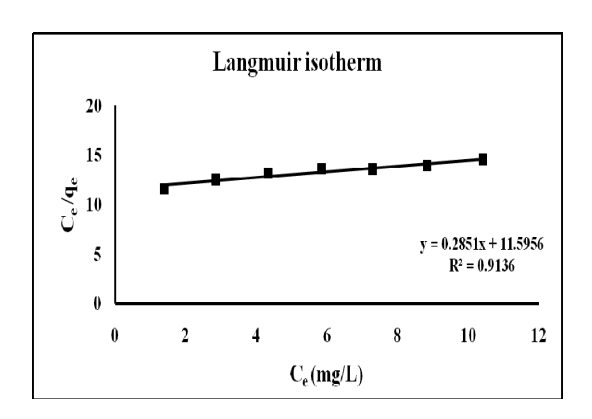


Figure 4: Langmuir plot of the isotherm of MO on AM at 30 $^{\circ}$ C

Table 1 Langmuir constants for adsorption of methyl orange on AM at 30 $^{\circ}\text{C}$

q _{max} (mg/g)	b (L/mg)	r ²
3.51	0.024	0.9136

4. Conclusion

The present study investigated the adsorption of MO from aqueous solutions by using an adsorbent of adsorbent material. AM has been demonstrated to be highly effective for the removal of the anionic dye MO with an adsorption equilibrium time at 80 min. The best-fit adsorption isotherm was achieved with the Langmuir model, indicating that adsorption occurs by monolayer coverage. The positive enthalpy change for the adsorption process confirms the endothermic nature of the adsorption. The low price and abundance of AM make this material particularly promising for the removal of anionic dyes in industrial wastewater treatment.

Acknowledgments

The authors would like to thank the Center of Excellence for Innovation in Chemistry: PERCH-CIC, Thailand, for partial finacial support of this research.

- [1] S. Chen, J. Zhang, C. Zhang, Q. Yue, Y. Li and C. Li, *Desalination* **252** (2010), pp. 149-156.
- [2] P. Dechprasitthichoke, Utilization of bottom ash and flue gas desulfurization gypsum for production of planting materials, Ph.D. Dissertation, Chiang Mai University, 2007.
- [3] A. Mittal, A. Malviya, D. Kaur, J. Mittal and L. Kurup, J. Hazard. Mater. 148 (2007), pp 229-240.
- [4] A. A. Jajil, S. Triwahyono, S. H. Adam, N. D. Rahim, M. A. A. Aziz, N. H. H. Hairom, N. A. M. Razali, M. A. Z. Abidin and M. K. A. Mahamadiah, J. Hazard. Mater. (2010), in press
- [5] E. Haque, J. W. Jun and S. H. Jhung, *J. Hazard. Mater.* (2010), in press

Synthesis and Characterization of Nickel Oxide/Multiwall Carbon Nanotube Nanocomposites on Fluorine-Doped Tin Oxide for Hydrogen Peroxide Detection

S. Chaiyasith¹, <u>B. Jandai</u> ^{1,*} and W. Pecharapa^{2, 3}

¹Department of Chemistry, Faculty of Science, King Mongkut's Institute of Technology, Ladkrabang, Bangkok 10520 Thailand

²College of KMITL Nanotehnology King Mongkut's Institute of Technology, Ladkrabang, Bangkok 10520 Thailand ³ThEP Center, CHE, 328 Siayutthaya RD.,Bangkok 10400

* E-mail: fias_2@hotmail.com

Abstract: The new electrode for detection of hydrogen peroxide was developed based on crosslinking between Nickel oxide/multiwall carbon nanotubes (NiO/MWCNTs) and fluorine-doped tin oxide (FTO) using nafion as binder. The MWCNT was purified by classical oxidative with acid treatment. The purified MWCNTs was mixed with 0.2 M Nickel acetate and adjusted to pH 8 with ammonium hydroxide. The suspension of MWCNT was calcined to NiO/MWCNT at 300°C for 1.5 hrs. The NiO/MWCNT and nafion was fabricated onto FTO electrode. The physical properties were investigated by Field Emission Scanning Electron Microscope (FE-SEM) and X-ray Diffractometer (XRD). The SEM result is indicated that NiO nanoparticles were well distributed on the surface of MWCNTs. The cyclic voltammetry were used to confirm the successful procedure synthesis of NiO/MWCNTs/FTO and the concentration hydrogen peroxide was determined by amperometry, by mean of the NiO/MWCNTs/nafion/FTO as working electrode. The linear correlation between current and concentrations was achieved up to 1.0×10^{-4} mol dm⁻³ (r²=0.9996). The detection limit of the electrode was found to be 32.84 μM based on signal-to-noise ratio of 3. Consequentlythe NiO/MWCNT/FTO can be probably useful as working electrode for the development of hydrogen peroxide sensor.

Introduction

Carbon Nanotubes (CNT) have attracted much attention because of their unique physical, chemical, mechanical and electronic properties science [1]. Due to their high conductivity and stability at high temperature, CNT have been used as a support material for the dispersion and stabilization of metal nanoparticle[2]. It has been report that CNT properties can be influenced by surface modification with nanoparticle[3] and metal oxide nanostructure[4].

Nickel oxide is a material of interest for practical applications, such as boi chemical sensing [5], gas sensing [6], catalysis [7], and electrochemical capacitors [8].

The FTO films are used as conducting layers in electro chromic devices and they serve also as the passive working and counter electrode. The electro chromic properties of the devices are characterized by the transparency and resistivity of the

conducting layer. Electro chromic materials exhibit a reversible change their optical properties upon charge insertion—extraction induced by an external voltage [9].

Hydrogen peroxide appears to be a ubiquitous molecule and plays an important role in textile/food industries, pharmaceutical and health care. Multiple papers have claimed substantial levels of H₂O₂ in human blood plasma [10] and in freshly voided human urine [11]. Therefore it is quite important to monitoring of H₂O₂ concentrations. Conventional methods. including titrimetry [12],chemiluminescence [13], fluorescence [14] and spectrophotometry [15], tend to be complex, timeconsuming and suffer from various interferences. Consequently, the rapid and reliable methods for measuring H_2O_2 are naturally required. catalytic activity of nickel oxide was found to be sensitive to H_2O_2 catalyst [16].

The several alternatives for NiO composition such as electrodepsition [17], support on alumina [18], and sol-gel technique [19].

In this report, the first step to purify of CNT by acid at high temperature [20], the purified MWCNTs was mixed with 0.2 M Nickel acetate and adjusted to ammonium hydroxide. suspension of MWCNT was calcined NiO/MWCNT at 300°C for 1.5 hrs. NiO/MWCNT and nafion was fabricated onto FTO electrode. Prepare nickel oxide mixed with multiwall carbon nanotubes. The second step of physical characteristic with techniques X-ray diffraction (XRD) and Field Emission Scanning Electron Microscope (FE-SEM). The third step is to measure the modified electrode by voltammetry amperometry to investigate techniques hydrogen peroxide.

Material and method

Chemicals and material

Multiwalled Carbon nanotube(MWCNT) and nickel (II) acetate tetrahydrate purchased form sigaldrich (St. Louis, MO,USA). Nitric acid (70% w/w) form Mallinckrodf-Chemical (Thailand). Sulfuric acid (98% w/w) form Ajax Chemical (New Zealand), Nafion (5% in a mixture of lower aliphatic alcohol) form Fluka

(Switzerland). Ethanol absolute from Carlo Erba (Italy). Methanol analytical grate for nafion preparation form lab-scan Co.,Ltd (Ireland). Sodium dihydrogen phosphate from Carlo Erba (Italy). Di-sodium hydrogen orthophosphate dodecahydrate from Fisons Scientific Equipment (England). Hydrogen peroxide (30% w/v) from Fisher Scientific (UK) and fluorine-doped tin oxide (FTO) form Solaronix (Switzerland).

Other chemicals were purchased in analytical grade and used without further purification. All solutions were prepared with distilled water, which was purified with a Milli-Q purification system (Branstead,USA) to a specific resistivity of >18 $M\Omega\ cm$.

Instruments

Microstructure and morphology were study by X-ray diffraction (08 Advance, Burker AG) field-emission scanning electron microscopy (FESEM, JEOL-6700), and electrochemical measurements were performed using a potentiostat (Autolab/PGSTAT20).

Purified of MWCNT

Prior to reflux, 400 mg MWCNT ultrasonicated for 1.5 h in the mixture of 68% HNO₃ and 97% H₂SO₃ in the ratio of 3:1, to disperse agglomeration and eliminate of purities that may exist. Subsequently, reflux under stirring at 100 °C for 8 h as purified MWCNT. The purified sample was washed and neutralized by DI water until pH 7. Finally, the purified MWCNT was dried at 45 and 400 °C for 12h.

Preparation of NiO/MWCNT composites

0.5 ml nickel (II) acetate (0.2 M) form Ni(COO)₂.4H₂O to 5 mg of MWCNT and adjust to pH 8 with ammonium hydroxide. After that ultrasonicated for 20 min, were soaked in the solution for 5 h after, the WMCNTs were centrifiugally separated product and calcined at 300 °C for 1.5 h, respectively. The NiO/MWCNT composites were obtained.

Modification of NiO/MWCNT/FTO electrode

Before modification, the FTO surface was carefully ultrasonicated successively in ethanol and distilled water for 5 min, respectively. The preparation of the suspension NiO/MWCNT concentration of 20 mg NiO/MWCNT with 0.5% nafion 0.5 ml sonicated for 30 min to be a black suspension is homogeneous. It will be the solution. Then, micropipette $10\mu L$ pipettes onto the surface of a FTO and then left to dry.

Result and discussion

X-ray diffraction study

The X-ray pattern of MWCNT and NiO/MWCNT nanocomposites (Fig. 1) a fitter heat at

300 °C for 1.5 h. The diffraction angle at $2\theta = 37.34$ °, 43.38° and are assigned to (002), (111) and (200). The average size of the nickel oxide crystallites in NiO/CNT nanocomposite was calculate form Scherer's equation

$$D = \frac{\kappa\lambda}{\beta\cos\theta}$$

Where D is the grain diameter, K is the shape factor (0.9), λ is the X- ray wavelength (1.5406 x 10^{-10} m), β is the full-width at half maximum and θ is the Bragg angle. The calculated average particle sizes of NiO by heating are approximately 4.7-4.9 nm.

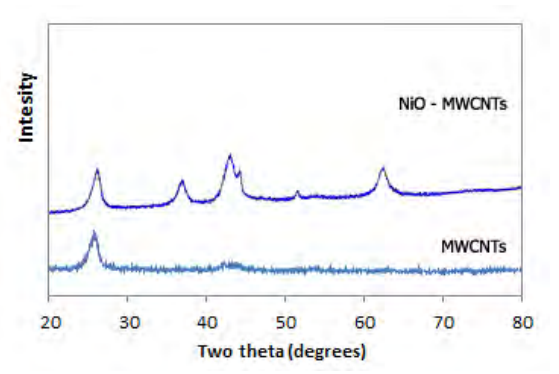


Fig 1 XRD pattern for MWCNT and NiO/MWCNT nanocomposite.

Scanning Electro Microscope

The morphology of the NiO/MWCNT nanocomposites were investigated is SEM as shows in fig. 2 The SEM image of NiO nanocomposites synthesis by using nickel (II) acetate heat treated at 300 $^{\circ}$ C for 1.5 h . This image shows that the nickel particles are well dispersion in the MWCNT and they have neary uniform size.

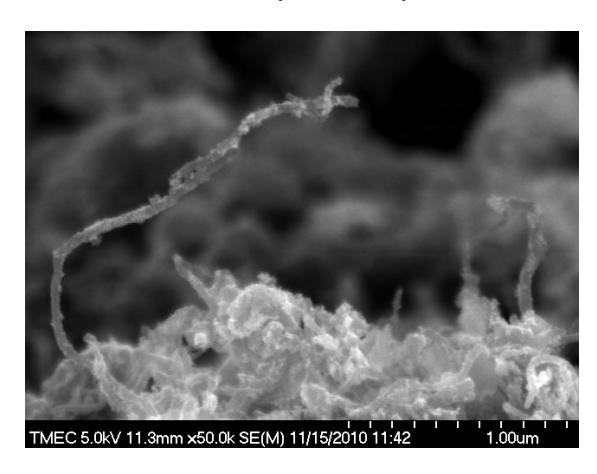


Fig.2 scanning electron micrograph of NiO/MWCNT coated on FTO electrode.

Cyclic Voltammetry (CVs)

Cyclic voltammetry was used to determine the electrical properties of NiO/MWCNT/FTO

electrode in 30 mM K₃ [fe(CN)₆], at 50 mV/s potential form -1 to 1 V. The result show modified electrodes have electrical behavior. Subsequently the modified electrode was used determination of hydrogen peroxide with bare FTO, MWCNT/FTO and NiO/MWCNT/FTO electrode as show in fig 3. The voltammetric current respond of electrode which is modified by NiO/MWCNT nanocomposite is more efficient than unmodified electrode.

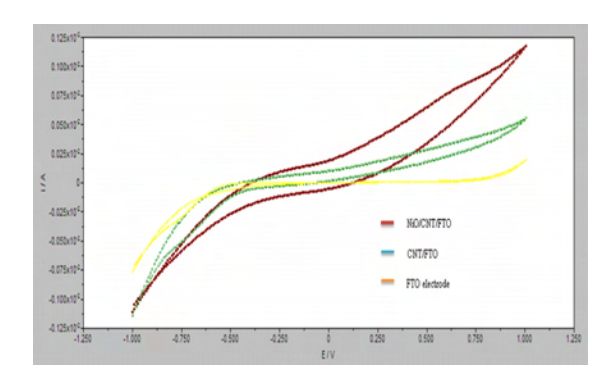


Fig. 3 Cyclic voltammogram (CVs) of FTO, CNT/FTO and NiO/CNT/FTO electrode recorded in $100 \text{ mM } H_2O_2$.

Determination of hydrogen peroxide using NiO/CNT/FTO electrode

The optimal concentration of nickel (II) acetate were studied in range 0.05 to 0.4 M nickel (II) acetate. The respond increased with increasing concentration of nickel (II) acetate until 0.2 M and become decrease over 0.2 M (fig. 4).

NiO Concentration.

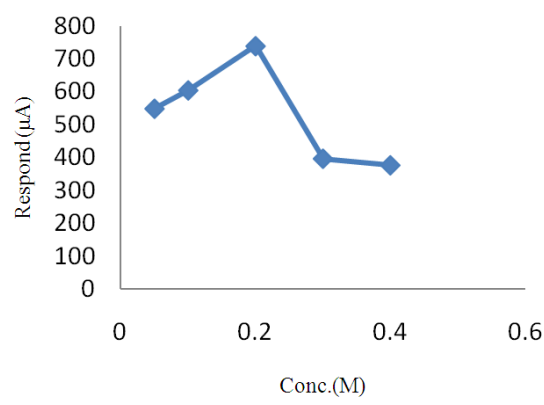


Fig.4 Effect of Nickel (II) acetate concentrations for NiO/CNT/FTO electrode.

The effect of amount of MWCNT (0.5-40 mg), it was found that the responds obtained by using of 20 mg of MWCNT was the highest. Hence, 20 mg of MWCNT was chosen (fig. 5).

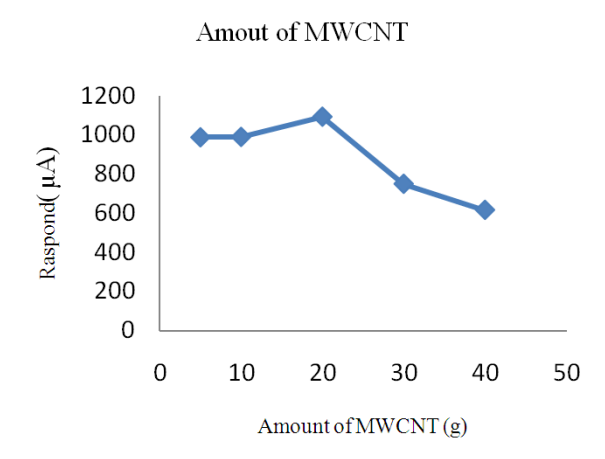


Fig. 5 The effect of amount of MWCNT for NiO/CNT/FTO electrode.

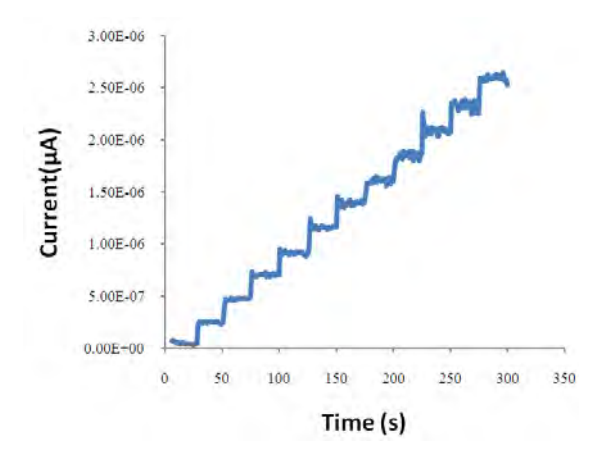


Fig. 6 Amperometric respond at the NiO/MWCNT/FTO electrode.

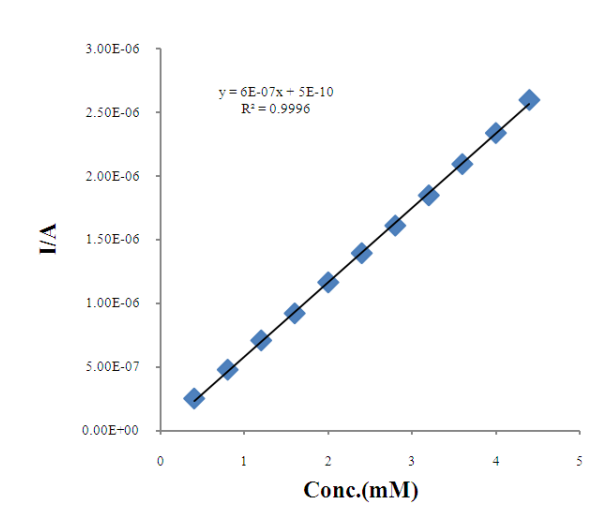


Fig. 7 Plot of current vs. concentration of H_2O_2 data form fig. 6

Amperometric detection of H_2O_2 at NiO/MWCNT/FTO electrode

As show the NiO/MWCNT/FTO modified electrodes have excellent and strong mediation and facilitate the low potential amperometric measurement of hydrogen peroxide. Fig. 6 shows a current-time the show typical of modified NiO/MWCNT/FTO electrode on successive additions 100 µM of hydrogen peroxide at applied potential of 0.8 V (vs. Ag/AgCl).

The plots of current respond vs. hydrogen peroxide plot is linear over a wide concentration rang. The linear squares calibration curve over the range of 0.4 to 4 μ M with a correlation coefficient of 0.9996. The detection limit (when signal to noise ration were 3) were 32.84 μ M (fig. 7)

Conclusion

The NiO/MWCNT/FTO modified electrode showed stable and reducible electrochemical behaviors. The proposed modified electrodes were used as sensitive amperometric hydrogen peroxide sensors. The fabricated hydrogen peroxide sensor possesses excellent characteristic and performance, such as fast response time, low detection limit and high sensitivity. The detection limit,sensivity and linear concentration range of the NiO/CNT/FTO modified electrode were 32.84 μM . These advantages make it promising for providing a simple method to develop a new amperometric sensor for H_2O_2 detection.

- V. Georgakilas, D. Gournis, V .Tzitzios, L. Pasquato, D.M. Guidie and M.J. Pratod, Journal of Materials Chemistry.17(2007) 2679
- 2. M. Zhang and L. Su. Carbon 44 (2006) 276
- 3. K.B. Malea, S. Hrapovic, Y. Liu, D. Wang, John H.T. Luonga. Analytica Chimica Acta 516 (2004) 35
- X. Wang, B. Xia, X. Zhu, J. Chen, S. Qiu and J. Li, Solid State Chem. 181 (2008) 822
- Ch. li, Y. Liu, L. Li, Z. Du, S. Xu and M Zhang, Talanta 77(2008) 455
- C. Luyo, R. Ionescu, L. F. Topalian, W. Estrada, E. Llobet, C. G. Granqvist and P. Heszler, Sensor and Actuators B 138 (2009) 14
- 7. D. B, Kim, H. J. Chun, Y. K. Lee, H. H. Kwon, and H. I. Lee, International journal of hydrogen energy 35 (2010) 131
- 8. J. Y. Lee, K. Liang, K. H. An and Y. H. Lee, Synthetic Metal 150 (2005) 153
- K. K. Purusthaman, M. Dhanashankar and G. Muralidharan, Current Applied Physics 9 (2009) 67
- A. N. Lawrence, D. H. wood and J.I.Sznajdar, Free Radical Biology Medicine 6 (1989) 479
- L. H. Long, P. J. Evans, and B. Halliwell, Biochemical and Biophysical Research Communications 262 (1999) 605

- M.S. Prasada Rao and R.M. Rao, Analytica Chemica Acta 242 (1991) 229
- A. Arnous, C. Petrakis, D. P. Makris and P. Kefalas, Journal of Pharmacological and Toxicological Methods 48 (2002) 171
- Z. H. Li, D. H. Li, K. Oshitab and S. Motomizu, Talanta 82 (2010) 1225
- Ch. A. Pappas, D. C. Stalikas, Ch. Y. Fiamegos and I.M. Karayannis, Analytica Chimica Acta 455 (2002) 305
- A.Noorbakhsh and A. Salimi, Electrochemica Acta 54 (2009) 6312
- A.B.Moghaddam, M.R.Gamjali, R. Dinarvand, A.A. Saboury, T. Razavi, A.A. Moosavi-MMovahedi,P. Norouzi, Biophysical Chemistry 129 (2007) 259
- S. Velu and S.K. Gangwal, Solid State Ionics 177 (2006) 803
- 12. M.S.Prasada Rao and R.M. Rao, Analytica Chemica Acta 242 (1991) 229
- A. Arnous, C. Petrakis, D. P. Makris and P. Kefalas, Journal of Pharmacological and Toxicological Methods 48 (2002) 171
- Z. H. Li, D. H. Li, K. Oshitab and S. Motomizu, Talanta 82 (2010) 1225
- Ch. A. Pappas, D. C. Stalikas, Ch. Y. Fiamegos and I.M. Karayannis, Analytica Chimica Acta 455 (2002) 305
- A.Noorbakhsh and A. Salimi, Electrochemica Acta 54 (2009) 6312
- A.B.Moghaddam, M.R.Gamjali, R. Dinarvand, A.A. Saboury, T. Razavi, A.A. Moosavi-MMovahedi,P. Norouzi, Biophysical Chemistry 129 (2007) 259
- S. Velu and S.K. Gangwal, Solid State Ionics 177 (2006) 803
- Q Yanga, J. Shaa,b, X. Maa and D. Yang, Materials Letters 59 (2005) 1967
- R.Yudianti, L. Indrati and H. Onggo, Journal of Applied Sciences 10 (2010) 1978
- L. Chung-Hun, W. Shih-Chang, Y.Chiun-Jye,W. Meng-Fang and Ch. Ku-Shang, Biosensors and Bioelectronics 22 (2007) 877
- D. Giovanelli, N.S. Lawrence, L. Jiang, Timothy G.J. Jones, and R.G. Compton, Sensor and Actuators B 88 (2003) 320

Preparation and Characterization of Manganese Dioxide and Copper Oxide/Multi-Walled Carbon Nanotube Nanocomposites Modified Glassy Carbon Electrode for Determination of Hydrogen Peroxide

S. Chaiyasith¹ and W. Kijboon 1*

¹Department of Chemistry, Faculty of Science, King Mongkut's Institute of Technology, Ladkrabang, Chalongkrung Rd., Ladkrabang, Bangkok 10520, Thailand * E-mail: kijboon@hotmail.com

Abstract: An electrochemical electrode for the detection of hydrogen peroxide (H2O2) was presented based on glassy carbon electrode (GCE 5 mm × 5 mm × 2 mm) covered with Multi-wall carbon nanotube (MWCNT) and manganese dioxide/copper oxide (MnO₂/CuO). In preliminary study, we investigated characteristic by using X-ray Diffrectometer (XRD) and Field Emission Scanning Electron Microscope (FE-SEM). The electrochemical behaviors of the sensor were studied by cyclic voltammetry (CV) and amperometry. Discussion will be made on optimization and analytical performance of the method. In addition, the MnO₂/CuO/MWCNTs are possibly useful working as electrode for determination of H₂O₂. The CuO/MWCNTs, MnO₂/MWCNTs and MnO₂/CuO/MWCNTs nanocoposities electrode exhibits a linear range for the detection of H2O2 was $0.2 \times 10^{-3} - 2.2 \times 10^{-3} \text{ M.}, 0.2 \times 10^{-3} - 1.2 \times 10^{-3} \text{ M.},$ $0.2\times10^{\text{--}3}-2.2\times10^{\text{--}3}$ M., respectively, and a detection limit of 0.17 μ M, 12.24 μ M, 33.0 μ M, respectively at a signal-to-noise ratio of 3. The low detection limit, wide liner range and high sensitivity of the sensor make it valuable for further application.

Introduction

The detection of H₂O₂ is very important in various fields including clinic, food, pharmaceutical and environmental analysis, because H₂O₂ is a chemical threat to the environment and the production of enzymatic reactions, at the same time, it has been recognized as one of the major factors in the progression of important diseases [1]. Accurate and reliable determination of H₂O₂ has been widely investigated using chromatography chemiluminscence [3] and electrochemistry [4] technologies. Among these methods, electrochemical detection is a most promising approach to achieve accurate, separate, and rapid H₂O₂ monitoring [5]. Electrochemistry technique based on a simple and low cost electrode has been extensively applied for accurate determination of For most electrochemistry sensors, the detection of H₂O₂ was achieved at a relatively high potential around 0.5 V. Thus, it becomes significant to construct a sensor to detect H₂O₂ at a lower potential. Although some chemically modified electrodes have been proposed to reduce the large overpotential required for the direct oxidation of H₂O₂, it is interesting to develop new materials with high efficiency and small dimensions for the detection of H₂O₂.

The many methods, such as sol-gel technique [6], electro deposition [7], and self-assembly [8], to immobilize various organic and inorganic electron transfer mediators on electrode surface to prepare chemically modified electrode (CME). So far numerous nano-metal oxides, such as nickel oxide [9], zinc oxide [10] and cobalt oxide [11], have attracted considerable interest in the bioanalytical area because of their large specific surface area, good biocompatibility, simple fabrication, and good chemical and physical stability, nano copper oxide and nano manganese dioxides has been to be a kind of suitable mediator to reduce the overpotenial for the electrochemical oxidation or reduction of H₂O₂[12-13]. Carbon nanotubes (CNTs), the micro porous carbon macromolecules discovered by Iijima, have been considered as promising materials to adsorb hydrogen in their regular nanometric microstructure[14]. CNT have novel properties, making them potentially useful in many applications in nanotechnology, electronics, optics, and other fields of materials science, as well as potential uses in architectural fields. They exhibit extraordinary strength and unique electrical properties, and are efficient thermal conductors. Also has advantages in electronics, nanotechnology and the used of other ingredients mixed with CNT modified electrode used for the detection of hydrogen peroxide [15-17].

In particular, modification of CNTs with metal oxides is of importance for the development of CNT-based devices. Up to now, different metal oxides such as TiO₂, SnO₂, ZnO, Fe₂O₃, MnO₂ and RuO₂ have been reported to modify CNTs [18-27]. In the present work, the first step to prepare copper oxide mixed with multi-wall carbon nanotubes and manganese dioxide mixed with multi-wall carbon nanotubes. Then, the preparation of copper oxide and manganese dioxide mixed with multi-wall carbon nanotubes modified on glassy carbon electrode (GCE). The second step of physical characteristic with techniques X-ray diffraction (XRD) and Field Emission Scanning Electron Microscope (FE-SEM). The third step is to measure the modified electrode by voltammetry and amperometry to investigate techniques for hydrogen peroxide.

Material and methods

Chemicals

Copper (II) acetate, manganese (II) acetate, N,N-dimethylformamide (DMF), ammonia solution 30% Sodium dihydrogen phosphate and Ethanol absolute were purchased from CARLO ERBA reagent, Italy. Nitric acid 70% from AJAX Finechem, New Zealand. Sulphuric acid 98% from Mallinckrodt, Thailand. Di-sodium hydrogen orthophosphate from fisons Scientific Equipment, England. Hydrogen peroxide 30% w/v from Fisher Scientific,UK. Multi - walled carbon nanotube, diam. = 110 - 170 nm, length = 5 - 9 micron, 90+% from Sigma-Aldrich, Japan.

Other chemicals were purchased in analytical grade and used without further purification. All solutions were prepared with distilled water, which was purified with a Milli-Q purification system (Barnstead, USA) to a specific resistivity of >18 $M\Omega\ cm$.

Instruments

The electrochemical measurements were performed a potentiostat (Auto using lab/PGSTAT20). A three-electrode configuration consisted of a modified GCE (5 mm \times 5 mm \times 2 mm) as a working electrode, a reference electrode (Ag/AgCl) and a counter electrode (carbon ink). Microstructure and morphology were investigated using X-ray diffraction (08 Advance, Burker AG) field-emission scanning electron microscopy (FESEM, JEOL-6700).

Purified of MWCNTs composites

The MWCNTs were then soaked in the acid solution (H_2SO_4 : HNO_3 = 1:3) for 24 h, to remove the Fe particles, followed by the step of washing, filtering and drying at 110 °C for 24 h.

Preparation of CuO/MWCNT composites

Prepare 0.5 mg of $\text{CuO}(\text{CH}_3\text{COO})_2.\text{H}_2\text{O}$ were dissolved in 5 ml deionized water. Then 0.10 ml NH₃.H₂O (25wt%) solution was slowly added into more than solution under continuous stirring to form the successor solution and 10 mg MWCNTs were soaked in the solution for 17 h after, the WMCNTs were centrifiugally separated product and calcined at 300 °C for 2 h, respectively. The CuO/MWCNTs composites were obtained.

Preparation of MnO₂/MWCNTs composites

Prepare 0.5 mg of Mn(CH₃COO)₂.H₂O were dissolved in 5 ml deionized water. Then 0.10 ml NH₃.H₂O (25wt%) solution was slowly added into more than solution under continuous stirring to form the successor solution and 10 mg MWCNTs were soaked in the solution for 17 h after, the WMCNTs were centrifugally separated product and calcined at

200 °C for 24 h, respectively. The MnO₂/MWCNTs composites were obtained.

Preparation of MnO₂/CuO/MWCNTs composites

Prepare 5.0 mg Cu (CH₃COO)₂.H₂O and 5.0 mg Mn(CH₃COO)₂.H₂O were dissolved in 10 ml deionized water. Then 0.10 ml NH₃.H₂O (25wt%) solution was slowly added into more than solution under continuous stirring to form the successor solution and 10 mg MWCNTs were soaked in the solution for 17h after, the WMCNTs were centrifugally separated product and calcined at 300°C for 5 h, respectively. The MnO₂/CuO/MWCNTs composites were obtained.

Modification of CuO/MWCNTs/GCE, MnO2/MWCNTs/GCE and MnO₂/CuO/MWCNTs/GCE electrode

Before modification, the GCE surface was carefully polished with aluminum (0.3μm diameter) slurry on polishing cloth and the sonicated successively in ethanol and distilled water for 5 min, respectively. The preparation of the suspension MnO₂/CuO/MWCNTs concentration of 1 mg MnO₂/CuO/MWCNTs/ml DMF was prepared by the MnO₂/CuO/MWCNTs 1 mg mixed with DMF 1 ml sonicated for 30 min to be a black suspension is homogeneous. It will be the solution. Then, micropipette 10μL pipettes onto the surface of a GCE and then left to dry.

Electrochemical measurement

CV was carried out in the solution 0.1 M of phosphate buffer pH 7.0 under potential range -1.0 to 1.0 V at 50 mVs⁻¹. Amperometry were carried out in the potential 0.5 V for 300s in 0.1 M phosphate buffer pH 7.0 solution containing 100 mM H_2O_2 .

Result and discussion

Morphological characterization of the MWCNTs, CuO/MWCNTs, MnO2/MWCNTs and MnO₂/CuO/MWCNTs nanocomposite electrodes

The samples were further characterized by XRD fig. 1 show the XRD pattern of the pure MWCNTs, MnO₂/MWCNTs and CuO/MWCNTs composites. The diffraction angles at $2\theta = 35.5^{\circ}$, 38.8° , 48.8° , 58.1° , 61.3° , 66.1° and 68.0° are assigned to $(1\ 1\ 1)$, $(1\ 1\ 1)$, $(-2\ 0\ 2)$, $(2\ 0\ 2)$, $(-1\ 1\ 3)$, $(-3\ 1\ 1)$, $(2\ 2\ 0)$ planes of monoclinic CuO structure. The peak at 37.1° and 66.3° endorse the presence of MnO₂. The peak at 26.26° was ascribed to the typical $(0\ 0\ 2)$ reflection of MWCNTs.

The morphologies of the products were then studied by the field emission scanning electron microscope. Fig. 2 shows the images of (A) MnO₂/MWCNTs, (B) CuO/MWCNTs and (C) MnO₂/CuO/MWCNTs composites. The distribution of metal nanoparticles dispersed well on a regular basis.

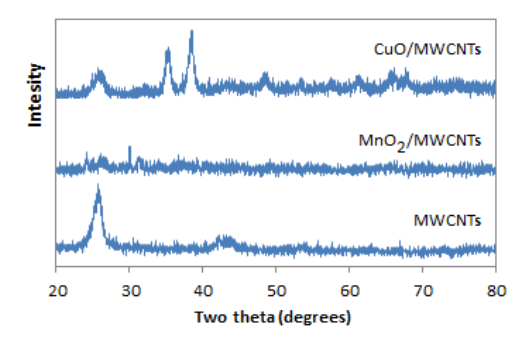


Fig. 1 XRD pattern of the pure MWCNTs, MnO₂/MWCNTs and CuO/MWCNTs composites.

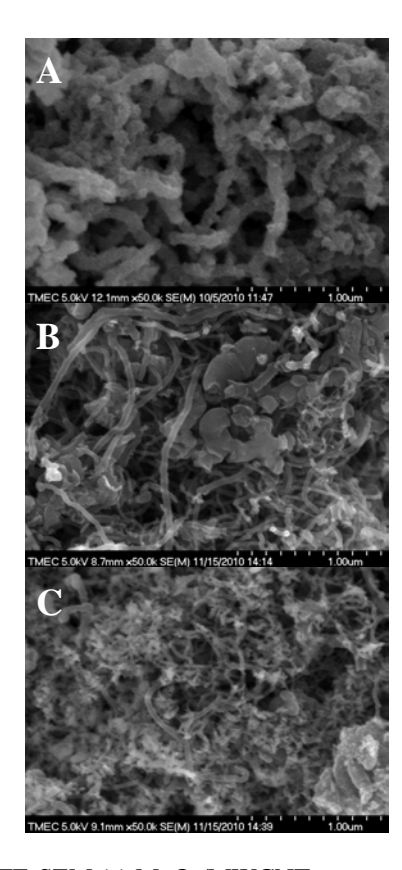


Fig.2 FE-SEM (a) MnO₂/MWCNTs, (b) CuO/MWCNTs and (c) MnO₂/CuO/MWCNTs composites.

Voltammetric behavior of H_2O_2 at the Bare GCE, CuO/MWCNTs, MnO₂/MWCNTs and MnO₂/CuO/MWCNTs electrodes

Fig. 3 shows the cyclic voltammetric behavior of Bare, $MnO_2/MWCNTs$, CuO/MWCNTs and $MnO_2/CuO/MWCNTs$ nanocoposties electrodes in the presence and absence of 1 mM H_2O_2 at scan rate of 50 mVs⁻¹. At the Bare, $MnO_2/MWCNTs$, CuO/MWCNTs and $MnO_2/CuO/MWCNTs$ electrodes oxidation of 0.5 V. However, no obvious oxidation and reduction peak of H_2O_2 was obtained

in the potential range of -1 to 1 V. It can also be seen that the current, the values are substantially higher than those obtained with uncoated surface of glassy carbon electrode. When the concentration of the $\rm H_2O_2$ in the electrolyte is increased from 1 to 100 mM, peak current at 0.5 V progressively increases Fig.4.

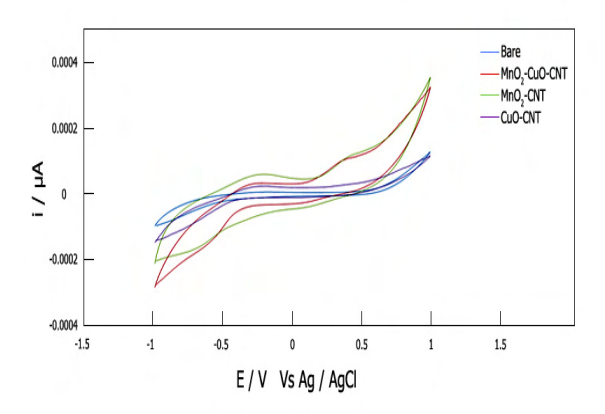


Fig. 3 Cyclic voltammograms (CVs) of the different electrodes recorded in phosphatebuffer pH 7.0 with a scan rate of 50mVs⁻¹.

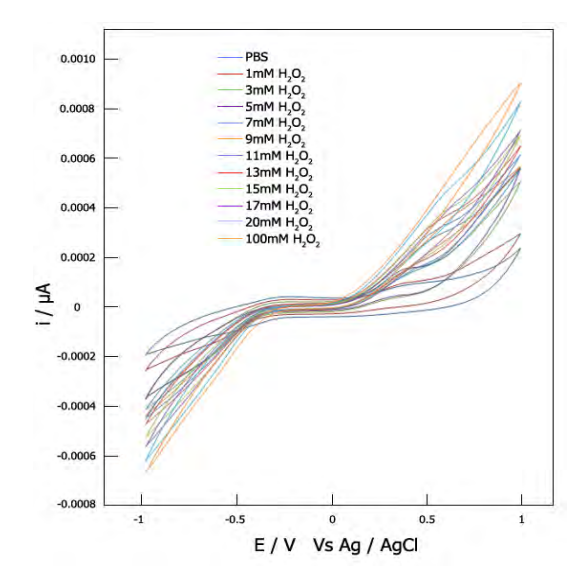


Fig. 4 cyclic voltammograms (CVs) of the $MnO_2/CuO/MWCNTs$ modified glassy carbon electrode recorded in different concentrations of H_2O_2 with a scan rate of $50mVs^{-1}$.

Amperometric response of the Bare GCE, CuO/MWCNTs, $MnO_2/MWCNTs$ and $MnO_2/CuO/MWCNTs$ nanocomposite electrode to H_2O_2

Fig.5 compares the amperometric response (at +0.50V) of the (A) Bare GCE, (B) CuO/MWCNTs, (C)MnO₂/MWCNTs and (D) MnO₂/CuO/MWCNTs to the successive addition of the $10~\mu M~H_2O_2$. Will be seen that the modified electrode to current is higher than non-modified electrode. As can be seen

electrode is as follows the CuO/MWCNTs, MnO₂/MWCNTs and MnO₂/CuO/MWCNTs linear response range of 0.2 \times 10 $^{\text{-3}}$ – 2.2 \times 10 $^{\text{3}}$ M. (R² = 0.998), 0.2 \times 10 $^{\text{-3}}$ – 1.2 \times 10 $^{\text{-3}}$ M. (R² = 0.996), 0.2 \times 10 $^{\text{-3}}$ – 2.2 \times 10 $^{\text{-3}}$ M. (R² = 0.995), respectively and detection limit of 0.17 μ M, 12.24 μ M, 33.0 μ M, respectively at a signal-to-noise ratio of 3.

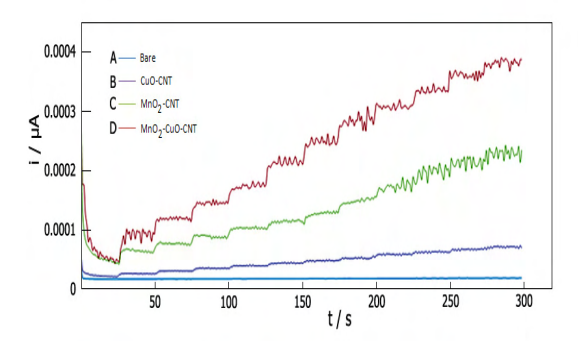


Fig. 5 Amperometric current–time recording obtained on increasing the H_2O_2 concentration in $10~\mu M$ step at (A) Bare electrode, (B) MnO2/MWCNTs, (C) CuO/MWCNTs and (D) MnO2/CuO/MWCNTs at an applied potential of 0.5~V~vs.~Ag/AgCl in pH 7.0 phosphate buffer.

Conclusion

The main feature of the present research lies in a novel method to detected H₂O₂ based MnO₂/CuO/MWCNTs /GCE electrode. assembly method was successful for fabricating a fast and simple sensor. Prepared CuO/MWCNTs, MnO₂/MWCNTs and MnO₂/CuO/MWCNTs on the GCE electrode surface nano-particles and the distribution on the electrode surface on a regular basis. Compared to the bare GCE electrode, the MnO₂/MWCNTs CuO/MWCNTs, $MnO_2/CuO/MWCNTs \quad nanocomposites \quad electrode$ reserves high electrocatalytic activity to wards the oxidation of H_2O_2 , a linear dependence ($R^2 = 0.998$, 0.995, respectively) on the H_2O_2 0.996, concentration from $0.2 \times 10^{-3} - 2.2 \times 10^{-3}$ M., 0.2×10^{-3} M. $10^{-3} - 1.2 \times 10^{-3}$ M., $0.2 \times 10^{-3} - 2.2 \times 10^{-3}$ M., respectively and a high sensitivity of combination of CuO, MnO2 particles and MWCNTs, which increases the electrocatalytic active area and promotes electron transfer. These advantages make it promising for providing a simple method to develop a new amperometric sensor for H₂O₂ detection.

- S. Yao, J. Xu, Y. Wang, X. Chen, Y. Xu, S. Hu, *Anal. Chim. Acta* 557 (2006) 78.
- 2. W. M. Weigert, Chem. Ztg. 99 (1975) 106.
- 3. H. Knorre, Galvanotechnik 66 (1975) 374.
- 4. X. M. Miao, R. Yuan, Y. Q. Chai, Y. T. Shi, Y. Y. Yuan, *J. Electroanal. Chem.* 612 (2008) 157.

- J. Gong, L. Wang, K. Zhao, D. Song, Electrochem. Commun. 10 (2008) 123.
- S.V. Aurobind, K.P. Amirthalingam, H. Gomathi, Sol-gel based surface modification of electrodes for electro analysis, Adv. Colloid Interf. Sci. 121 (2006) 1–7.
- D. Zhang, D. Chi, T. Okajima, T. Ohsaka, Catalytic activity of dual catalysts system based on nanomanganese oxide and cobalt octacyanophthalocyanine toward four-electron reduction of oxygen in alkalinemedia, Electrochim.Acta 52 (2007) 5400–5406.
- R.J. Collins, C.N. Sukenik, Sulfonate-functionalized siloxane-anchored selfassembled monolayers, Langmuir 11 (1995) 2322–2324.
- A. Salimi, E. Sharifi, A. Noorbakhsh, S. Soltanian, Immobilization of glucose oxidase on electrodeposited nickel oxide nanoparticles: direct electron transfer and electrocatalytic activity, Biosens. Bioelectron. 22 (2007) 3146–3153.
- J. Zang, M.L. Chang, X. Cui, J.Wang, X. Sun, H. Dong, C.Q. Sun, Tailoring zinc oxide nanowires for high performance amperometric glucose sensor, Electroanalysis 19 (2007) 1008–1014.
- A. Salimi, R. Hallaj, S. Soltanian, H. Mamkhezri, Nanomolar detection of hydrogen peroxide on glassy carbon electrode modified with electrodeposited cobalt oxide nanoparticles, Anal. Cham. Acta 594 (2007) 24–31.
- X.-M. Miao, R. Yuan, Y.-Q. Chai, Y.-T. Shi, Y.-Y. Yuan, Direct electrocatalytic reduction of hydrogen peroxide based on Nafion and copper oxide nanoparticles modified Pt electrode, J. Electroanal. Chem. 612 (2008) 157–163.
- K. Schachl, H.Alemu, K.Kalcher, J. Jezkova, I. Svancara, K. Vytras, Analyst 122 (1997) 985.
- Iijima S. Helical microtubules of graphitic carbon. Nature 1991; 354:56–8.
- Abdollah Salimi^{a,b,*}, Aazam Korani^a, Rahman Hallaj^a, Roshan Khoshnavazi^a, Hasan Hadadzadeh^c. Analytica Chimica Acta 635 (2009) 63–70.
- 16. Bin Xu, Min-Ling Ye, Yu-Xiang Yu, Wei-De Zhang*. Analytica Chimica Acta 674 (2010) 20-46.
- 17. Li Zhang*, Zhen Fang, Yonghong Ni and Guangchao Zhao. Int. J. Electrochem. Sci., 4 (2009) 407-413.
- C.S. Kuo, Y.H. Tseng, H.Y. Lin, C.H. Huang, C.Y. Shen, Y.Y. Li, S.I. Shah, C.P. Huang, Nanotechnology 18 (2007) 465607.
- 19. S. Banerjee, S.S. Wong, Nano Lett. 2 (2002) 195.
- 20. W.Q. Han, A. Zettl, Nano Lett. 3 (2003) 681
- G.M. An, N. Na, X.R. Zhang, Z.J. Miao, S.D. Miao, K.L. Ding, Z.M. Liu, Nanotechnology 18 (2007) 435707.
- X.Y. Wang, B.Y. Xia, X.F. Zhu, J.S. Chen, S.L. Qiu, J.X. Li, J. Solid State Chem. 181 (2008) 822.
- J.W. Liu, X.J. Li, L.M. Dai, Adv. Mater. 18 (2006) 1740.
- X.B. Fan, F.Y. Tan, G.L. Zhang, F.B. Zhang, Mater. Sci. Eng. A 454–455 (2007)37.
- Yan S.C., Wang H.T., Qu P., Zhang Y., Xiao Z.D., Synth. Met., 2008, doi:10.1016/j.synthmet. 2008.07.024.
- Z. Fan, J.H. Chen, B. Zhang, B. Liu, X.X. Zhong, Y.F. Kuang, Diamond Relat. Mater.17 (2008) 1943.
- Z.Y. Wang, G. Chen, D.G. Xia, J. Power Sources 184 (2008) 432.

The Use of Epoxy-Clay Nanocomposite for the Medical Electronic Implant Device Encapsulation

N. Nakthong^{1*}, Z. Lertmanorat² and T. Srikhirin³

* E-mail: nithimay99@hotmail.com

Abstract: Organoclay was used to reduce the water absorption rate of epoxy by fabricating epoxy-clay nanocomposite (ECN) for encapsulating implantable devices. The EPO-TEX® 302-3M, a biocompatible grade epoxy, was tested for its dispersibility with six commercially available organoclays from Elementis. The organoclays were tailored made to be suitable for dispersing in high (Bentone SD-2 and Bentone 27), medium (Bentone SD-1 and Bentone SD-3) and low (Bentone 38 and Bentone 34) polarity solvent. Only the high polarity organoclays formed a highly dispersed phase in the epoxy, appeared as the transparent liquid, while the medium and low polarity organoclays showed a lower dispersion in the epoxy. The dispersed organoclays were converted to ECN by room temperature cure for 24 hrs and followed by heat cure at 60°C for 3 hrs. The 3wt% clay concentration of high polarity-ECNs were not observed a strong broad peak in X-ray diffraction (XRD) pattern, indicating the high dispersed state of the organoclays in epoxy matrix. Scanning electron microscope (SEM) was used to observe morphology and orientation of clays in the matrix. The high polarity organoclays and low polarity organoclays were chosen for the encapsulation test. The circuit board was plasma treated to improve the adhesion between the board and ECNs. The water absorption of the composites was tested by submerging them in 50°C saline solution, applying 15 V_{DC} after that observe rusty, apply voltage for current detection, and compare with pure epoxy. The biocompatibility test is currently underway.

Introduction

Organic coatings have been widely used for implant because of biocompatibility property, good water moisture resistance, good processing characteristics and low cost such as silicone, parylene C, epoxy, PMMA, etc. [1,2]. Especially they are insulator materials which are suitable to encapsulate electric circuit for implant. Epoxy resin is well known insulating material has been used as protective coating and adhesive in this case due to its high chemical and heat resistance, excellent adhesion, very good electrical insulating properties, high strength, low volatility, low creep, low shrinkage and good processing characteristics^[3]. However the coatings are not permanent in long term because of its crack, corrosion, and void. There were two possible

mechanisms supported the reason for failure. First, water had entered via the cracks noted in the epoxy second, water had condensed out in voids between the epoxy and the substrate windings. Epoxy is water vapor permeable and present the hydrophilic property because of hydroxyl groups in the cured polymer network, so the main problem of this polymer is water absorption in its framework in long term situation. Epoxy-claycomposite are interesting to study and compare to pure epoxy.

Epoxy-clay nanocomposite is compound in which nanoclay (clay dimention range is 1-100 nm) particles are dispersed in an epoxy polymer matrix. In recent years, this material is interested in engineering and scientific coatings due to their excellent properties such as reduced gas permeability, high stability, optical clarity, flame retardation, reduced water absorption, reduced corrosion and others dramatic mechanical properties. Clay was added into the polymer for improve these properties however the efficiency of a filler to improve the physical or mechanical properties not only depended on raw materials but also depended on degree of dispersion of filler in the polymer matrix. High dispersion shows much highly interfacial area for reactions, so it leads to be larger surface area per unit volume and higher aspect ratios of the particulate constituent indicating higher composite properties. When the clay layer thickness changed from microscale to nanoscale, the surface area increased about one thousand times, so nanocomposite showed the excellent efficiency and could be improved the properties when compared to microscale. Three composite types (conventional microcomposite, ordered intercalated nanocomposite and disordered exfoliated nanocomposite) are usually observed and used to explain the morphology of clay in the epoxy matrix.

Conventional microcomposite: The polymer chain or epoxy (blue line) cannot insert between silicate layers of clay (red bar), so that we can observe a strong peak in X-ray diffraction pattern and show the opaque specimen.

Ordered intercalated nanocomposite: This composite type is higher clay dispersion, because polymer can insert between silicate layers and generate higher lattice spacing (d). It will show a broad peak at

¹ Material Science and Engineering Programme, Faculty of Science, Mahidol University, Rama VI Road, Bangkok, Thailand 10400

² Department of Electrical Engineering, Faculty of Engineering, Mahidol University, Putamonton sai4, Salaya, Nakornpathom, Thailand 73170

³ Department of Physic, Faculty of Science, Mahidol University, Rama VI Road, Bangkok, Thailand 10400

lower angle in X-ray diffraction pattern, and it is rather transparent when compare with convensional type.

Disordered exfoliated nanocomposite: Clay can disperse very well in the polymer and disappear any stack of clay in the matrix. Polymer can insert to silicate layer and separate very well, thus amorphous phase is generated instead of clay crystalline and disappear any peak in X-ray diffraction pattern. In addition the clearly transparent nanocomposite is observed.

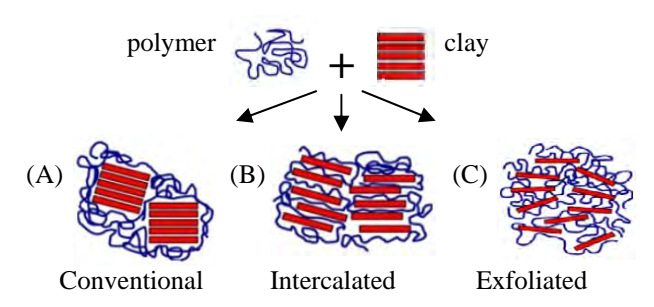


Figure 1: Three types of epoxy-clay composite [4].

Attempt of the research to reduce the water permeability of epoxy coatings had been done in term of epoxy-clay nanocomposite for encapsulating the implant electronic circuit and compare to pure biocompatible grade epoxy.

Materials and Methods

Materials

Electronic circuit boards were machined into 17.0 x 15.0 x 0.8 mm and encapsulated with epoxy-clay nanocomposite for comparing to pure epoxy in long term testing. Five capacitances that were parallel on two wires with lead free were encapsulated by epoxy and ECNs for accelerated test. The epoxy used in this study was EPO-TEK® 302-3M composting of two components (resin and hardener) with biocompatible grade. Six commercially available organoclays (Elementis) were used for dispersion test. There are suitable for high (Bentone SD-2 and Bentone 27), medium (Bentone SD-1 and Bentone SD-3) and low (Bentone 38 and Bentone 34) polarity solvent. Flux for electronic processes was used the non corrosive type.

Metodology

Cleaning the electronic circuit

Electronic circuit boards were cleaned before encapsulated with coating to increase the adhesion between the coating and surface. Moreover it can protect the corrosion will be occurred. The surface treatment of electronic circuits was adjusted from Wong and McBride method ^[5]. First of all, the circuit boards were soaked in flux reagent for 5 min afther

that they were soaked in flux reagent during ultrasonic cleaning for 5 min and rinsed in deionized (DI) water. Second, they were soaked in detergent for 5 min and then sonicated in detergent solution, 5 min and rinsed in DI water again. Third, they were soaked in DI water during ultrasonic cleaning for 5 min and following by the same steps with isopropanal, alcohol and DI water, respectively. After that, rinsed in DI water and Blowed the circuits with Nitrogen gas. Finally, baked in clean oven at 120°C for 5 h and keeped them in desicator. Plasma treatment about 5 min was performed before encapsulation. The cleaning efficiency was determined by contact angle measurement.

Epoxy-clay nanocomposite fabrication

Direct mixing method with hotplate stirrer was used for mixing between epoxy and organoclay. First the epoxy resin was vacuumed until no bubbles before the organoclay powder was mixed in epoxy resin, added some dispersant (EtOH:DI water = 95:5) and stirred at 900 rpm for 5 hrs at 30°C after that the mixture was sonicated in a sonicator for 1 h. Finally, curing agent was added into the mixture, and the composite solution was poured into the silicone mold for electric circuit encapsulation. Thickness was about 2 mm per each direction. The sample was cured at room temperature for 24 h and followed by heat cure at 60°C for 3 h. Epoxy-clay composites were fabricated with various types of organoclay to determine which type of organoclay will be suitable to fabricate the ECNs and compared the property of ECNs to pure epoxy.

Characterization

Contact angle measurement was used to examine the changing of chemical property on the electronic board and indicate the degree of adhesion between circuit board and coating (epoxy and ECNs) after plasma treatment. The scanning electron microscope (SEM) was used to demonstrate the dispersion, morphology, orientation and thickness of organoclay in the epoxy matrix. The composites were fractured under liquid nitrogen and polymer matrix was eliminated by strong acid. X-ray diffraction (XRD) was used to evaluate degree of intercalated between the clay basal layers. High and low polarity-ECNs were chosen for the encapsulation test. The water absorption of the composites was tested by submerging them in 50°C saline solution, applying 15 V_{DC} after that observe rusty, apply voltage for current detection, and compare with pure epoxy.

Results and Discussion

Cleaning processes investigation

After set up the electronics on the circuit boards, there are usually some flux on the surface. This flux

distributes adhesion between the circuit board and epoxy for coating, thus flux and moisture on the circuit boards had to get rid of by cleaning processes above and used the contact angle to determine the property. Table 1: Contact angle measurement with DI drop (0.5 µl) to evaluate the cleaning process of electronic circuit boards.

Circuit Board Condition	Average Angle	Picture
Before cleaning and no flux	81.0°	
Having flux	70.0°	
After cleaning	81.5°	(A)
After plasma treatment	20.5°	

The contact angle between circuit board and DI water was performed before and after cleaning processes. From table 1, before cleaning processes and no flux on the circuit board showed contact angle value was 81.0°. When flux was performed on the surface the value of contact angle was 70.0°, it was mean that flux reduced friction force between DI water and circuit boards, so it can reduce contact angle however it did not increase adhesion property because a drop of water was easy to move on the electronic surface board. After the circuit boards having some flux were cleaned. The contact angle changed from 70.0° to 81.5° showing that flux was eliminated. Moreover, plasma treatment improved the adhesion about 4 times, the contact angle was decreased from 81.5° to 20.5° due to changing of chemical and physical on the circuits after plasma treatment.

Nanocomposite measurement

Table 2: Comparison properties of high, medium and low polarity-ECNs with XRD and SEM techniques

Organoclay	High		Medium		Low	
polarity	Bentone SD-2	Bentone 27	Bentone SD-1	Bentone SD-3	Bentone 34	Bentone 38
Transparent Property	ification	s are over	stringen	for most i	Rather opaque	are usual
XRD	3wrs SD-2 8 8 8 8 8 8 8 8 8 8 8 8 8 8 8 8 8 8 8	3wt% B27	3wf% SD. 3wf% SD. 10	- ==	20 20 20 20 20 20 20 20 20 20 20 20 20 2	3 3 3 3 3 4 Bentons 38
SEM (3,000X)	600027 (SKY - 80100071813aa - 800	801 1507 351886 ILDAn	1800 150V MINN'IND-	200007 150V 33100 1810us	ANALIC 150V ELIANCIDIA.	SON STATE OF THE S
composite		1.1			1 . 1 1	. 1
Type	extoliated-inte	ercalated	Intercalated -	ınterc	alated and conver	itional

In this study, 3.0wt% of high, medium and low polarity-ECNs were fabricated with same condition to compare the different properties by using vision inspection, XRD and SEM technique. White area in SEM pictures referred to organoclay in ECNs. From table 2, SEM technique indicated that only the high polarity organoclays formed thin shape of particles and highly dispersed phase in the epoxy which related to transparent property. For the medium and low polarity organoclay composites showed aggregation of particles and bigger stacks of clay in the epoxy matrix, so they were lower dispersion and

rather opaque for visual inspection. The red lines of XRD patterns in the table 2 showed a strong peak in each organoclays while the yellow lines were XRD patterns of epoxy-clay composites. All of composites was not observed strong peak in XRD patterns when it was compared to pure clays. Moreover the yellow lines in XRD patterns showed a little broad peak that were shifted to lower value of 2θ for the composite from high polarity organoclays while medium and low polarity organoclays composites the lines were shift to the opposite way. It was assumed that all of organoclays had been dispersed in epoxy matrix.

From $2d\sin\theta = n\lambda$ when the little broad peak shifted to left hand assumed that intercalated between the clay basal layers was occurred (d spacing was increased) if it shifted to the right hand trended to aggregate of clay. The issue could demonstrate by SEM technique from the pictures in table 2. Only high polarity organoclay showed nanoscale of clay thickness (36-120 nm) in epoxy matrix. In the other hand, the medium and low polarity organoclays showed the clay thickness in term of microscale (210 nm-23µm). Total information was assessed that the high polarity organoclays (Bentone SD-2 and Bentone 27) showed a good mixing with the epoxy when compared to medium (Bentone SD-1 and Bentone SD-3) and low (Bentone 34 and Bentone 38) polarity organoclays because they were the highest dispersion property, so they were the best clay to form epoxy-clay nanocomposites.

Water absorption test

Bentone 27 and Bentone 34 or high and low polarity organoclay, respectively were chosen for encapsulation test and compared to pure epoxy in 50°C saline solution, applying 15 V_{DC} after that observe rusty, apply voltage for current detection. The electronic circuit will not be destroyed when water and air is not absorbed and diffuse through the coating. This study used the temperature acceleration and non acceleration to fine the coating aging at 50°C and 37°C , respectively. The samples have been survived and non rusty in this solution for 4 months, and further. The accelerated aging of material for encapsulation in human condition could calculate after they occur rusty by following the equation $(1)^{[6]}$.

$$F = 2^{(\text{Ti -Tref})/10}$$
 (1)

Where F is accelerated aging in human condition. T_{ref} is equal to human temperature (37°C) and Ti is elevated temperature (50°C). The result form calculation showed aging of total samples in the present has been 2.46 years in human body condition. Biocompatibility test is currently underway in qualitative and quantitative methods^[7].

Conclusions

Nanocomposites between biocompatible grade epoxy and organoclay could be fabricated from high polarity organoclay (Bentone SD-2 and Bentone 27) that showed highly dispersion in epoxy resin and performed exfoliated-intercalated nanocomposite in XRD and SEM technique while medium and low polarity organoclay exhibited in conventional form in microscale for epoxy-clay composites. These micro and nano composites have been used to test the water absorption property compare to pure epoxy for electronic encapsulation. However total coating samples have could protect electronic circuits from normal saline solution at 37°C and 50°C, and these

devices have been survived for 4 months moreover non rusty has been occurred. It means the composites and pure epoxy can be used in human body at least 2.46 years. In addition, the cleaning process can eliminate flux from the circuit board before encapsulation, and adhesion was improved to 4 times by plasma treatment.

- 1. Y.K. Song, J. Stein, W.R. Patterson and C.W. Bull Neural Eng. **4** (2007), pp. 213-218.
- G.E. Loeb, M.J. Bak, M. Salcman and E.M. Schmidt, IEEE Trans. Biomed. Eng. 24 (1977), pp. 121-128.
- 3. M.E. Frigione, L. Mascia and D. Acierno, J. Eur. Polym. **31** (1995), pp. 1021.
- 4. www.netcomposites.com
- C.P. Wong and R. McBride, IEEE Trans. CPMT. Part A, 174 (1994), pp. 542-552.
- 6. D.W.L. Hukins, A. Mahomed and S.N. Kukureka Med. Eng. Phys. **30** (2008), pp. 1270-1274.
- 7. T. Stieglitz, S. Kammer, K.P. Koch, S. Wien and A. Robitzki, 7th Annual Conference of IFESS. (2002), pp. 231-233.